

# Infrasound

**A summary of 35 years of infrasound research**



**Ludwik Liszka**

**Swedish Institute of Space Physics**

**Umeå, Sweden**



Infrasound: A summary of  
35 years of infrasound research

Ludwik Liszka

IRF Scientific Report 291  
January 2008

ISBN 978-91-977255-0-7  
ISSN 0284-1703

**INSTITUTET FÖR RYMDFYSIK**  

---

**Swedish Institute of Space Physics**

**Umeå, Sweden**

**Cover photograph:**

Infrasound microphone together with a wind barrier during propagation experiments in Southern France in March 1983. Photo: Ludwik Liszka

**To my family: Maj-Britt, John and Per**

## Preface

The author's interest in infrasound emerged from a decade of studies of wave phenomena in the ionosphere. These phenomena appeared frequently on radio-recordings of signals from artificial satellites, which started to populate space at the end of the 1950's. These oscillations in the electron density, influencing the propagation of radio signals, were evidently a result of the propagation of low-frequency pressure waves through the atmosphere. When infrasound and its unusual propagation properties was rediscovered during the 1960's in connection with atmospheric nuclear tests, it became obvious that the recording of infrasonic waves at the ground level could contribute to a better understanding of wave phenomena in the atmosphere.

This book is a summary of more than 35 years spent by the author and his co-workers within the field of infrasound. The work was strongly biased towards development of detection techniques with highest possible sensitivity and accuracy of pinpointing direction of origin.. The infrasound studied here, with frequencies between 0.5 and 10 Hz, at the levels occurring in the environment, is completely undetectable by human hearing. We are thus surrounded by a world of non-audible sounds, carrying vast amounts of information, which we cannot apprehend. It has therefore been a very exciting journey through a process of identifying new signal types and their properties, and finally finding their origins. This journey is, apparently, far from over. We continually find new infrasonic signatures, which cannot be immediately explained.

The main purpose of this book is to present for the interested reader the history of work in the area of infrasound at the Swedish Institute of Space Physics. It contains previously published, as well as unpublished, material. Another purpose of this book is to serve as a manual for users of our home page containing both the real-time data from the Swedish Infrasound Network (SIN), as well as an archive of infrasonic data (complete time-series) since 1994.

This book would not have been possible without the help of my co-workers. The early, fixed frequency, 2Hz recording system was developed by Kjell Englund. The present broadband system was developed (and is constantly improved) by Pär-Ola Nilsson, Jan Karlsson and Fredrik Rutqvist. The people who encouraged me both in my work within the field of infrasound and also to write this book are former and present directors of the Swedish Institute of Space Physics, Professor Bengt Hultqvist, Professor Rickard Lundin and Dr. Lars Eliasson. Professor Bengt Hultqvist also read and commented an early draft of this book.

The author is indebted to Mrs. Lisa Holmström who reviewed the manuscript of this book.

I am also grateful to my family for their patience during all the years I spent working within the area of infrasound, and later with this book.

## Table of Contents

Table of Contents .....	1
Introduction .....	8
Chapter 1 .....	9
Origins of the infrasound research at the Swedish Institute of Space Physics.....	9
Optimum frequency for the long-distance propagation of infrasound.....	9
Long-distance propagation of 2 Hz infrasound.....	12
Influence of atmospheric irregularities .....	14
References to Chapter 1 .....	15
Chapter 2.....	16
Shock Waves and Infrasound.....	16
Propagation of shock waves generated by aircraft.....	16
Detection of the shock wave-related infrasound on the ground and in the ionosphere .....	17
Calculation of flight trajectories.....	17
Results of the aircraft experiments.....	19
Table 1.....	19
References to Chapter 2.....	22
Chapter 3 .....	23
The Work on the Optimal Design of a Recording System .....	23
Tripartite array with a phase-detection system .....	23
Extracting more information from a tripartite array.....	25
Wind noise protection .....	27
Computerization of infrasonic stations .....	29
The application of the entropy concept to infrasonic data analysis .....	31
Definitions.....	31
The applications .....	32
References to Chapter 3 .....	33
Chapter 4.....	34
The Auroral Infrasound.....	34
Morphology of auroral infrasonic waves (AIW).....	35
Comparison of AIW with 2 Hz infrasound .....	35
References to Chapter 4 .....	36
Chapter 5 .....	37
The Discovery of Long-Distance Propagation of Infrasound from Man-made Sources .....	37
Results of the first year of operation of the arrays.....	37
Reference to Chapter 5 .....	40
Chapter 6.....	41
Concorde as an Infrasound Source.....	41
Principle of long-distance focusing of sonic booms .....	41
Results of early observations of Concorde.....	45
Conclusions concerning first observations of the Concorde.....	47
References to Chapter 6 .....	48
Chapter 7.....	49
High Resolution Observations of Infrasound Generated by the Supersonic Flights of Concorde .....	49
Again about generation of infrasound by a supersonic flight .....	49

Observations of the angle of arrival of Concorde signals .....	50
Angle-of-arrival variations and the atmospheric structure.....	60
References to Chapter 7 .....	62
<b>Chapter 8</b> .....	<b>63</b>
Wavelet Analysis of the Concorde-generated Infrasound.....	63
References to Chapter 8 .....	73
<b>Chapter 9</b> .....	<b>74</b>
Infrasound from Other Aircraft .....	74
Small supersonic aircraft.....	74
SR-71.....	76
Infrasound from subsonic aircraft .....	77
References to Chapter 9 .....	81
<b>Chapter 10</b> .....	<b>82</b>
Infrasound as a Detection Tool .....	82
Entry of large meteoroids.....	82
Jokkmokk event.....	83
Signal characteristics.....	84
Statistical detection of small meteor events .....	89
Detection of high altitude discharges: sprites .....	90
Possible generation mechanism .....	91
Search for chirp signatures.....	92
Occurrence of infrasonic chirps at Jämtön station .....	94
Observations on May 13, 2003 .....	98
Results of the ray-tracing for the event on May 13, 2003.....	100
Infrasound from thunderstorms.....	102
Volcano eruption: Hekla February 26, 2000.....	105
Observations of the February 26 <sup>th</sup> event .....	105
Spectral analysis of the event .....	108
Phase velocity determination .....	111
Distant gas explosion .....	112
Observations.....	112
Burning oil fields.....	115
Propagation of infrasound .....	116
Recording and analysis technique.....	116
Results of multivariate analysis.....	119
References to Chapter 10 .....	123
<b>Chapter 11</b> .....	<b>125</b>
Statistical Properties of the Infrasonic Wave Field on the Ground.....	125
Anisometry of the cross-correlation.....	125
Examples .....	127
Concorde .....	127
Small supersonic jets at distances of 400 - 500 km.....	128
A large gas explosion on April 24, 1995, distance 1400 km .....	129
A local storm passing by the microphone array - minimum distance 10 km.....	130
The anisometry of the cross-correlation on the ground and its consequences for signal detection .....	131
References to Chapter 11 .....	133
<b>Chapter 12</b> .....	<b>134</b>
Detection of Low-Flying Helicopters .....	134

Chapter 13 .....	137
Infrasound as an Environmental Factor – Effects on Humans .....	137
The exposure chamber .....	138
Experimental design .....	140
Results of the experiment .....	140
References to Chapter 13 .....	142
Appendix 1 .....	143
The Swedish Infrasound Network (SIN).....	143
Infrasound source locator .....	144
Time series viewer .....	145
Experimental infrasound viewer (with filters) .....	147
Basic data analysis .....	148

## Introduction

Sound waves with frequencies below 20 Hz are no longer perceived by the human ear as a sound. The frequency range down to a fraction of Hz is known as infrasound. During the last 40 years, the infrasound has become widely known for its unusual long-distance propagation. The first discovery of long distance propagation of infrasound is dated to the eruption of Krakatau, August 27, 1883 when the pressure pulse from the eruption was recorded in Europe after it travelled around the earth. When the long-distance propagation of infrasound was re-discovered during the 1960's, the research was concentrated on cataclysmic events, like nuclear explosions in the megaton-class. The knowledge that even many commonly occurring human activities may generate infrasound, which may be recorded over long distances, first came during the 1970's (Liszka, 1974). The research on the long-distance propagation of infrasound from man-made sources was in 1975 awarded the Wallmark Prize by the Royal Swedish Academy of Sciences. The phenomenon was confirmed by numerous researchers around the world and the long-distance propagation of infrasound became gradually common knowledge.

The physics of infrasound is sometimes called the seismology of the atmosphere. In both cases, it is a question of propagation of low frequency mechanical waves. There is, however, an essential difference between the wave propagation in the solid earth and in the atmosphere: the first medium is static while the atmosphere is a dynamic, "living" medium. Applying the same detection technique to infrasound as to seismic waves, one introduces serious limitations of the detecting potential. Therefore, the detection methods developed for the Swedish Infrasound Network (SIN) differs, to a large extent, from those used by the "seismologically-influenced" infrasound community. There are, instead, some similarities between the propagation of infrasound and radio wave propagation, as first pointed out by Davies (1973). Since the author of this book has a past within the ionospheric research and the radio wave propagation, it was natural that some concepts of the detection system and data analysis used in the SIN were adopted from that area.

The infrasound project with continuous recording of infrasound started in October 1973 at Kiruna Geophysical Observatory, which later became Kiruna Geophysical Institute and finally, the Swedish Institute of Space Physics (IRF). The recording equipment evolved through different stages; the present broad-band, computerized equipment started its operation at all stations in 1994. Infrasound recordings in Sweden are the longest continuous time series of its kind in the world. The network of infrasound stations has delivered a large amount of high-quality data during the past three decades. This data was used in several studies generating a number of new results about, for example, long distance propagation, detection of meteor impacts and infrasound emission from sprites.

The infrasound project received, during its early years, certain economical support from the Swedish Defence Research Institute. Recently, a substantial grant was received from the Kempe Foundation, which made it possible to modernize the SIN and develop an Internet-connected data base containing all data collected by the Network.

The present book is a summary of research conducted by the author and, mainly, based on the data from the SIN. This book is addressed principally to researchers working in the area of infrasonic detection, to users of the SIN's homepage and data base, but also to people generally interested in infrasound.

## Chapter 1

### Origins of the infrasound research at the Swedish Institute of Space Physics

At the end of 1950's, a major research field in geophysics worldwide was ionospheric physics. So a main objective of the Kiruna Geophysical Observatory (KGO), the present Swedish Institute of Space Physics (IRF), established during the International Geophysical Year, was to carry on research in ionospheric physics. However, already early on in its activity a great deal of attention was paid to mechanical waves in the upper atmosphere/ionosphere. The first time strong infrasonic waves at the ground level were observed was during the nuclear weapon test series at Novaja Zemlja between September 10 and November 4 1961. In addition to a number of ionospheric measurements, an attempt was made to construct a simple microbarograph using a loudspeaker in base-reflex-like box. That precursor to an infrasonic microphone was not very efficient: the poor loudspeaker technology in combination with a noisy radio tube amplifier resulted in low sensitivity and a low signal-to-noise ratio. Only after the three largest explosions on October 23, 30 and 31, 1961 could infrasonic signals be seen through the noise. However, the magnitude of these explosions were so large that even audible signals (like the rumble of a distant thunder) were reported in Northern Sweden, more than 1000 km from the explosion site. These events resulted in, for the first time at the Kiruna Geophysical Observatory, an interest in the infrasound and its propagation mechanism.

#### ***Optimum frequency for the long-distance propagation of infrasound***

Although the existence of long-distance propagation of low-frequency pressure waves in the atmosphere was well known, since long ago, the full explanation, based on experimental data, was given for the first time by Procnier and Sharp (1971). They could confirm, using the rocket-grenade experiments, their model calculations showing the highest frequency, which may be used to reach a given atmospheric height. The results clearly showed that lower optimum frequencies correspond to higher altitudes (see Fig. 1). This is a result of the increasing high-frequency attenuation with altitude. The long-distance propagation (through a reflection in the upper atmosphere) is possible when the wave can reach one of the temperature gradients where the reflection takes place. There are two height intervals at which infrasonic waves may be reflected: in the upper stratosphere (the lower sound channel at 45 – 50 km) and in the lower thermosphere (the upper sound channel at 90 – 100 km).

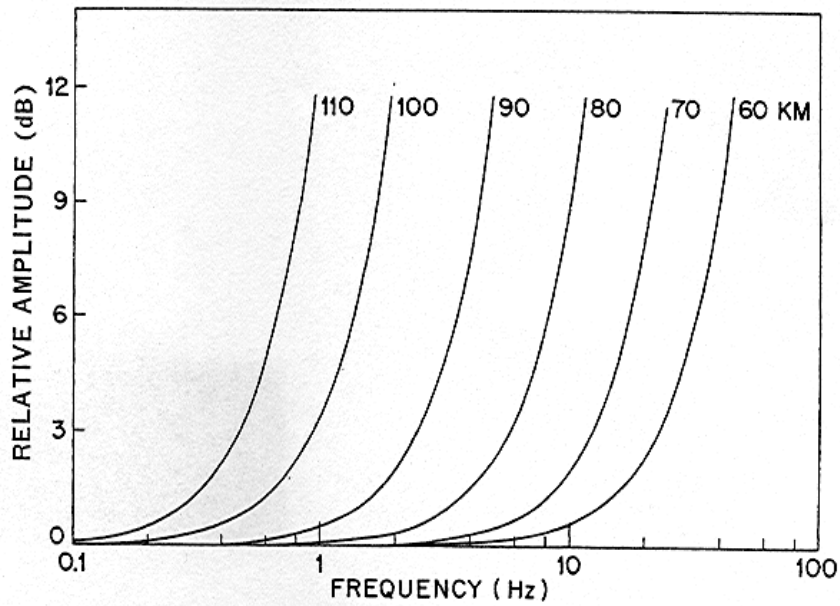


Fig. 1. Attenuation of an acoustic wave propagating to sea level from a range of source altitudes (after Procnier & Sharp, 1971).

At a first glance, the lower the frequency, the higher the probability is of long-distance propagation. However, there is another limiting factor: the atmospheric background noise, mainly the wind noise, which increases rapidly with decreasing frequency. It has been demonstrated by Procnier and Sharp that the optimum frequency for long-distance propagation is a trade-off between the attenuation at the reflection height, decreasing with the decreasing frequency, and the atmospheric background increasing with the decreasing frequency (see Fig. 2).

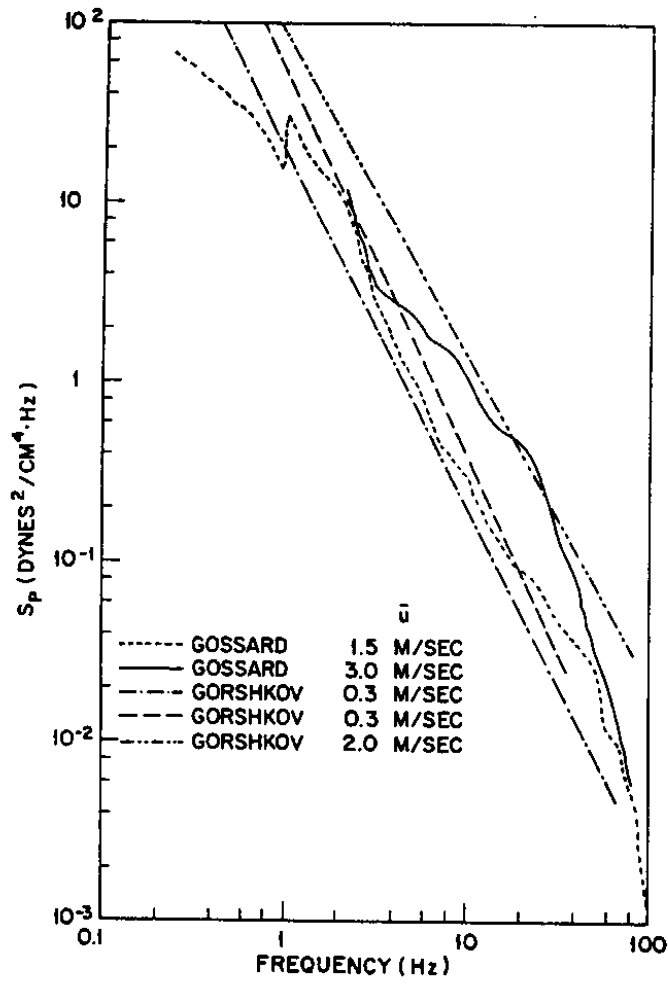


Fig. 2. Atmospheric pressure spectra (after Procnier & Sharp,1971).

These two factors determine the signal-to-noise ratio for a signal recorded at ground level after travelling from a given altitude. Results of calculations based on both theoretical knowledge and on the experimental data are shown in Fig. 3.

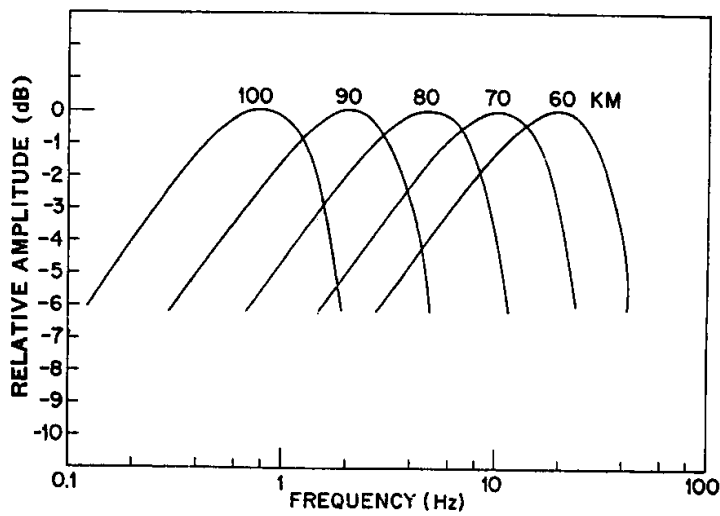


Fig. 3. Signal-to-noise ratio for different source heights versus frequency (after Procnier & Sharp,1971).

When the source is located on the ground, the long distance propagation will take place only when the signal with a given frequency may be detected after reflection in the upper atmosphere at the stratospheric or the termospheric temperature gradients. Fig. 3 shows that only signals between 1 and 2 Hz will be detected with the optimal signal-to-noise ratio at the ground after a reflection in the lower thermosphere (90 – 100 km).

For the above reason, the frequency of 2 Hz was selected for studies of the long-distance propagation of infrasound which started in Kiruna at the beginning of the 70's. Signals with frequencies below 1 Hz may, of course, be detected at long distances, but at a lower signal-to-noise ratio.

### ***Long-distance propagation of 2 Hz infrasound***

The propagation of infrasound in the atmosphere depends on the temperature distributions in the atmosphere and on the frequency of infrasound. At 2 Hz, the effects of gravity on the propagation are negligible. The propagation at frequencies in Hz-range is similar to that of sound waves, with the only exception that these waves are able to reach considerable heights in the atmosphere, where wind and temperature gradients will reflect them back to the ground. Using models of temperature- and wind distributions in the upper atmosphere, it is possible to compute the wave propagation. The temperature may be converted into the local speed of sound,  $C$  (in m/sec), since

$$C = 20.75\sqrt{T}$$

Where  $T$  is temperature in degrees Kelvin.

Examples of local speed of sound profiles for summer and winter mid-latitudes are shown in Fig. 4.

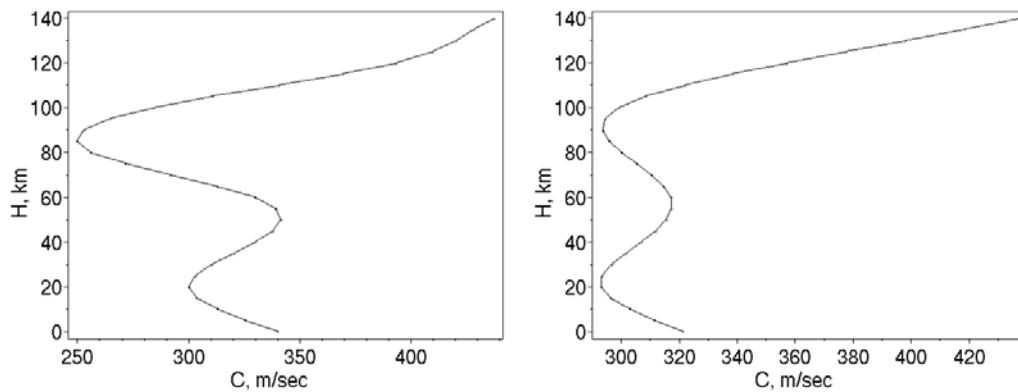


Fig. 4. Examples of speed of sound profiles for summer (left) and winter mid-latitudes.

The speed-of-sound profile depends both on the geographic position and on the time of the year. The wind profile, which is even more variable with respect to both position and time, must also be known in order to compute the infrasound propagation. The atmospheric wind field is usually described by the magnitude of a wind vector and its direction, or by representing through its components: the zonal component (in E-W direction) and the meridional component (in N-S direction). In particular, its larger zonal component is important for infrasound propagation.

At high altitudes, above 90 km, there is, in addition to the seasonal dependence, also a significant dependence of the wind on the local time. Examples of the height profiles of the

wind vector and its direction (in degrees measured clockwise from N) for midlatitude noon during summer (left) and winter are shown in Fig. 5.

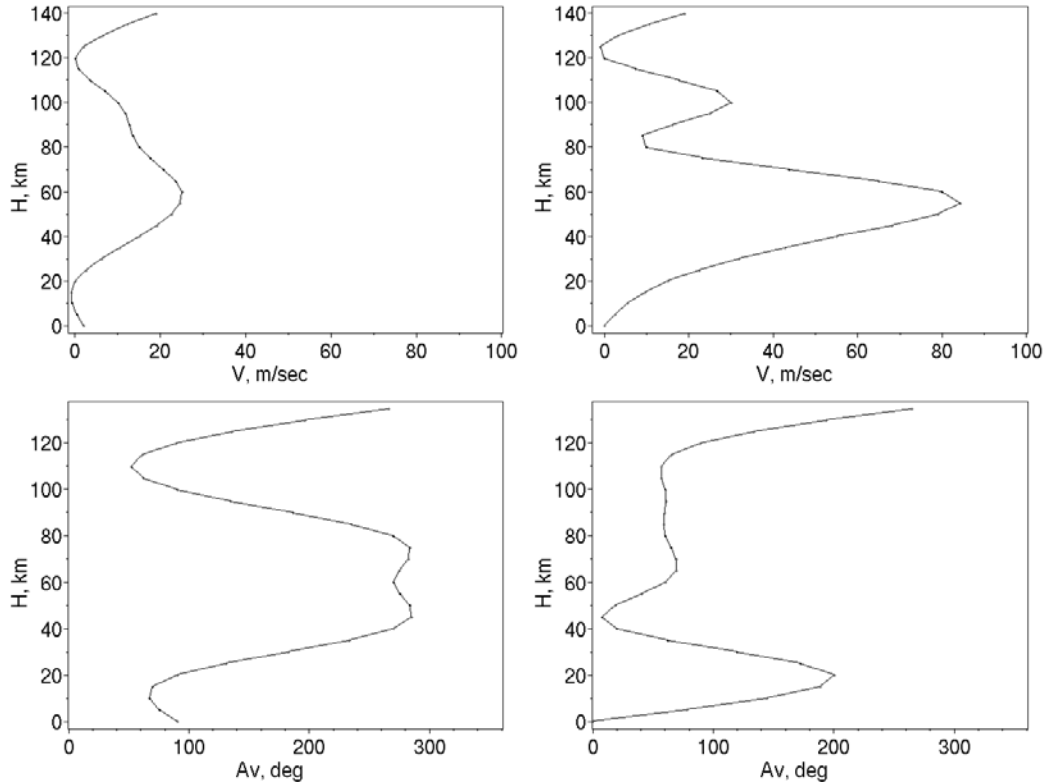


Fig. 5. Examples of the height profiles of the wind vector and its direction (in degrees measured clockwise from N) for midlatitude noon during summer (left) and winter.

The computations of the wave propagation must be done numerically, dividing the atmosphere into small cells of constant refractive index. A wave is usually described by the wave vector  $\mathbf{k}$  and its components. The wave vector has the same direction as the normal to the wave fronts and thus the *phase velocity*,  $v_p$ . The value of  $k$  is inversely proportional to  $v_p$ :

$$k = \omega/v_p$$

where  $\omega$  is the wave frequency.

In the atmosphere with the wind field  $\mathbf{w}$ , the Doppler-shifted value of  $\omega$ ,  $\Omega$  will be observed:

$$\Omega = \omega + \mathbf{k} \cdot \mathbf{w}$$

The energy of the wave is carried in the direction of the *group velocity*, defined as:

$$\mathbf{v}_g = d\Omega/d\mathbf{k}.$$

When computing the wave propagation using the ray-tracing method, the direction of the ray is assumed to be the direction of the group velocity.

Computations are started with a given angle of incidence (relative the horizontal plane) of the wave vector. The direction of the ray is then calculated in each cell it is passing. A reflection takes place in a cell where the vertical component of the wave vector,  $k_z$ , becomes zero. The calculations require a considerable computer capacity. The cell size is usually limited by the computer capacity. Examples of ray-tracing computations are shown in Fig. 6.

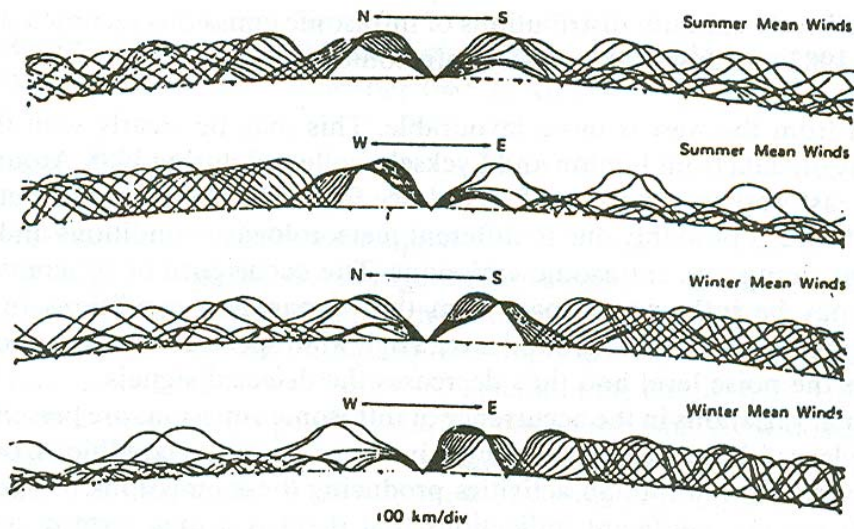


Fig. 6. Acoustic ray-paths projected onto vertical north-south and east-west planes, for the winter- and summer-mean wind models. The receiver is located in the centre of each plot (after Georges and Beasley, 1977).

The above example shows the difference between the summer and winter propagation. Differences between upwind, downwind and cross-wind propagation are also clearly visible. The ray-tracing method will be referred to on several occasions in this book.

### ***Influence of atmospheric irregularities***

In order to study effects of atmospheric irregularities on propagation of infrasonic waves, the temperature and wind models were modified by superposition of Gaussian fluctuations of  $c$  and/or  $w$ . Wave propagation in the “randomly” fluctuating atmosphere was then simulated (Liszka, 1907) by launching up to 20 rays with the same starting parameters, but passing each time through different sequence of Gaussian-distributed irregularities in  $c$  and  $w$ . The difference between propagation in a homogenous atmosphere (left) and an atmosphere with irregularities is shown in Fig. 7.

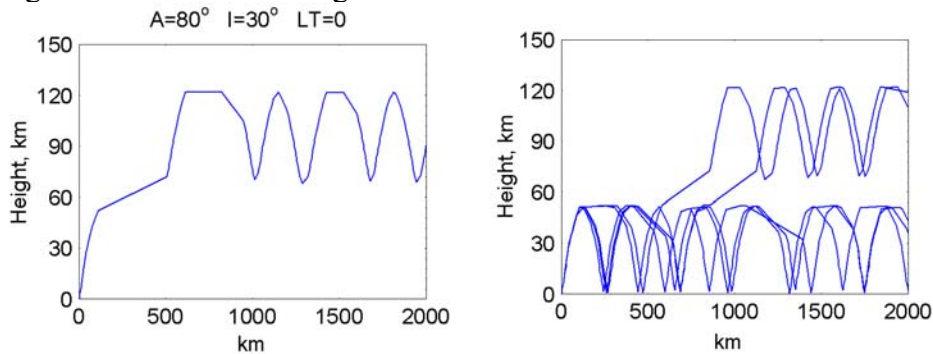


Fig. 7. Propagation of rays launched in the direction of  $80^\circ$  at an inclination angle of  $30^\circ$  at the local midnight for an uniform atmosphere (left graph) and for an atmosphere with Gaussian-distributed irregularities with the maximum amplitude of 5% of the ambient temperature.

As can be seen for the case of Fig 7. that in a uniform atmosphere, the rays escape into the thermosphere, trapped between the thermospheric gradient and the top of the stratosphere and never reach the ground. In an atmosphere with irregularities, only a fraction of rays will be trapped in the thermosphere. The majority of rays will propagate through reflections in the lower sound channel and reach the ground at a range of distances from the source. Another interesting observation was that atmospheric irregularities introduce “bundling” of rays leaving a point source, see Fig. 8. The example shows rays launched from a point source in the centre of a 4800 x 4800 km square at each even 2° azimuth at an inclination of 10°.

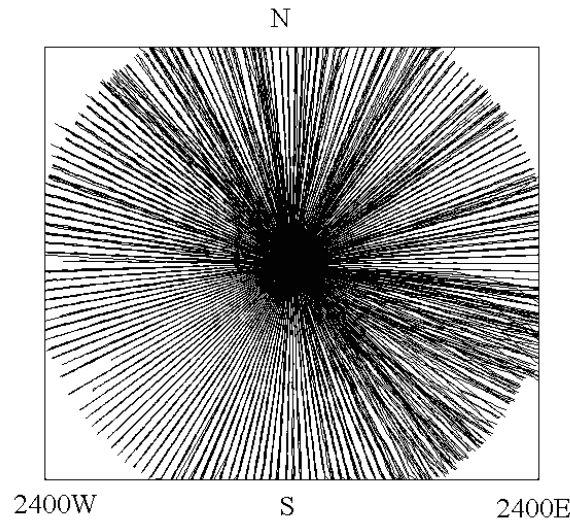


Fig. 8. Rays launched from the centre of the graph at 2° intervals of the azimuth and at an inclination angle of 10°. An atmospheric model with Gaussian-distributed irregularities with a maximum value of 1% of the ambient temperature.

It may be shown that even a weak fluctuation field of  $c$  and/or  $w$  may introduce quasi-ordered structures in the propagation pattern. When the standard deviation in the fluctuation field increases above a certain level, the quasi-ordered structures disappear.

The main conclusion is that the propagation mode may be changed by properties of the fluctuation field without changing the average values of  $c$  and/or  $w$ . These results indicate that even the best atmospheric model has a limited predictive power when compared to real-time measurements of the wind- and temperature fields.

### **References to Chapter 1**

- Georges, and T.M., Beasley, W.H. (1977). Refraction of infrasound by upper atmospheric winds. *J. Acoust. Soc. Am.* Vol. 61, p p. 28-34.  
 Liszka, L. (1997). Paper presented at the AGU Fall Meeting 1997, San Francisco.  
 Procnier R. W. and G. W. Sharp, *J. Acoust. Soc. Am.* 49, 622 (1971).

## Chapter 2

# Shock Waves and Infrasound

During the 60's, the interest in wave phenomena in the upper atmosphere gradually increased. Methods of studying propagation of acoustic gravity-waves in the atmosphere were developed. One of the early ray-tracing methods for the group path was developed by Cowling et al. (1970). The method applies to a model atmosphere with stratified winds. One of the possible applications was to trace sources of waves observed by radio methods in the ionosphere. A question arose if an auroral arc moving with a supersonic speed at a height of 100 km height could generate acoustic waves detectable at the ground level. However, it was not certain how accurate the ray-tracing technique was when applied to the real atmosphere. A possible test method became available using shock waves from supersonic aircraft. During that time, supersonic aircraft flights became common worldwide and the scientific community started to be interested in problems concerning the propagation of shock waves generated by these aircraft.

### ***Propagation of shock waves generated by aircraft***

It was shown by Meyer (1962), that the shock front produced by a supersonic source is in the far zone followed, at any given point in space, by a decaying oscillation. The major part of the oscillation energy is located within the uppermost frequency range of internal gravity waves and the lowest frequencies of acoustic gravity waves. The waves traveling upwards are amplified (Daniels et al., 1960) due to the density stratification in the atmosphere.

The idea of influencing the ionosphere by the shocks produced by supersonic aircraft has been developed by Marcos (1966). Flight trajectories of supersonic aircraft were chosen to obtain focusing of the shock at ionospheric altitudes. Effects of the shock on the ionosphere were detected studying frequency shifts of radio waves reflected at the point where the waves were focused. It was not obvious that the reported experiment could be successful also at high, auroral latitudes.

A further elaboration of Marcos' experiment was performed at auroral latitudes by the author (Liszka, 1971). In that experiment, possible due to a generous support from the Swedish Air Force, flight trajectories of Saab-35 Draken supersonic aircraft were programmed in two different ways in order to obtain

- (1) Focusing of waves on the ground after reflection from the stratosphere at about 40 km altitude,
- (2) Focusing of waves at the E-layer.

During the first test period, 12-15 January 1971, six flights were performed, three along each of two types of trajectories. In all three flights along the type (1) trajectory, clear ground effects were observed: a coherent infrasonic signal was detected at the ground. During three flights with ionospheric focusing, clear effects were observed during two of them. During the second test period, February 1-3, 1971, five flights were performed. The flight trajectories were then of type (2), although the deceleration of the aircraft in the final part of the flight was programmed to obtain focusing effects on the ground. During four flights, rather clear effects were observed both on the ground and in the E-layer. During the flight on February 1, 1971, ground measurements of 2 Hz signal were impossible due to a strong wind and the ionospheric measurements were uncertain because the E-layer reflection was very weak and unstable. The results indicated that the ray-tracing method may be

satisfactorily applied for calculation of flight trajectories for which the focusing of waves will occur.

### ***Detection of the shock wave-related infrasound on the ground and in the ionosphere***

In the beginning of 70's a question was raised as to whether shock waves generated by a supersonic aircraft could still be detected at the ground level after a reflection in the upper atmosphere. An experiment, using supersonic aircraft was therefore designed at the KGO for that purpose. Detection techniques for studies of effects of shock waves did not exist at that time and had to be developed.

It was expected that the shock wave generated by an aircraft after reflection in the stratosphere would not contain any audible components. The frequency of 2 Hz was selected for detection of possible stratospheric returns. At the beginning of the 70's the microphones for that frequency range were not easily accessible. Fortunately, Dr Per Bruel, the co-founder of the world-famous acoustic equipment company Bruel & Kjaer, became interested in the problem of infrasound detection and supplied the KGO with a modified piezoelectric microphone B&K4117. The frequency response of the microphone was shifted down in frequency partially closing the pressure equalizing channel. The microphone thus became sensitive at frequencies down to at least 1 Hz. This modified microphone was used for infrasound detection by the SIN stations until the middle of 1994. Having a microphone, the next step was to design a detection system.

The atmospheric waves focused on the ground were detected only in the infra-acoustic range, at a frequency of 2 Hz using a specially constructed correlator-interferometer (Liszka and Koskenniemi, 1971). The correlator measured true cross-correlation between two 2 Hz signals recorded by two spaced piezoelectric microphones. The baseline of the correlator was oriented in the direction perpendicular to the expected direction of arrival of focused infra-acoustic signals.

The atmospheric waves focused in the ionosphere were detected using a modified vertical sounding method. The 'first reflection recorder' developed in Kiruna (Olsson, 1971) was used to record the virtual height of vertical reflections of 3-MHz pulsed radio transmission. The virtual height was measured with an accuracy of 1 km. During that experiment the height interval 85-185 km was selected on the recorder. The height of the first reflection appearing in this interval was recorded. On January 15, a weak ionospheric disturbance associated with ionospheric absorption occurred which limited the amount of radio interference at 3 MHz and enabled high-accuracy measurements of the reflection height. Also during flights on February 2-3, 1971 a stable E-layer was present, which enabled measurements of reflection height.

### ***Calculation of flight trajectories***

It has been assumed that the direction of the group velocity of the wave packet following the shock front is normal to the shock front. The orientation of the shock front is determined by the direction of the motion (see Fig. 9) and the Mach angle.

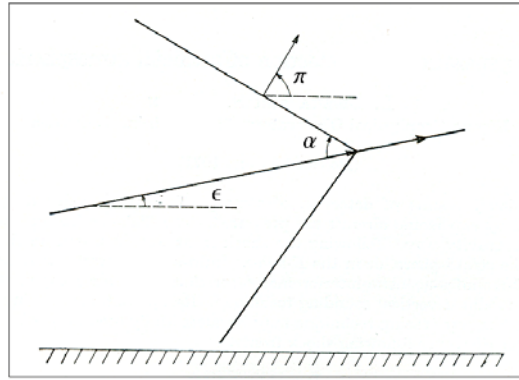


Fig. 9. Orientation of the shock front.

The Mach angle  $\alpha$  is defined as

$$\sin \alpha = a/v = 1/M \quad (1)$$

where  $a$  is the local sound velocity,  $v$  is the velocity of the aircraft and  $M$  is the Mach number. For a flight trajectory with elevation  $\epsilon$ , the slope of the normal to the upward going shock front is  $\text{tg} \pi$  given by

$$\text{tg} \pi = 90^\circ + \epsilon - \arctg(1/M^2 - 1). \quad (2)$$

The principle for focusing of the wave packets is shown in Fig. 10 (a, b) for trajectories type (1) and (2), respectively. In order to obtain focusing at point X of rays generated along the trajectory between points 1 and 2, the following conditions must be fulfilled for any pair of points  $i, j$  of the trajectory part 1-2:

(1) Ray paths from points  $i$  and  $j$  must intersect in the point X,

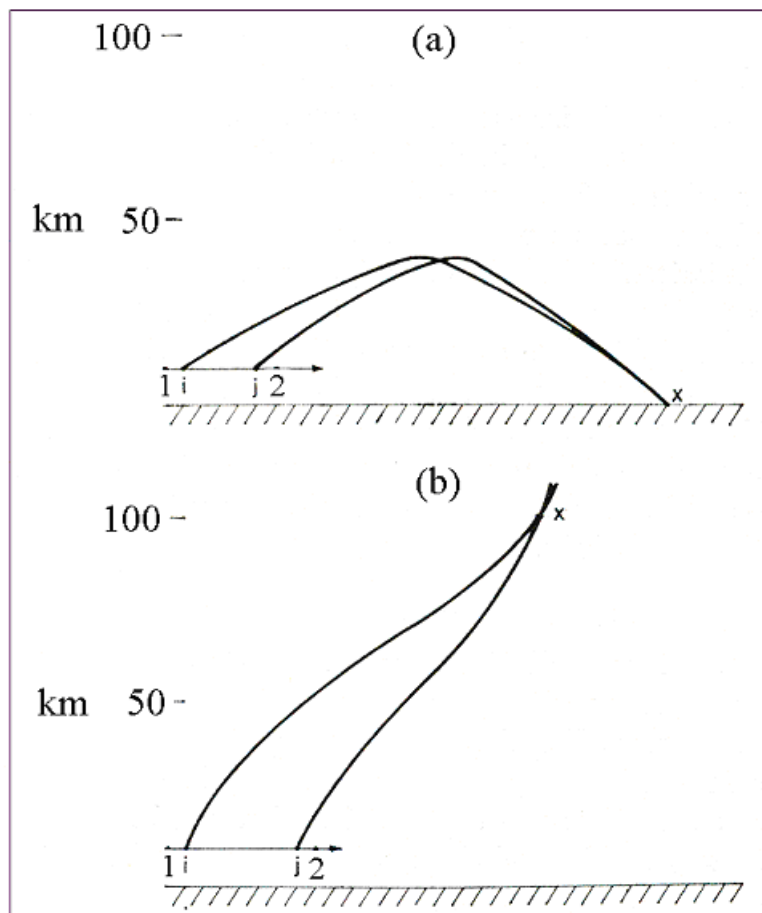


Fig. 10. The principle for focusing of the wave packets: (a) focusing on the ground after reflection from the stratosphere, (b) focusing at the E-layer.

- (2) The intersection must take place at the same time, i.e. the travel time between points  $i$  and  $X$  must be equal to the sum of the travel time between  $j$  and  $X$  and the flight time between  $i$  and  $j$ .

Ray paths and travel times were calculated using the ray-tracing method of Cowling et al. (1970). Winds and air temperatures up to 20 km were taken from local radiosonde measurements. Temperatures above 20 km were taken from the 1966 US Standard Atmosphere adjusted to the observed 20 km value. The wind model used in the height interval 20-70 km was based on rocket measurements made in January 1970 at the rocket range ESRANGE in Kiruna, using a falling parachute method. In the final reduction of the last three flights made on January 15, 1971, rocket measurements of the wind made on the same day at ESRANGE were used. In the height interval 70-120 km, the wind profile was taken from a contour map given by Murgatroyd (1966) for 60°N and adjusted to observed 70 km values. Temperature profiles were converted to sound velocity profiles. Also during the second test period, February 1-3, 1971, wind measurements from ESRANGE were used.

### **Results of the aircraft experiments**

Table 1 shows parameters of all 11 flights. The first three flights were performed along the type (1) trajectory, giving ground focusing. An example of the corresponding correlator-recording from January 14, 1971 is shown in Fig. 11. The vertical scale on this figure gives approximate values of the cross-correlation between two signals at 2 Hz recorded at a distance of 60 m. The broken line along the time axis shows the approximate duration of the supersonic part of the flight. The solid line indicates the part of the flight programmed for the focusing of infra-acoustic waves at the observing site on the ground.

**Table 1**

No.	Date	Time MET	Traject. type	Max. Mach no.	Infra-acoustic signals	Ionospheric effects	Remarks
1	12 Jan. 1971	09 20	1	1.14	Yes	-	
2	12 Jan. 1971	10 44	1	1.14	Yes	-	
3	14 Jan. 1971	09 22	1	1.14	Yes	-	
4	15 Jan. 1971	09 33	2	1.40	No	Yes	Variation in reflection height +6 km
5	15 Jan. 1971	10 14	2	1.40	No	Yes	Variation in reflection height -2 to +5 km
6	15 Jan. 1971	11 08	2	1.45	Yes	Yes	Variation in reflection height -3 to +4 km
7	1 Feb. 1971	13 40	2d	1.45	No	?	Surface wind, very weak and variable E-reflection results doubtful.
8	2 Feb. 1971	09 35	2d	1.45	Yes	Yes	Variation in reflection -4 to +3 km. Unusual short duration $E_e$ echo at 130 km 50 sec before the expected arrival of infra-acoustic waves. Clearly audible acoustic signal on the

							ground.
9	2 Feb. 1971	1042	2d	1.45	Yes	Yes	Variation in reflection height +7 km.
10	3Feb. 1971	0926	2d	1.45	Yes	Recorder failure	Variation in reflection height -2 to+7 km.
11	3 Feb. 1971	1033	2d	1.45	Yes	Yes	Variation in reflection height -2 to+6 km.

Explanation: Type 2d is the trajectory of type 2 followed by a deceleration part.

As can be seen that the 2 Hz signal is modulated with a low frequency. In particular, in the initial phase of the focusing, a period of 2 min may be clearly observed. The solid arrow on the diagram shows the expected start of the infra-acoustic signal, calculated under the assumption that the waves propagate with the velocity of sound. The duration of the signal is very large and cannot be simply explained. No ground wind was measured during this experiment. It must be remembered that the waves recorded on the ground traveled along a distance of the order of 200 km. No acoustic signals were heard during this experiment at the recording site.

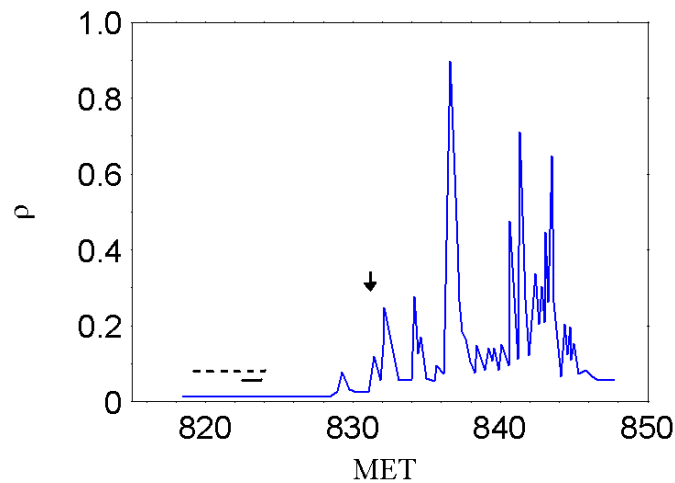


Fig. 11. An example of the 2 Hz correlator recording during flight No. 3 on January 14, 1971. The broken line along time axis shows the approximate duration of the supersonic part of the flight. The solid line indicates the part of the flight programmed for the focusing of infra-acoustic waves at the observing site on the ground.

An example of recording of ionospheric effects of shock focusing during flight No. 6 on January 15, is shown in Fig. 12. The recording gives the reflection height of 3 MHz pulses transmitted from Kiruna. The broken line along the time axis shows the approximate duration of the supersonic part of the flight. The solid line indicates the part of the flight during which the infra-acoustic waves were focused in the E-layer.

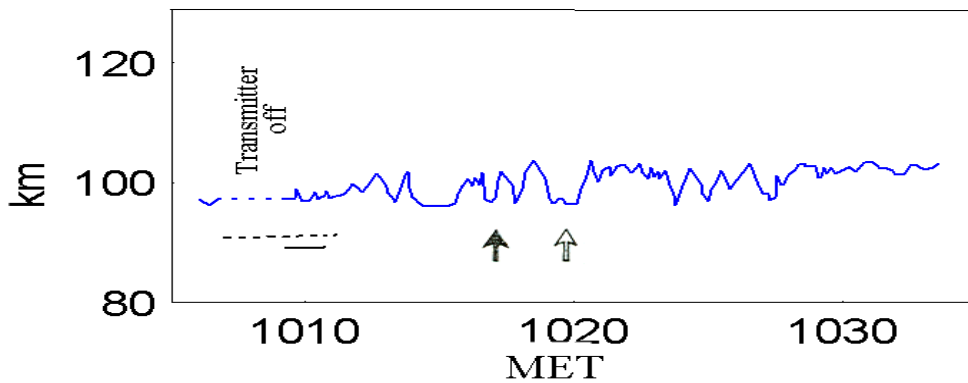


Fig. 12. An example of reflection height recording during No. 6 on January 15, 1971. Duration of supersonic and focusing portions of the trajectory is shown as in Fig. 11. The solid arrow indicates the expected time of arrival of waves with the period of 6 sec; the empty arrow indicates time of arrival of waves with the period of 2-5 min.

The oscillation of the reflection height represents the response of the ionosphere to the passage of acoustic waves into which the shock has evolved after propagation through the atmosphere. The signal reaching E-layer should contain a broad spectrum of waves with periods from 0.5 sec (2 Hz) up to the Brunt period (approx. 6 minutes). Due to the dispersion, waves with different periods will reach the ionosphere at different times. The solid arrow indicates the computed time of arrival of infra-acoustic waves (6-sec period) to the 100 km level measured from the start of focusing trajectory. The empty arrow indicates the expected time of arrival of waves with periods close to the Brunt period (2-5 min). As can be seen that the reflection height starts to oscillate long before the expected time of arrival of infra-acoustic waves. This is the case during two other flights on the same day and it is difficult to say if the flights coincided with a natural variation of the reflection height, or if it was caused by shock waves produced at the very beginning of the supersonic trajectory. One reason for the earlier onset of the ionospheric response may be that waves with periods shorter than 6 sec reach the E-layer height. Another reason for the earlier onset of oscillations may be due to the fact that the shock front travels, in general, with a velocity  $V_s$  larger than the velocity of sound. After Friedman et al. (1963)  $V_s$  is related to the pressure jump in the shock front as follows:

$$V_s = a \left| 1 + \frac{\gamma + 1}{4\gamma} \delta \right| \doteq a \left| 1 + 0.43\delta \right|$$

where  $a$  is the sound velocity,  $\gamma$  is the ratio of specific heats, and  $\delta$  is the relative overpressure. As the shock traveling upwards is amplified (Daniels et al., 1960), velocities appreciably larger than the sound velocity may easily be achieved at ionospheric heights even for shocks which are weak in the lower atmosphere.

It is interesting to compare present results with those obtained during similar experiments by Marcos (1966): ionospheric effects were detected there by a phase path technique giving merely the derivative of the phase path length. His experiments have shown small phase path changes of the order of 1 Hz with durations from 20 to 50 seconds. This corresponds to the resulting overpressure at E-layer of 20 percent. Ionospheric effects observed by Marcos seem to be caused by the redistribution of the ionization during the passage of the shock front. Decaying oscillations following the

shock front, which were observed in the discussed experiment, are too slow to be easily observed by the phase-path technique.

The main result of the discussed experiment was that the ray-tracing technique based on the linear theory may be satisfactorily applied in studies of propagation of atmospheric waves following shock fronts, if the real-time atmospheric data are available. Using solely the atmosphere model data, successful focusing could not be obtained.

Another interesting aspect of the discussed experiment is that even a relatively small supersonic aircraft, when accelerating in a particular manner, may influence the E-layer in a measurable way.

Only direct rays have been taken into consideration in the discussed experiment. Rays reflected from the ground are attenuated at the reflection and by the much longer propagation path. For an aircraft flying at an altitude of 10 km at Mach 1.42, the propagation path to the E-layer for reflected rays is about 25 km longer than for direct rays.

The experiment had an important impact on the future development of the infrasound program at IRF: the 2 Hz correlator recordings showed that highly correlated infrasonic emissions of unknown origin are very common at that frequency band. It also indicated the importance of proper wind noise reduction. Conventional plastic-foam wind noise filters, designed for the audible sound, appeared totally inadequate at 2 Hz.

The research pertaining to the generation and detection of infrasonic waves utilizing supersonic aircraft constituted a part of the PhD thesis of Sixten Olsson, defended at the Swedish Institute of Space Physics, Kiruna in May 1973.

## **References to Chapter 2**

- Daniels F. B., Bauer S. J. and Harris A. K.: 1960 *J. geophys. Res.* 65, 1848.  
Friedman M. P., Kane E. J. and Sigalla A.: 1963 *AIAA Journal* 1, 1327.  
Meyer R. E.: 1962 *J. geophys. Res.* 67, 2361.  
Murgatroyd R. J.: 1966 *Proc. R. Soc.* A288, 575.  
Wilson C. R.: 1969 *Planet. Space Sci.* 17, 1817.

Reference is also made to the following unpublished material:

- Cowling D. H., Webb H. D. and Yeh K. C.: 1970 *Tech. Rep. 38, Ionosph. Radio Lab., Univ. of Illinois.*  
Liszka L. and Koskenniemi K. 1971 *KGO Report.*  
Marcos F. A. 1966 *Airforce Surveys in Geophys. No. 175, AFCRL, Bedford Mass.*  
Olsson S.: 1971 *KGO Report.*

## Chapter 3

# The Work on the Optimal Design of a Recording System

The results of the experiments described in Chapter 2 and considerations about the most efficient frequency range for infrasound detection, directed the author to the frequency range around 2 Hz. As described earlier, the choice of that frequency range is a result of a compromise between the increasing probability of long-distance propagation with decreasing frequency and the fact that the atmospheric noise increases rapidly with decreasing frequency. This chapter discusses also the choice of the detection system and problems of wind noise reduction.

Due to the frequent occurrence of correlated signals at 2 Hz mentioned in Chapter 2, it was decided that the detecting device must provide the direction-of-arrival of infrasonic signals and, possibly, the inclination of the incoming ray. The previous experience with detection of low frequency acoustic signals, as documented in the literature, was limited to detection of acoustic pulses, like those in artillery direction finding and rocket-grenade experiments. Here, only the envelope of the pulse is recorded after it passed through a threshold detector. In a microphone array the differences between time-of-arrival across the array are used to calculate the angle-of-arrival of the wave package. Since the infrasound observed at 2 Hz usually lasts for seconds or even minutes, more information may be extracted from the signal by phase difference measurements of a continues wave. The signal is often highly irregular and the use of an envelope detector is difficult. At least three microphones (not located along a straight line) are needed to calculate the average properties of the wave-field over the array.

### ***Tripartite array with a phase-detection system***

The first measuring equipment developed in Kiruna used a narrow-band (6% bandwidth), fixed frequency (2 Hz), phase-detection technique which makes it possible to detect weak infrasound from point sources, far below the background level. Details of the equipment have been given earlier. The main part of the equipment was a tripartite array with microphones located at  $(x_1, y_1)$ ,  $(x_2, y_2)$  and  $(x_3, y_3)$ , where distances between microphones are shorter than one wavelength. Phase differences between microphone pairs 1-2 and 1-3 ( $\Delta\phi_{12}$  and  $\Delta\phi_{13}$ ) are measured by means of a two-channel phase comparator. These two phase differences give complete information about the wave vector of the incident wave. The wave vector may be described by the azimuth of the direction of arrival of the wave,  $A$ , and the apparent horizontal velocity of the wave across the array  $V_p$ . These two quantities may be calculated from phase differences  $\Delta\phi_{12}$  and  $\Delta\phi_{13}$ , i.e.,

$$A = -\arctan \left[ \frac{y_1 - y_2 - P \cdot (y_1 - y_3)}{x_1 - x_2 - P \cdot (x_1 - x_3)} \right],$$

where

$$P = \Delta\phi_{12} / \Delta\phi_{13}$$

and

$$V_p = \frac{2\pi f}{\Delta\phi_{12}} [(y_1 - y_2) \cos A - (x_1 - x_2) \sin A].$$

Here  $f$  is the wave frequency. The above expressions have been derived by Cowling, Webb, and Yeh (1971) in their study of acoustic gravity waves. In the present work another method of presentation of the wave vector is used. A unit vector in the direction of the wave vector is projected onto the horizontal plane. The vertical component of the unit vector,  $Z$ , may be calculated from components of the projected vector  $X$ ,  $Y$  as

$$Z = (1 - X^2 - Y^2)^{1/2}$$

The azimuth  $A$  of the direction of arrival of the wave is then

$$A = \arctan(X/Y),$$

and the horizontal trace velocity across the array is

$$V_p = \frac{L}{X^2 + Y^2}$$

where  $L$  is a constant which depends on the distance between microphones and on the wave frequency. The slope of the vector  $E$  may be calculated if the local sound velocity  $c$  is known:

$$E = \cos^{-1}(c/V_p).$$

Digital equipment which converts phase differences  $\Delta\phi_{12}$  and  $\Delta\phi_{13}$  into components of the unit vector  $X$ ,  $Y$  has been constructed.

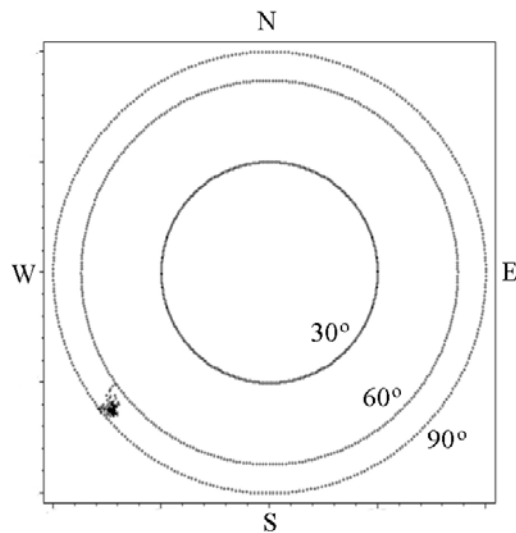


Fig. 1. A representation of the sky at the infrasound frequency of 2 Hz. The concentric circles represent zenith angles of 30°, 60°, and 90°. The accumulation of points at  $A = 230^\circ$  shows the apparent position of a distant infrasound source on the sky.

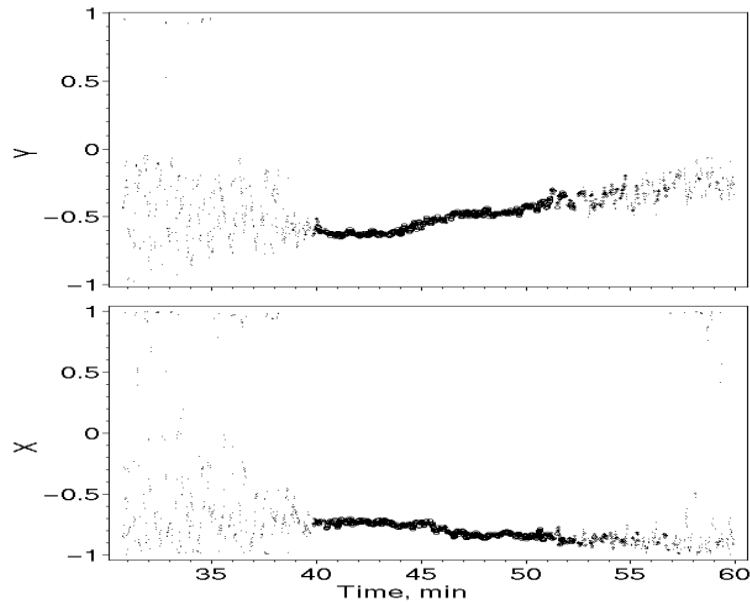


Fig. 2. A continuous recording of the unit vector components X and Y. One pair X, Y is obtained during each wave cycle.

Two methods for recording the components of the unit vector were used:

(1) X and Y are presented on a CRT screen as a bright spot with coordinates X and Y. By accumulation of directions of the wave vector during a time much longer than the wave-period, a representation of the sky at the infrasound frequency is obtained. In this presentation, the zenith corresponds to the center of the screen; the principal directions are marked outside the graph. Circles of constant zenith angle are represented by concentric circles centered at the middle of the screen. An example of such a view of the sky for infrasound obtained at a frequency of 2 Hz by accumulation of wave vectors during one minute is shown in Fig. 1. The concentric circles represent zenith distances of  $30^\circ$ ,  $60^\circ$ , and  $90^\circ$ . The accumulation of points at  $A=230^\circ$  shows the apparent position of a distant infrasound source in the sky.

(2) The components X and Y of the unit vector were recorded separately on a continuously moving photographic film. An example of such recording is shown in Fig. 2. Each simultaneous pair of coordinates X and Y gives the direction of the wave vector. This second recording method was used for routine recordings at all stations.

The azimuth of the direction of arrival of the infrasonic wave may, in many cases, be determined with an accuracy of  $\approx 1^\circ$ . Measurements of the direction of arrival at two or more stations may be used for location of infrasound sources. The accuracy of location depends upon the distance between the stations and upon the direction to the source with respect to the line joining both stations. The accuracy of location is increased when more than two stations are used.

The detection threshold of the equipment is, under favorable meteorological conditions, 77 dB below  $1 \mu\text{Pa}$ . The detection threshold may be lowered if microphones are placed in Helmholtz resonators tuned to the detected frequency. At all of our recording stations, the infrasound amplitude and wave vector components at 2 Hz were recorded.

### ***Extracting more information from a tripartite array***

In the above consideration, the angle-of-arrival is determined using only one baseline pair. A better accuracy may be obtained by repeating the above calculations for all three pairs of baselines (microphone pairs).

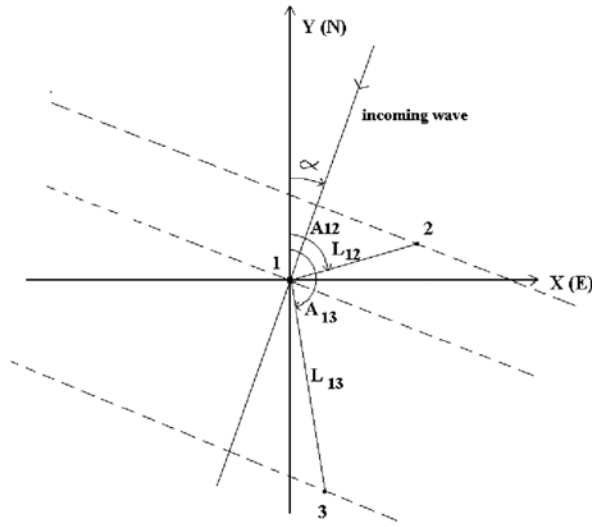


Fig. 3. Principle of determination of the angle of arrival

Fig. 3. shows the principle of the determination. The wave front passes the triangle with the microphones #1, 2 and 3 from the direction  $\alpha$ . The triangle's sides (baselines between the microphones) are  $L_{12}$ ,  $L_{13}$  and  $L_{23}$ . Each baseline is oriented at an angle  $A_{ij}$  from the North. The wave front passes the microphones at slightly different times. The time differences between the microphones are determined from the cross-correlation function using half of a data block at a time (256 samples). Time differences  $\tau_{ij}$  are expressed in number of sampling intervals, or when calculating the apparent phase velocity, in seconds.

The determination of the angle of arrival is possible under assumption that the wave fronts are projecting on the microphone plane as straight lines. For each pair of baselines (each corner of the triangle), for example for the microphone #1, the following relation is valid:

$$L_{12} \cos(A_{12} - \alpha)/\tau_{12} = L_{13} \cos(A_{13} - \alpha)/\tau_{13}$$

From the above relation, components of the projection of the wave vector  $(\xi, \psi)$  may be calculated:

$$\begin{aligned} \xi &= \tau_{12} L_{13} \cos A_{13} - \tau_{13} L_{12} \cos A_{12} \\ \psi &= \tau_{13} L_{12} \sin A_{12} - \tau_{12} L_{13} \sin A_{13} \end{aligned}$$

The direction of arrival  $\alpha$  for that pair of baselines may be calculated from

$$\alpha = \arctan(\xi/\psi).$$

The direction of arrival may be calculated for all three corners of the triangle. It has been found that calculating the average vector  $(\xi, \psi)$ , instead of an average  $\alpha$ , gives more stable results. This is due to non-linearity of the  $\arctan(\alpha)$  function.

When  $\alpha$  is determined, the value of the apparent phase velocity (trace velocity), related to the projection of the wave vector on the horizontal plane, may be found.

## ***Wind noise protection***

After it was decided that the signal detection system has to be based on phase measurements, the next step was to decide which system of wind noise reduction should be used. The wind noise, generated by the turbulence in the airflow, is the major obstacle in detecting distant infrasonic signals. The dominating wind noise reduction system is based on spatial filtering. In spatial filtering, the total sound pressure signal is collected at a large number of low-impedance inlets distributed over a large area (see Fig. 4a), and further on by a system of pipes gathering the total signal at a central transducer. It is assumed that the wind noise will be averaged out over the area of the filter, while the infrasonic signal will add-up to its average value across the filter. This is valid under the assumption that the signal coherence above the entire filter is constant. In the opposite case, the phase of the averaged signal will be modified in an unpredictable way.

At the SIN stations, the problem of wind noise was solved using the wind barriers (see Fig. 4b). A wind barrier removes the turbulence from the immediate area surrounding the microphone.

The advantage of the wind barrier is that the microphone is recording the sound pressure at a single point in space, without averaging over a large area.

Spatial filters and wind barriers were compared experimentally by Hedlin and Raspet (2003). Results of the investigation are quoted below.

Concerning the wind noise reduction:

“Comparison of the scaled reductions in wind noise produced by the rosettes and wind barrier with the reductions afforded by a spherical wind screen hold promise for significant wind noise reduction with a smaller foot print device. The rosettes only produce reductions if the scale size of the turbulence is smaller than the size of the rosette since such devices rely on the incoherence of the turbulence at each port. The wind barrier displayed large reductions only when the scale size of the turbulence is smaller than the height of the barrier. However, a small reduction of about 4 dB was realized when the scale size was larger than the barrier. This reduction may correspond to the large reductions realized by foam windscreens. In the spherical windscreens, these reductions occur since the pressure measured at the center is the area average of the pressures generated at the surface of the sphere. For large turbules, the pressure generated by an increase in wind speed is positive at the front of the sphere and negative at the back, and the average is less than the pressure measured at a bare sensor. This result holds promise that a properly designed windscreen on or near the ground surface may achieve significant reductions even for turbulence scales greater than the size of the screen.” .

The authors' conclusions concerning preservation of signals while attenuating noise:

“Ultimately, we seek a device that will provide maximum attenuation of unwanted noise and minimally distorted recordings of signals from remote sources. Signals and noise are received at a single point inside the barrier. This is potentially a significant advantage of the barrier over spatial filters, such as the two considered in this paper, which rely on the different coherence lengths of signal and noise. Spatial filters are used to increase the ratio of signal-to-noise by sampling air pressure at numerous locations at offsets at which the noise is believed to be incoherent and the signal remains coherent. If phasing between the multiple samples of

the signal is not correctly taken into account, and if the signal is not coherent across the area spanned by the spatial filter, the waveform of the signal will be degraded. Rosette filters are tuned to signals arriving with infinite phase velocity. Signal attenuation caused by 70-meter aperture rosette filters becomes acute at low angles of incidence and at frequencies above 1 Hz (McDonald, Douze and Herrin, 2002)”.

The final conclusion:

“Unlike spatial filters currently in use at IMS array sites, the barrier does not propagate the signals through narrow pipes. Ambient signal and noise enter the microbarometer from free-air and therefore, dispersion of broad-band signals that is known to occur in narrow pipes (e.g. Benade, 1968) is not a concern”.

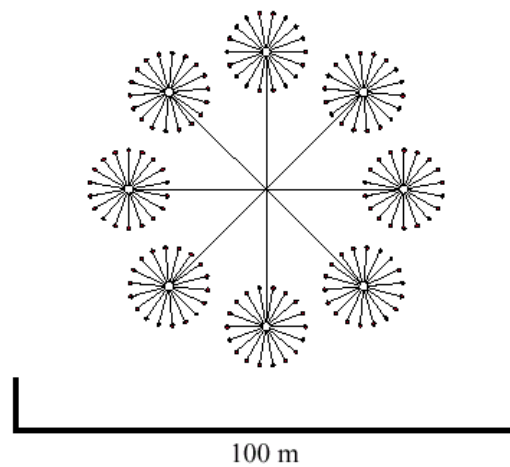


Fig. 4a. A large, 144 inlet port, spatial "rosette" filter.

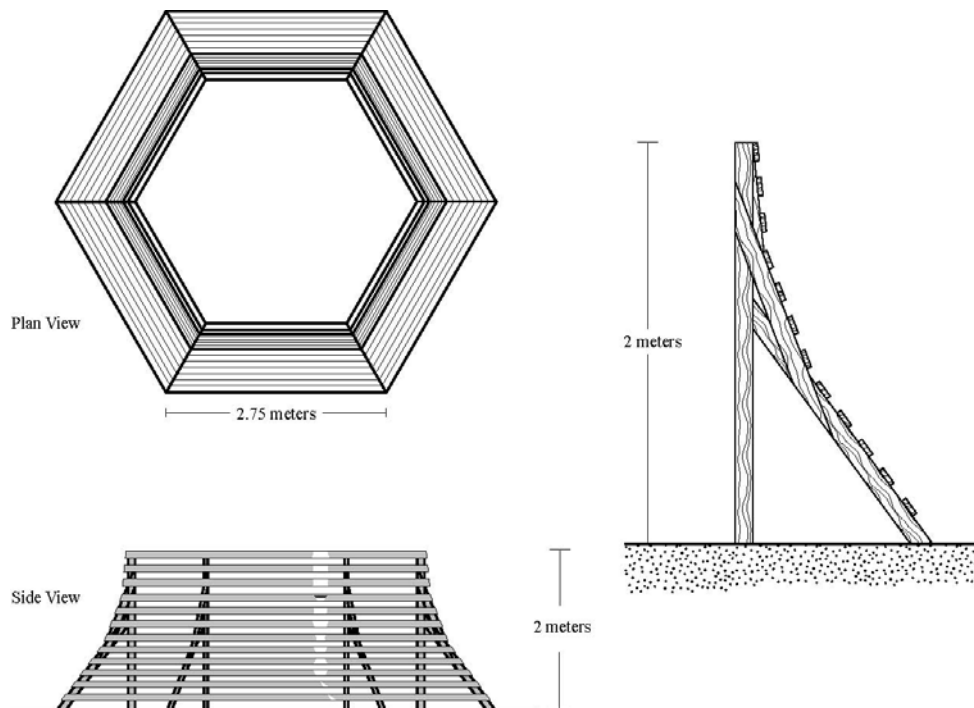


Fig. 4b. A wind barrier of the type used at the SIN recording stations.

## Computerization of infrasonic stations

In December 1981, all stations had been computerized using a small Swedish-manufactured computer: ABC80. The computer, in its basic model, was only equipped with RAM and a floppy-disk reader for software input and storage and an audio cassette unit for the data storage. Due to the limited storage capacity, complete X, Y data could not be stored. The X, Y data was converted into the azimuth-of-arrival and the horizontal trace velocity and stored in RAM for each 30-seconds period, after which distributions of both variables were created. Then the distributions were stored on the audio-cassette at the end of each half-hour period. An example of 30 minutes of angle-of-arrival distributions during a 30 minutes period is shown in Fig. 5. One audio-cassette was enough to store data during approximately 10 days. Infrasound recordings based on ABC80 were continued until May 1996. The stored data was used to construct distributions of angle-of-arrival, one distribution for each 30-seconds period.

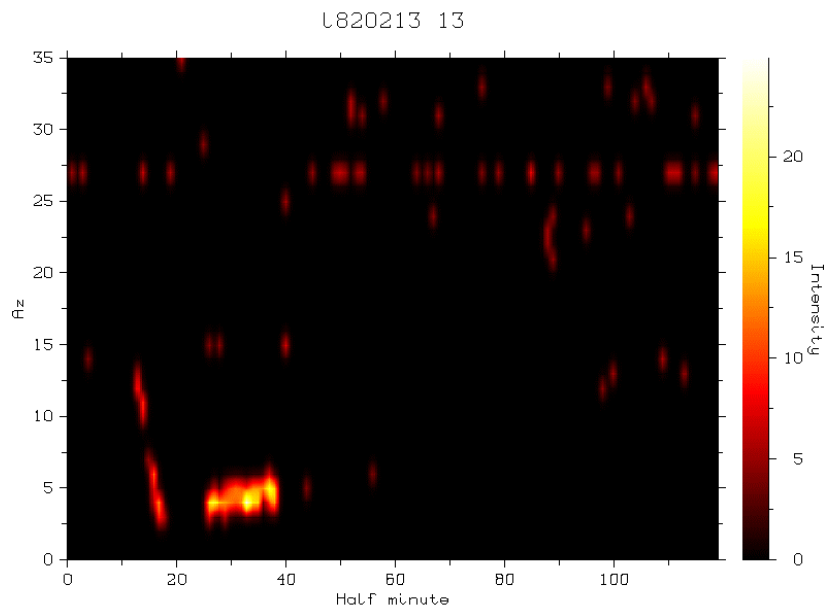


Fig. 5. 3D distributions of angle-of-arrival from Lycksele on February 13, 1982 between 1300 and 1330 UT showing two infrasonic sources: one moving between 140 and 30° and one stationary at approximately 40°. Y-scale in 10° units.

Angle-of-arrival distributions of 2 Hz signals for the entire period December 1981 – May 1996 may be accessed at the IRF-Umea home page.

In the beginning of 90's, when inexpensive personal computers became available, a new concept of infrasound recording was introduced. Instead of a narrow-band, single frequency recording, broad-band (0.45 – 9 Hz) digital recordings of the original time series, taken at all three microphones, were made and stored in the form of 30-minute files. Also a new, remarkable Lidström-microphone was introduced. The microphone, originally developed in the beginning of 80's in Sweden for helicopter detection, is extremely sensitive and it can operate in a harsh climate. The frequency response of the microphone is shown in Fig. 6 and its external view in Fig. 7.

The recorded time series, from all 3 microphones in the array, are automatically searched for coherent signals, correlated over the array. For all data, the angle-of-arrival and the horizontal trace velocity are calculated using a “total signal” cross-correlation method (Waldemark, 1995). Another signal-processing technique based on information theory approach is given in the next section. The angle-of-arrival calculated using this method appeared more reliable than that using the cross-spectrum analysis. A typical graph showing the angle-of-arrival (upper graph) and the horizontal trace velocity (lower graph) is shown in Fig. 8.

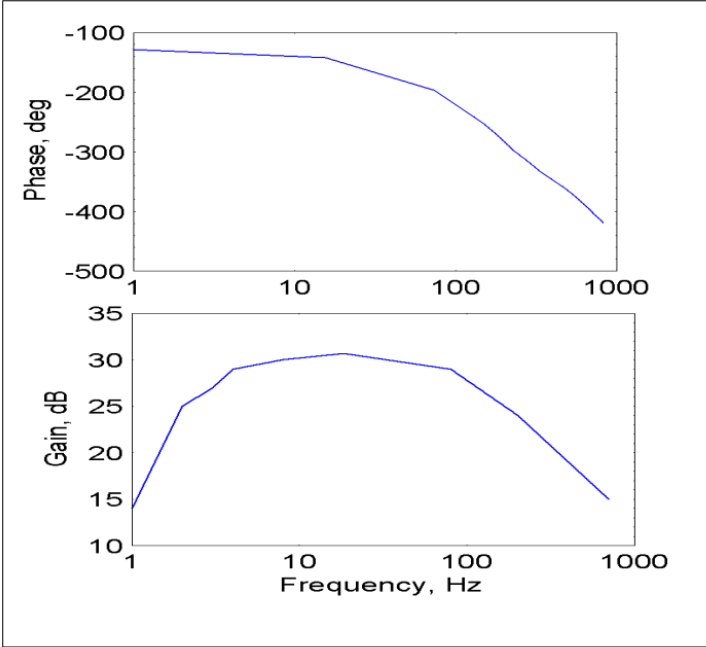


Fig. 6. The Lidstrom-microphone characteristics.



Fig. 7. The Lidström Infrasonic Microphone.

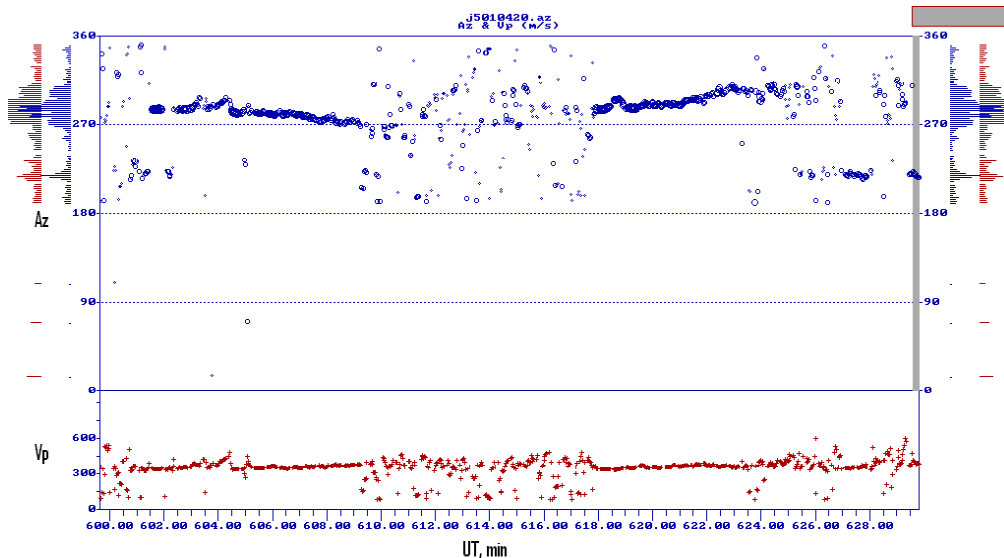


Fig. 8. A typical graph showing the angle-of-arrival in degrees from N (upper graph) and the horizontal trace velocity in m/sec (lower graph). The time on the x-axis is in minutes UT. The infrasonic source is probably a supersonic aircraft above the Northern Atlantic.

### ***The application of the entropy concept to infrasonic data analysis***

Most of the infrasonic data analysis is based on applications of auto- and cross-correlation functions. There are two main problems in infrasonic data analysis:

- determination of the angle-of-arrival of infrasonic waves
- triangulation of sources using data from several stations.

In the case of determination of the angle-of-arrival it must be assumed that there is a single wave pattern moving across the microphone array, unless a beam-forming technique is applied. However, it is unpractical to use the beam-forming technique with only three microphones. Also transients in the signal will influence the use of classical cross-correlation technique.

In the case of source triangulation angle-of-arrival data from at least two stations is used to determine position of the source. In the case of several simultaneous sources, the triangulation may be very difficult, since it is usually not known which events from one station correspond to events observed by the second station. Due to large variations in the propagation time, it is difficult to use the time-of-arrival information for triangulation.

The entropy concept, which may be applied to any kind of discrete data, may remove the above problems in processing the infrasonic data.

#### **Definitions**

Let  $X$  be a discrete random variable with a set of values  $\Xi$  and probability mass function

$$p(x) = \Pr\{X=x\}, x \in \Xi$$

The **entropy**  $H(X)$  of a discrete random variable  $X$  is defined by:

$$H(X) = - \sum p(x) \log p(x), x \in \Xi$$

For a pair of discrete random variables  $X$  and  $Y$  with a joint distribution  $p(x,y)$ , the **joint entropy**  $H(X,Y)$  is defined as

$$H(X,Y) = - \sum_{x \in \Xi} \sum_{y \in \Gamma} p(x,y) \log p(x,y)$$

The **conditional entropy**  $H(Y | X)$  of  $Y$  given  $X$  is defined as

$$\begin{aligned} H(Y | X) &= - \sum_{x \in \Xi} p(x) H(Y | X=x), \\ &= - \sum_{x \in \Xi} \sum_{y \in \Gamma} p(x,y) \log p(y | x), \end{aligned}$$

The average amount of common information contained in the variables  $X$  and  $Y$ , is quantified by the **mutual information**  $I(X;Y)$ , defined as

$$I(X;Y) = H(X) + H(Y) - H(X,Y)$$

A basic reference for the entropy method is: M. Palus (1996).

If a variable may be considered as a random discrete variable, then the above concepts may be used.

### **The applications**

Complex infrasonic signals from a microphone, contaminated by noise and quantized by an A/D converter may certainly be considered as suitable for analysis using the mutual information instead of the cross-correlation function.

When determining the direction of arrival using the cross-correlation technique, the waveforms from different microphones are shifted in time in order to obtain the highest correlation between the waveforms. When the method is applied to spaced microphones measurements, the signals  $X$  and  $Y$  at respective microphones 1 and 2 are quantized into  $N$  intervals. When the entropy concept is applied, the joint distributions  $p(x,y)$ , i. e. probability of a simultaneous occurrence of specific values  $x, y$  at both microphones, are calculated for varying shift  $\delta$  between the sequences of measured series  $X$  and  $Y$ . The varying shift  $\delta$  is analogous to the time lag in the cross-correlation function. The determined joint entropy, and thus the mutual information between two channels  $X$  and  $Y$ , will be a function of  $\delta$ :  $I(X;Y,\delta)$ . For the range of possible  $\delta$  there will be one maximum of the mutual information if there is a single wave pattern over the microphones and more than one for complex wave patterns.

An example of mutual information function between 3 microphones for a typical signal sample is shown in Fig. 9. The microphones are located at corners of a triangle with a right angle at microphone 1 and 75 meters distance between microphone pairs 1-2 and 1-3. It is obvious that for above curve set it is possible to determine the angle of arrival both for the dominating wave pattern and for the secondary patterns corresponding to other allowed combinations of peaks in the mutual information functions.

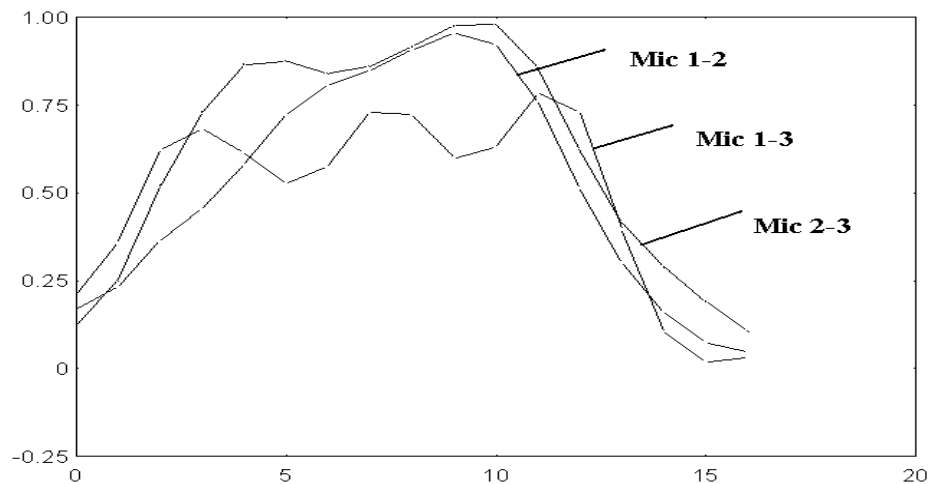


Fig. 9 Mutual information functions for 3 microphone pairs of a 3-microphone array.

At present, a software exists to determine the angle-of-arrival of the dominating wave pattern, i. e. having the same function as the cross-correlation method. The entropy software needs, of course, considerably more computer time than the cross-correlation software. However, it may be used when the signal consists of a series of pulses, a case in which the cross-correlation method may be difficult to use.

A similar method may be developed for triangulation of sources using infrasonic data from several stations..

### **References to Chapter 3**

Benade, A.H., (1968), On the propagation of sound waves in a cylindrical conduit, *J. acoust. Soc. Am.*, 44, 616-623. 1968.

Cowling D. H., Webb H. D. and Yeh K. C.: 1970 Tech. Rep. 38, Ionosph. Radio Lab., Univ. of Illinois.

Hedlin A. H. and Raspet M.(2003) [J. Acoust. Soc. Am. 114](#) (3)

McDonald, J. A., Douze, E. 1., and Herrin, E. (1971). "Structure of Atmospheric Turbulence," *Geophys. J. R. Astron. Soc.* 26, 99-109.

M. Palus, *Physics Letters A* 213 (1996) 138-147.

Waldemark, K.: *Studies of the Atmosphere Using Infrasound Recordings*, PhD Thesis, Swedish Institute of Space Physics, 1995.

## Chapter 4

### The Auroral Infrasound

It was shown in mid 60's by Dr. Charles R. Wilson (1969) at the University of Alaska, that traveling pressure waves are radiated when large-scale auroral forms move with supersonic speed (see Fig. 1). During periods of high geomagnetic activity, infrasonic waves with an amplitude of a few dynes/cm<sup>2</sup> and with periods from 40 to 80 sec have been observed at subauroral stations to come from a source in the polar regions. Wilson explained these infrasonic signals using a shock-wave model. An auroral form moving with the supersonic speed at heights above 100 km generates a pressure pulse, which propagates down to the ground. The direction of propagation is optimal in the direction of motion of the auroral form.

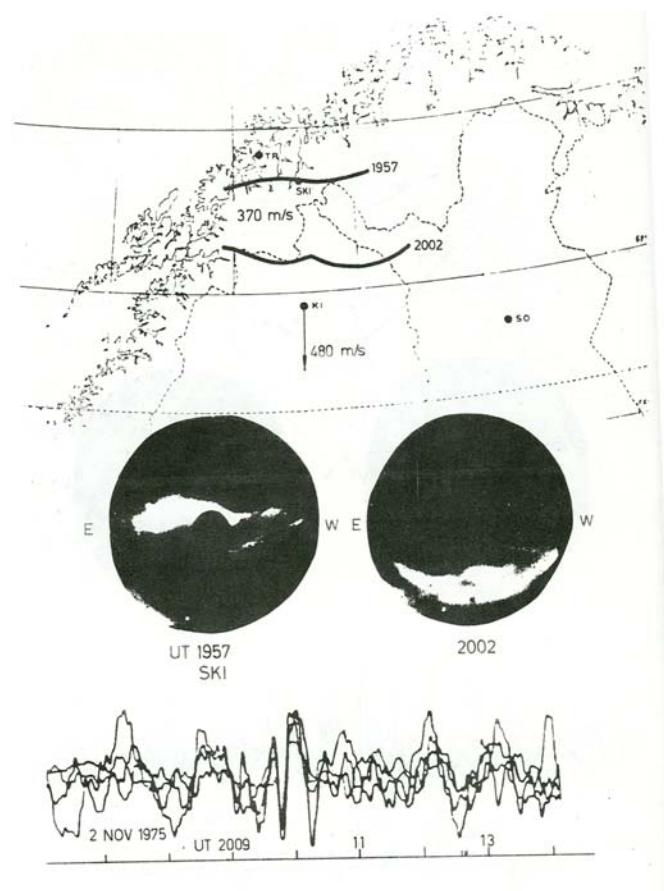


Fig. 1. Geographic location of an auroral arc during a 5 minutes period together with corresponding All Sky Camera frames and resulting Auroral Infrasound Waves (AIW) recorded in Kiruna on November 2, 1975 at 1010 UT

When the infrasonic recordings were started in Kiruna in 1971, Wilson's results made it natural to start the search for the auroral emissions. The bandwidth of the Kiruna equipment was, however, at much higher frequencies than those observed in Alaska. There was no clear association of 2 Hz infrasonic events with the auroral activity (Liszka and Westin, 1972). In order to study that difference between 2 Hz observations and recordings in 40 – 80 sec band, in March 1973 Dr Wilson placed in Kiruna his recording equipment of the same kind as that used in College, Alaska. The equipment was in operation until December 1975.

Data collected during those 21 months was later analyzed in the PhD thesis of Hans Westin (1976) summarized here.

### ***Morphology of auroral infrasonic waves (AIW)***

A typical auroral infrasonic event suddenly appears out of the background with the highest frequencies arriving first and then it dies off after just a few cycles. The mean period of the first cycle is 41 seconds and the mean horizontal trace velocity 516 m/s, which corresponds to an elevation angle of  $52^\circ$ . The azimuth of arrival of the auroral infrasonic waves observed in Kiruna changes with time in a characteristic way. Waves observed in the evening come from sources east of Kiruna magnetic meridian, probably related to the average direction of auroral arcs in evening and morning. They are most likely generated by westward travelling auroral surges. In the morning, fast loops and omega bands move rapidly eastward. They are probably the sources of AIW recorded after geomagnetic midnight when the AIW mostly are coming from west of the meridian. This drift in azimuth during the progress of the magnetic storm was also found for AIW recorded in Alaska.

Most of the signals come from directions perpendicular to the oval. This is also the general direction of moving auroral forms during the midnight- and early-morning hours. The westward travelling surge of the evening hours often pass well to the north of Kiruna, why signals from the side of the supersonic source have to traverse the oval to reach the Kiruna station. Many of the fast moving auroral features observed in the morning pass Kiruna's zenith and there are indeed more auroral infrasonic waves arriving to Kiruna along the oval in the morning than there are in the evening.

For several of the AIW, the sources have been identified on all-sky pictures and on latitude profiles of perturbations of the vertical component of the geomagnetic field. AIW are associated with supersonic electrojets moving southward, eastward or westward, but they have never been observed in connection with the poleward motion of an auroral arc. Theoretical works show that the Lorentz force and Joule dissipation terms add when the motion of the westward electrojet is equatorward but subtract when it is poleward. As these terms are of comparable magnitude, this can partly explain the observed asymmetry in the direction of the AIW.

### ***Comparison of AIW with 2 Hz infrasound***

Infrasound with a frequency of 2 Hz have, as mentioned earlier, been recorded in Kiruna continuously since 1971. It will be shown in the next chapter that infrasound with frequencies around 2 Hz is dominated by man-made signals. An attempt was, however, made to study infrasound associated with geomagnetic activity already during the first year of observation (Liszka and Westin, 1972). Periods with favourable wind conditions both in the upper atmosphere and at the ground level made it possible to minimize the number of unwanted signals. Four nights in August and September 1971 were selected for a comparison of horizontal phase velocities and azimuths of arrival of recorded infrasonic waves with simultaneous magnetic activity. As the optical aurora can not be seen from Kiruna at this time of the year, magnetograms from five stations were used to deduce

motions of auroral electrojets from latitude diagrams composed from these magnetograms.

The recording of 2 Hz infrasound is given as a pair of points representing phase differences at the east-west and the north-south pair of microphones. No information is thus available of the waveform of the recorded infrasound. Instead, the recordings were scaled once every minute. Phase differences were then converted into horizontal phase velocity and direction of arrival. The amplitudes, which were recorded with a separate pen-recorder, were scaled in the same manner. Ray-tracing technique was then applied to five selected periods for more than five hours altogether. We found that the infrasound observed during these magnetically disturbed periods originated from sources within 120 km to the north of Kiruna, notwithstanding that as many supersonic electrojets came near or passed Kiruna zenith from the south as from the north. The 2 Hz infrasound thus propagated from north to south during these studied substorms.

The 2 Hz recordings have also been searched for signals simultaneous with the low frequency auroral events (AIW) observed at Kiruna (Westin, 1976). Signals from other sources forming the background are extremely frequent, which makes it very difficult to find the signals that could be of auroral origin. No comparison was possible for more than a fourth of the waves due to blocking by strong man-made signals or malfunction of the 2 Hz equipment. A 2 Hz counterpart was found for every AIW for which a comparison was possible. Due to the high number of background signals, the determination of azimuth was ambiguous for many events. The background, including both natural and man-made emissions was a serious limitation of the possibilities to identify the 2 Hz signals for a comparison with the AIW.

### ***References to Chapter 4***

- Liszka L. and Westin H.: Detection of 2 Hz Infrasound by Moving Auroral Electrojets. 1972. In: Effects of Atmospheric Acoustic-Gravity Waves on Electromagnetic Wave Propagation. AGARD, 1972.
- Westin H.: Studies of Infrasonic Waves in the Auroral Zone, PhD Thesis, Swedish Institute of Space Physics, 1976.
- Wilson C. R.: Auroral Infrasonic Waves, J. Geophys. Res. 74, 1812, 1969.

## Chapter 5

### The Discovery of Long-Distance Propagation of Infrasound from Man-made Sources

The continuous operation of the first two infrasonic stations: Kiruna and Jämtön started in October 1972. Having two infrasonic arrays spaced about 230 km it became possible to localize infrasound sources. Already within the first month of operation the first source of infrasound was localized and identified. Strong bursts of 2 Hz infrasound were observed at both stations on early evening of November 20, 1972 (see Fig. 1).

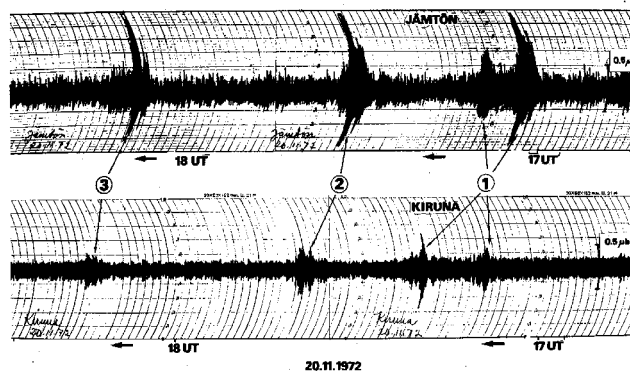


Fig. 1. Strong bursts of 2 Hz infrasound observed at both infrasonic arrays during the early evening of November 20, 1972

The source of bursts was immediately localized to a large hydroelectric power plant Tuggen in Northern Sweden, as will be shown in the following section.

#### **Results of the first year of operation of the arrays**

Analysis of data taken during one full year pertaining to the location of infrasound sources indicates that the majority of discrete sources at 2 Hz are of artificial origin. This may be seen from the weekday distribution of located events during the period October 1972 - October 1973 shown in Fig. 2. The number of infrasound events on Sundays is found to be nearly one order of magnitude smaller than on weekdays Monday - through Friday which indicates that these events must be of industrial origin.

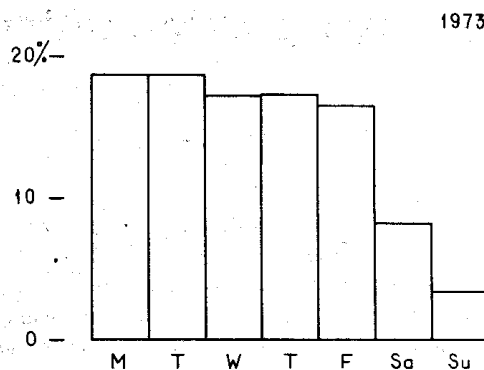


Fig. 2. The weekday distribution of located events during the period October 1972 - October 1973.

Amplitude recording for one of the first events, whose source has been located using stations at Kiruna and Jämtön, is shown in Fig. 1. The event mentioned above consists of a series of infrasound emissions coming from the same source. The time delay and the amplitude ratios for the recordings at the two stations indicate that the source was closer to the Jämtön station. By comparison of the directions at which the source was seen at both stations namely,  $191^\circ$  at Kiruna and  $231^\circ$  at Jämtön, it was found that the source must be located at  $64.5^\circ\text{N } 18.8^\circ\text{E}$ . Amplitudes recorded at both stations ( $2 \mu\text{bar}$  at Jämtön and  $0.5 \mu\text{bar}$  at Kiruna), and an application of elementary acoustic concepts, indicate that the radiated acoustic power must be between 1 and 10 MW. The only possible source at this geographical location was a large hydroelectric power plant Tuggen (105 MW).

The fall of 1972 was characterized by a late freeze-up of water reservoirs at hydroelectric power plants in Northern Sweden. Under these conditions: temperatures below freezing and no ice cover in the water reservoir, ice crystals were formed in water at the intake, influencing the efficiency of the turbine. Parasitic oscillations in the water flow may then occur. Depending on the construction of the power plant, these oscillations may couple to the surrounding atmosphere, being a powerful source of infrasound. After introducing the continuous remote control of hydroelectric power plants in the beginning of 1980's this kind of events became unusual. The discovery of powerful infrasound emissions from large hydroelectric power plants increased the awareness of power companies about the problem of oscillations in the water flow. The phenomenon is not only a source of loss of energy production, it is also a cause of increased fatigue of the plant components.

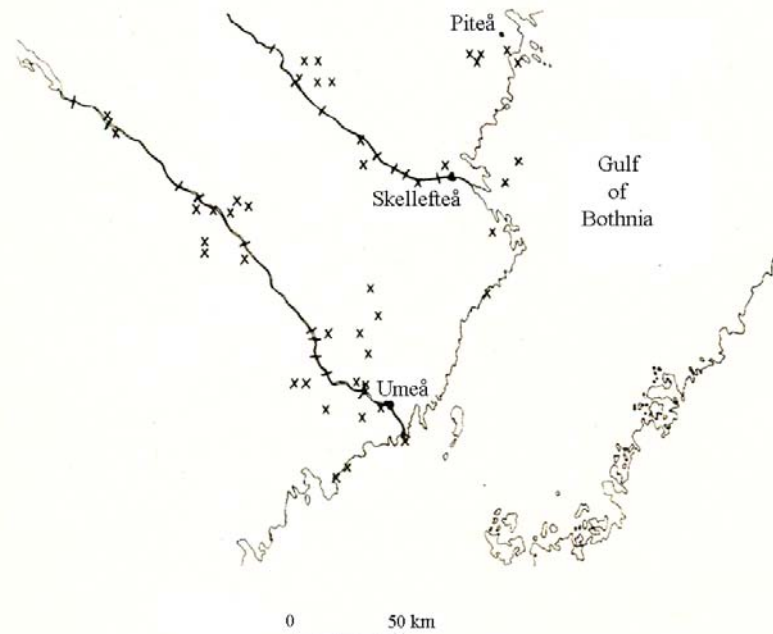


Fig. 3. Location of infrasound sources in Northern Sweden (crosses). Major hydroelectric power plants are indicated by bars.

Location of infrasound sources during the winter 1972/73 showed that the majority of sources are, within limits of location accuracy, at large hydroelectric power plants (see Fig. 3). Infra-acoustic energy is probably generated and radiated by oscillating water masses in the dam or in headrace or tailrace tunnels.

Another type of infrasound emissions has been traced to those types of industrial installation where exhausts of gas or steam occur under high pressure. In Sweden, the

most common type producing these intense, short-duration, infrasound emissions is the cellulose industry. At the top of Fig. 3, there are few infrasound events localized to surrounding of Piteå, where two large paper mills are located.

At larger distances, spectacular infrasound sources have been found at oil fields where gas exhausts and burn-off frequently take place. Fig. 4 shows some results regarding location of sources of infrasound emissions in the North Sea during 1973. Infrasound sources are marked by crosses. Positions of oil derricks on January 1, 1974 are shown by circles. Difference between locations of sources and positions of oil derricks are not only due to location errors but also due to the fact that positions of oil derricks changed during the period of measurement.

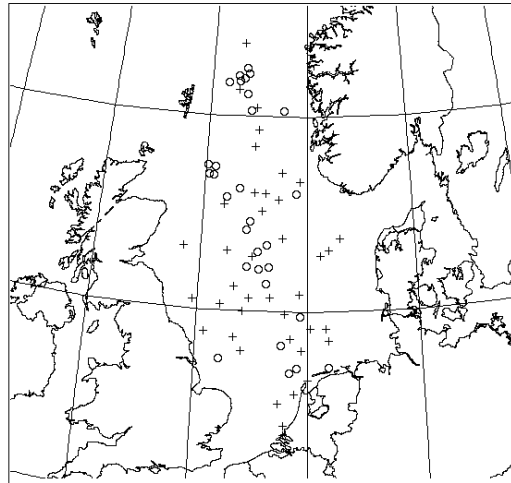


Fig. 4. Location of sources of infrasound emissions in the North Sea during 1973. Infrasound sources are marked by crosses. Positions of oil derricks on January 1, 1974 are shown by circles.

Knowing the wind and temperature profiles, one may investigate propagation of the infrasound using the ray-tracing technique, which was discussed in Chapter 1. Depending on the angle of incidence, temperature, and wind profiles and the direction of propagation, long-distance propagation will take place through reflections mainly in two height regions (see Fig. 5).

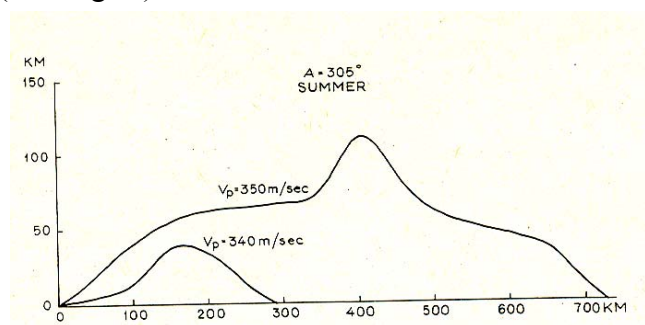


Fig. 5. Examples of ray tracing showing propagation through the stratospheric and the upper sound channel.

The distance at which the infrasound returns to the ground after a single reflection in the stratospheric sound channel varies between 100 and 300 km for typical wind and temperature conditions. The distance varies between 300 and 800 km when the reflection takes place in the upper sound channel. Multi-hop propagation can take place, particularly when propagation is through the stratospheric sound channel. This

can be seen from Fig. 6, which shows a distribution of distances to the infrasound sources located during the months April-September 1973. The distribution shows four peaks at 250, 500, 750, and 1000 km, corresponding probably to 1- to 4-hop propagation through the stratospheric sound channel.

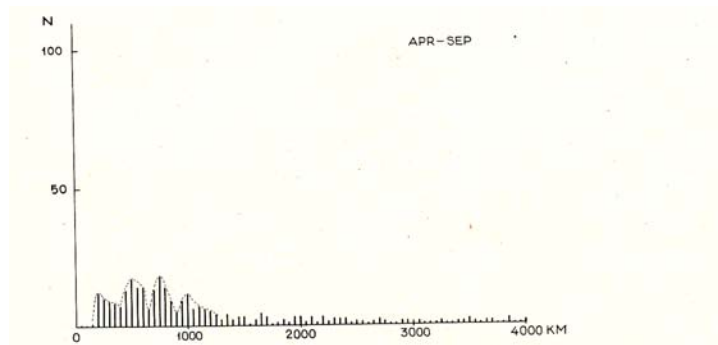


Fig. 6. The distribution of distances to the infrasound sources located during the months April-September 1973.

It has been found that during winter months infrasound usually propagates through the upper sound channel. The multi-hop propagation through the upper sound channel seems to be less probable than through the stratospheric sound channel. This can be seen from Fig. 7, which shows a distribution of distances to the infrasound sources located during October 1972 - March 1973. The distribution shows only one distinct maximum for distances of the order of 500 km. The lack of clear multi-hop propagation through the upper sound channel is probably caused by the severe attenuation of 2 Hz infrasound at heights above 100 km.

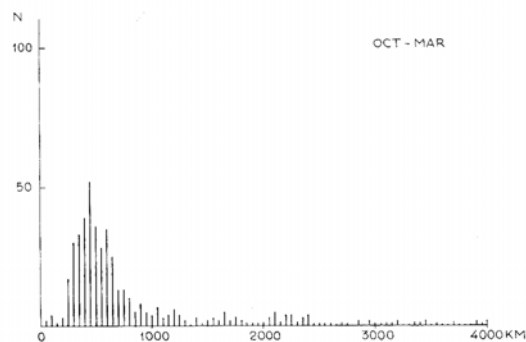


Fig. 7. The distribution of distances to the infrasound sources located during October 1972 - March 1973.

A conclusion of above results was that propagation through the upper sound channel dominates during winter, but during summer it is most often via the stratospheric sound channel.

The most important result of the above studies was that also “ordinary” industrial activities generate infrasound strong enough to be detected hundreds of kilometers away.

## **Reference to Chapter 5**

Liszka, L. J. *Acoust. Soc. Am.* 56, 1383 (1974).

## Chapter 6

### Concorde as an Infrasound Source

It was shown in 1971 (Liszka and Olsson, 1971) that sonic booms from supersonic aircraft may be detected at infrasonic frequencies even at distances larger than 100 km, where no audible signal is received. The sonic boom of the supersonic airplane Concorde has been studied at about 300 km from the flight route, during its test flights, using an infrasonic array (Grover, 1973). The amplitude of the infrasonic signal was between 0.4 and 0.8 N/m<sup>2</sup> and the dominating frequency 0.3-0.5 Hz. At distances above 100 km, the sonic boom from supersonic aircraft, if recorded by a broadband device, no longer shows the typical N-signature, but rather appears in the form of an infrasonic pulse dominated by frequencies of a few Hertz. The same has been reported for weak shocks from thunder (Murphy, 1972) and for shocks from distant explosions on the ground surface (Cox et al., 1952).

During a large part of the 1970's infrasound from distant artificial sources thus was successfully detected at a frequency of 2 Hz (Liszka, 1974). This frequency had been predicted to be an optimum frequency for detection of distant acoustic sources (Procunier and Sharp, 1971).

Scheduled flights of Concorde between the United States and Europe started in 1976. In the light of earlier experience, the question has been raised by the author whether the Concorde sonic boom could be detected at infrasonic frequencies in Northern Scandinavia.

An examination of infrasonic recordings made continuously at automatic recording stations run in Northern Sweden by the present Swedish Institute of Space Physics has shown that the Concorde sonic boom may easily be identified. As all stations are spaced over a distance of more than 1000 km, there are good possibilities to find the location of a source by a simple cross-bearing method. At large distances the method must, of course, include the effect of winds. Consequently, a source that moves with supersonic speed, follows a typical aircraft route, and follows the timetable of a particular aircraft may be identified with a reasonably good probability. Already in November 1977, more than 500 Concorde flights had been recorded. Infrasonic signals from the Concorde frequently reached as much as 0.1 N/m<sup>2</sup> (rms value), which, for distances between 2000 and 4000 km, is very large in comparison with 0.4 - 0.8 N/m<sup>2</sup> values observed by Grover 300 km from the flight route. As the infrasonic recordings supply the information on the direction of arrival of the signal and its horizontal trace velocity, it was possible to perform a detailed analysis of the Concorde generated infrasound. It has been found that the high infrasound pressure level observed in Northern Sweden is due to a kind of long-distance focusing that will be discussed in the subsequent section.

#### ***Principle of long-distance focusing of sonic booms***

A theory of focused sonic booms, so-called super-booms, has been developed by Rao (1956). Most of the later work was concerned with methods of eliminating unwanted super-booms (e.g., Ribner). Until now the whole work was concerned with sonic booms

focused at relatively short distances when a supersonic aircraft changes the direction of flight or its velocity. However, a SST flying with a constant velocity along a great circle around the earth will also produce a focused sonic boom. This can be seen in Fig. 1, where the line  $AB$  represents the flight trajectory. The sonic boom will be focused at a point  $O$  for which the following condition must be fulfilled:

$$AO/c = AB/v + BO/c ,$$

where  $c$  and  $v$  are the sound and aircraft velocity, respectively. The condition must also be fulfilled for each pair of points  $A_i, B_i$  along the flight trajectory. For a known flight trajectory and aircraft velocity, numerical calculations of the focus may easily be done. In practice, due, for example, to variations of the aircraft velocity and horizontal gradients in the atmosphere, the ideal focus can never be observed. It is convenient to define the focus areas as those where the sonic boom from the whole flight trajectory arrives in less than 5 minutes.

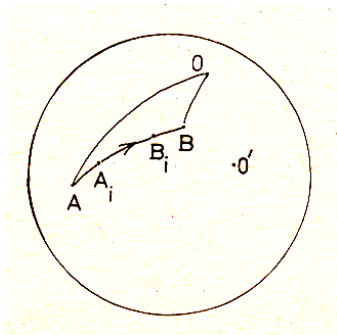


Fig. 1. Principle of long-distance focusing of a sonic boom.

There will be in general two focus areas (at  $O$  and  $O'$ ) located symmetrically with respect to the flight trajectory. As an example, the northern focus area for Concorde flight route Washington-Paris/ London has been calculated for both flight directions. One can see in Fig. 2 that the focus area is strongly elongated and that its position is determined by the aircraft velocity. For flights towards Europe, the focus is located in Northern Scandinavia and for flights towards the United States, it is located northwest of the Great Lakes district.

The influence of aircraft velocity is also illustrated by the example in Fig. 3. For a hypothetical flight trajectory, close to that of the Concorde Washington-Europe route, the direction of arrival of the infrasonic signal has been calculated as a function of time elapsed from the beginning of supersonic flight. Calculations have been made for three stations in Northern Sweden: Kiruna (67.8 N, 20.4 E), Luleå/Jämtön (65.8 N, 22.5 E) and Lycksele (64.6 N, 18.7 E). It can be shown that for a low supersonic aircraft velocity (1200 km/h), the infrasonic signal is first received from the westernmost part of the flight route. This signal is followed by signals from more easterly parts of the route. The total duration of the infrasonic signal from the whole flight trajectory would then be about 45 min. For the larger aircraft velocity (1500 km/h), the infrasonic signal from the whole flight trajectory will arrive to all stations in less than 10 min. The difference in slope between Lycksele (L) and Kiruna (K) indicates that the focus area for this aircraft velocity must be located somewhere between these two stations.

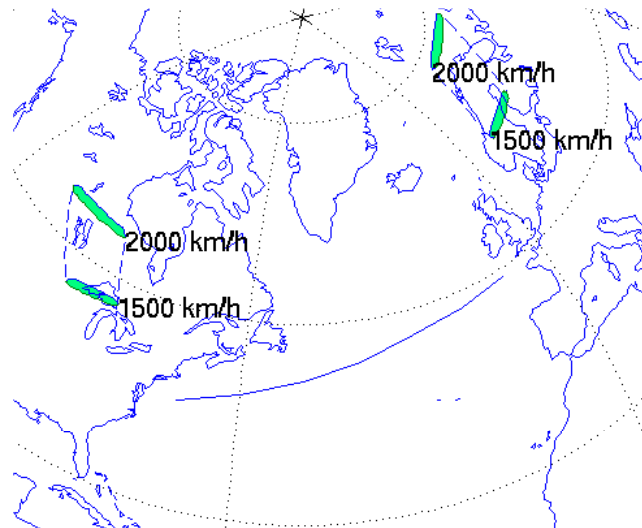


Fig. 2. Northern focus areas for the Concorde routes Washington-Europe (Northern Scandinavia) and Europe-Washington (northwest of the Great Lakes district) for two different aircraft speeds.

For the third case considered, that of aircraft velocity of 2000 km/h, an infrasonic signal from the end part of the flight route will arrive first at the recording stations, followed by signals from earlier parts of the route. An observer will thus "see" the flight history in reverse.

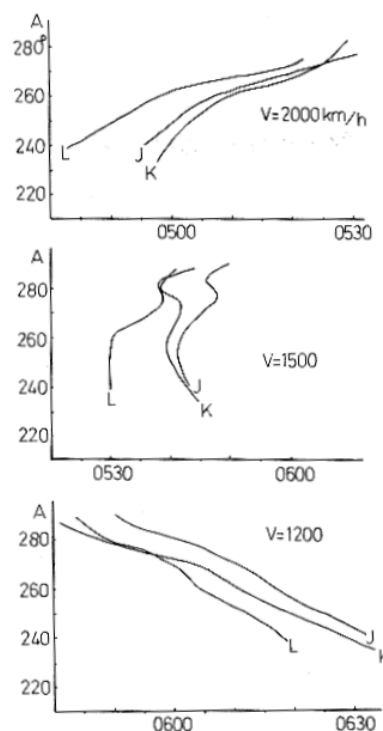


Fig. 3. Azimuth curves calculated for a hypothetical flight route from Washington to Europe for three different aircraft velocities, as seen at three recording stations in Northern Sweden. The horizontal axis shows the time elapsed from the beginning of supersonic flight.

Introduction of a wind system will modify results of calculation of the focus area and of the azimuth-time function. A realistic wind model for the North Atlantic area, with wind speeds increasing towards the north, up to about  $65^\circ$  N will, for example, for the curve 2000 km/h, increase its slope and thus move the focus area towards the south.

One can see in Fig. 3 that for a given flight trajectory and known wind system there is a potential for determining the aircraft velocity by measuring the slope of the azimuth-time function.

Similar calculations may be made concerning the horizontal trace velocity of the received infrasonic signal, which is dependent on the direction of the propagation vector at the source. Using simple ray considerations, one can see (Fig. 4) that the sonic boom from a supersonic aircraft is propagated into the atmosphere at different angles of propagation in different directions with respect to the flight direction. In the direction of flight, the propagation angle (with respect

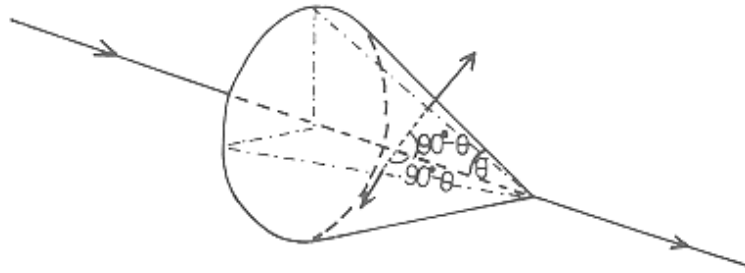


Fig. 4. The geometry of the Mach cone at the aircraft. Propagation directions in vertical and horizontal planes are indicated by arrows.

to the horizontal plane) will be  $90^\circ - \theta$ , where  $\theta$  is the Mach angle, given by

$$\sin \theta = c/v = 1/M,$$

where  $M$  is the Mach number. The wave propagated into the atmosphere in this direction will have a horizontal trace velocity  $V_p$  given by

$$V_p = c (1 + \cot^2 \theta)^{1/2}.$$

In the direction  $90^\circ - \theta$  from the flight direction, the propagation angle will be  $0^\circ$ ; i. e., the wave can not reach the reflection height in the atmosphere unless its propagation angle is altered by local wind or temperature gradient. According to this simple consideration, the acoustic energy will be radiated in the horizontal plane in a sector limited by  $\pm(90^\circ - \theta)$  around the flight direction. The variation of the propagation angle with respect to the flight direction will influence horizontal trace velocities recorded on the ground after long-distance propagation. This effect has been verified in an unpublished experiment carried out in 1974 by the author using small supersonic aircraft at distances between 600 and 900 km.

The above consideration shows that both the width of the sector in which the acoustic energy is radiated by the aircraft and the range of horizontal trace velocity variations are dependent on the aircraft velocity. For the three aircraft velocities used in Fig. 3, the maximum  $V_p$  will be 360, 420, and 555 m/s for  $V = 1200, 1500,$  and  $2000$  km/h, respectively.

In our particular case, the Concorde is viewed nearly from the front when it leaves the U. S. coast and nearly from the side when it approaches Europe. This means that the infrasonic signal originating at the westernmost part of the flight route will show the highest horizontal trace velocities. On the other hand, the infrasonic signal from the final part of the supersonic route will have trace velocities close to the sound velocity.

## Results of early observations of Concorde

During the winter months of 1976-77 and 1977-78, the Concorde was regularly recorded at the above-mentioned stations in Northern Sweden. Besides standard narrowband recordings at 2 Hz, broadband recordings were made on several occasions at one of the stations (Jämtön). It has been found that the infrasonic signal is dominated by frequencies between 1 and 3 Hz. An example in Fig. 5 shows the FFT frequency spectrum of the Concorde signal taken in the frequency range 2-20 Hz using a Bruel and Kjaer 2120 frequency analyzer.

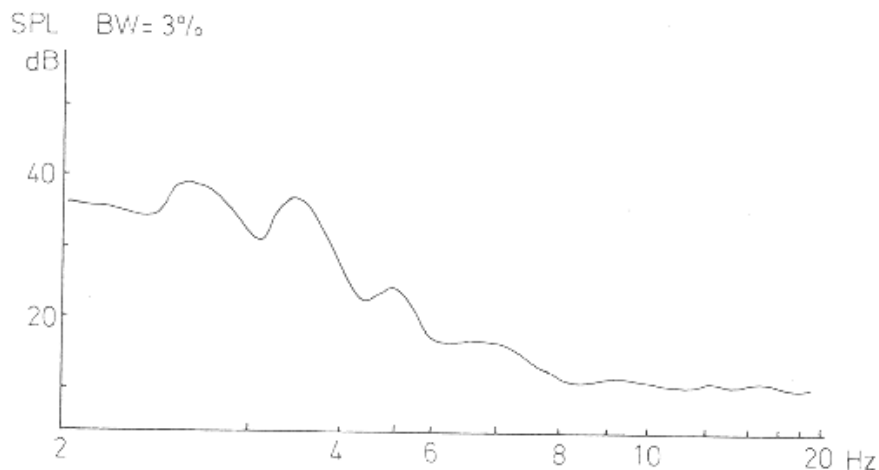


Fig. 5. Frequency spectrum of the infrasonic signal from the Concorde in the frequency range 2 – 20 Hz

Typical rms amplitude of the infrasonic signal is  $0.05 \text{ N/m}^2$  when the signal duration is of the order of 10 min. Closer to the focus area, the signal amplitude frequently exceeds  $0.1 \text{ N/m}^2$  so that it significantly contributes to the low-frequency background level. As an example, the total background level, during a Concorde flight on March 21, 1977, including environmental noise up to approximately 700 Hz, is shown in Fig. 6.

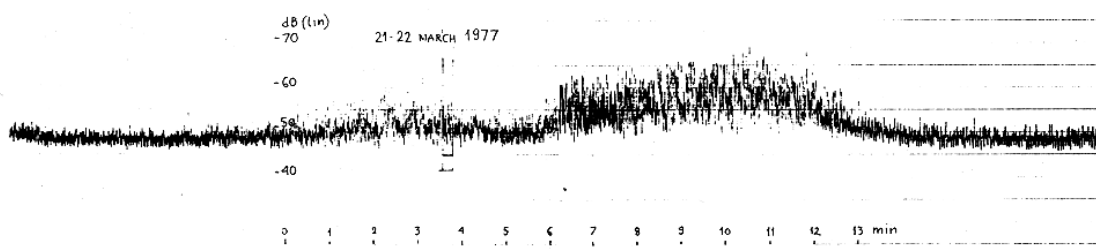


Fig. 6. Total sound pressure level recording of the infrasonic signal from the Concorde, March 21, 1977.

Examples of azimuth and horizontal trace velocity curves for three typical Concorde flights are shown in Figs. 7-9. It may be seen that the most distant Concorde signal is usually recorded at Lycksele. This signal originates at a distance of about 4500 km from the station, Southeast of Newfoundland. Recordings of December 27, 1976, shown in Fig. 7, indicate an apparent aircraft velocity of 1900-2000 km/h. This is in agreement with the nominal aircraft velocity (about 2100 km/h), which means that on this day the effect of the wind system was rather small.

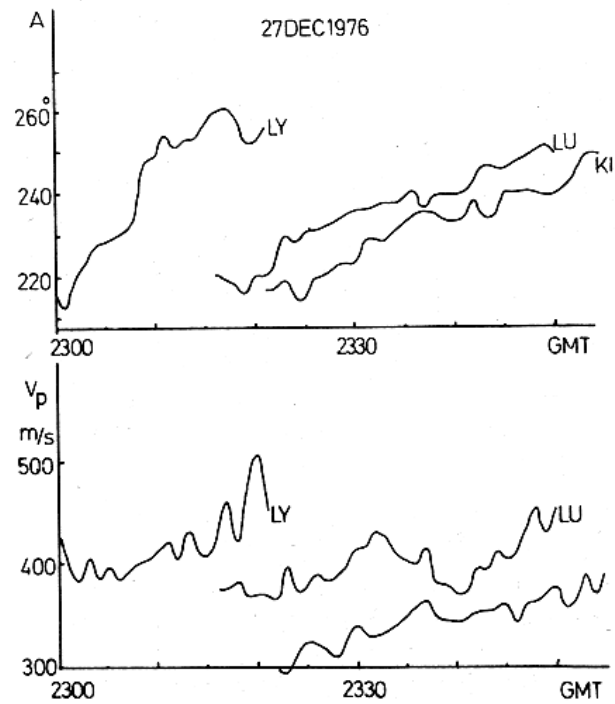


Fig. 7. Azimuth and horizontal trace velocity curves recorded at three stations in Northern Sweden, December 27, 1976.

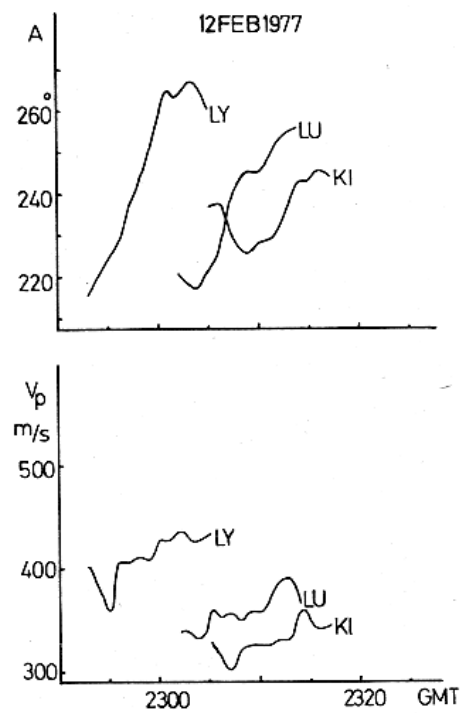


Fig. 8. Azimuth and horizontal trace velocity curves recorded at three stations in Northern Sweden, February 12, 1977.

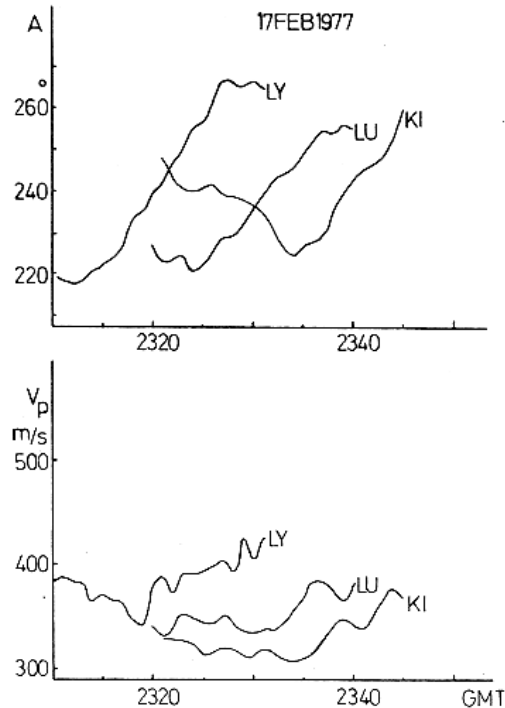


Fig. 9. Azimuth and horizontal trace velocity curves recorded at three stations in Northern Sweden, February 17, 1977.

Recordings of February 12, 1977 (Fig. 8) indicate that the apparent aircraft velocity was only 1500-1600 km/h (observe the large positive slope of azimuth curves) indicating a strong influence of the wind system. The recording from Kiruna shows at its beginning an interesting feature, which is even more pronounced in the example of Fig. 9: The supersonic route is seen there twice. The first part of the azimuth curve with a negative slope probably corresponds to "precursor" waves propagating with an apparent velocity larger than the velocity of sound. The shape of the azimuth curve is probably due to propagation through regions with different wind conditions. For example, propagation through the jet stream may influence recordings at the northernmost station.

### ***Conclusions concerning first observations of the Concorde***

Large supersonic aircraft like the Concorde may be detected at infrasonic frequencies at very large distances from the flight route. This is possible due to favorable propagation conditions at frequencies about 2 Hz and due to a long-distance focusing mechanism. Infrasonic signals from the Concorde with amplitudes on the order of 0.1 N/m<sup>2</sup> (74 dB re 20  $\mu$ N/m<sup>2</sup>) are observed in Northern Sweden due to focusing. Infrasonic signals with such amplitude may easily be detected using a standard sound level meter with a microphone sensitive for infrasonic frequencies (for example, B & K 2209). The shortest distance between the Concorde with supersonic speed and the Swedish infrasound stations was about 2000 km.

The Concorde may be considered as an infrasonic source located at a known distance, strong enough to be recorded at distances up to 5000 km. Multistation recordings of Concorde signals provided information about the atmosphere: horizontal wind- and

temperature variations. Scheduled flights of Concorde thus offered during many years new possibilities for atmospheric research.

The research described in this section was submitted to publication in JASA during the fall of 1977. However, the work was received by referees with considerable skepticism. Opinions about: "author's lack of understanding of the basic geometry of shock wave propagation" were expressed. Propagation of infrasound from supersonic aircraft at distances larger than 1000 km was considered impossible with reference to work of Balachandran et al. published during the summer of 1977. The then-Associate Editor, Dr Allan Pierce, overrode the referees' opinion and the work was finally published during the summer of 1978.

### **References to Chapter 6**

L. Liszka, and S. Olsson, J. Atmosph. Terr. Phys. 33, 1933 (1971).

F. H. Grover, Q. J. R. Astron. Soc. 14, 141 (1973).

B. L. Murphy, "Upward propagation of a weak shock in an exponential atmosphere, "  
Paper presented at Symposium on Atmospheric Acoustic and Noise Propagation,  
National Bureau of Standards, Gaithersburg, AID (27-29 September 1972).

E. F. Cox, H. J. Plagge, and J. W. Reed, "Damaging Air Shocks at Large Distances from  
Explosions, " Operation Buster-Jangle Rep. WT-303, Scandia Corporation (April  
1952).

L. Liszka, J. Acoust. Soc. Am. 56, 1383 (1974).

R. W. Procnier and G. W. Sharp, J. Acoust. Soc. Am. 49, 622 (1971).

L. Liszka, Res. Prog. 4, 76 (1977) (in Swedish).

P. S. Rao, "Supersonic Bangs I, <sup>o</sup>1 Aero Q. 7, 21-44 (1956); "Supersonic Bangs II," Aero  
Q. 7, 135-155 (1956).

H. S. Ribner, J. Acoust. Soc. Am. 52, 1037 (1972).

## Chapter 7

### High Resolution Observations of Infrasound Generated by the Supersonic Flights of Concorde

Since the scheduled flights of Concorde between the United States and Europe started in 1976, infrasound generated during practically all flights towards Europe has been recorded at infrasonic recording stations in Sweden. The results of the observations have shown that the infrasound generated by supersonic flights may be recorded at distances of at least 4000 kilometers due to a focusing mechanism (Liszka, 1978). Close to the focus area the signal may be observed both in the temporal order, i. e. the earliest generated signal received first, and in the reversed order (when the flight trajectory is observed "backwards") (Liszka, 1981). The order of the received signal is entirely determined by the temperature and wind profiles between the aircraft and the observer.

The recording equipment used at all stations until 1994 was operated at a fixed frequency of 2Hz (for description see Lundqvist, 1986). The accuracy with which the angle of arrival was determined by that equipment was rather poor: on average  $\pm 7^\circ$ . For that reason, the fine structure of the angle of arrival of the Concorde signal could not be performed. However, it was suspected that at least a part of the structure observed on the the azimuth vs time curves of the Concorde signal was real and not only due to measuring errors. Not until 1994, when a high resolution, broad band recording equipment (Waldemark, 1994) was put into operation at two infrasonic stations ( Jämtön and Uppsala), did it become possible to study the fine structure of the angle of arrival of the Concorde signal. In this chapter some properties of the fine structure of the signals are reviewed and possible propagation mechanisms responsible for the observed phenomena are discussed.

#### ***Again about generation of infrasound by a supersonic flight***

During a supersonic flight, a shock wave cone, a so-called Mach cone, is formed around the aircraft (see Fig. 1). The opening angle of the cone is  $2\theta$  given by

$$\sin \theta = 1/M \quad (1)$$

where M is the Mach number.

Due to irregularities in the temperature and wind distribution in the atmosphere between the aircraft and the observer, the regular shock wave will be, after a certain propagation

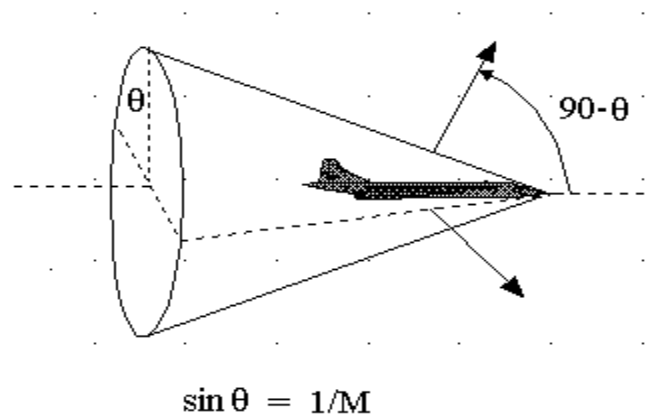


Fig. 1. The geometry of the Mach cone at the aircraft. Propagation directions in vertical and horizontal planes are indicated by arrows.

distance, converted into a package of infrasonic waves with frequencies between 0.5 and 6 Hz. In this study, we will assume that the infrasound formed at a distance from the aircraft has the same direction of propagation as the normal to the original shock wave. It means that the infrasound from a supersonic aircraft is propagated into the atmosphere at different inclination angles at different azimuths with respect to the flight direction. In the direction of flight the inclination of the wave vector (with respect to the horizontal plane) will be  $90^\circ - \theta$ . At the azimuth  $90^\circ - \theta$  from the flight direction, the inclination angle of the wave vector will be  $0^\circ$ ; i. e. the wave can not reach the reflection height in the atmosphere unless its propagation angle is altered by local wind or temperature gradients. According to this simple consideration, the acoustic energy will be radiated in the horizontal plane in a sector limited by  $\pm(90^\circ - \theta)$  around the flight direction. The inclination angle of the wave vector  $\iota$  when the propagation takes place in the direction  $\alpha$ , may be calculated from the following equation:

$$\cos \iota = \cos(90^\circ - \theta) \sqrt{1 + \tan^2 \alpha} \quad (2)$$

where  $\alpha$  is azimuth measured from the direction of flight. The equation (2) will be used during ray-tracing calculations in the present work.

### ***Observations of the angle of arrival of Concorde signals***

The new infrasonic equipment used in the present study produces, in the default mode, 464 readings of the azimuth of arrival per hour, i. e. one reading each 7.8 seconds. Due to a high sensitivity of the equipment, it is not uncommon that the infrasonic signal from the Concorde was received for up to 30 minutes. It has been found that during winter conditions, the angle of arrival is not varying in a uniform way but is rather showing a few "jumps" between some discrete directions. Typical azimuth recordings from Jämtön of two Concorde flights on February 6, 1995 are shown in Fig. 2. The azimuth readings are shown by circles, the diameter of which is proportional to the amplitude of the maximum signal in the frequency spectrum between 0.5 and 4.5 Hz. It is clearly seen that during that day the signal was arriving from three discrete directions, probably corresponding to three different propagation modes. The first two propagation modes are characterized by very high signal amplitudes, the third one shows weak signal, just above, or even below the noise level (see Fig. 3). The signal amplitude drops during the transition between the Mode 1 and Mode 2. The frequency distributions of the azimuth of arrival for both flights are shown in Fig. 4.

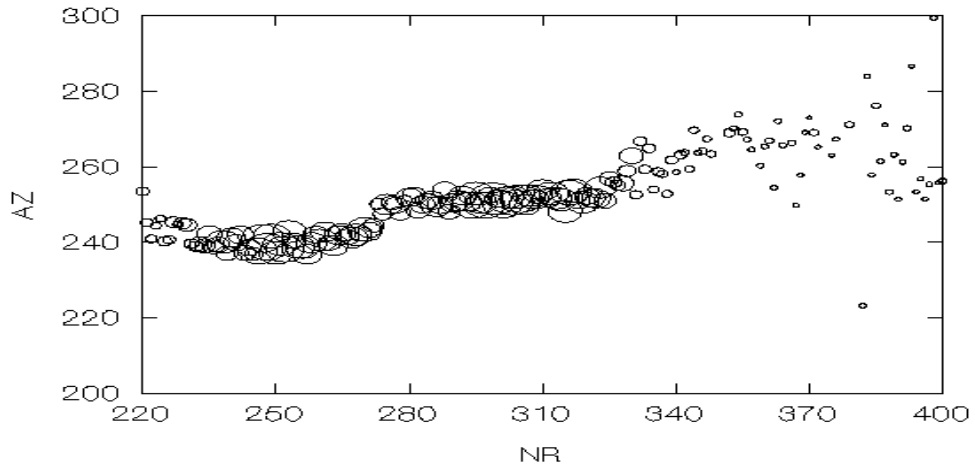
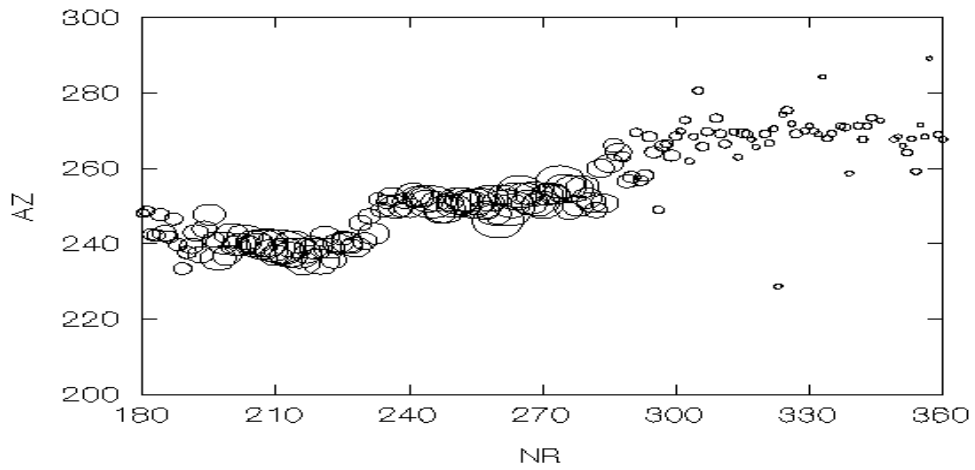


Fig. 2. Azimuth of arrival of Concorde signals from two BA flights New York - London on February 6, 1995. The size of symbols representing azimuth readings is proportional to the spectral amplitude of the maximum signal. The horizontal axis represents the reading number. The corresponding time readings are 1854 - 1917 UT for the upper recording and 2355 - 0018 UT for the lower recording.

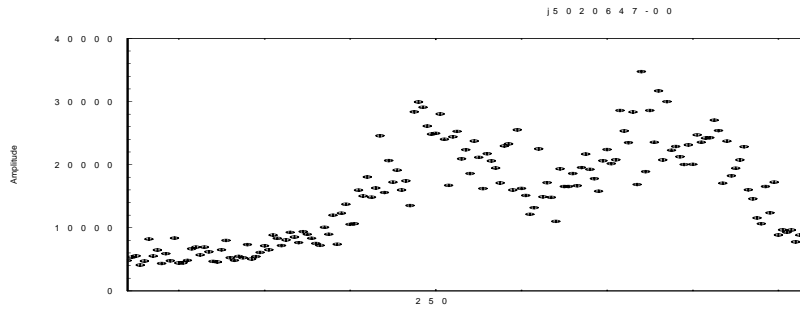


Fig. 3. The spectral amplitude of maximum signal between 0.5 and 4.5 Hz plotted as a function of the reading number (time) for the same two flights of February 6, 1995 as in Fig.2.

There is a significant difference between frequency spectra observed during different modes. An example of frequency spectra for all three modes is shown in Fig. 4 for the same flight as shown in the lower part of Fig. 2. One can see that, despite different amplitudes, the spectrum of Modes 1 and 2 shows a different shape than that observed during Mode 3.

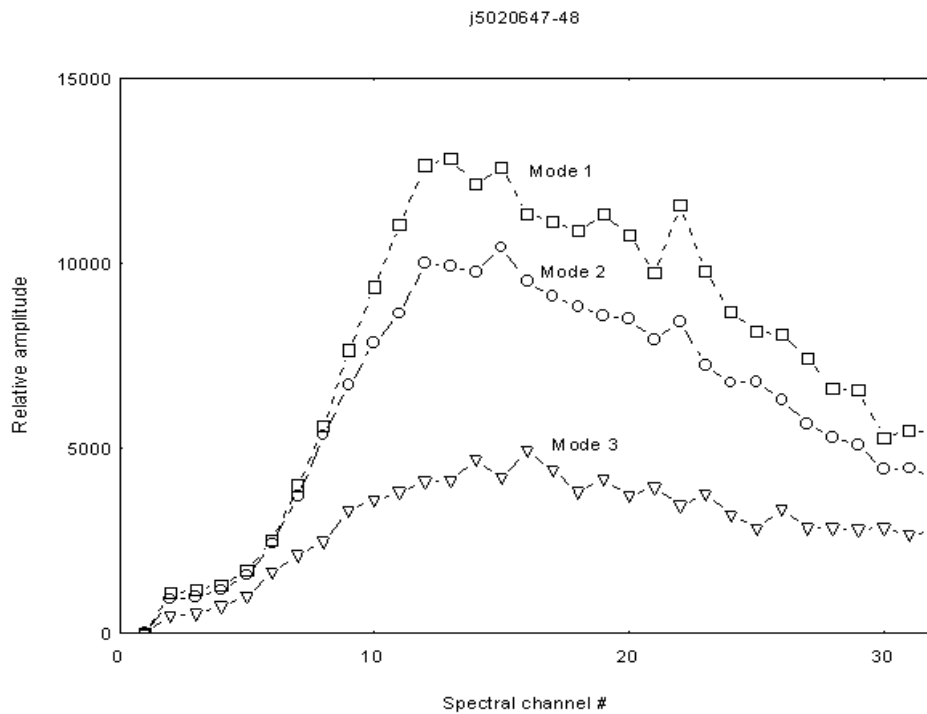
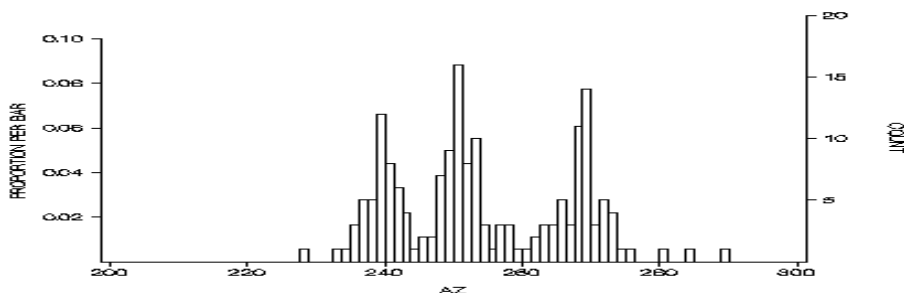


Fig. 4. Frequency spectra of Concorde infrasonic signal corresponding to three observed propagation modes. Spectral channel #32 corresponds to 4.5 Hz.



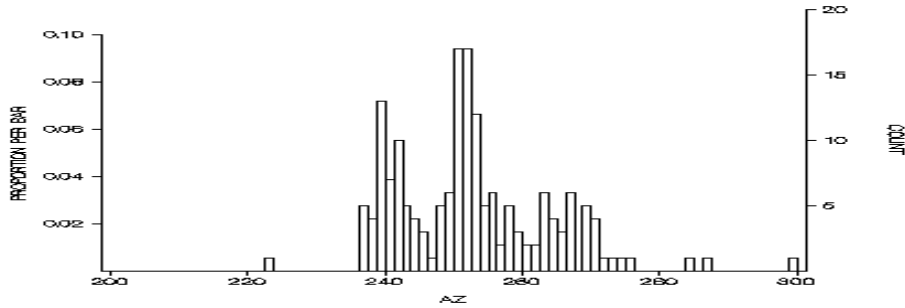


Fig. 5. The frequency distributions of azimuth of arrival for Concorde infrasonic signal from the same two flights on February 6, 1995 as in Fig. 2..

The direction of arrival of the signal corresponding to different modes when observed from a given station, appears to be constant during consecutive flights on the same day. An example is shown in Fig. 5. The same flight observed at different stations, see Figures 6a - 6d, shows different angles of arrival for the same mode.

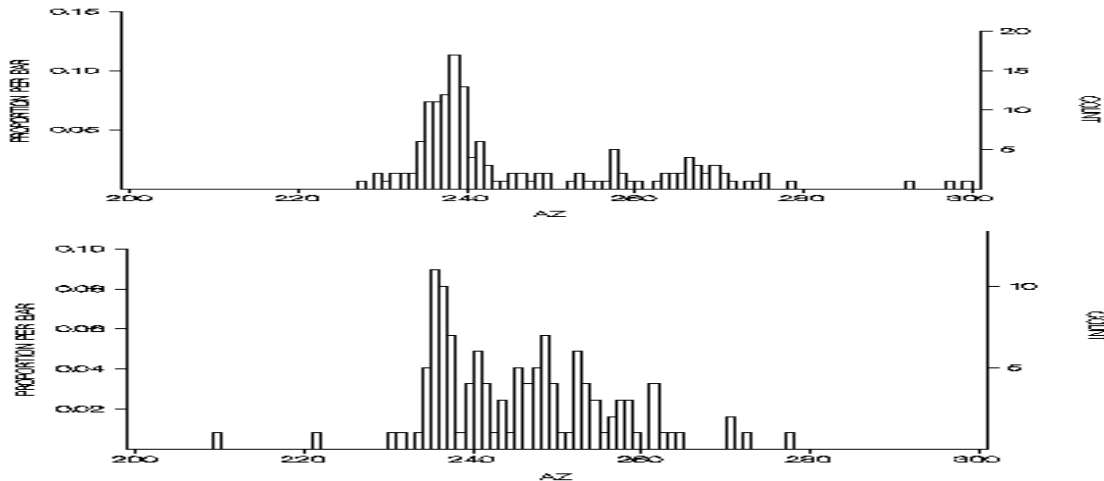


fig. 6a. Frequency distributions of azimuth of arrival for Concorde infrasonic signal from a BA flight New York - London on February 7, 1995 measured in Luleå (65.8N, 22.5E) (upper diagram) and in Uppsala (59.8N, 17.6E) (lower diagram).

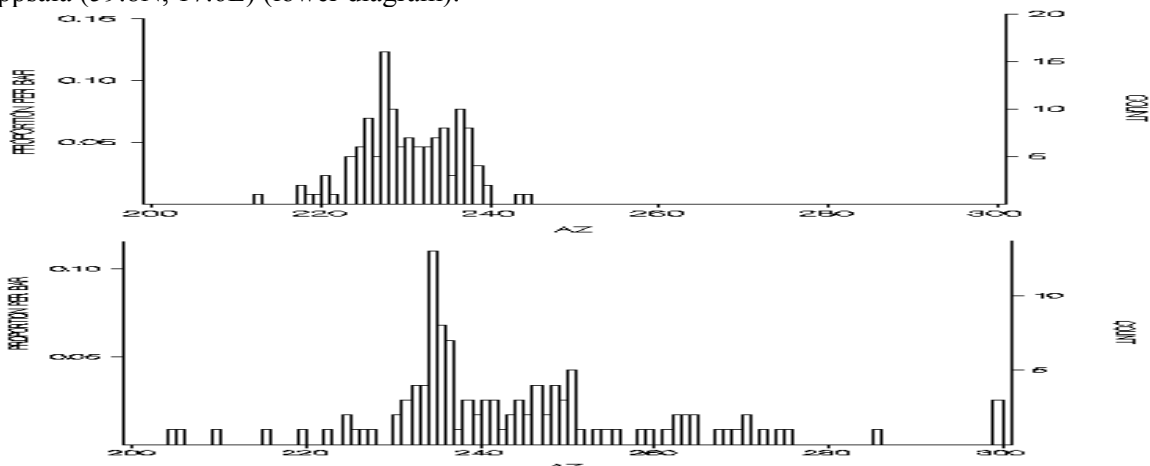


Fig. 6b. Frequency distributions of azimuth of arrival for Concorde infrasonic signal from an AF flight New York - Paris on February 10, 1995 measured in Jämtön (65.8N, 22.5E) (upper diagram) and in Uppsala (59.8N, 17.6E) (lower diagram).

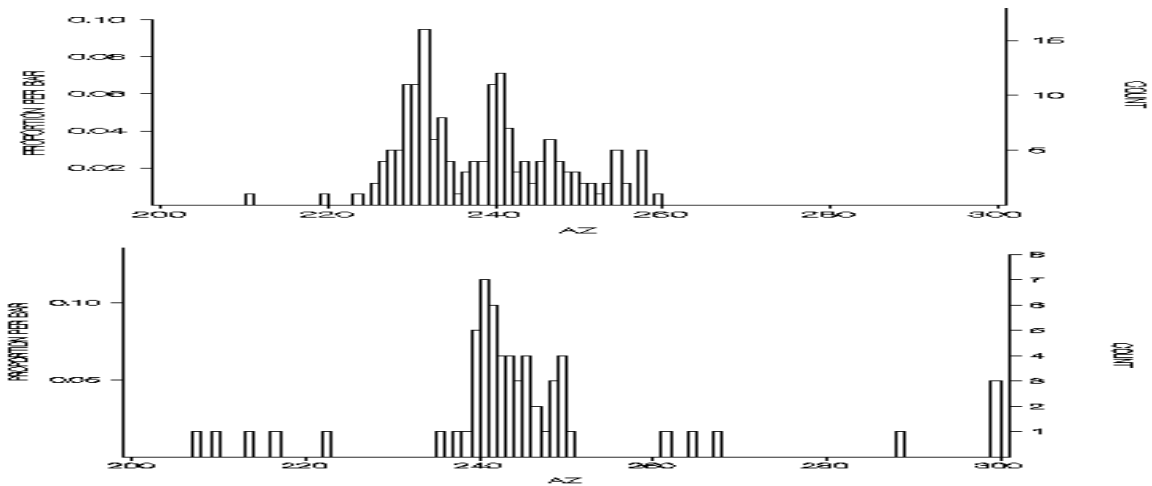


fig. 6c. Frequency distributions of azimuth of arrival for Concorde infrasonic signal from a BA flight New York - London on February 10, 1995 measured in Luleå (65.8N, 22.5E) (upper diagram) and in Uppsala (59.8N, 17.6E) (lower diagram).

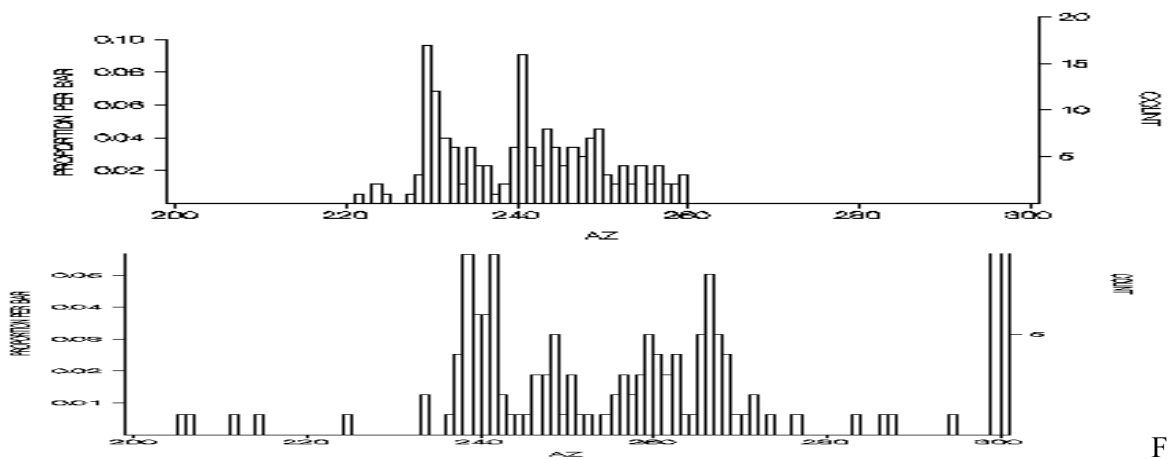


Fig. 6d. Frequency distributions of azimuth of arrival for Concorde infrasonic signal from a BA flight New York - London on February 11, 1995 measured in Luleå (65.8N, 22.5E) (upper diagram) and in Uppsala (59.8N, 17.6E) (lower diagram).

The nature of the observed phenomenon may be explained using ray-tracing calculations in a model atmosphere. A ray-tracing technique similar to that used by Cowling, Webb and Yeh (1970) has been used (Fig. 7). Assuming the aircraft in the middle of the bottom side of the diagram, heading the azimuth of  $70^\circ$ , the possible rays propagating towards NE from the aircraft ( a half of the propagation cone) have been calculated each  $0.5^\circ$ . The angle of incidence of each ray with respect to the vertical direction has been calculated using the formula (2). The reflection points in the atmosphere are marked with circles. One can see that rays farthest from the direction of flight, propagating at lowest angles of incidence, are clustered in two groups. These two clusters of rays coincide with the directions in which Modes 1 and 2 of the arriving Concorde signal are usually observed. The mode 3 corresponds to the front-on part of the ray pattern. Vertical plane projections of the calculated rays corresponding to rays within the Modes 1, 2 and 3 are shown in Figs. 8 -10. The lower part of each diagram displays the slope of the ray as a function of the horizontal distance travelled by the ray. It may be clearly seen that those three propagation modes correspond to three different reflection height-intervals in the atmosphere. The Mode 1 corresponds to propagation through reflections in the stratosphere, Modes 2 and 3 correspond to propagation

through reflections in the lower and upper thermosphere. In Mode 1 the signal is, from time to time, trapped at the reflection height.

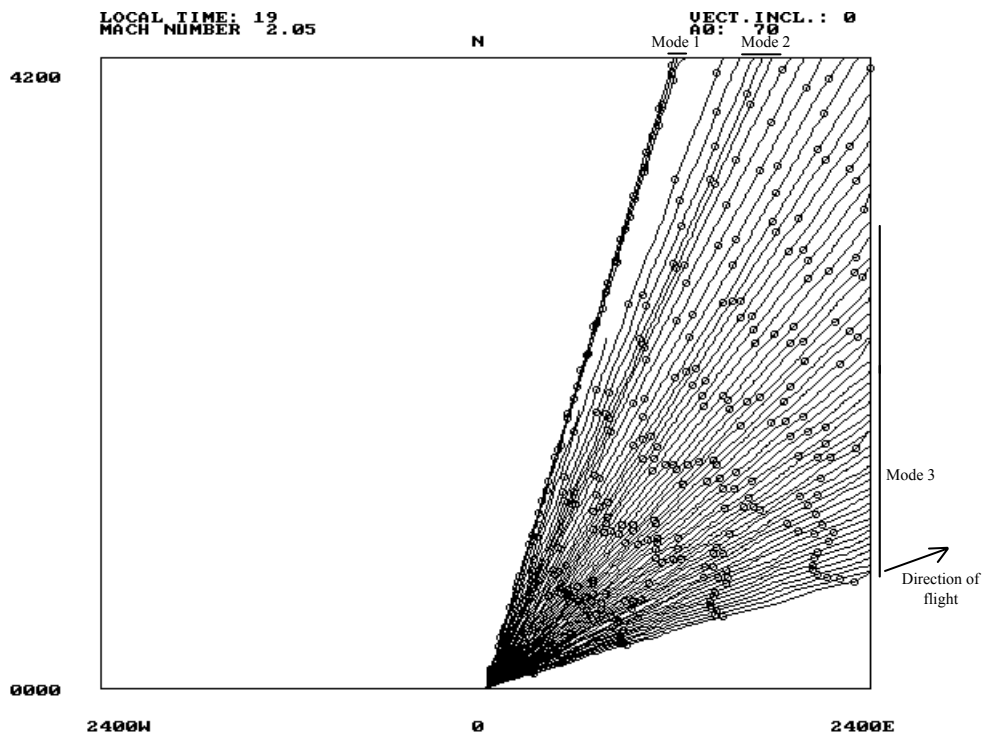


Fig. 7. Horizontal projection of ray tracing for infrasonic signals generated by the left side of the Mach cone of an aircraft flying Mach 2.05 towards the azimuth =  $70^\circ$ .

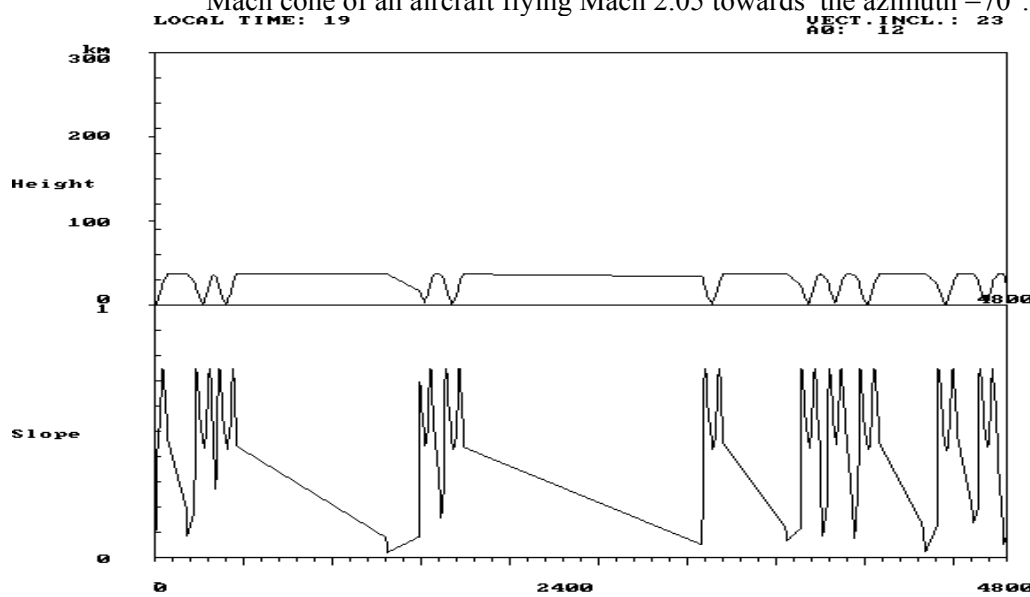


Fig. 8. Projection of rays propagating from the aircraft towards the azimuth =  $12^\circ$  (corresponding to Mode 1). The lower diagram shows the slope of the ray.

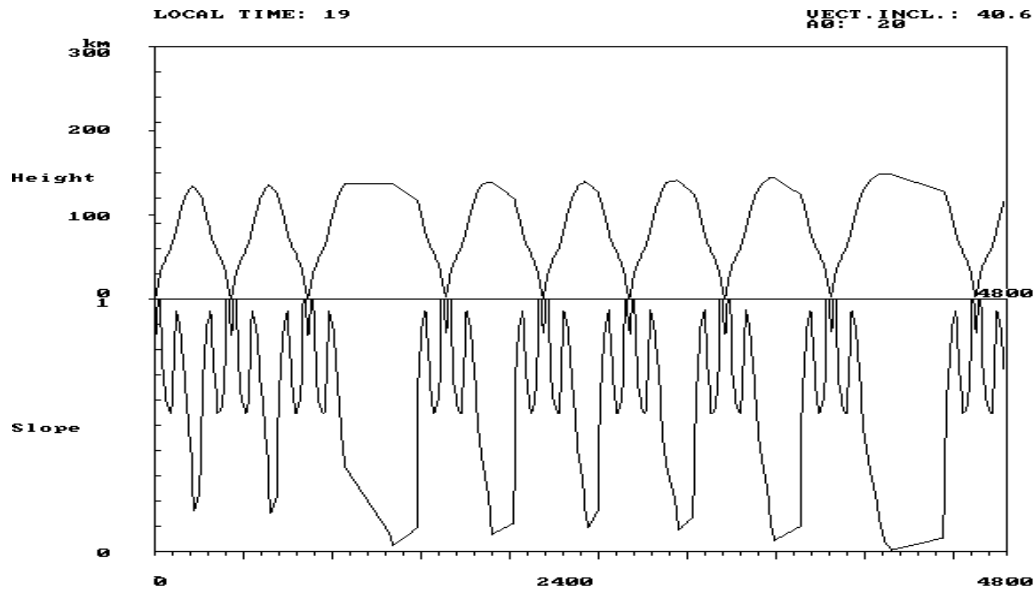


Fig. 9. Projection of rays propagating from the aircraft towards the azimuth=20° (corresponding to Mode 2). The lower diagram shows the slope of the ray.

Clustering of rays may be enhanced by adding, to the wind and temperature models, small fluctuations of both wind and temperature. A Gaussian distribution of fluctuations has been assumed. The clustering phenomenon seems to disappear when the fluctuation amplitude increases above a certain level.

Interesting results may be obtained from multiple ray-tracing calculations in an atmospheric model with fluctuations. Assuming a given geographic position of both the source and the recording station, the rays leaving the source were calculated at each 0.5 degree. Rays approaching the recording station at a distance less than 80 km were identified and the propagation time between the source and the closest point of the ray

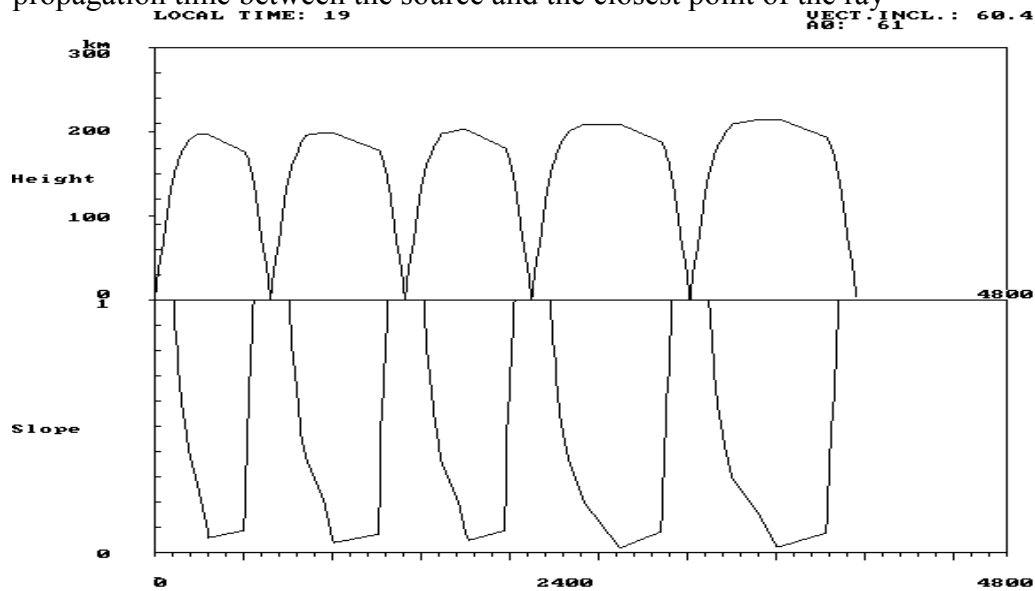


Fig. 10. Projection of rays propagating from the aircraft towards the azimuth=61° (corresponding to Mode 3). The lower diagram shows the slope of the ray.

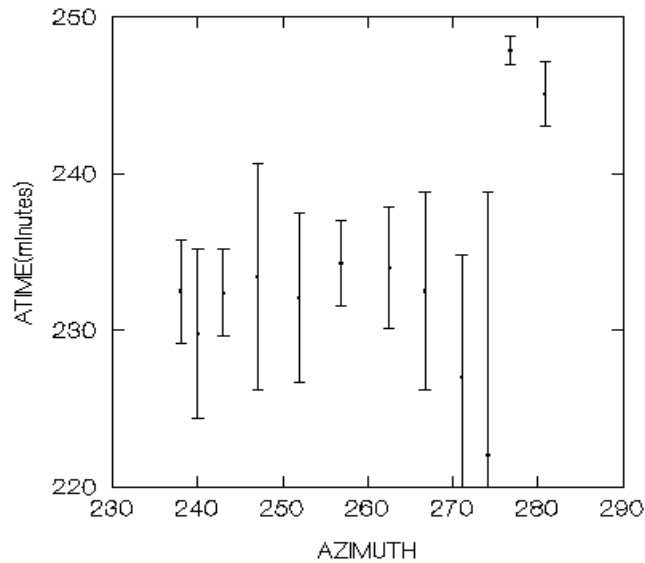


Fig. 11. Time of arrival (in minutes) of signals arriving from the flight trajectory as a function of the azimuth of arrival. The scatter of the time of arrival is determined by ray-tracing in a model atmosphere with normally distributed fluctuations in the wind and temperature profiles. Time of arrival is counted from the start of the supersonic trajectory of the aircraft on the route New York – London.

was calculated. A statistical study was made over propagation times between a number of selected points of a typical flight trajectory and the recording station in Northern Sweden (Luleå). The scatter of calculated propagation times is shown in Fig. 11 as the function of azimuth from which the signal from that particular point of the trajectory is recorded. One can see that signals arriving from parts of the flight trajectory corresponding to azimuths of arrival around 245° and 265 - 275° may be spread over a considerable period of time due to a variety of possible propagation paths. Under favourable conditions the infrasonic signal from a limited portion of the trajectory (and thus a fixed azimuth) may arrive to the recording station during several minutes, which shows as "steps" on the azimuth - time curve (see e. g. Fig. 2). The present results may also explain the variety of observed forms of the azimuth - time curve.

An interesting feature may be seen in Fig. 11 at the azimuth of about 280°. The signal arriving from that direction originated at the beginning of supersonic flight, almost 5000 kms (see Fig. 12) from the recording station. The signal, apparently propagating through reflections in the thermosphere, arrives after an extraordinary long propagation time, probably due to trapping in the thermosphere. The late arriving signal is a part of Mode 3 propagation.

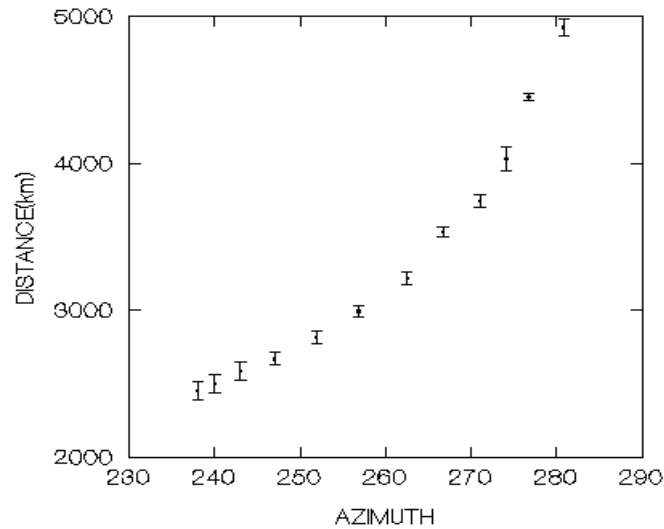


Figure 12. Average distances to the aircraft as a function of the azimuth of arrival of infrasonic signals.

The diagram of Fig. 11 with all three modes marked is shown in Fig. 13.

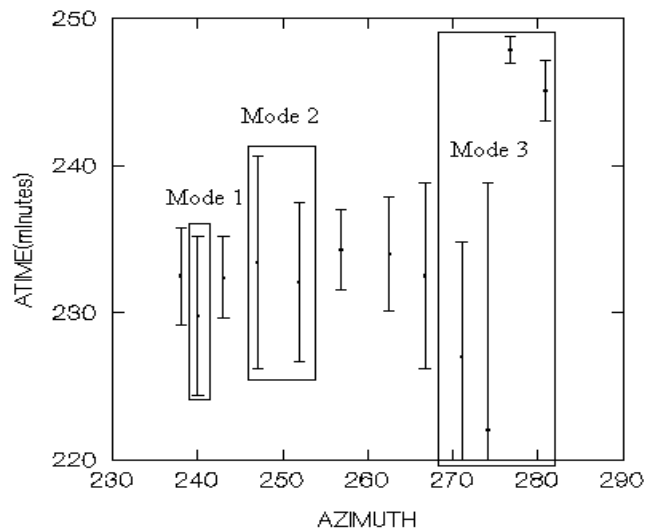


Fig. 13. Time of arrival (in minutes) of signals arriving from the flight trajectory as a function of the azimuth of arrival. All three propagation modes are indicated in the diagram.

Some of the Concorde recordings do not show clear propagation modes. An example of a recording where the azimuth varies continuously with time is shown in Fig. 14. There is some evidence that this particular type of azimuth variation, which does not show the clustering phenomenon, is associated with the occurrence of larger and more frequent irregularities in the wind system and in the large scale temperature distribution. This topic was a subject of another study (see the next paragraph).

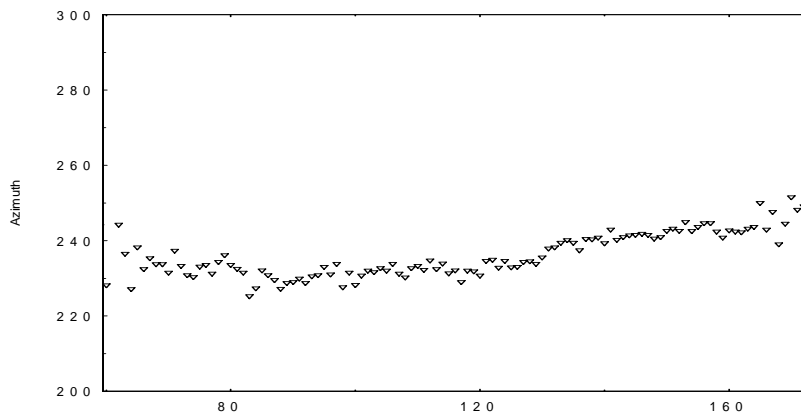


Fig. 14. An example of an azimuth recording of a BA flight of Concorde on February 10, 1995 without clear propagation modes. The horizontal axis shows the number of azimuth readings during 2330 - 0000 UT.

The phenomenon of late arriving signal from the direction  $280^\circ$  has been occasionally observed since the end of the 70's. However, the reliability of the recordings was at that time not good enough and there was no proof that the late signal was in fact generated by Concorde. First at present, using an improved ray tracing technique

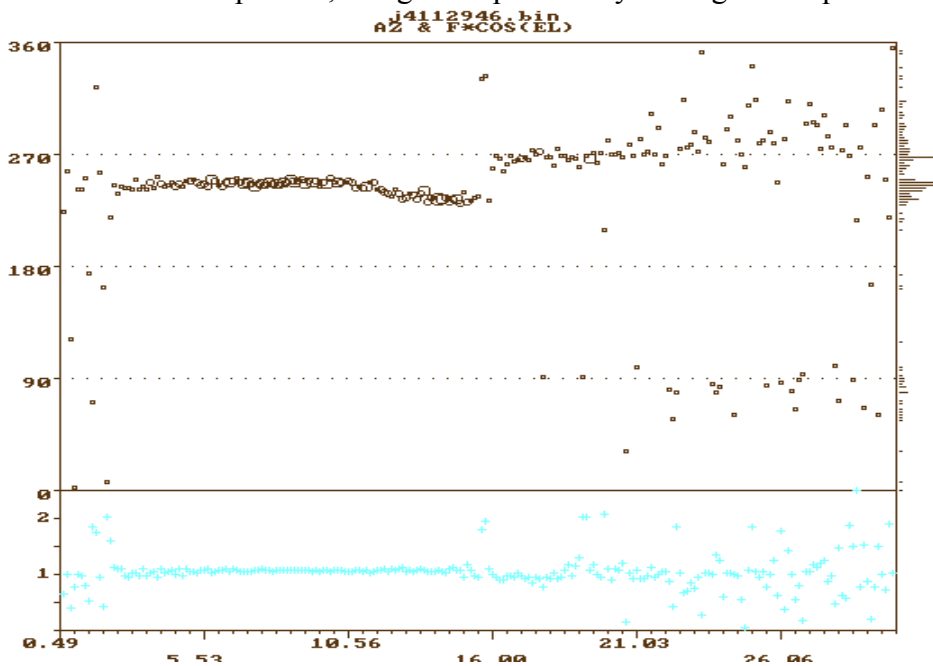


Fig. 15. An azimuth recording (upper diagram) of an AF flight of November 29, 1994 2300 - 2330 UT showing the late arriving signal from the direction range  $270 - 300^\circ$ .

and high resolution measurements, it was possible to explain that phenomenon. An example of a Concorde recording showing the late signals is given in Fig. 15.

If the azimuth readings of Fig. 15 are plotted on the diagram of Fig. 11, one can see that there is a satisfactory agreement between the predicted limits of azimuth and the observed values during a particular flight (see Fig. 16). It must be remembered that the actual flight is an Air France flight New York - Paris with the final part of supersonic trajectory further south than during the flights New York - London. The southernmost azimuth, as seen from the Jämtön station, reaches an azimuth of  $230^\circ$  during Paris-flights. It is very likely that the "late arriving signals" from the directions between  $265$  and  $280^\circ$  are in fact arriving whole the time after about 220 minutes after the reference time, but are completely obliterated by the very strong

signals arriving from a shorter distance from the directions 230 - 250°. A high resolution microphone array using a beam-forming technique would be needed to confirm this last statement.

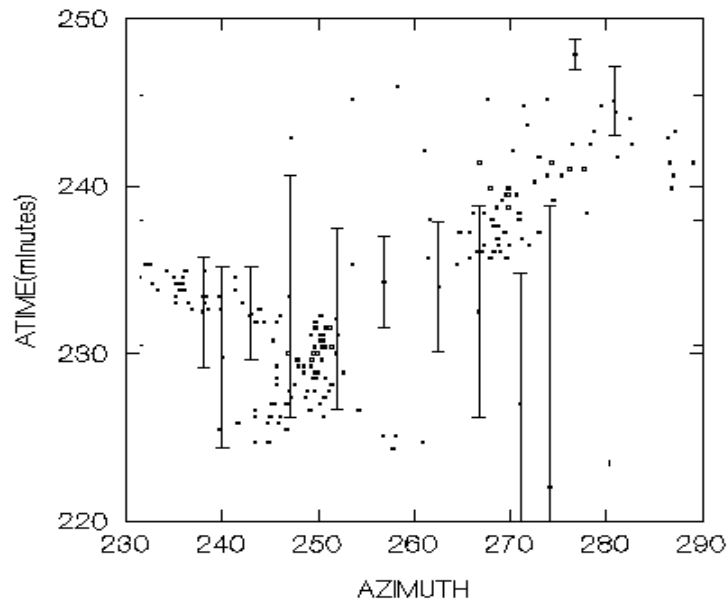


Fig. 16. The azimuth recording shown in Fig. 15 overlaid on the possible azimuth ranges estimated using a ray tracing technique.

### ***Angle-of-arrival variations and the atmospheric structure***

Recording of infrasonic signals from supersonic flights of Concorde was a unique and powerful tool for studying propagation of infrasonic waves through the atmosphere. The phenomenon of clustering of rays would not be possible to demonstrate by observations of stationary sources.

An important consequence of the clustering phenomenon is that the observed azimuth of a distant source may not be correct, i. e. it may be by up to 10° different than the geometrical direction to the source, even when corrected for the effect of winds. If the infrasound measurements are to be used for monitoring of distant events, the clustering phenomenon must be taken into consideration. It must be remembered that a single, stationary source may not be detected by a single observing station if it occurs just between two areas from where different propagation modes are possible. Only by combining data from several, properly located observing stations, is it possible to detect and localize a source of infrasound. Also, knowledge of meteorological conditions, such as wind and temperature profiles in the atmosphere, over the propagation area is important for the accurate location of infrasonic sources.

The complexity of the effect of winds on long-distance propagation was further confirmed by the work of Waldemark (1997). The study was based on statistical data about all scheduled flights of Concorde during the time: January 1 – December 31, 1995. total of 535 flights (3 flights/day). Each flight recording was described by four variables:

1. start-azimuth
2. end-azimuth
3. azimuth difference
4. signal duration.

These descriptive variables were compared with simultaneous atmospheric data, in particular the zonal wind above the North Atlantic. Only zonal winds at 100 hPa (16 km height) and 50

hPa (20 km) were available. The North Atlantic area over which the signals originated covered the latitude range between 40N and 65N and the longitude range between 40W and 5W in 5° steps. The zonal wind was thus described by a 6 x 8 matrix. The flight recordings were divided into 5° intervals of azimuth: the southernmost between 220 and 225° and the northernmost interval between 255 and 260°. Since the three daily flights were slightly different with respect to both the local time and to the flight trajectory, the analysis was performed for each of three flights separately. An important question in this study was if the descriptive variables of infrasound recordings were correlated with zonal winds across the North Atlantic area. It may be expected that conditions above the tropopause, where the aircraft were moving, would influence the infrasonic signals generated there. At long distances, as here, between the aircraft and Scandinavia, one could expect that also close to location of ground bounces, there would be such a correlation. The correlation analysis was performed for different time intervals in order to localize in time the transition between the summer and the winter atmosphere. Results of the correlation analysis show a complex picture. Two examples, each correlated with zonal winds at both 16 (left diagram) and 20 km (right diagram) for the last flight of the day, are shown in Fig 17 and 18. Fig. 17 shows the correlation with the southern part of flight trajectory (azimuths 225 - 230°), while Fig. 18 corresponds to the northern part of flight trajectory (245 – 250°).

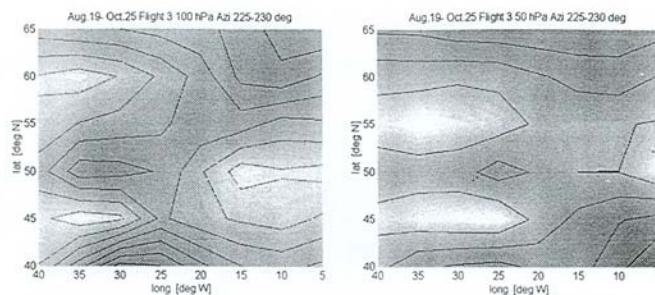


Fig. 17. Contour plot of absolute values of correlation coefficients between Concorde azimuth histogram data at a specific azimuth interval 225-230° and 48 wind data points at a time for levels 100 hPa and 50 hPa. Data is from flight 3 and the period August 20 to October 29.

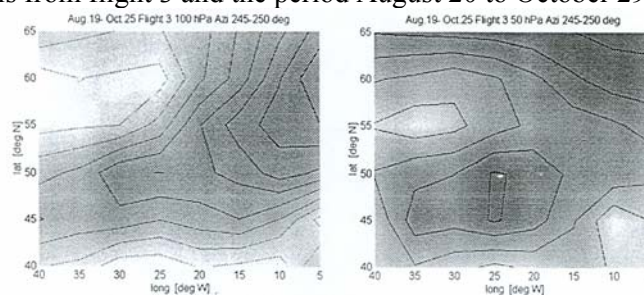


Fig. 18. Contour plot of absolute values of correlation coefficients between Concorde azimuth histogram data at a specific azimuth interval 245-250° and 48 wind data points at a time for levels 100 hPa and 50 hPa. Data is from flight 3 and the period August 20 to October 29.

The lack of correlation is depicted by the white colour, while the black corresponds to a correlation coefficient equal to 1. One can see that areas of high correlation are not simply related to areas where the signal was either generated or bounced from the ground. Structures appearing in Figs. 17 and 18 seem to be in agreement with, ideas discussed in the previous section, about horizontal clustering of rays.

The research about the fine structure of Concorde-signals constituted a part of the PhD thesis of Karina Waldemark, defended at the University of Umeå in May 1997.

### ***References to Chapter 7***

- Cowling, D. H., H.D.Webb and K.C. Yeh, (1970). Tech. Rep. 38, Ionosphere Radio Laboratory, University of Illinois.
- Lundkvist, B., (1986). J. Low Frequency Noise & Vibration, Vol. 5, No.4, 137.
- Liszka, L., (1978). J. Acoust. Soc. Am., Vol. 64(2), 631.
- Liszka, L., (1981). Proc. Int. Symposium on Acoustic Remote Sensing of the Atmosphere and Oceans, June 22-25, 1981. The University of Calgary, Calgary, Alberta, Canada.
- Waldemark, K., (1994). High Resolution Infrasonic Recording Equipment, Scientific Rep., Swedish Institute of Space Physics.
- Waldemark, K., (1997), Studies of the Atmosphere using Infrasound Recordings, PhD Thesis, Swedish Institute of Space Physics.

## Chapter 8

### Wavelet Analysis of the Concorde-generated Infrasound

The recording equipment used at all stations until 1994 was operated at a fixed frequency of 2Hz (for description see Lundqvist, 1986). The accuracy with which the angle of arrival was determined by that equipment was rather poor: on average  $\pm 10$  degrees. For that reason the fine structure of the angle of arrival of infrasonic signals could not be determined. However, it could be suspected that at least a part of the structure observed on the the azimuth *vs* time curves of the Concorde signal was real and not only due to measuring errors. Not until 1994, when a high resolution, broad band recording equipment (Waldemark, 1994) was put into operation at two infrasonic stations ( Jämtön and Uppsala), did it become possible to study the fine structure of the angle of arrival of the Concorde signal. Results published in 1995 (Liszka and Waldemark, 1995) have shown a mode-structure of the signals (as mentioned above).

A further progress in studies of the structure of infrasonic signals became possible through introduction of signal processing technique based on the wavelet transform. The aim of this chapter is to demonstrate how the wavelet technique can be used to decompose complex signals and to enhance signals below the threshold of the recording equipment. The data analysis is illustrated by a 30-minutes data file from Jämtön recording station (65.8N, 22.5E). The data file consists of 59 data blocks. Each block contains 512 A/D readings from 3 microphones, covering 28.4 seconds. Within the data file used here there is a recording of Concorde signals starting at 1901 UT on March 22, 1997. The angle-of-arrival recording for that file is shown in Fig. 1. The variable shown in the bottom graph of Fig.1 is proportional to the horizontal trace velocity of the signal.

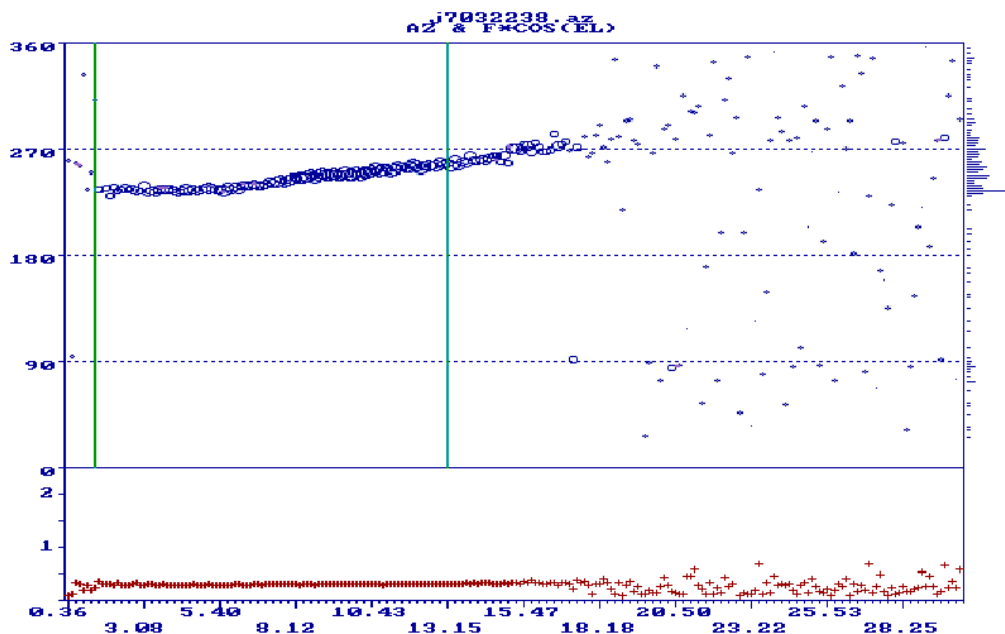


Fig. 1. The angle-of-arrival recording for the Jämtön station, 1900 - 1930 UT on March 22, 1997. The size of symbols is proportional to the cross-correlation between microphones. The variable shown in the bottom graph is proportional to the horizontal trace velocity of the signal.

## 1. Wavelet transform

The wavelet transform has become a powerful tool for frequency analysis, in particular for non-stationary time series. Discussions of the wavelet transform and its applications can be found in a number of recent books and review articles (e. g. Chui, 1992, Chui et al., 1994, Farge, 1992).

The wavelet transform of a function  $y(t)$  is defined as (here \* denotes complex conjugation):

$$w(a,b) = a^{-1/2} \int_{-\infty}^{+\infty} y(t) g^*((t-b)/a) dt \quad (1.1)$$

where variable  $a$  is the scale dilation parameter and  $b$  the translation parameter. Both parameters are dimensionless. The real- or complex-valued function  $g(t)$  is called a mother (or analyzing) wavelet.

Here a particular wavelet transform, the Morlet wavelet, will be used.

The Morlet wavelet, being a locally periodic wavetrain, is related to windowed Fourier analysis. It is obtained by taking a complex sine wave, and by localizing it with a Gaussian (bell-shaped) envelope.

The Morlet wavelet is defined as:

$$g(t) = \exp(i\omega_0 t - t^2/2) \quad (1.2)$$

and its Fourier transform:

$$G(\omega) = \sqrt{2\pi} \exp[-(\omega - \omega_0)^2/2] \quad (1.3)$$

The Morlet wavelet gives the smallest time-bandwidth product (Lagoutte et al. 1992).

$\omega_0$  is a phase constant ( in the present study  $\omega_0 = 5$ ). For large  $\omega_0$  the frequency resolution improves, though at the expense of decreased time resolution.

In the present study, dilation #1 corresponds to the highest frequency (a half of sampling rate).

The highest dilation # corresponds to the lowest observable frequency.

## 2. Time-series decomposition using wavelet transform

Many time series observed in physics consist of a deterministic part with a superimposed stochastic component. A powerful technique to separate both components has been proposed by Farge (1993) and implemented in a practically usable software by Wernik (1997). In that method, being a kind of non-linear filtering, a wavelet frequency spectrum of the time series is calculated. The time series is decomposed into two parts in the following way:

- A deterministic “strong” part is obtained by setting to zero all wavelet coefficients less than a certain threshold level. The inverse wavelet transform is used to calculate the corresponding time series.

- A stochastic “weak” part is obtained by setting to zero all wavelet coefficients greater than that threshold level. The inverse wavelet transform is also used here to calculate the corresponding time series.

- New wavelet spectra are calculated for each partial time series.

Signal discrimination using the magnitude of wavelet coefficients as a discrimination criterium would correspond to discrimination with respect to the spectral density when using Fourier transform.

The stochastic part must follow a Gaussian probability distribution function. As a measure of departure from a Gaussian distribution, the kurtosis is used. If the threshold is properly selected, the integral of the kurtosis of the stochastic part over the entire frequency range reaches a minimum.

The above principle may be applied to decompose two or more deterministic signals, if the signals correspond to different magnitude of wavelet coefficients (different spectral densities).

### 3. The ampligram

There is a straightforward generalisation of the above technique, which may be used to separate independent components of the signal, assuming that the different components are characterized by different spectral densities.

The experience from studies of oscillations in complex mechanical systems indicate that a given oscillation mode usually occurs with a certain amplitude/spectral density. The amplitude ratios between possible modes are usually constant in such a system. This observation may be used to generalize the above non-linear filtering technique. For a time series of  $N$  values ( $N$  must be an integer power of 2) the following operations are performed

1. A Morlet wavelet transform is performed with at least 128 dilations. Thus, three  $N \times 128$  matrices,  $\mathbf{A}$ ,  $\mathbf{R}$  and  $\mathbf{I}$ , are obtained. The matrix  $\mathbf{A}$  is a matrix of magnitudes of  $w_{ij}$ :

$$\mathbf{A} = \{ |w_{ij}| \} \quad i=1, \dots, N \quad j=1, \dots, 128 \quad (3.1)$$

$\mathbf{R}$  and  $\mathbf{I}$  contain respective real and imaginary parts of  $w_{ij}$ .

2. Instead of using the low-pass or high-pass filtering of wavelet coefficient magnitudes, as described in §2, a kind of band-pass filtering of wavelet coefficient magnitudes is used in order to separate possible modes in the signal. The entire range of coefficient magnitudes: 0 to  $w_{\max}$ , or its lowest 20%, is divided into  $M$  intervals such that the  $k$ -th interval is limited by:

$$w_{\max} * (k-1)/M \quad \text{and} \quad w_{\max} * k/M \quad \text{where} \quad k=1, \dots, M \quad (3.2)$$

Two sets of intervals are used in the present work: 10 equal intervals between 0 and 100% of  $w_{\max}$  and in the other set 20 equal intervals between 0 and 20% of  $w_{\max}$ . For each  $k$ , the coefficients outside the range defined by (3.2) are identified and zeroed in matrices  $\mathbf{R}$  and  $\mathbf{I}$ , creating two new matrices  $\mathbf{R}_k$  and  $\mathbf{I}_k$ . The inverse wavelet transform is performed using  $\mathbf{R}_k$  and  $\mathbf{I}_k$  and a new version of the original time series,  $y_k(t_i)$  is created.  $y_k(t_i)$  is what the signal would look like if only a narrow range of spectral densities would be present with the same frequency content.

3. The operation is repeated  $M$  times at 1 or 10% intervals over the interesting range of coefficient magnitudes, usually 0 - 20% of maximum wavelet coefficient magnitude. A real-valued matrix  $\mathbf{M}$ , consisting of  $M$  columns and  $N$  rows is created:

$$\mathbf{M} = \{ y_k(t_i) \}$$

Each column corresponds to a time series which would be observed if only a narrow range of coefficient magnitudes would contribute to the observed signal. A 3-D plot of the matrix  $\mathbf{M}$ , called here an **ampligram**, may be constructed. An ampligram covering 0 - 100% of coefficient magnitudes is called here the **total** ampligram while the ampligram covering 0 - 20% of coefficient magnitudes is called here the **low-20** ampligram. The second one is most convenient when studying very weak components of the signal. A total ampligram for a sample of Concorde signal is shown in Fig. 2.

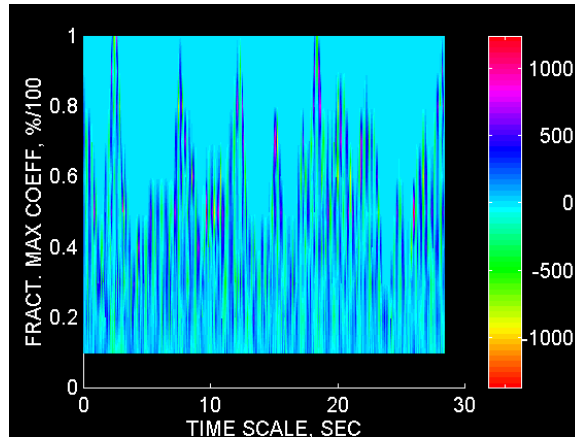


Fig. 2. A total ampligram of a 512-point sample of Concorde signal. Sampling frequency is 18Hz. The colour scale is expressed in A/D converter units.

The summation of the matrix  $M$  according to  $k$  should result in the original sample  $y(t_i)$ , if there would be no energy leakage from outside the filter band (3.2). Fig. 3 shows results of summation (red line) of the first 5.5 sec of ampligram in Fig. 1 together with the measured data (blue line). One can see that the differences between the observed and reconstructed data are less than 1%, which means that for infrasonic signals the energy leakage from outside the pass-band is negligible.

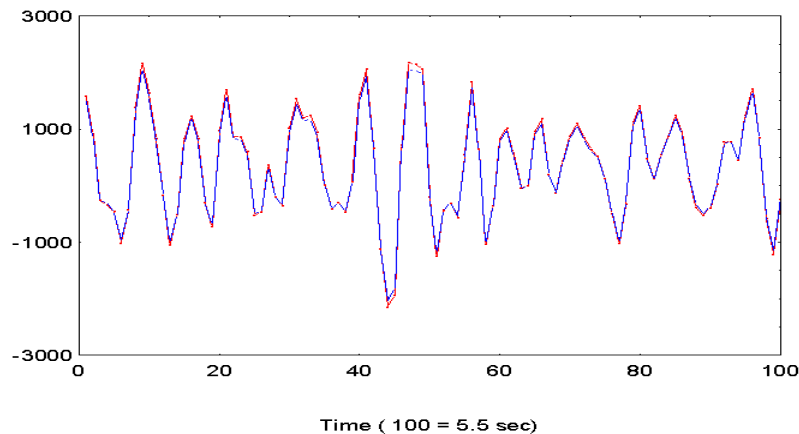


Fig. 3. Results of summation (red line) of the first 5.5 sec of ampligram in Fig. 1 together with the measured data (blue line).

In order to investigate the presence of weak components in the signal, the low-20 ampligram is a useful tool. The low-20 ampligram for the data shown in Fig. 1 is shown in Fig. 4. Another presentation method is used here. Only the positive portion of the ampligram is plotted for clarity. The color scale shows the natural logarithm of the amplitude  $y_k(t)$ . The use of logarithmic z-scale enhances the lowest amplitudes.

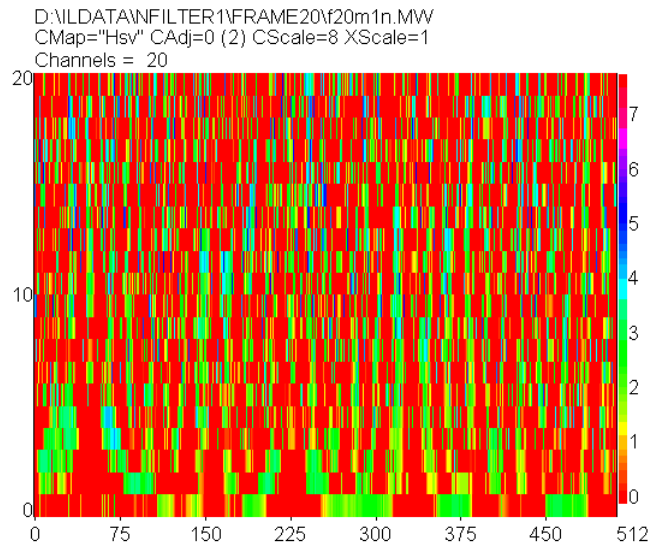


Fig. 3.3. The low-20 ampligram of the same data as shown in Fig. 1. Only the positive portion of the ampligram is shown for clarity, logarithmic z-scale.

The ampligram is a useful method of presentation of the physical properties of the signal. The signal in Fig. 1 with highest coefficient magnitudes (45 - 100%) is burst-like, with frequencies between 1 and 2 Hz. Higher frequencies (2 - 4 Hz) are present in the signal component between 30 and 45% of coefficient magnitudes. That component, due to its high frequency, must be propagated through stratosphere. At the bottom of the signal, below the lowest 3% of the coefficient magnitude, in Fig. 3 there is a very low frequency ( $\approx 0.25$  Hz) component, most likely due to microbaroms. All these components may be decomposed and used for determination of angle-of-arrival. A decomposition technique for an ampligram is discussed in the following section.

#### 4. Principal component analysis (PCA)

Since the ampligram may be considered as a multivariate time series ( $M=20$ ,  $N=512$ ), the principal component analysis may be used to identify the number of independent modes in the data.

A multivariate time series consisting of  $M$  variables measured at  $N$  equally separated instants forms a matrix  $\mathbf{M}$ .

The next step of the analysis is to perform the principal component analysis (PCA) of the matrix  $\mathbf{M}$ . The results of PCA are:

- The vector of eigenvalues of the matrix (latent roots  $\lambda_i$ ), telling how much of the total variance in the matrix can be explained by the consecutive principal components.
- The matrix of component score coefficients  $\mathbf{a}$ , a transformation matrix between the old system of  $N$  variables and the principal components (the new coordinate system).
- The matrix of component scores  $\mathbf{S}$ , with one column for each principal component, being a projection of old  $N$  variables upon the new coordinate axis (directions of principal components).

The matrix of component scores  $\mathbf{S}$  is thus the new multivariate time series in the principal component space. It has been found by this author that, in all cases when filtering was performed in the principal component space, a considerable improvement of signal-to-noise ratio has been obtained without distorting the signal.

Each column of  $\mathbf{S}$  is low-pass filtered using a simple filter of moving average type. The result of filtering is matrix  $\mathbf{S}_f$ .

After filtering an inverse transform:

$$\mathbf{M}_f = \mathbf{S}_f \cdot \mathbf{a}^{-1} \quad (4.1)$$

is performed resulting in a new version of the matrix  $\mathbf{M}$ .

It is possible to combine the filtering procedure with a decomposition procedure (Liszka, 1997).

If one wants to know what the variations of the M-component vector would be with only one mechanism (or cause), corresponding to the principal component  $l$  active, it is possible to mask with zeros all other columns in  $\mathbf{S}_f$ , except column  $l$ , and to perform a calculation of a new matrix  $\mathbf{M}_{lf}$ :

$$\mathbf{M}_{lf} = \mathbf{S}_f \cdot \mathbf{a}^{-1} \quad (4.2)$$

The operation may be repeated for each interesting component  $l$ .

As the principal component transformation preserves the variance, the sum of all latent roots,  $\lambda_l$ , is equal to the total variance. If the data is standardized, i. e. normalized to standard deviation for each variable, the sum of latent roots is equal to number of variables. The magnitude of latent roots is usually expressed in percent of the total variance. If the data contains only pure noise, all variables will be uncorrelated, and the total variance will be evenly distributed between all latent roots:

$$\lambda_l \text{ noise } (\%) = \frac{100\%}{M} \quad (4.3)$$

The real data, measured or computer-simulated, is never perfectly uncorrelated and the variance will not be evenly distributed between all latent roots.

When all variables are related to the same common factor there will be one latent root (the first one, corresponding to the first principal component) significantly larger than the value indicated by (4.3).

## 5. Decomposition into independent modes

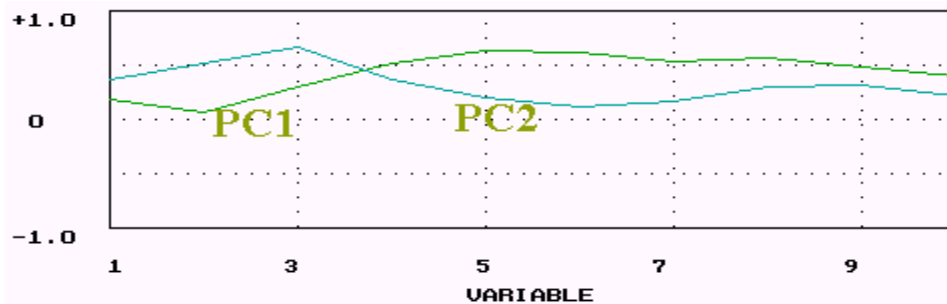


Fig. 5. Component loadings of the principal components PC1 - 2 for the ampligram of Fig. 2

The principal component analysis of the ampligram matrix must be performed to identify the number of significant independent components in the data. As a result, the matrix of component loadings, being the correlation coefficients between significant principal components of the ampligram and the M columns of the ampligram, is obtained. An example of component loadings is shown in Fig. 5. The diagram shows which ranges of magnitude contribute to the two modes present in the data of Fig. 2. The mode 1 (dominating) corresponds to coefficient magnitudes 45-100% and the mode 2 corresponds to magnitudes of 15 - 45%.

The non-linear filtering is now repeated once for each observed mode, the bandpass of magnitude is now selected from Fig. 5. The result, after the inverse wavelet transform, shows time series corresponding to the significant modes. An example of decomposed modes is shown in Fig. 6.

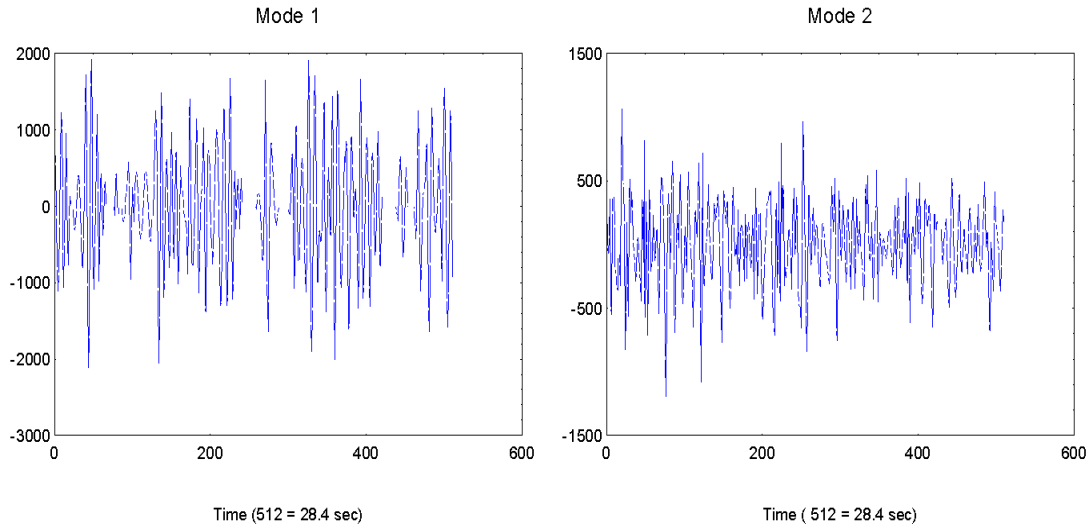
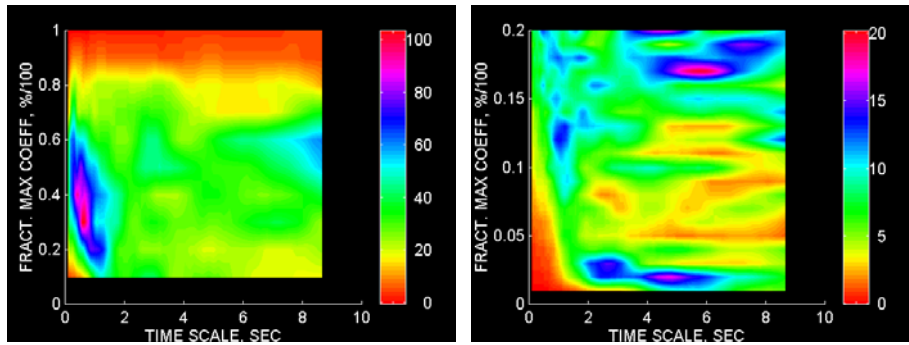


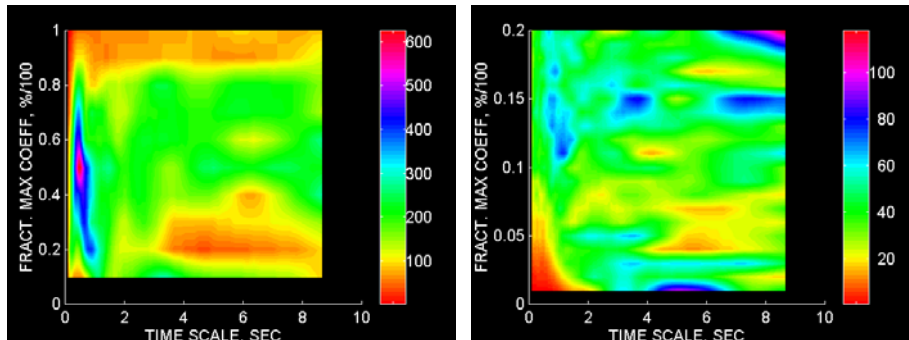
Fig. 6. Modes decomposed from the signal of Fig. 2.

The ampligram may be used for calculation of average wavelet spectra, one for each coefficient magnitude. The procedure will generate a 3-D graph showing the frequency (or time scale of the signal) on the x-axis, the wavelet coefficient magnitude of the original signal, in percent of its max value, on the y-axis and the wavelet coefficient magnitude (power spectral density) of the decomposed component as the color scale. A graph of that kind will show the average properties of the different modes, if such exist, during the sample period. Examples of time scale spectra of total ampligrams (left) and low-20 ampligrams (right) of few data blocks of the file in Fig. 1 are shown in Fig. 7.

Block #1



Block #20



Block #59

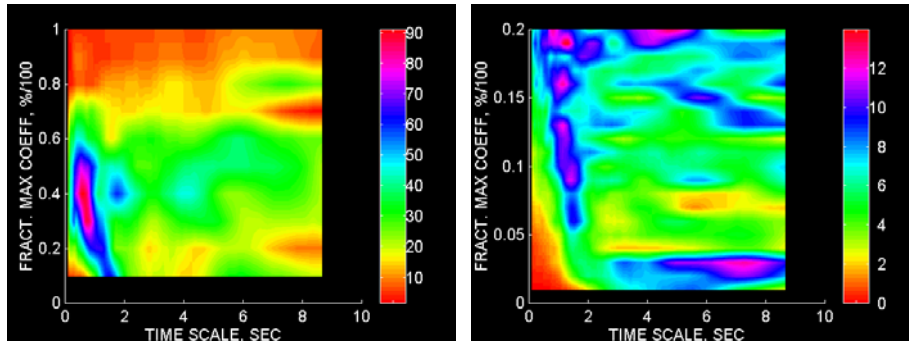


Fig. 7. Examples of time scale spectra of total ampligrams (left) and low-20 ampligrams (right) of few data blocks of the file in Fig. 1 are shown below.

Time scale spectra of low-20 ampligrams show, in the bottom part, a peak corresponding to microbaroms (3 - 9 sec). There are also other low frequency peaks clearly seen in blocks 1 and 59. These peaks are suppressed in the block #20 due to a very strong Concorde signal. This component, decomposed for the block #59 for all three microphones, is shown in Fig. 8.

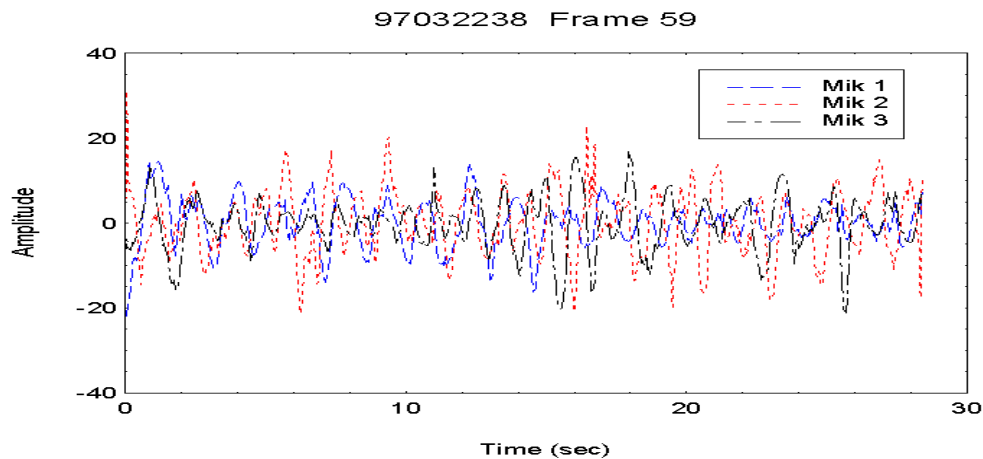
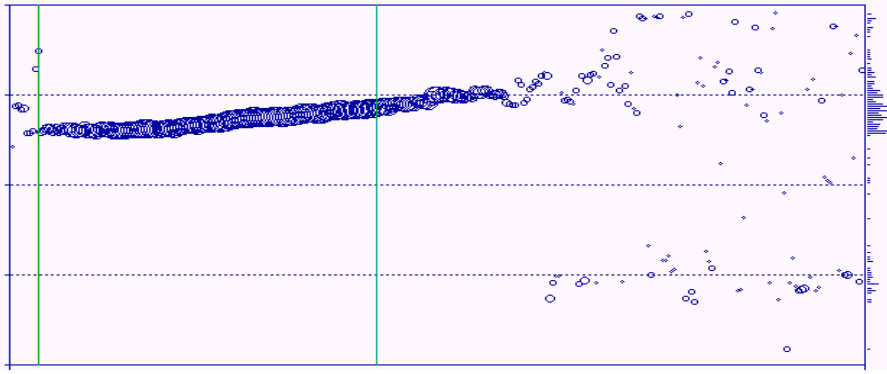


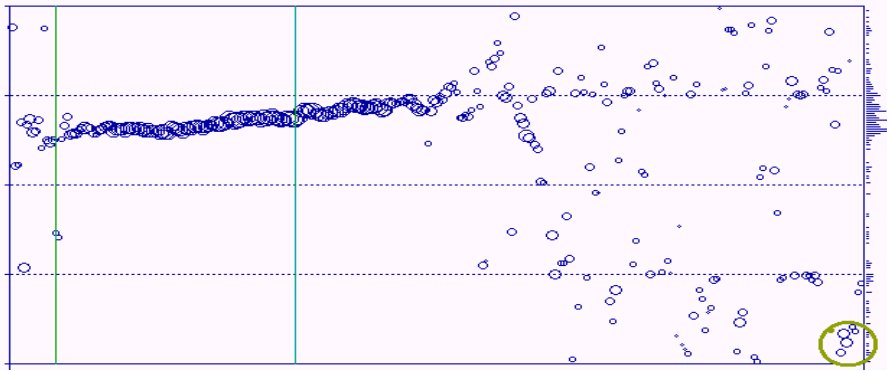
Fig. 8. Low frequency signal during the block #59 decomposed for all three microphones.

It must be remembered that the microphone triangles are designed to work around 2 Hz. Due to the short distance between microphones (75 meters between EW and NS microphone pairs) the angle-of-arrival accuracy is rather low at frequencies below 0.5 Hz. In the case of Fig. 8. the angle-of-arrival is found to be within 10 - 40°. The signal is very likely an intense microbarom originated in the region of Nordkap.

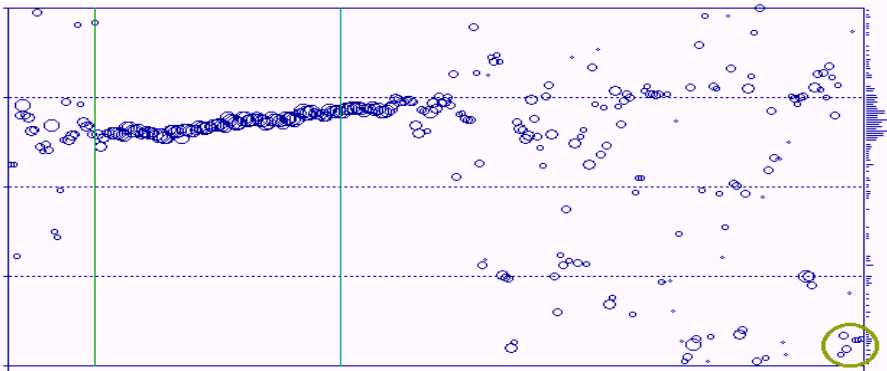
A software has been developed to low-pass or band-pass filter the infrasound recordings. The computations are relatively time consuming. A sequence of low-pass filterings of the file in Fig. 1 is shown below in Fig. 9 the angle-of-arrival computations are made now with a correlation time of 256 seconds (128 seconds in Fig. 1) and correlation step of 64 samples. The first graph of the sequence corresponds thus to Fig. 1, but is made with a higher time resolution. The following graphs show the angle-of-arrival of the signal remaining after the low-pass filtering at the indicated level of maximum magnitude of the wavelet coefficients (spectral density). The signal of Fig. 8 during the block #59 (which is the last data block in that file) is encircled.



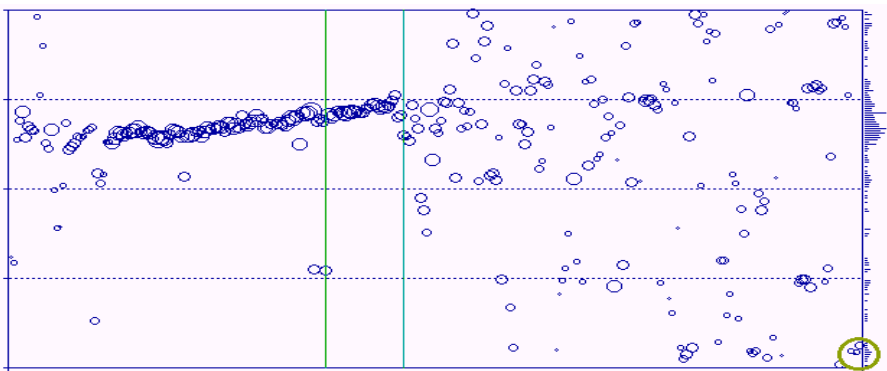
Total signal



20%



15%



10%

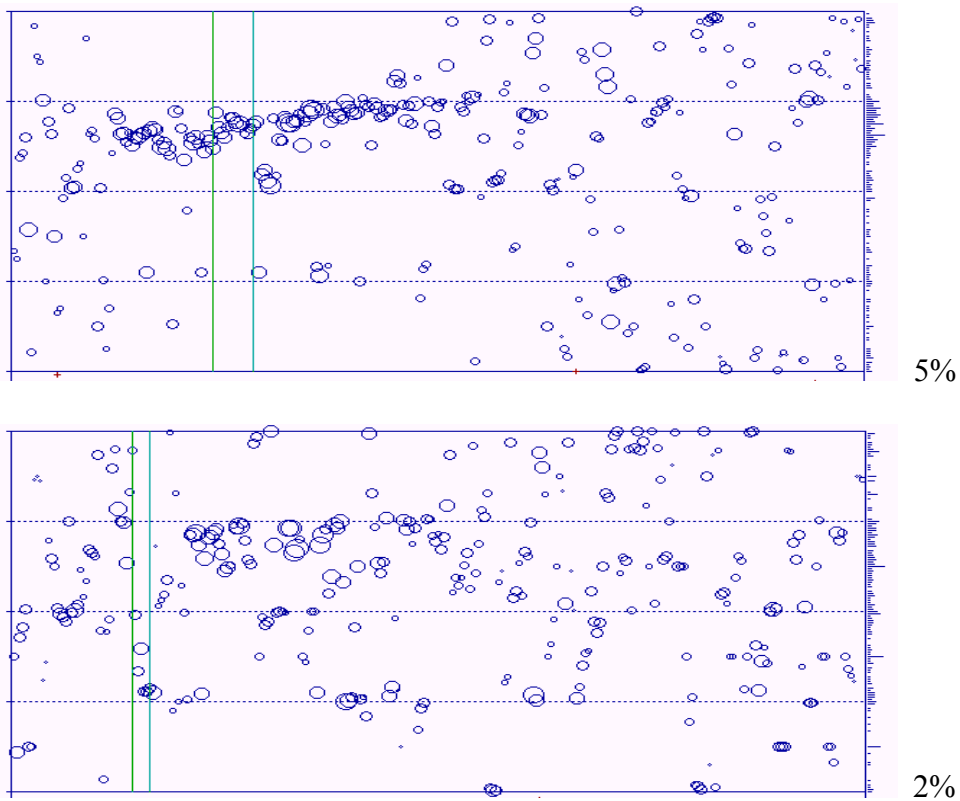


Fig. 9. A sequence of low-pass filterings of the file in Fig. 1. The signal in the block #59 (the last data block of the file) is encircled on 10 - 20% filterings.

An interesting application of wavelet filtering is that the decomposed modes from all three microphones may be used for determination of the angle-of-arrival. A result of such determination for both modes during the Concorde flight of Fig. 1 is shown in Fig. 10.

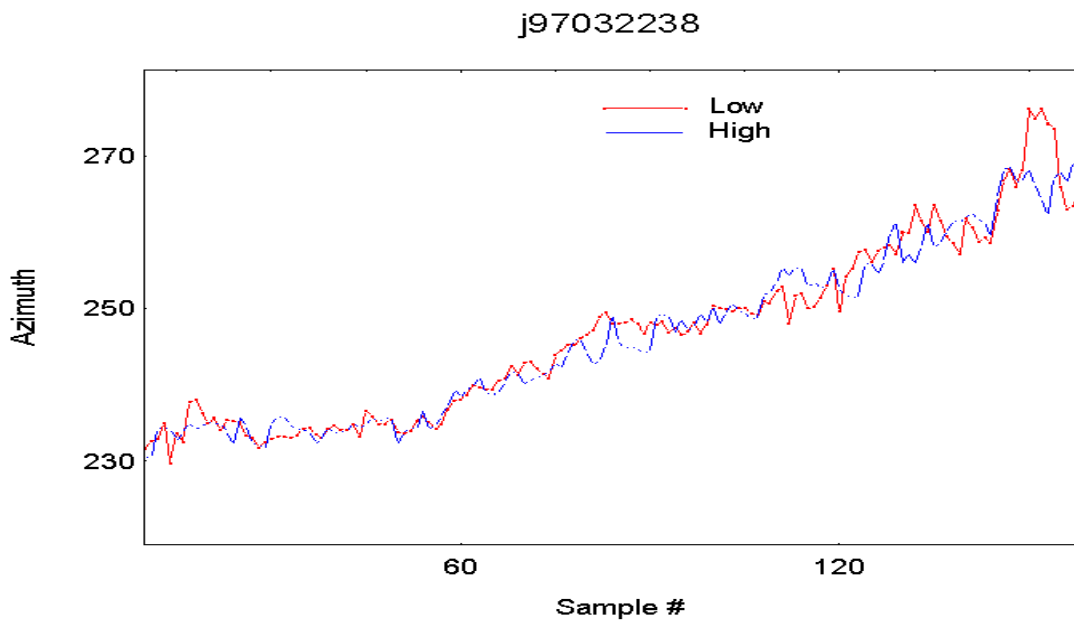


Fig. 10. Angle-of-arrival measured for both propagation modes separately.

In the above example, the distance to the aircraft increases with time due to the supersonic speed of the aircraft. The distance at the beginning of recording is slightly above 2000 km, while at the end it is about 4500 km. The mode 1, called here 'high', dominated by the low frequencies, is likely to propagate through the thermosphere. The other mode, containing much higher frequencies, is probably propagating through the stratosphere. It is obvious that the thermospheric winds, usually significantly higher than those in the stratosphere, will strongly influence the angle-of-arrival of the high mode. Therefore, the average difference between the angle-of-arrival of both modes may be used to estimate the distance to the source for a given type of source.

## **6. Conclusions**

The use of wavelet transform for signal filtering and decomposition increases dramatically the capacity of the infrasound technique as a monitoring tool. In addition to that, the present technique facilitates high resolution studies of the infrasound propagation. Separation of modes, recording of weak signal components, normally obscured by strong components, will be essential for understanding the infrasound propagation.

## **References to Chapter 8**

- Chui, C.K.: *An Introduction to Wavelets*, Academic Press, Boston, 1992.
- Chui, C.K., L. Montefusco, L. Puccio (eds.): *Wavelets: Theory, Algorithms and Applications*, Academic Press, Boston, 1994.
- Farge, M.: Wavelet transforms and their applications to turbulence, *Ann. Rev. Fluid Mech.*, 24, 395-457, 1992.
- Farge, M. and Th. Philipovitch: Coherent structure analysis and extraction using wavelets, in *Progress in Wavelet Analysis and Applications*, eds. Y. Meyer, S. Roques, Editions Frontieres, Gif-sur-Yvette, 477-482, 1993.
- Liszka, L., *J. Acoust. Soc. Am.*, Vol. 64(2), 631, 1978.
- Liszka, L. and K. Waldemark, *J. Low Freq. Sound. Vib.*, 14, No. 4, 1995.
- Lundkvist, B., *J. Low Frequency Noise & Vibration*, Vol. 5, No.4, 137, 1986.
- Wernik, A.W. and M. Grzesiak: Analysis of ionospheric plasma turbulence with the wavelet transform. *Proc. Int. Symp. 'Plasma 97'*, Jarnoltowek, June, 1997, Published by the Space Research Center, Polish Academy of Sciences, v. 1, pp.391-394, 1997.

## Chapter 9

### Infrasound from Other Aircraft

All supersonic aircraft may be observed at infrasonic frequencies when they move towards the observing microphone array. The beamwidth of the transmitted infrasound is related to the aircraft speed.

#### *Small supersonic aircraft*

Unlike the Concorde, which may be observed at distances above 2000 km, there are numerous observations of small, most likely military aircraft flying with supersonic speeds during short time intervals (typically  $\approx 1$  minute). When only data from one station is available, an absolute distance determination can not be done. However, it is possible to make a rough estimate of the distance using the character of the infrasonic frequency spectrum. It is well known, that the shock wave from a supersonic aircraft, travelling through the atmosphere, modifies its frequency spectrum. The acoustic energy at higher frequencies is, probably by non-linear mechanisms, transferred into low frequencies. It has been found by the author (2000) that a ratio between the average spectral amplitude (FFT) in the frequency range 2.5 - 3.4 Hz,  $A_l$ , and the average spectral amplitude within 5.6 - 6.2 Hz,  $A_h$ , ( $A_l/A_h$ ) is a convenient measure of the distance to the aircraft. The method has been calibrated using observations in Sweden, where the distance to the aircraft was determined by triangulation from SIN stations. A typical dependence of  $A_l/A_h$  on the distance to the aircraft is shown in Fig. 1.

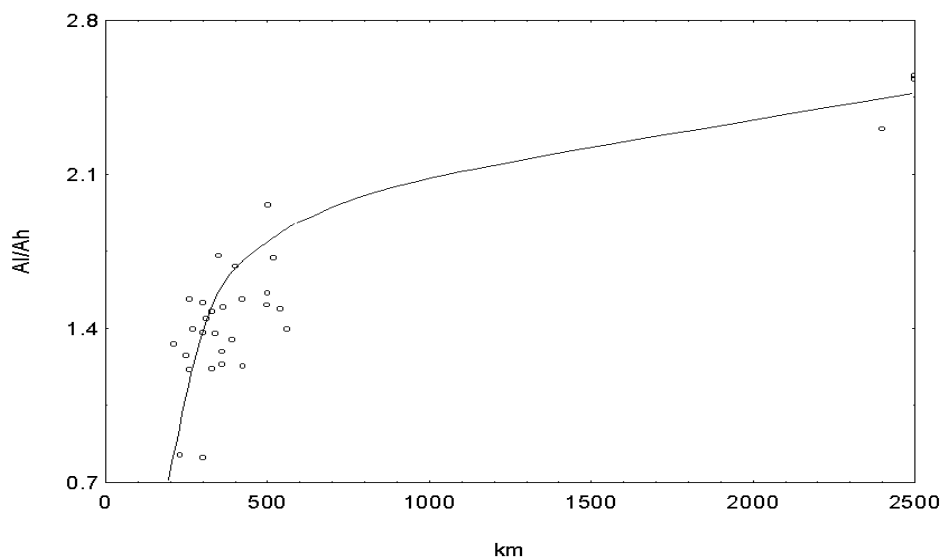


Fig. 1. The dependence between  $A_l/A_h$  and the distance to the aircraft

The above dependence was determined using observations of medium-size jet fighters at distances up to 600 km and of Concorde. The dependence seems also to be related to the aircraft size. However, it was impossible to study the dependence using only one aircraft size. It is, of course, uncertain what is happening with the slope of the infrasonic spectrum between 600 and 2000 km and more studies are needed. There are some indications that the slope of the above dependence is decreasing above 600 km. There is no reliable data for

distances below 150 km because the signal is then so strong that it saturates the recording equipment and there is no meaning to draw any conclusions from the shape of frequency spectrum. It may be concluded that the above estimate of the distance may be used between 150 and 600 km. The accuracy of the estimate is +/- 100 km.

Since the general form of the frequency spectrum is distance dependent, it may be interesting to test, using the entire frequency spectrum in the range 0.4 – 4.5 Hz, whether there are significant differences between different types of sources. Only signals of known origin could be used to test the method. The discrimination process was based on a vector of 64 components consisting of the average FFT spectrum during the signal duration (32 channel spectrum) and of the average standard deviations of the spectrum (32 channels):

$$[\langle a_i \rangle, \langle a_i^2 \rangle], \quad i=1, \dots, 32$$

Both the average spectrum and the average standard deviations were normalized to the respective maximum value.

The 64-point vectors were categorized using a Self-Organizing Map (SOM) neural network. The network used consists of a 64-processing element input layer, a 2-D SOM-layer of 10 x 10 processing elements and a coordinate layer which is used to decode the position of a given vector on the self-organizing map. During the learning phase, the network weights are adjusted and during the recall phase, the position of each vector on the map is read out. Vectors projected close to each other on the map are similar. The distance between points on the map is a measure of similarity. The categorization process is based on finding similarities between the data vectors. The projection onto the map is highly non-linear, it depends on the nature of the data used for the training.

Also vectors containing the third and fourth moments (skewness and kurtosis) were tested.

A selection of infrasonic measurements from Lycksele (64.61N, 18.71E) is used here to demonstrate results of categorization of FFT frequency spectra and their standard deviations. A sample of 73 Concorde recordings from December 1995 is used as a reference. A number of interesting sources is then compared with the reference. Results of categorization with SOM are shown in Fig. 2. The compared sources are:

- aircraft SAAB 37 at a distance of about 400 km;
- aircraft F-18 at a distance of about 400 km;
- unknown source on 990410, probably a chartered Concorde flight;
- unknown source on 990411;

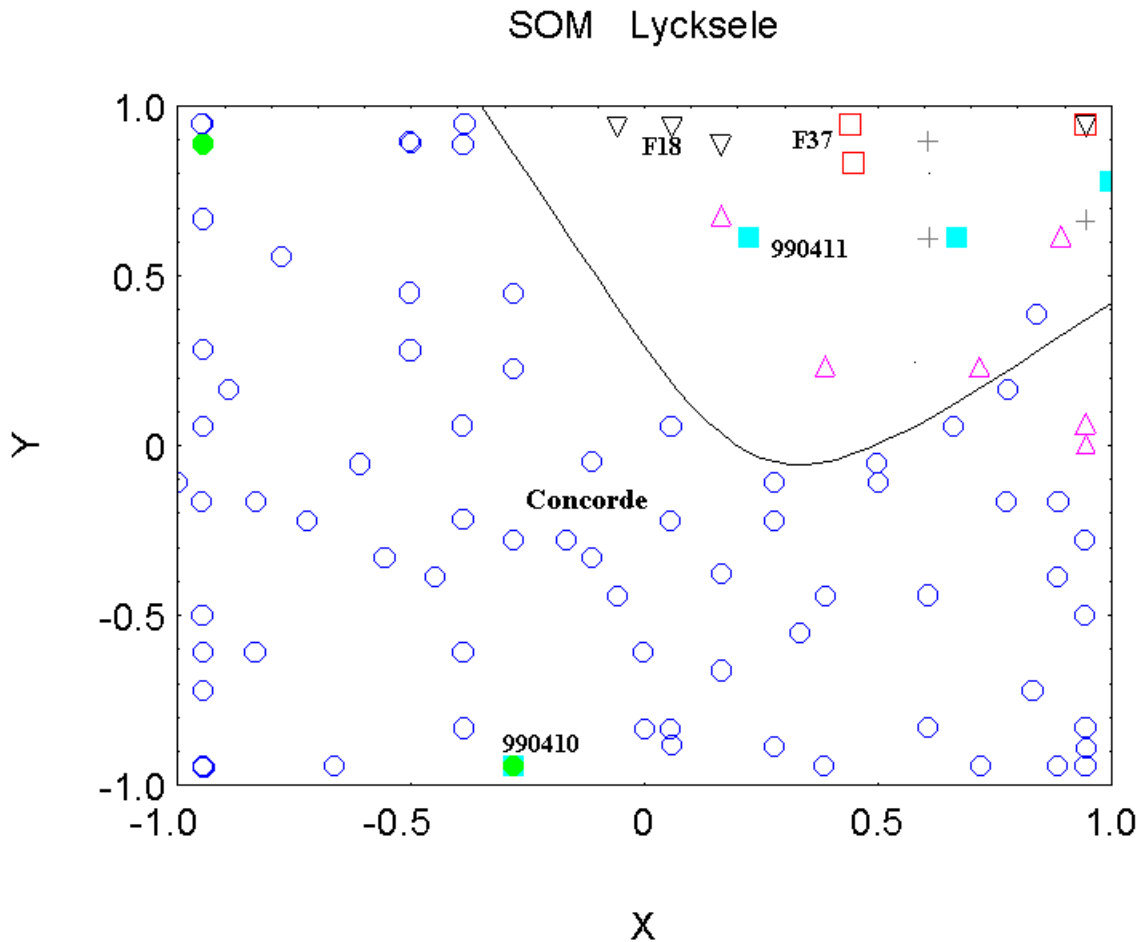


Fig. 2. . Categorization of Lycksele-data. The decision boundary indicates the area in which the Concorde data (circles) are gathered. Most of compared signals are located outside the area filled by Concorde signals.

The results of categorization show that signals from supersonic fighters are well separated from Concorde signals. The signal on 990410, as well the signal projected in the upper left corner are most likely generated by chartered flights of Concorde (do not agree with the Concorde flight schedule).

### **SR-71**

During 1979 a new type of signals appeared on infrasonic recordings from SIN. The source of the signals could be localized to Northern Atlantic, west of Scandinavia. Triangulations performed using the data from Kiruna and Lycksele indicated high supersonic speeds, up to Mach 3. It was therefore concluded, that the source could be the new reconnaissance aircraft, SR-71. At that time the Swedish Defence Research Institute operated an infrasonic station on the coast of Baltic Sea, SE of Stockholm. That station could also confirm the source above the Northern Atlantic, but also when it was flying with subsonic speed above the Baltic Sea. The aircraft was also recorded when it was making, in subsonic speed, a turn around the island of Gotland (see Fig. 3). Results of infrasonic monitoring of SR-71 were published later by Hagelstein et al., 1993).

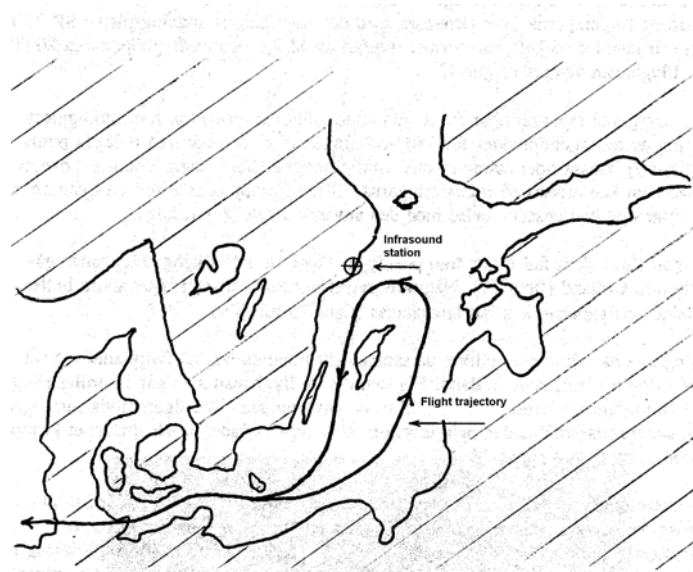


Fig. 3. The subsonic flight trajectory of SR-71

### ***Infrasound from subsonic aircraft***

The engine noise and turbulent flow around the aircraft produce considerable infrasound levels, detectable, depending on the aircraft type, at distances up to 50 km. That range has been found from the author's measurements at different locations in Sweden. In order to determine the flight trajectory from infrasonic observation, the following geometry of the problem is considered.

It is assumed that the flight trajectory is a straight line at a constant height  $z_0$  above the ground-plane of the observer. A horizontal projection of flight trajectory with respect to the observer is shown in Fig. 4.

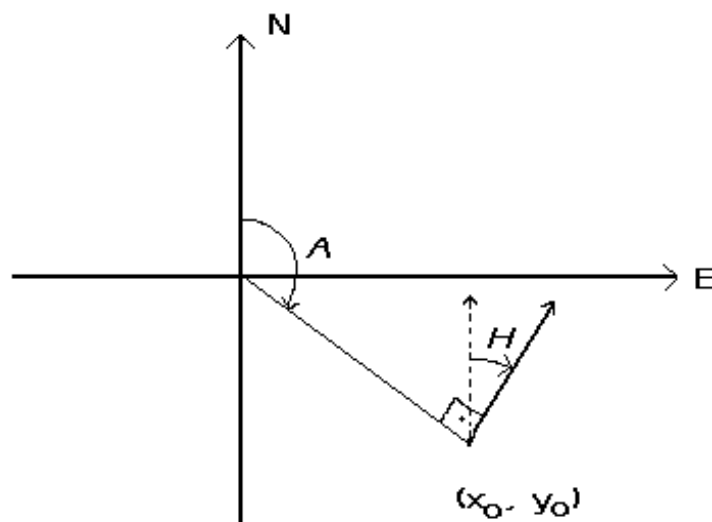


Fig. 4. The geometry of the flight

At the point of closest approach, the aircraft coordinates are  $(x_0, y_0, z_0)$  and the heading of the aircraft is  $H$ . If the flight trajectory is a straight line, the azimuth to the point of closest approach,  $A$ , is related to the aircraft heading:

$$H = A - 90^\circ$$

If the ground speed of the aircraft is  $v$ , the aircraft position after time  $t$  will be:

$$x = x_0 + vt \sin H$$

$$y = y_0 + vt \cos H$$

$$z = z_0$$

The azimuth to the aircraft at time  $t$  is:

$$A = \arctan(x/y)$$

but the infrasonic signal from the aircraft will be delayed by a time interval  $\Delta t$ :

$$\Delta t = D/c$$

where  $c$  is the speed of sound and  $D$  is the slant range to the aircraft:

$$D = \sqrt{x^2 + y^2 + z^2}$$

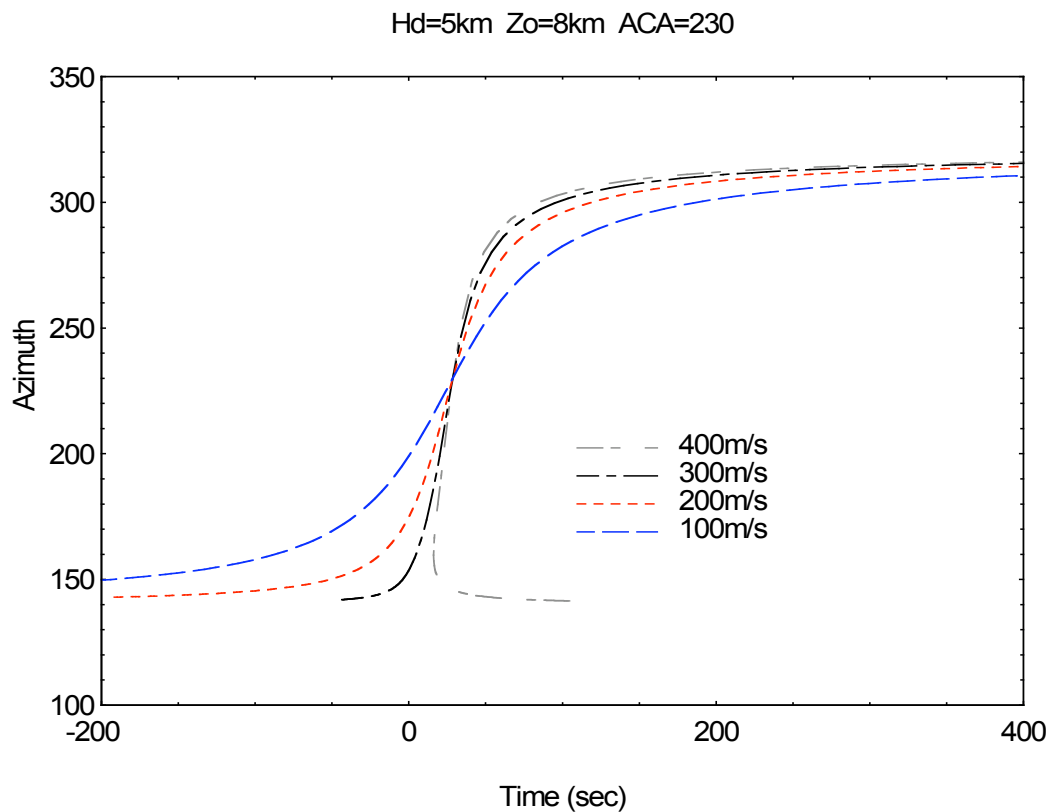


Fig. 5. Simulated variations of the azimuth to the aircraft for three subsonic aircraft speeds and one supersonic. Horizontal distance at ACA is 5 km.

An example of simulation showing how the azimuth to the aircraft is changing for a given flight trajectory and varying aircraft speed is shown in Fig. 5. The point of symmetry of all curves, where all curves are intersecting, is the point of closest approach. The azimuth to the point of closest approach is, as shown above, related to the aircraft heading. For a supersonic speed there is no signal before the time of closest approach

An example of observed azimuth curve is shown in Fig. 6. The total duration of the signal is here approximately 9 minutes. Here a method to determine parameters of flight trajectory from infrasonic observations is presented. In the case of observation of Fig. 6, it may be determined that the azimuth to the point of closest approach is  $261.5^\circ$ , the distance to the point of closest approach is 1.3 km, the approximate altitude of the aircraft relative to the observing site is 6000 meters and its speed is 175 m/sec (630 km/h). The heading of the aircraft is 351 degrees.

Since it is practically impossible to solve the above problem analytically, a neural network model trained with the simulated data has been used. As input, 21 azimuth values at 4-second intervals, centred around the point of closest approach, were used. The outputs of the model are:

- direction to the point of closest approach
- distance to the point of closest approach
- aircraft altitude
- aircraft ground speed
- aircraft heading index (+1 for clockwise motion, -1 for counter-clockwise motion)
- in/out index indicating if an aircraft signature is present in the 21-points window.

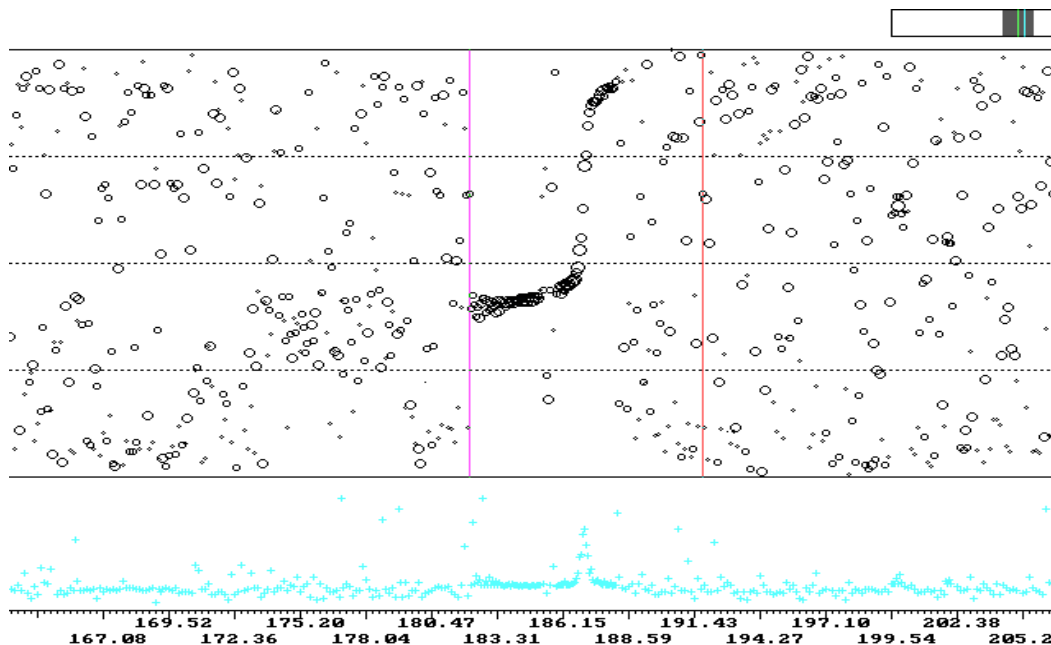


Fig. 6. An example of infrasonic recording of a subsonic aircraft, the angle of arrival in the upper graph and the horizontal trace velocity in the lower graph.

The 21-points window is moved through the result file .az and aircraft signatures are automatically detected by the model together with trajectory parameters. Preliminary tests of the above technique

were performed. However, further development is needed to improve the accuracy of results. In the present example a half-manual, simplified technique has been used.

The **simplified method** works as follows:

A time series of differences between adjacent azimuth readings (4 sec values) is constructed (a derivative of the azimuth curve). In that time series symmetrical peaks, corresponding to S-shaped aircraft signatures in the azimuth time series, are automatically detected in portions of azimuth data which were manually identified as containing aircraft signatures. For each event, the point of closest approach (the point of symmetry of the s-shaped curve and the peak of the derivative curve) is identified and the azimuth to the point of closest approach (ACA) determined. The azimuth data is then transformed by subtracting the ACA+180, which means that **all points of closest approach are moved to the azimuth of 180°**. The azimuth window is then centered around  $A = 180^\circ$ . The output of the neural network model may thus be limited to a smaller number of variables:

- distance to the point of closest approach
- aircraft altitude
- aircraft ground speed
- aircraft heading index (+1 for clockwise motion, -1 for counter-clockwise motion). Even here the network model is trained using simulated data.

It has been found that the simplified model produces accurate results for all output variables, except for the aircraft altitude. The reason is that the method is based upon the direction of arrival and thus rather insensitive for the aircraft altitude.

The aircraft heading may be calculated from the ACA and the aircraft-heading index.

In order to test the above described method, a number of aircraft recordings from the period April 14 - 25, 1996 were processed. The estimated flight trajectories within a square of 100 x 100 km, centered on the location of one infrasonic station, are shown in Fig. 7.

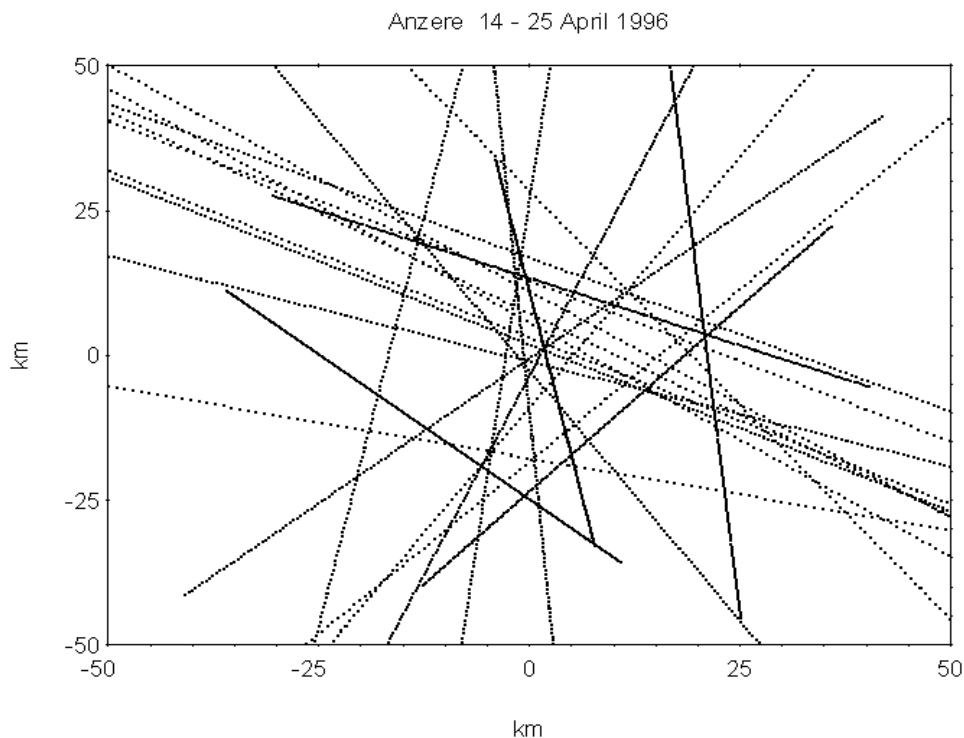


Fig. 7. Some estimated flight trajectories during the period April 14 - 25, 1996.

Aircraft positions for each 4 seconds are calculated and marked by a dot on the graph. This means that the speed of the aircraft is reflected in the character of the line. The almost continuous line corresponds to a slow aircraft; a dotted line with largest spacing between the dots corresponds to a fast jetliner. Aircraft speeds between 60 and 250 meters/sec were obtained for the trajectories in Fig. 7.

### ***References to Chapter 9***

Liszka, L.: Categorization of Infrasonic Sources. Paper presented at CTBT Infrasonic Workshop 2000, Passau, Germany.

Hagelstein, C. H. and Nygren, H. G.: Infraljudsteknik för Övervakning av Luftrummet /in Swedish). FOA Rapport C 20898-2.2, August 1992, ISSN 0347-3694.

## Chapter 10

### Infrasound as a Detection Tool

The most important application of an infrasound network is detection of remote events, both natural and man-made. In this chapter, the authors work on the detection of meteor impacts, high altitude discharges (sprites). Catastrophic events, like volcano eruptions, explosions and giant fires will be summarized.

#### *Entry of large meteoroids*

Large meteoroids enter the atmosphere with high supersonic speeds, typically between 10 and 75 km/sec. Since the Mach cone is very narrow at speeds of that order, the flight trajectory may be considered as a source of cylindrical shock wave. At large distances, that shock wave will be transformed to infrasound. During its travel through the atmosphere, the meteoroid heats up due to the friction and undergoes fragmentation. The fragmentation may be of explosive nature and a source of spherical shock. Sometimes a series of fragmentations may occur along the meteoroid's trajectory through the atmosphere. The total signature of an entry of a meteoroid will thus be very complex. It will be even more modified if the event is recorded at a large distance.

The most important parameter of an entry event is its kinetic energy, which depends on both the mass of the object and on its speed. According to the method by ReVelle (1997) based on infrasound measurements of atmospheric nuclear tests:

$$\text{Log}(E/2) = 3.34 \log(P) - 2.58$$

where, P is the period, in seconds, of the infrasound signal at maximum strength, and E is the pre-atmospheric entry kinetic energy in kton TNT equivalent (1 kton TNT  $\Leftrightarrow$  4.185  $\cdot 10^{12}$  J).

Another method to determine the total energy of the meteor is based on measurements of the pressure of the infrasound wave generated by the entry (ReVelle, 1997). Both methods usually give different results.

Attempts have been made to determine the last part of the meteor's trajectory using the infrasonic measurements (Le Pichon et al, 2002).

During the recent years, the SIN stations recorded several meteor impacts over Scandinavia and some more distant, over Europe. Table 1 shows events recorded over Sweden, Table 2 contains more distant events.

Table 1. Recent meteor events in Sweden

Date	Location
2002-02-15	Vemhån
2002-12-30	Morjärv
2004-01-17	Jokkmokk
2004-05-23	Lycksele
2004-07-12	Bygdsiljum

The events listed in Table 1 were described by Svedhen et al (2004).

Table 2. Major meteor events over Europe recorded by SIN

Date	Location
1997-12-09	Greenland
2001-10-27	North Sea
2002-04-02	Bavaria
2002-06-06	Mediterranean

### **Jokkmokk event**

A spectacular meteor event occurred over Northern Sweden on January 17, 2004 at approximately 1405 UT. The impact area was located about 50 km NW of the village of Jokkmokk, north of the Arctic Circle. During the following days, local newspapers reported a number of eyewitness observations of the event (although the impact area is very sparsely populated). It was clear from all reports that what had happened on January 17 was a major event. At this time of the year the area in the neighbourhood of the meteor event is very close to darkness: yet, the inhabitants of this area reported that at the time of the impact the landscape was illuminated briefly as during full daylight. A number of loud explosions were also reported and there was apparently an eyewitness standing just below the bolide trajectory about 30 km NNE of the impact area.

An interesting fact about the event is that the impact area was close to the triangle formed by the northernmost stations of the Swedish Infrasound Network. The approximate impact area is shown in Fig. 1 as the centre of the map. All four stations (Kiruna, Jämtön, Lycksele, Uppsala) are indicated on the map with letters: K, J, L and U, respectively. The list of stations together with the distances to the impact area is shown in Table 1.

Table 1: Swedish Infrasound Network and the impact area

Name	Latitude (Degs)	Longitude (Degs)	Distance to impact area, km
Kiruna	67.8°N	20.4°E	160
Jämtön	65.87°N	22.51°E	182
Lycksele	64.61°N	18.71°E	212
Uppsala	59.85°N	17.61°E	740

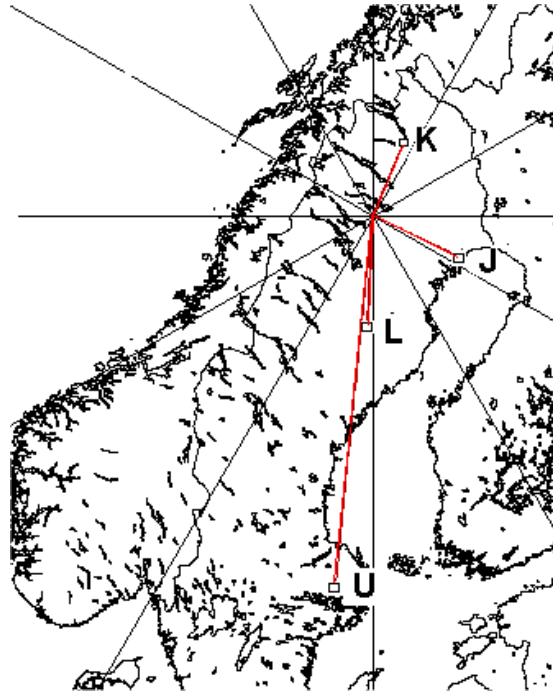


Fig. 1. . The approximate impact area in the centre of the map. The four stations are indicated on the map with letters: K, J, L and U

As shown in Fig.1, the bolide trajectory was close to the NS direction: therefore, the stations Kiruna, Jämtön and Lycksele were aligned with the direction of its trajectory, while the station Jämtön was approximately perpendicular to it.

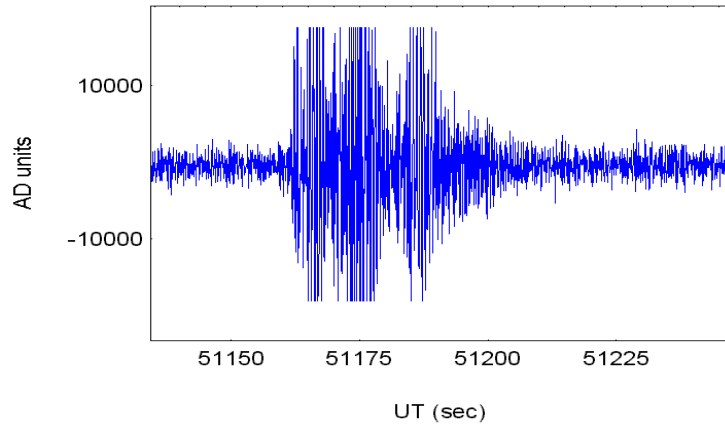
### **Signal characteristics**

The infrasonic signal produced by the entry of the bolide into the atmosphere and the subsequent explosions were recorded at all four stations: the recordings are shown in Fig. 2. It can be observed that the signal amplitude at the 3 northern stations is clipped. Only in the records of Uppsala, 740 km distant from the impact area, is it possible to make an accurate reading of the maximum signal amplitude: this amplitude corresponds to 0.056 Pa.

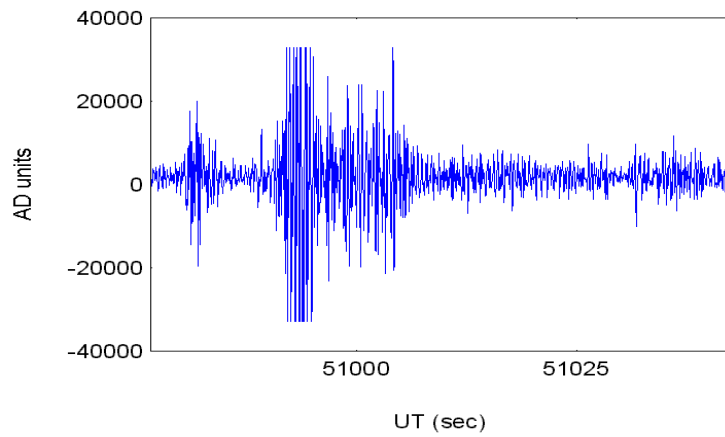
Unfortunately, on the date of the event there was an offset problem at the Lycksele station. However, the offset didn't bias the estimation of the direction of arrival of the signal and the horizontal trace velocity readings.

On the basis of the observed signal amplitudes, of the signal duration and of the spectral content, Dr. Douglas ReVelle, at Los Alamos National Laboratory, estimated that the energy release of the main explosion corresponded to about 1.7 tons of TNT. He also estimated that the energy at the source before it entered the atmosphere could have been 10 to 100 times larger.

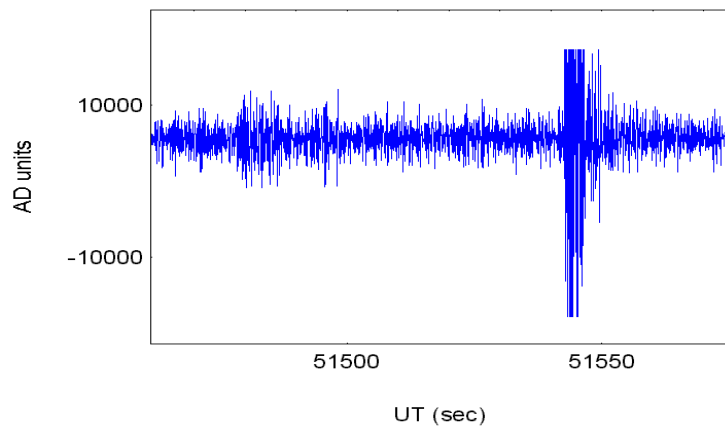
It is interesting to observe how the horizontal trace velocity of the incoming signal varies according to the distance of the source from the recording stations. For the three northernmost stations, close to the impact area, the trace velocity should be directly related to the height of the source: due to the short source-to-station distance, only a direct ray should reach the stations, while at Uppsala a reflection in the upper atmosphere should be expected before the signal reaches the sensor. Fig. 3 shows the trace velocity as a function of the angle-of-arrival of the signal. There is a considerable difference between the trace velocities observed at Kiruna and Jämtön: this is probably due to different aspect-angles with respect to the atmospheric wind system along the bolide trajectory. However, it is assumed that the start of the infrasonic signal observed at both stations corresponds to the same point of the trajectory.



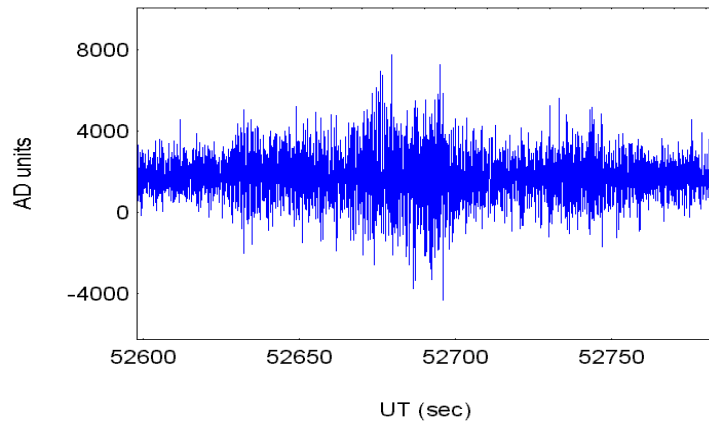
Kiruna: max. amplitude > 0.2 Pa



Jämtön: max. amplitude > 0.2 Pa

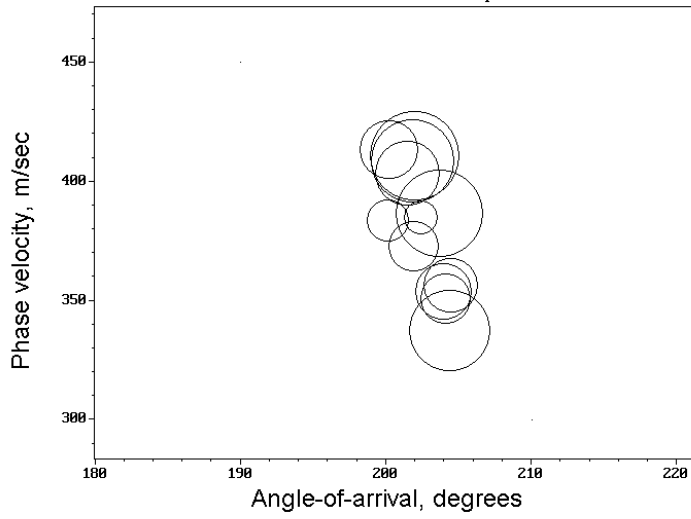


Lycksele: max. amplitude > 9.2 Pa

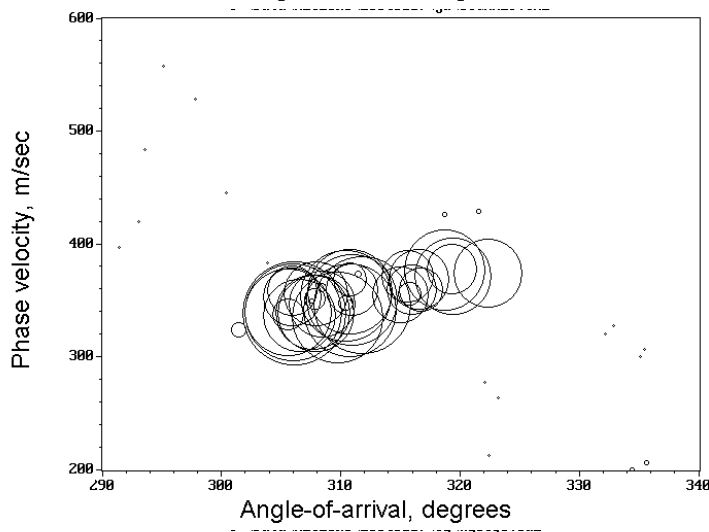


Uppsala: max. amplitude = 0.056 Pa

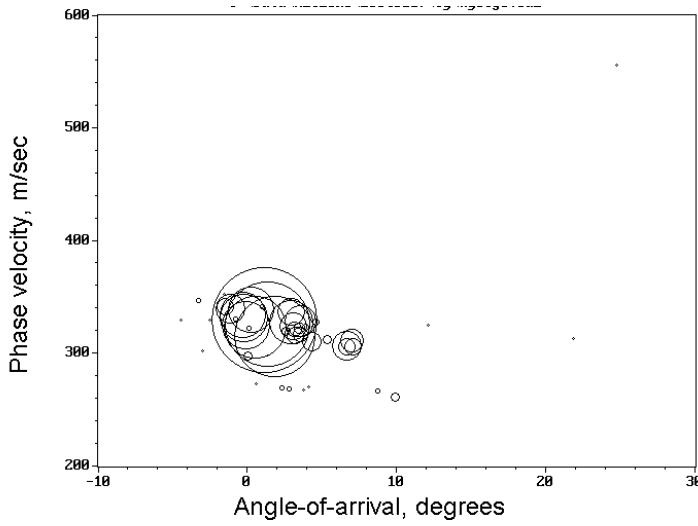
Fig. 2. Amplitude recordings from all stations in the Swedish Infrasound Network.



Kiruna



Jämtön



Lycksele

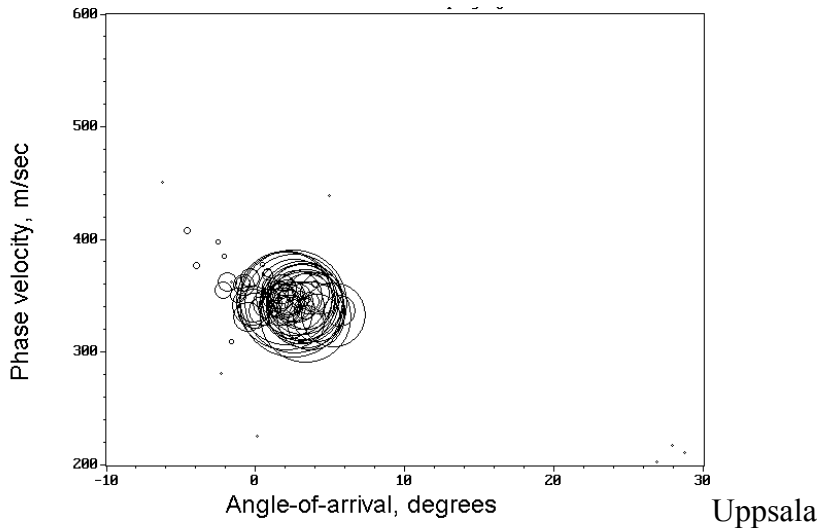
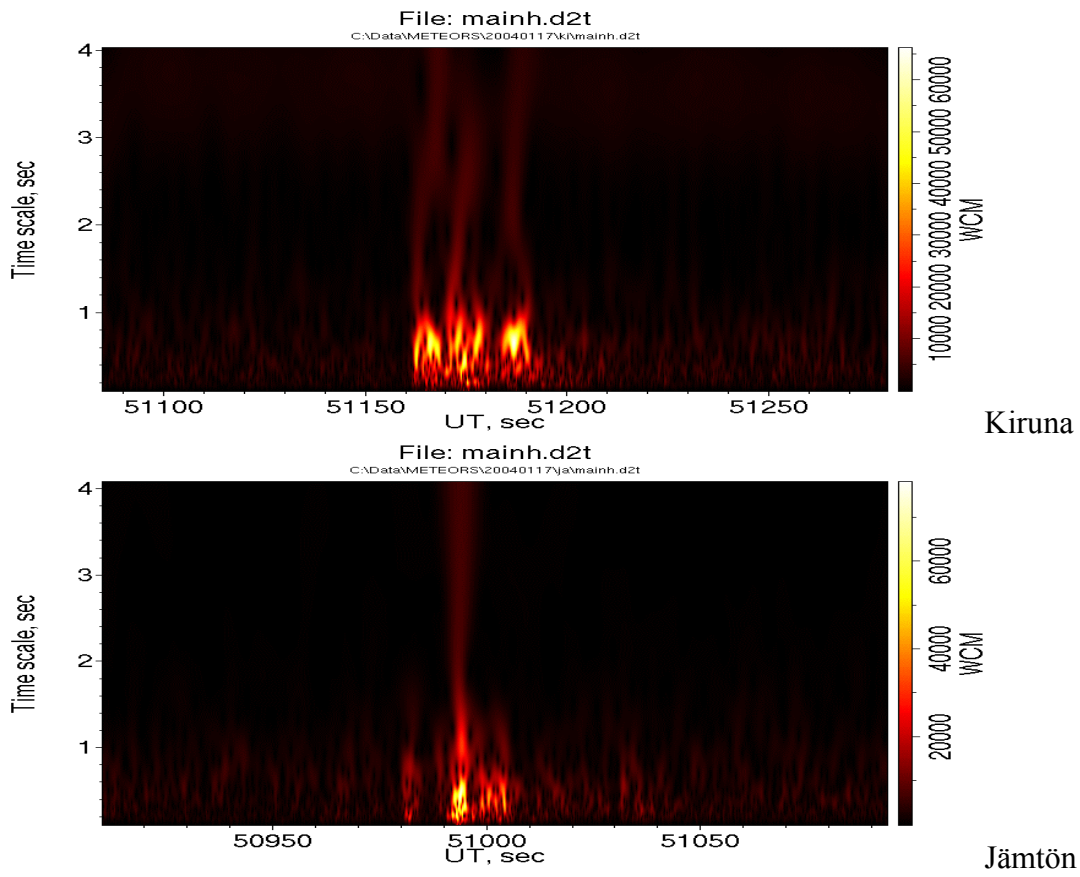


Fig. 3. The horizontal trace velocity (m/sec) vs angle-of-arrival (degrees) for all stations. The radii of the circles are proportional to the average cross-correlation across the array.



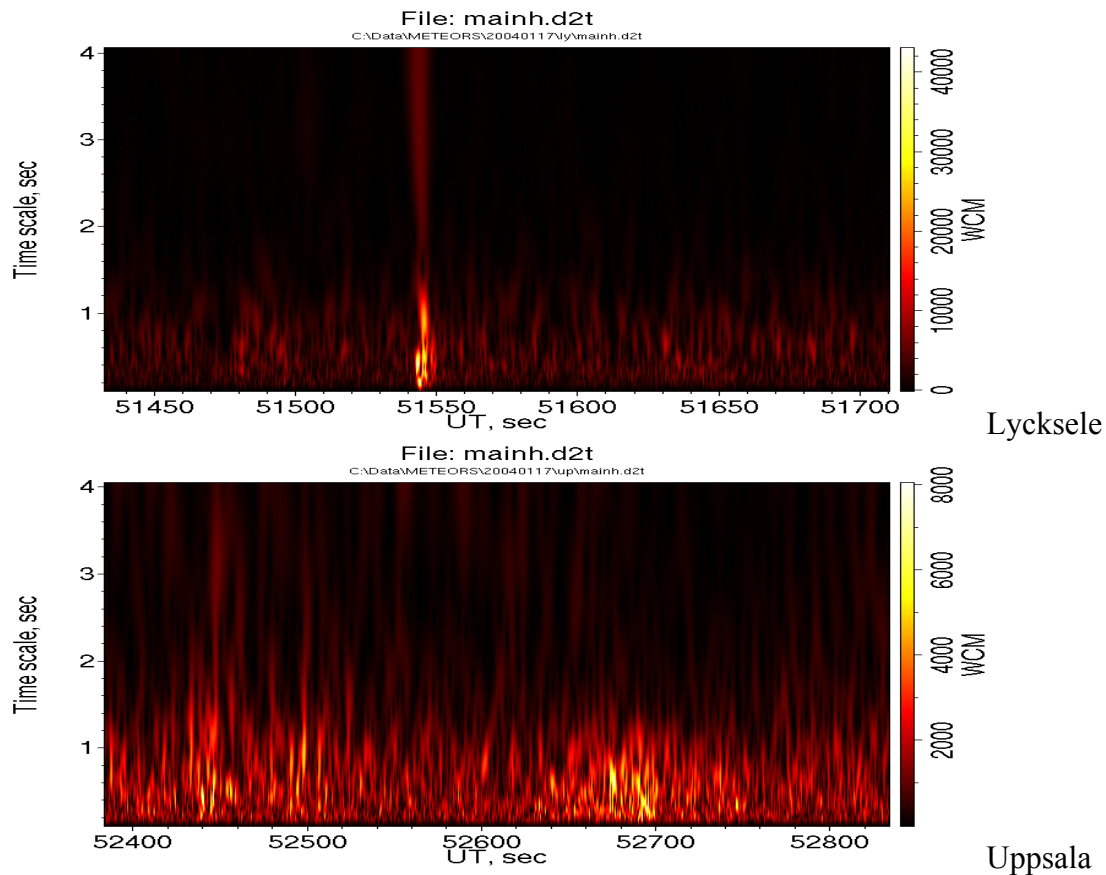


Fig. 4. Wavelet scalograms of the bolide signal recorded at all four stations.

The energy distribution in the frequency domain may be seen in wavelet scalograms of Fig 4. A scalogram displays the wavelet coefficient magnitude as a function of the time scale (inverted frequency) and of the elapsed time.

Since the actual wind and temperature profile during the period this event occurred are not known, it is impossible to convert the phase velocity information into the absolute height of the source. However, assuming that the highest phase velocities observed at Kiruna and Jämtön correspond to the same point of the trajectory and using that as a reference, it is possible to combine the azimuths measured at both stations and to determine the horizontal projection of the bolide's trajectory. The results of the triangulation are shown in Fig. 5. The figure shows an enlarged part of the map shown in Fig. 1, and it is centred at the Jämtön station. Kiruna and Lycksele stations are indicated by letters K and L, respectively and the horizontal projection of the bolide's trajectory is indicated by a thick line. The cross on the line shows the position of the main explosion. The length of the projection, calculated by combining the source-to-station directions from Kiruna and Jämtön, is approximately 86 km. At its entry into the atmosphere, the bolide was heading to the direction 206.9°.

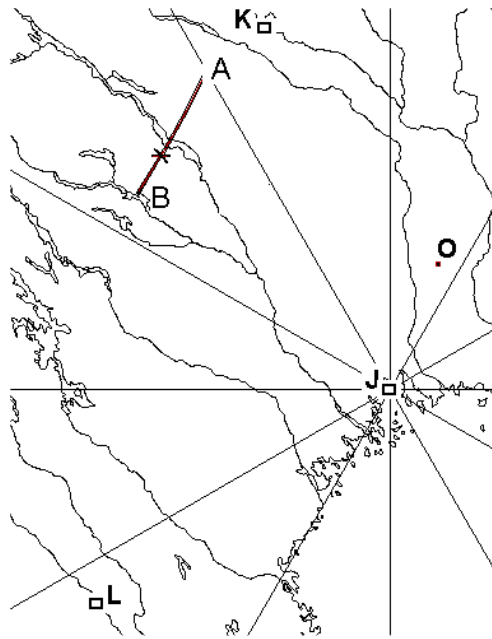


Fig. 5. The northernmost stations together with the horizontal projection of the bolide trajectory (thick line), as determined from directional data from the Kiruna and Jämtön stations. The cross on the trajectory projection marks the position (67.06N, 19.23E) of the main explosion.

Given the length of the trajectory's projection A-B, a trajectory's inclination of around  $40^\circ$  should be expected in order to obtain a realistic altitude at which the infrasound waves started to be generated. However, there is observational evidence that apparently contradicts the above conclusion: At the point marked as O in Fig. 5, almost 200 km ESE from the impact area, a photograph of the meteor trail has been taken, "shortly" after the main explosion (see Fig. 6). In this picture one can clearly see that the trail is nearly vertical. A most probable explanation is, that the picture, taken some time after explosion, shows the part of the diffusing trail and not the trajectory of the bolide responsible for generation of infrasound.



Fig. 6. A photograph of the meteor trail taken some time after the main explosion from point O (cf. With Fig. 5), approximately 200 km from the impact area (Photo: H. Eliasson)

### **Statistical detection of small meteor events**

Even small meteor events, which are close to the detection limit at a single station, may still be detected using a statistical approach. The method is based on Principal Component Analysis (PCA) of multiple indicator data. Indicators are distributions of variables within a given analyzing window:

- Angle-of-arrival
- Horizontal phase velocity
- Cross-correlation across the array
- Spectral slope

The method has been calibrated using infrasound recordings of known meteor events. The method has been tested looking for possible effects of meteor showers on the infrasound background. The combination of indicators which was found to fit the observed events was determined and used as a filter applied to tested data. The magnitude of filter response was proportional to the probability of unknown meteor events. Fig. 7 shows results of filtering of infrasound recordings from Lycksele and Jämtön during the Leonid meteor shower on November 19, 2002. The uppermost graph shows the global meteor count as a function of UT. The middle graph shows the filter response from Lycksele and the lowermost from Jämtön. Two spikes between approx 18 and 19 UT correspond to Concorde, which due to its extremely high signal strength could not be properly discriminated by the filter.

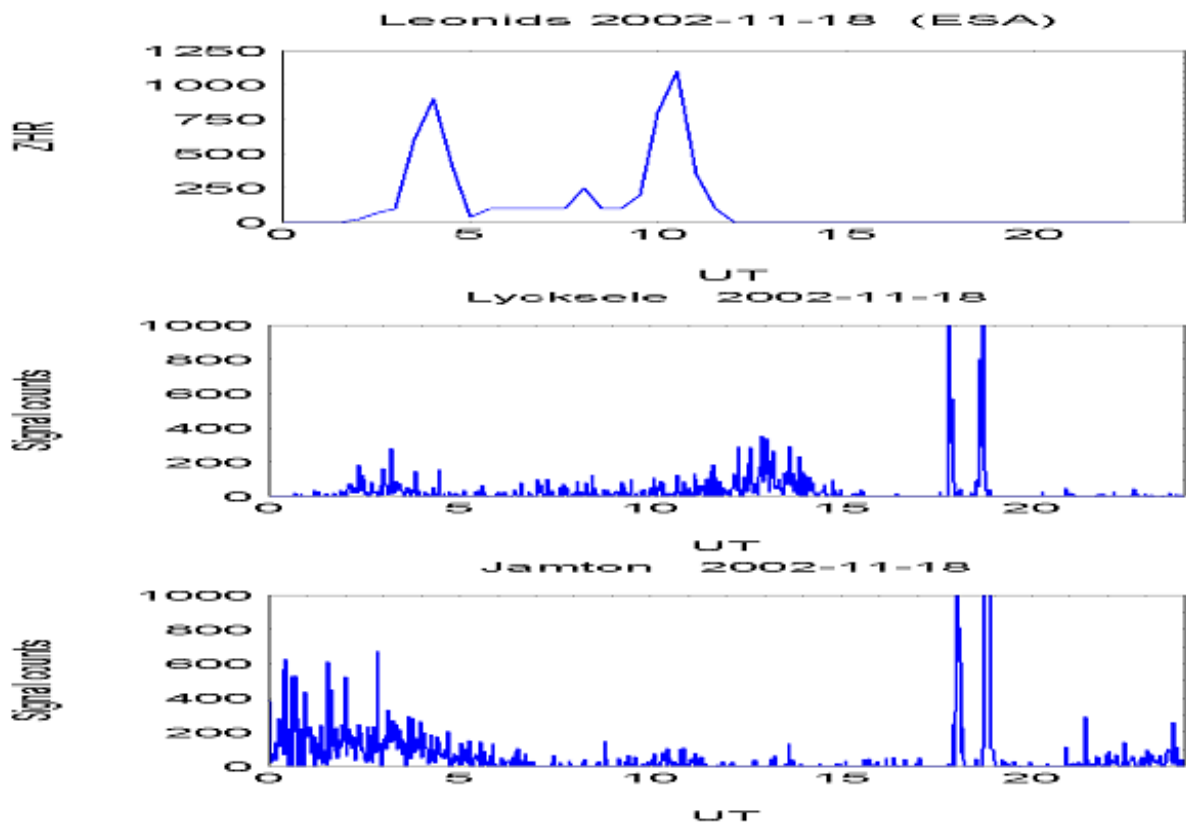


Fig. 7. Statistical search for changes in the infrasound background due to the Leonid meteor shower.

One can see that in Lycksele in particular, which is the station with the most favourable infrasonic background, that there is a similarity between the global meteor counts and the filter response. It must be remembered that the maximum of meteor showers interact with the atmosphere at different areas than those covered by the optimal propagation of infrasonic signals. Therefore, one can not expect that there will be a very close resemblance between the graphs.

### ***Detection of high altitude discharges: sprites***

During the last 10 years, infrasonic chirps in the frequency range 0.5 – 8 Hz were occasionally observed by arrays belonging to the Swedish Infrasonic Network (SIN). These

chirps have been attributed to certain types of thunderstorm activity associated with the high altitude discharges, sprites (Liszka, 2004). A method for automatic detection of chirps in the recorded data has been developed and applied to 10 years of data from two arrays belonging to the SIN: Jämtön and Lycksele. The temporal and directional distribution of the phenomenon is described. Also, long-term variability and possible relation to the solar cycle is studied.

During a night in May 1995, an unusual type of infrasonic signature, a few seconds in duration, rising in frequency from about 0.5 – 8 Hz, was observed. Since the observations were associated with the passage of an intense thunderstorm area, it was plausible to assume that the phenomenon could be related to the thunderstorm activity. One possibility was that the infrasonic chirps were produced by the high altitude discharges, sprites. That particular night was studied in detail and results were presented several years later (Liszka 2003, 2004). The occurrence of infrasonic emissions from sprites was recently confirmed by other researchers (Farges, T. et al., 2004).

#### **Possible generation mechanism**

According to optical observations (cf. e.g. Franz, R. C. et al., 1990, Lyons, W. A., 1994) the sprite is a discharge ranging from the top of a thunderstorm cloud at heights above 20 km up to the ionosphere at 100 km. The discharge fills up a conical volume in space: it is nearly cylindrical at low altitudes and it broadens with increasing altitude. Since the discharge takes place during a very short time, the Joule heating produced within the volume may be considered as a source of the pressure pulse. The pressure pulse will be, during its propagation towards the ground, converted into a wave package with the frequency related to the height at which it was generated. The highest frequency received from a given height is determined by the neutral collision frequency at that height. The principle of the infrasound generation is shown in Fig. 1. At low altitudes the wave vector of the generated infrasound pulse is nearly horizontal, while with the increasing altitude, where the discharge becomes more conical, the inclination angle of the wave vector becomes more negative.

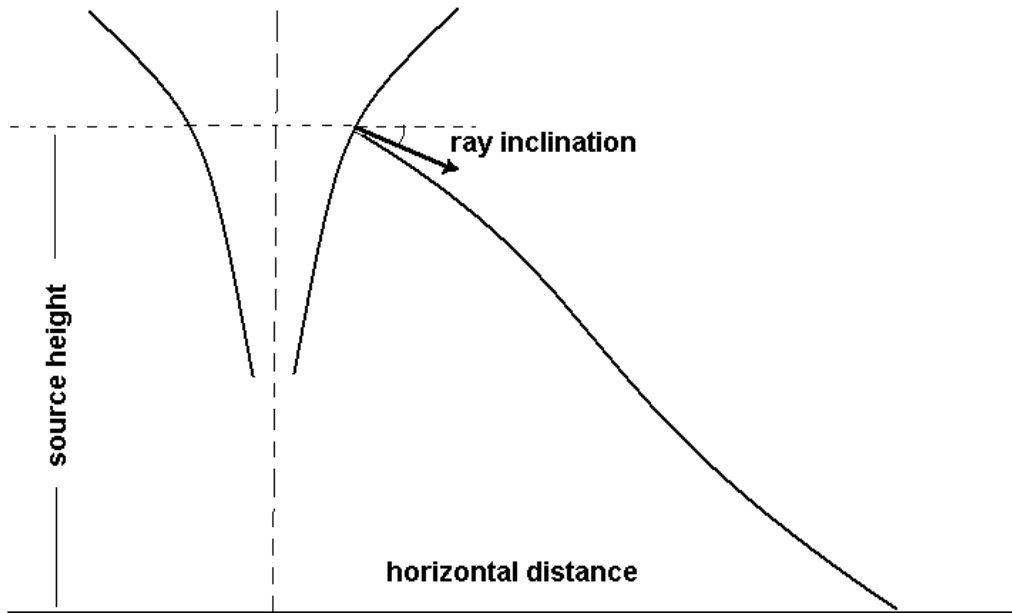


Fig. 1. The geometry of the infrasound generation by the high altitude discharge.

When the infrasound with the largest scale (lowest frequency) reaches a point on the ground about 10 seconds before the shortest time scale (highest frequency) an infrasonic chirp will occur. As will be shown later, for the medium/high latitude and the summer temperature and wind models, there will be two ranges of altitudes from which the infrasound may reach the ground: 30 – 65 and 90 –110 km.

### Search for chirp signatures

The search for the chirp signatures was performed running the Morlet wavelet transform on all 30-minute files (approx. 32k time series/microphone) from all stations belonging to the SIN. The obtained scalograms were divided into 200 sample-windows, each covering 11.1 sec. Each window was searched for the occurrence of chirps. Different search methods were tested: neural networks, multiplication with a template and a rule system. The rule system was finally selected for the analysis of the entire data. During the studied 10-year period, more than 28 million window positions per station were analyzed.

A typical infrasonic chirp appears on the scalogram as a sloping trace (Fig. 2). For simplicity, the y-axis of the graph is expressed in dilation numbers (dilation number is the number of time-scale intervals). The conversion of dilation numbers into the time scale for 30-minute scalograms is shown in Fig. 3. An advantage of using the dilation number instead of the time scale is that the chirp is nearly linear on the dilation number – time plane. It simplifies the search algorithm used to find chirps signatures in the data.

The search algorithm identifies all signals which are continuous during at least 50 samples (2.78 sec) and moves across at least 6 dilations. Sometimes a chirp may be amplitude modulated (discontinuous trace). Such a chirp may not be detected by the search algorithm. All automatically detected chirps were confirmed by visual inspection.

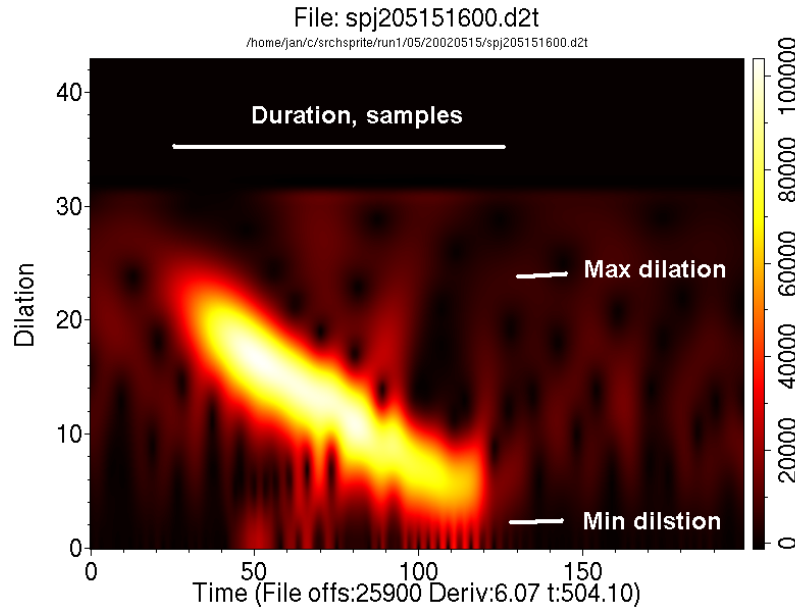


Fig. 2. A typical infrasonic chirp. The x-axis in number of samples (18 Hz sampling rate).

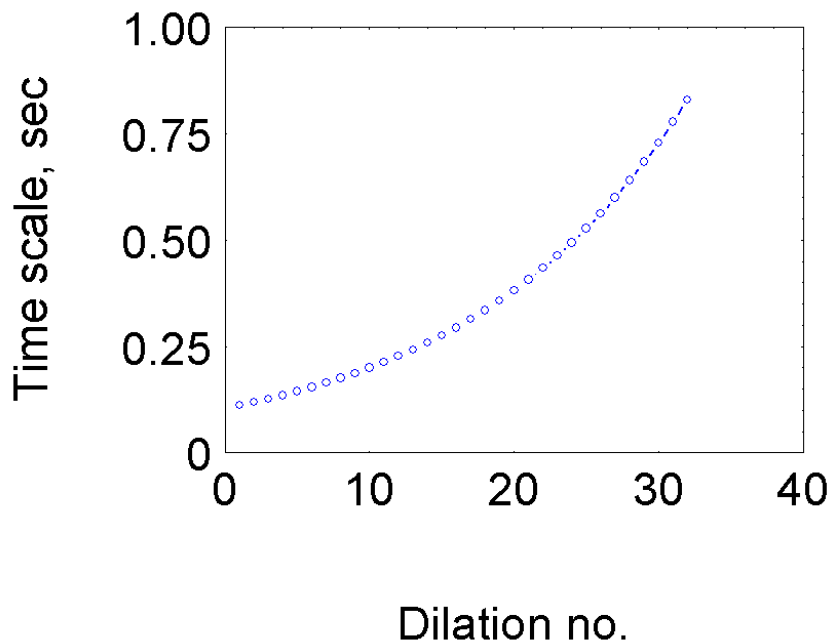


Fig. 3. Conversion of the dilation number into the time scale in seconds

Each chirp may be characterized by at least four variables:  
 Lowest dilation, DMIN, in which the chirp signal is detected, it corresponds to the highest frequency present in the chirp and probably to the lowest height at which the signal is generated.

1. Highest dilation, DMAX, in which the chirp signal is detected, it corresponds to the lowest frequency present in the chirp and probably to the largest height at which the signal is generated.
2. Length of the chirp, LEN, measured in number of samples.
3. The average slope of the chirp, SL, calculated as number of samples LEN divided by the range of dilations covered by the chirp  $DIFF = DMAX - DMIN$ .

There are other variables recorded together with chirp parameters and which may be related to the occurrence of chirps:

1. Month (time of the year)
2. Time Z at the beginning of a chirp (UT in minutes after midnight)
3. Azimuth of arrival at the maximum cross-correlation
4. Phase velocity at the maximum cross-correlation
5. Average amplitude (in arbitrary A/D units) at the maximum cross-correlation
6. The maximum product of all 3 cross-correlations within the array

All 10 variables will be used to study possible relations among them.

The search results

The search showed rather unexpected results. The occurrence frequency of infrasonic chirps is very different at different stations. The results are given below.

Station	Number of observed chirps during the analyzed period
Kiruna	None
Jämtön	114
Lycksele	4
Uppsala	2

It is not surprising that no chirps could be found in Kiruna due to the high background level. Also Uppsala with a large populated area only 10 km from the station and the largest Swedish airport 40 km from the station may be not a convenient place for chirp observations. The most surprising result is the difference between the stations Jämtön and Lycksele. A possible explanation will be discussed in a later section.

#### **Occurrence of infrasonic chirps at Jämtön station**

There is a remarkable variation in the occurrence of the chirps during the period 1994 - 2004. The monthly number of observed chirps is plotted in Fig. 5 as the function of time.

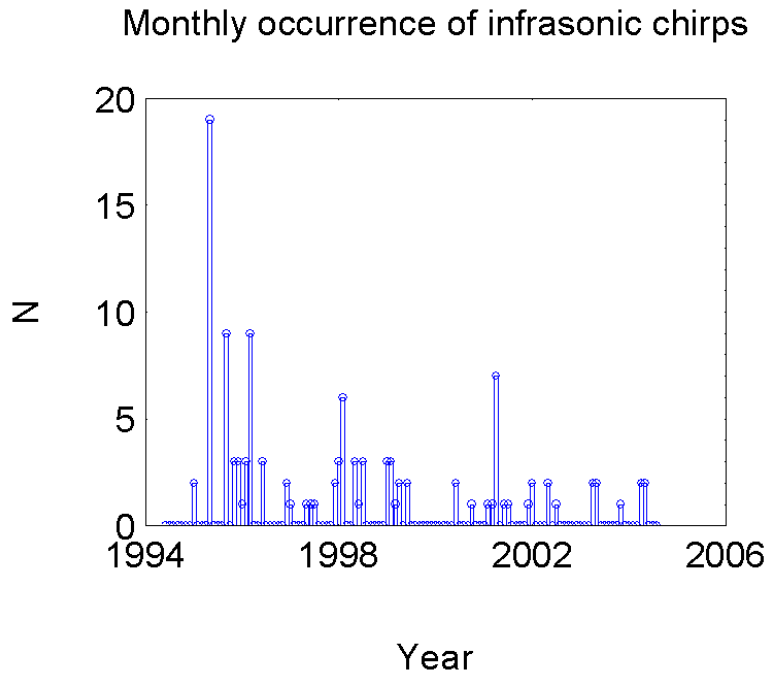


Fig. 5. Monthly occurrence of infrasonic chirps at the Jämtön station during the period 1994 – 2004

It is obvious that the occurrence frequency was very high during 1995. One possibility is that the occurrence frequency is related to the solar activity. A plot of monthly averages of the sunspot number for the same period is shown in Fig. 6.

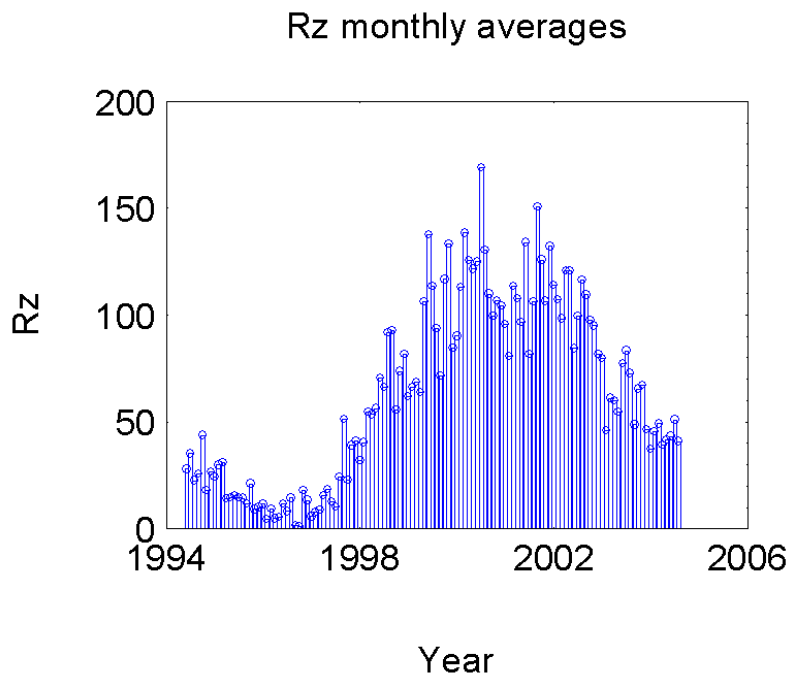


Fig. 6. Monthly averages of sunspot numbers during the period 1994 – 2004.

Also the distribution of the direction-of-arrival at the Jämtön station was studied. It appeared that the most intense infrasonic chirps were, during the entire period, from the same range of directions as during the analyzed night May 25, 1995 (Liszka, 2004). The distribution is shown in Fig. 7. The area where chirps are generated seems to coincide with the narrowest

part of the Gulf of Bothnia, named Kvarken. The two distinct peaks seem to coincide with the Finnish and Swedish coastlines within that area.

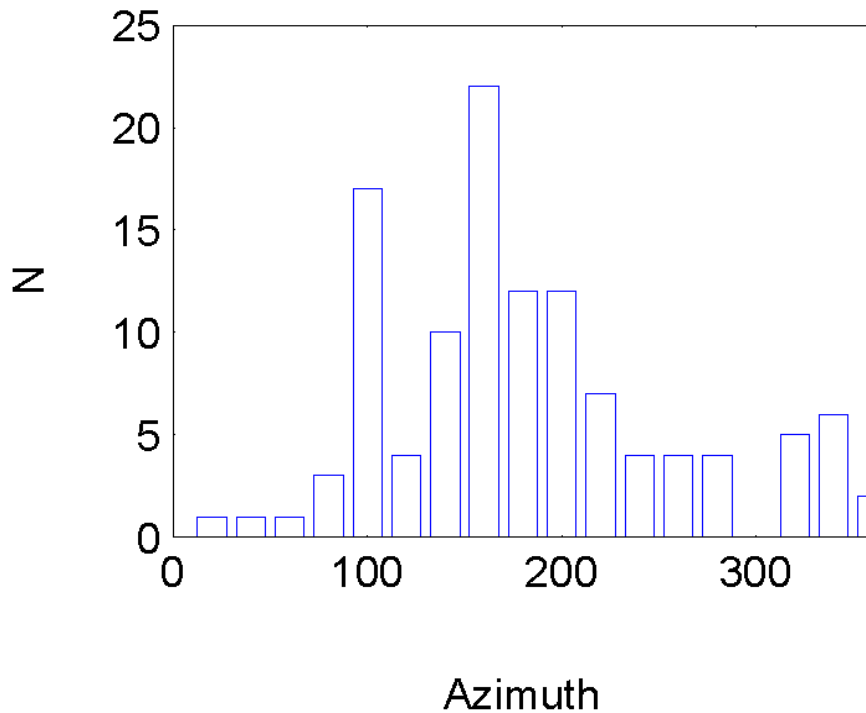
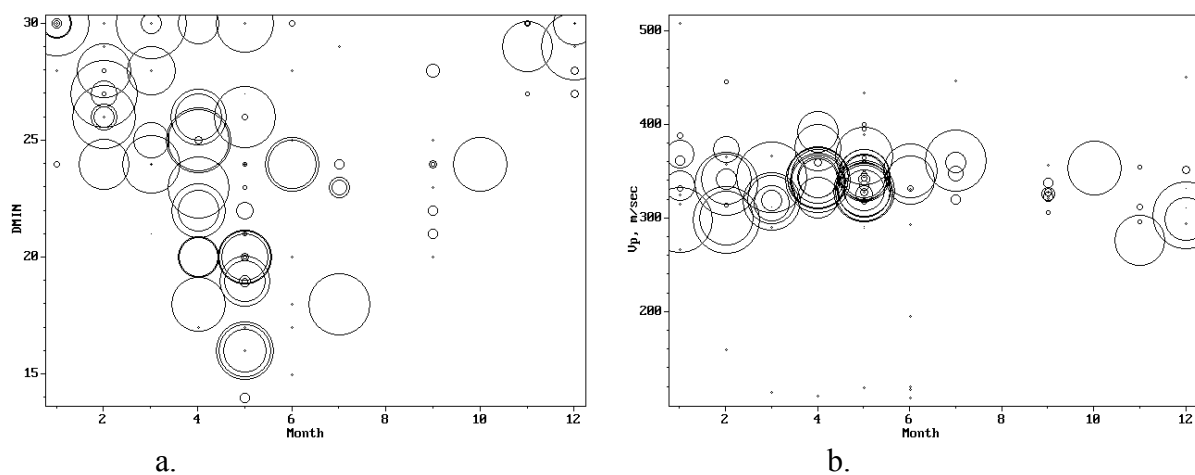


Fig. 7 The distribution of angle-of-arrival of infrasonic chirps observed at the Jamton station during the period 1994 – 2004.

Simple plotting of different variables of the problem against each other was done to obtain a first indication which relations between variables may be expected. Some of the plots of different pairs of variables are shown in Fig. 8. The size of the symbols is proportional to the last variable on the list: the maximum product of all 3 cross-correlations within the array, related to the signal-to-noise ratio within the chirp.



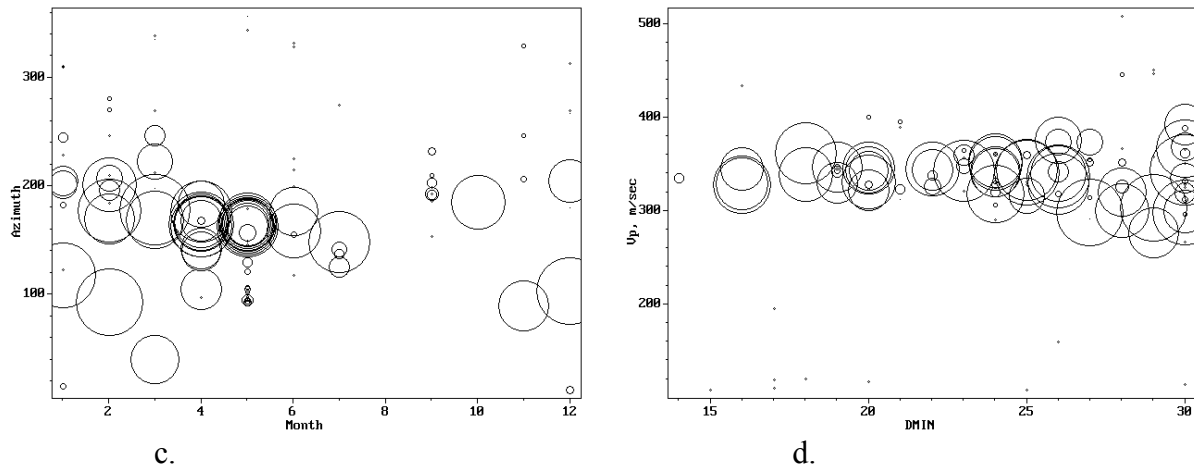


Fig. 8. Selected pairs of variables plotted against each other: a/ Minimum dilation DMIN as a function of the time of the year. b/ Phase velocity  $V_p$  as a function of the time of the year. c/ Azimuth-of-arrival as a function of the time of the year. d/ Phase velocity  $V_p$  as a function of the minimum dilation DMIN. The size of the symbols is proportional to the last variable on the list: the maximum product of all 3 cross-correlations within the array, related to the signal-to-noise ratio within the chirp.

Since plotting of variable pairs against each other, in a multivariate problem like this, may lead to incorrect results, the complete causal analysis was performed on the data matrix using the TETRAD-software (for review and application descriptions, see Liszka, 2003). The analysis finds both correlated variables and true causal relations (if such exist) in the data. The result of the analysis is shown in a form of a causal graph in Fig. 9.

```
File: var.ut3 Significance: 0.05
Assuming causal sufficiency
Optvalue: 8/18
* INCLUDED
```

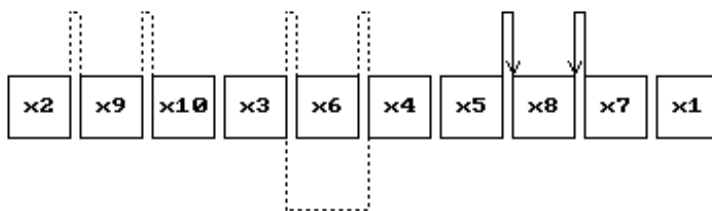


Fig. 9. The causal graph of the chirp-data. Variables are represented by numbered boxes. Correlated variables are connected with dashed lines. Solid, directed arrows indicate true causal relations at the given significance level (0.05). Order of variables is optimized in order to obtain the simplest possible graph. Explanation of variable numbers: x1 – month, x2 – starting time of the chirp, x3 – slope of the chirp, x4 – duration of the chirp, x5 – lowest dilation, x6 – extension of the chirp in the dilation domain, x7 – azimuth-of-arrival, x8 – phase velocity, x9 – average amplitude, x10 – cross-correlation product.

One can see that the horizontal trace (phase) velocity, being the measure of the angle of incidence, is controlled by both the lowest dilation of the chirp (highest observable frequency or probably the starting altitude) and by the azimuth-of-arrival. The latter may suggest that the chirp phenomenon is strongly aspect-sensitive due to the propagation across the complicated wind system.

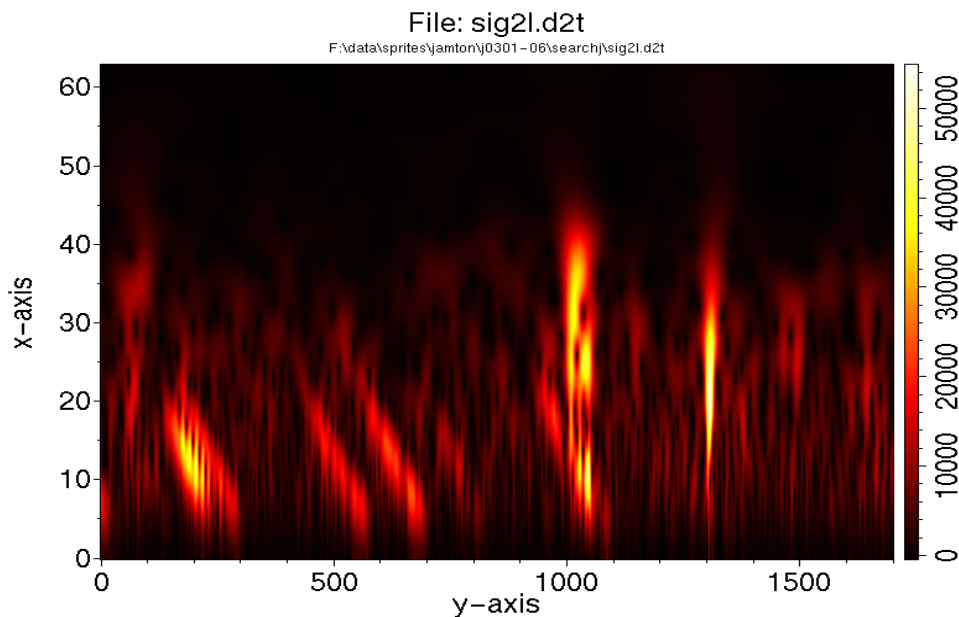
The above evidence is in agreement with the hypothesis that the infrasonic chirps are an infrasonic manifestation of high altitude discharges – sprites.

There are also two independent groups of correlated variables:

1. Starting time – amplitude – cross-correlation
2. Slope – duration – extension of the chirp

### **Observations on May 13, 2003**

In most cases it was impossible on Lycksele-recordings to find infrasonic signals corresponding to chirps observed in Jämtön. However, during the morning hours of May 13, 2003, two groups of emissions were observed in Jämtön, for which it was possible to identify corresponding emissions in Lycksele. Here, one of the emission events, starting in Jämtön after 07:26UT is analyzed. Scalograms for that event, recorded in Jämtön and Lycksele, are shown in Fig. 10. The time scale on both scalograms are presented in dilation numbers. On the upper scalogram (Jämtön) it is easy to see at least 5 infrasonic chirps, while the background level in Lycksele (lower scalogram) is so high that it is impossible to say if any chirps are visible. The average signal amplitudes (expressed in arbitrary A/D units) are multiplied with the cross-correlation across the array are plotted in Fig. 11. The signals observed in Lycksele are, however, perfectly enough to determine the angle-of-arrival. The geographic position of the region where the infrasonic emission was generated could be determined by triangulation and found to be located at 64.42N and 23.53E over the Gulf of Bothnia. The distance from this location to Jämtön and Lycksele is 168, respectively 232 kilometers.



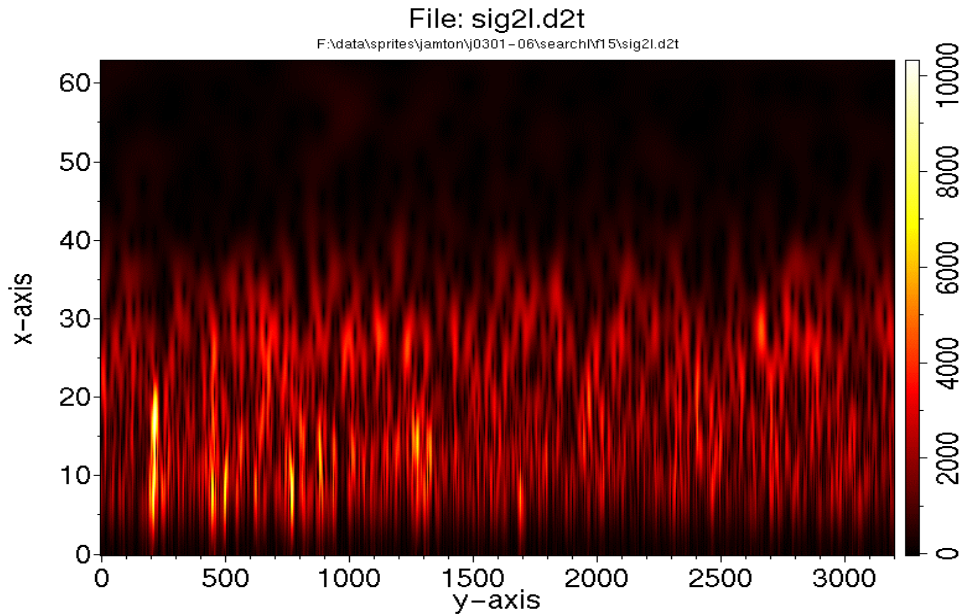


Fig. 10. Scalograms from Jämtön (upper) and Lycksele (lower) of the same emission event. Observe that chirps observed in Jämtön can not be identified in Lycksele.

It may be seen in Fig. 11 that the general form of the signal is very similar at both stations. However, no chirps may be distinguished in Lycksele. Most likely it is not the matter of lower signal-to-noise ratio. On the contrary, Lycksele shows on that particular date the lowest amplitude of the uncorrelated background of all SIN stations, only 0.014 Pa (peak value). At Jämtön the corresponding amplitude is 0.045 Pa. The main difference is due to different directions of propagation to both arrays with respect to the wind system. This will be demonstrated in the next section using the ray-tracing technique.

2003-05-13

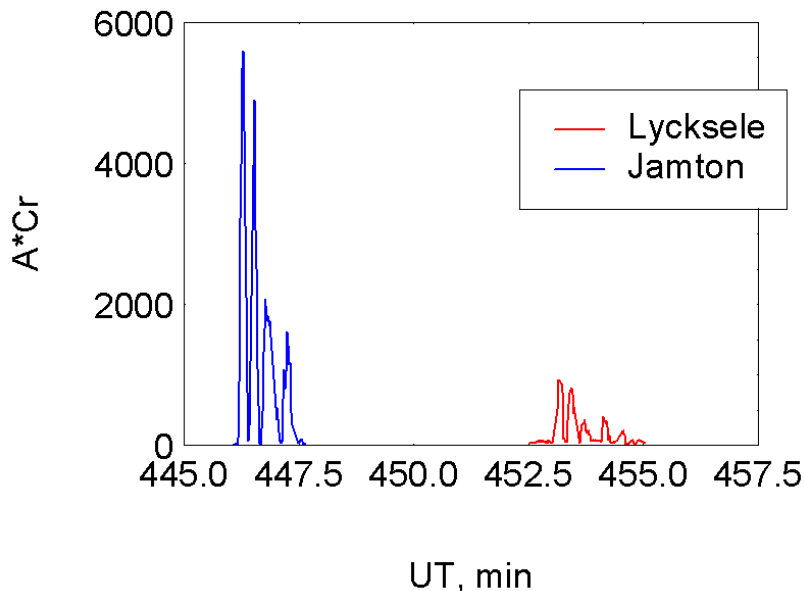


Fig. 11. The average signal amplitudes at both stations (expressed in arbitrary A/D units) multiplied with the cross-correlation across the array.

### **Results of the ray-tracing for the event on May 13, 2003**

For this event, the directions of propagation to both stations and the distances are known. Therefore, it is possible, using the ray-tracing technique, to study effects of the wind system and the temperature profile on the signals generated at different heights. The wind and temperature model used in calculations is identical to that used in the previous publication (Liszka, 2004). That model, used in infrasound propagation studies at the Swedish Institute of Space Physics since the mid-70's, is a compilation of different high-latitude measurements, mainly of rocket measurements at the ESRANGE rocket range in Kiruna, Sweden.

The aim of the investigation is to calculate the propagation time as a function of horizontal distance for different heights (5 km steps) of the source and different inclination angles (1-degree steps) of the wave vector. Interesting differences may be seen comparing the propagation directions to both stations. A schematic graph showing calculation results for the Jämtön station is shown in Fig. 12. The graph shows the values of the propagation time as a function of the horizontal distance for varying angle-of-incidence and height. A two-branch curve is obtained for each source height: the upper, where the propagation time and the horizontal distance decreases with the increasing inclination angle and the second, after a turning point, where the propagation time and the horizontal distance increases with the increasing inclination angle. The increasing source height moves the curve upwards to the left. It may be shown that the upper branch of the curve, together with the fact that in the high altitude discharge the inclination angle increases with height (see Fig. 1) is responsible for formation of infrasonic chirps. In the direction of propagation towards the Lycksele station there is only the lower branch on the curve. For some heights there is, however, a single "kink" on the curve, being a residual of the two-branch curve. Results of actual calculations for the event of May 13 and for both stations are shown in Fig. 13 (Jämtön) and Fig. 14 (Lycksele).

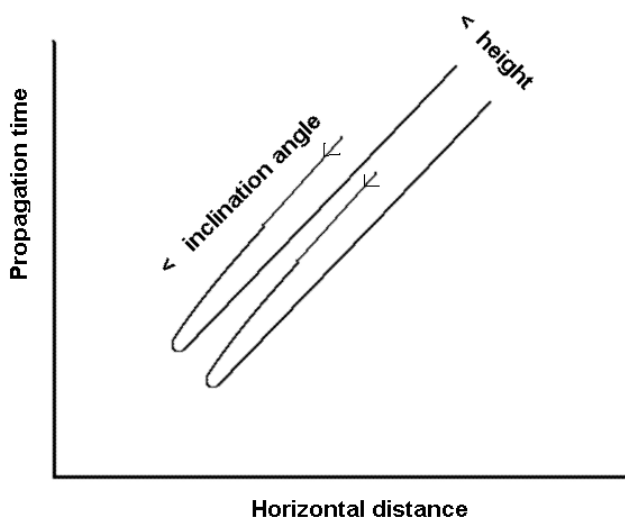


Fig. 12. The values of the propagation time as a function of the horizontal distance for varying angle of incidence and height.

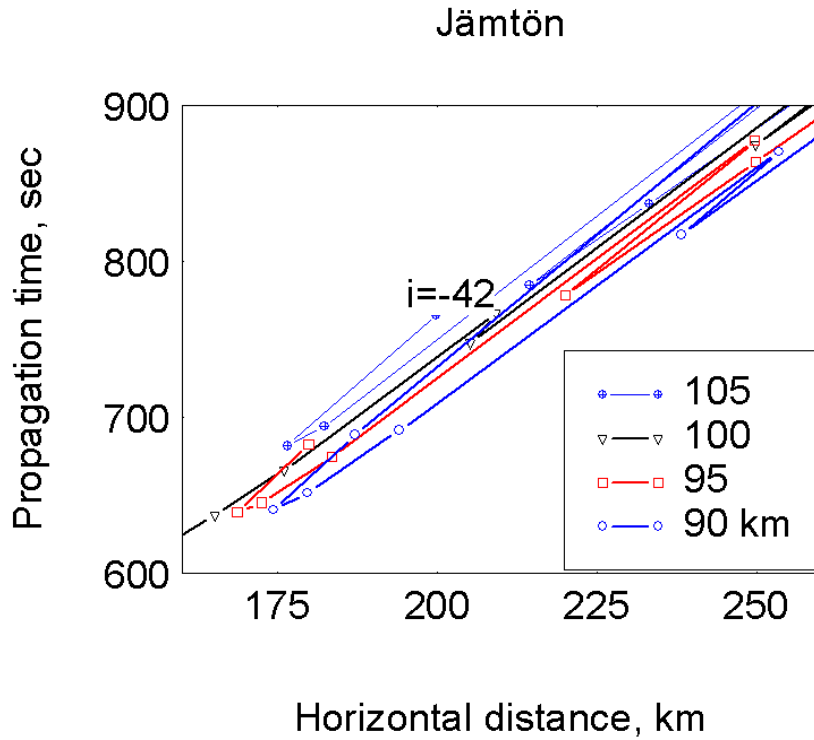


Fig. 13. Results of ray-tracing for the Jämtön station: The values of the propagation time as a function of the horizontal distance for varying angle of incidence and height.

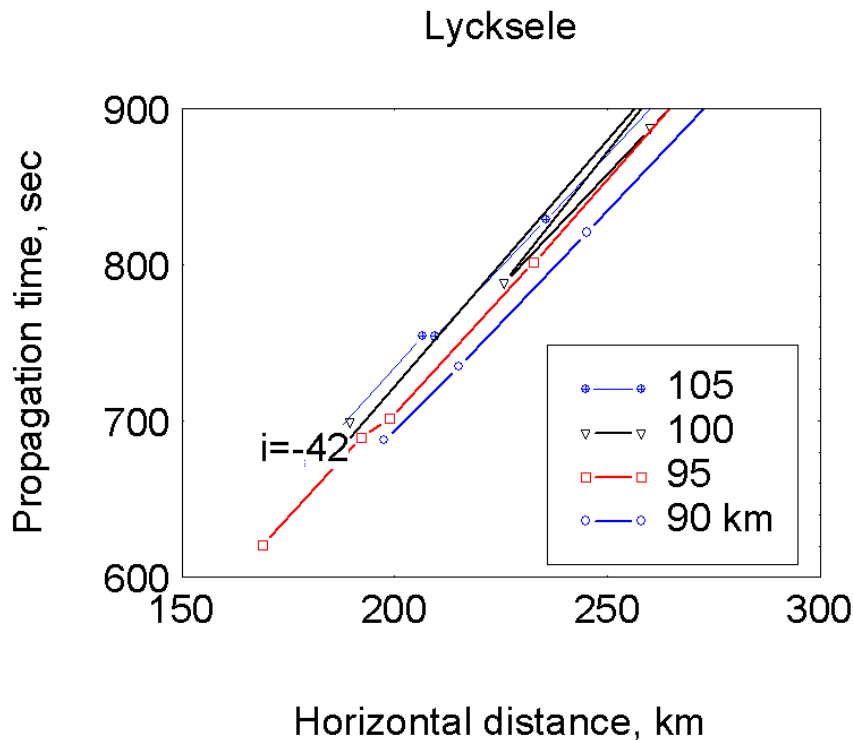


Fig. 14. Results of ray-tracing for the Lycksele station: The values of the propagation time as a function of the horizontal distance for varying angle-of-incidence and height.

The above event, which was observed both from Jämtön and Lycksele, indicates that the phenomenon of infrasonic chirps is due to dispersion of infrasonic waves in the upper atmosphere. The fact of dispersion is confirmed by ray tracing calculations.

## ***Infrasound from thunderstorms***

A lightning in the atmosphere acts like a source of cylindrical shock waves. When the distance from the source increases, more and more energy is transferred into the low-frequency range through the same mechanism as for shock waves from supersonic aircraft (see Chapter 2). It is difficult to estimate maximal distances at which infrasound from a single lightning may be detected. It is, however, clear that distances between the SIN arrays are too large in order to identify the same lightning from at least two arrays. For this particular purpose two relatively close spaced arrays (30 – 50 km) would be needed.

The overview display presented on the SIN home page, showing the angle-of-arrival and the horizontal trace velocity of incoming infrasonic signals, may be used to view the development and movement of thunderstorm cells around each array, typically within a 100 km radius. An example showing three thunderstorm cells passing by the Kiruna-array.

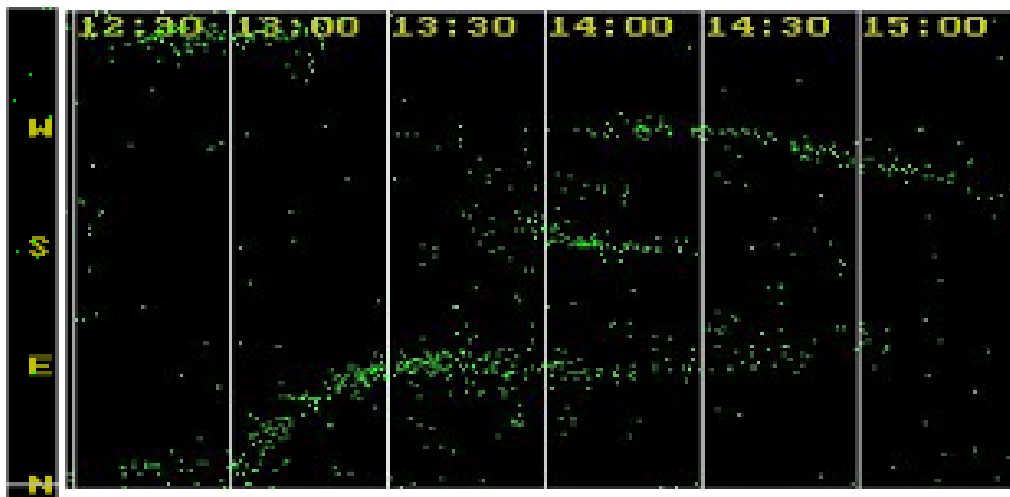


Fig. 15. A detail from the overview display presented on the SIN home page for Kiruna-array on July 8, 2005. The horizontal axis shows the UT (30-minute marks) and the vertical axis shows the angle-of-arrival of infrasonic signals. A signal from each single lightning is shown as a bright dot. Three individual thunderstorm cells may be seen moving by the array (diffuse bright bands).

In order to study the fine structure of individual signals, a high-resolution presentation has to be used. A small fraction of the above period, shortly before 1400UT, is shown in Fig. 16.

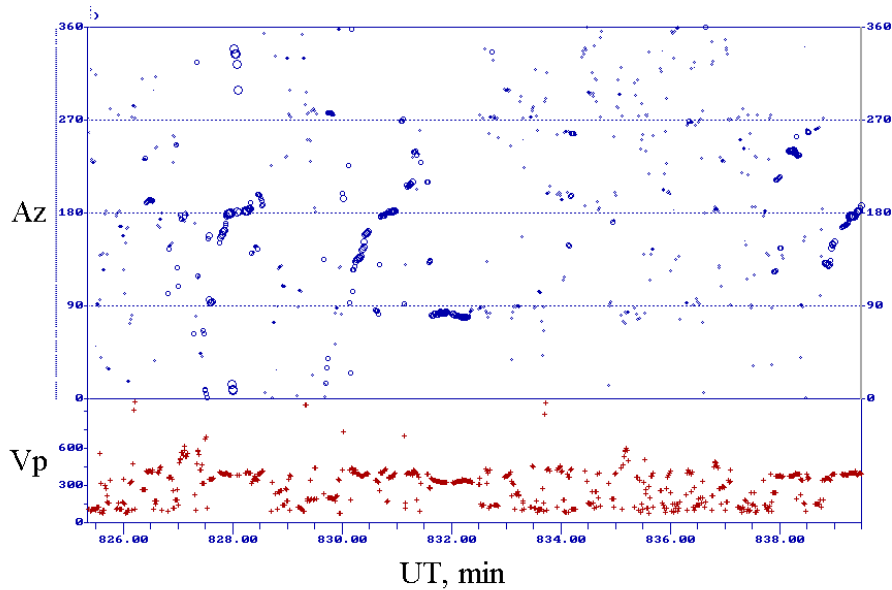


Fig. 16. High-resolution recording of infrasonic signals at the Kiruna-array between 1345 and 1400 UT. The upper graph shows the angle-of-arrival of infrasonic signals, the lower one shows the horizontal trace velocity. The size of the symbols on the upper graph is proportional to the cross-correlation across the array.

Accumulations of points on the upper graph correspond to signals from distant flashes: short in time and limited in azimuth correspond to cloud-to-ground (CG) flashes, while signals extended in time, and often in azimuth probably correspond to intracloud (IC) flashes or CG flashes with substantial horizontal extents (see picture of Fig. 17). IC flashes can produce spectacular infrasonic signals, sometimes up to 30 seconds long.



Fig. 17 An IC flash over Mt. Lemon, Tucson, Arizona (photo by J. Liszka-Hackzell)

The long duration of infrasonic signals from IC flashes is due to their large horizontal extent. The geometry of IC signals is explained in Fig. 18.

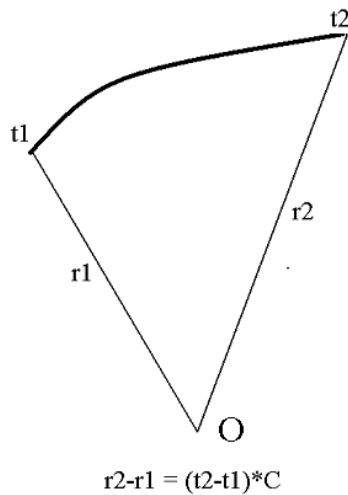


Fig. 18. The geometry of an infrasonic signal from an IC flash. C is the speed of sound.

The signal generated at both end points of the discharge channel arrives to the observer O at instants  $t_1$  and  $t_2$ . The duration of the signal,  $t_2 - t_1$ , is thus proportional to the difference of distances  $r_2 - r_1$ . Knowing the angle between  $r_2$  and  $r_1$  and the inclination of the ray between  $r_2$  and  $r_1$ , it is possible to estimate the geometrical extension of the discharge channel. Since at a close range the horizontal trace velocity is proportional to the inclination of the ray to the horizontal plane, the graph trace velocity vs azimuth will uniquely describe the morphology of the discharge channel. An example of trace velocity vs azimuth graph for one of the IC flashes of Fig. 16 is shown in Fig. 19.

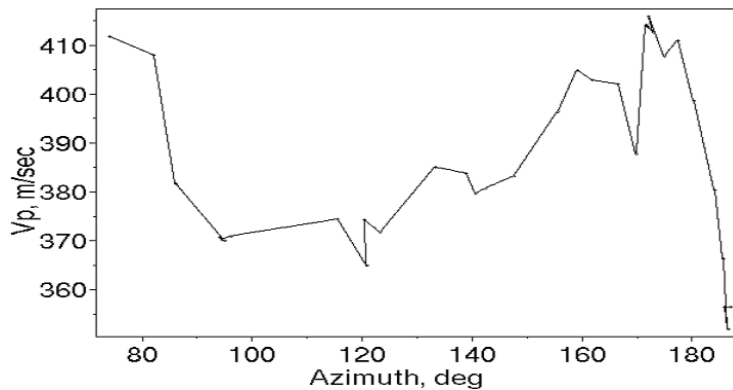


Fig. 19. A trace velocity vs azimuth graph for one of the IC flashes of Fig. 16

Knowing the temperature distribution in the atmosphere, it is possible to convert the trace velocity into the inclination of the ray with respect to the horizontal plane. Most of the acoustic energy from a lightning at distances of the order 10 – 50 km is located in the frequency range 1 – 10 Hz (0.1 – 1 sec). It may be seen on the wavelet spectrum (scalogram) of the infrasonic signal from an IC flash during the same thunderstorm of July 8, 2005.

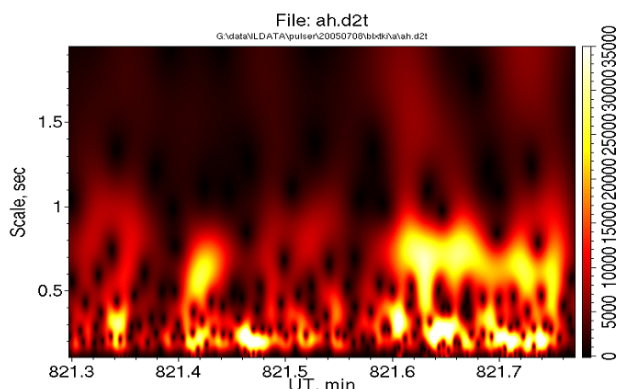


Fig. 19. Wavelet spectrum (scalogram) of infrasound from a CG flash (at 821.4 min UT) and of an IC flash (821.6 – 821.75 min UT), duration of the signal 9 sec.

### ***Volcano eruption: Hekla February 26, 2000***

On February 26-27, 2000 infrasonic signals from Iceland area were recorded at the Swedish network of infrasonic stations, SIN. The signals were immediately identified as having originated from the eruption of the volcano Hekla. The frequency range, within which the observations were performed was, as usual, 0.5 – 6 Hz. A sampling rate of 18 Hz was used at all stations.

At all stations the microphones are located in corners of a right angle triangle, with two shorter sides oriented EW and NS. The length of these perpendicular baselines is only 75 meters. Wind shelters are used to eliminate the wind noise at the microphones.

Geographical coordinates of stations and their locations with respect to Hekla are given in Table 1.

Table 1: Swedish infrasonic stations

Name	Latitude	Longitude	Distance to Hekla	Observed azimuth
Kiruna	67.8	20.4	1825	272.9
Jämtön	65.87	22.51	1951	271.5
Lycksele	64.61	18.71	1816	283.5
Uppsala	59.85	17.61	1964	303.0

The operating principle of the stations is to detect a coherent signal and determine the angle-of-arrival of that signal. The angle-of-arrival is determined using a modified cross-correlation method. Since the amplitudes of infrasonic waves in that frequency range are strongly influenced by atmospheric conditions, the absolute amplitude is not measured on the routine basis.

#### **Observations of the February 26<sup>th</sup> event**

Fig. 20 shows the angle-of-arrival at all stations during the period 1900 and 2400 UT. Fig. 21 shows the average cross-correlation across the microphone array at all stations during the same time period.

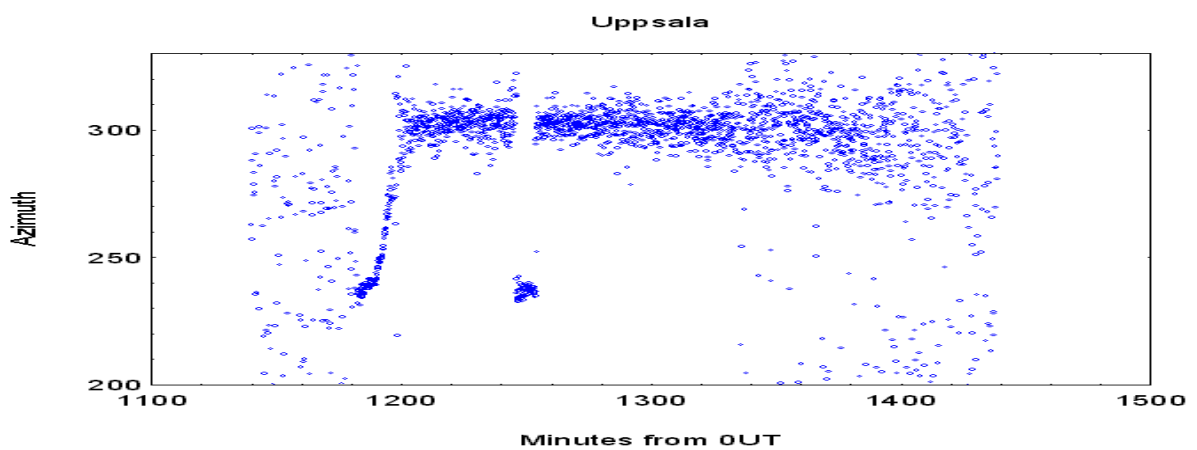
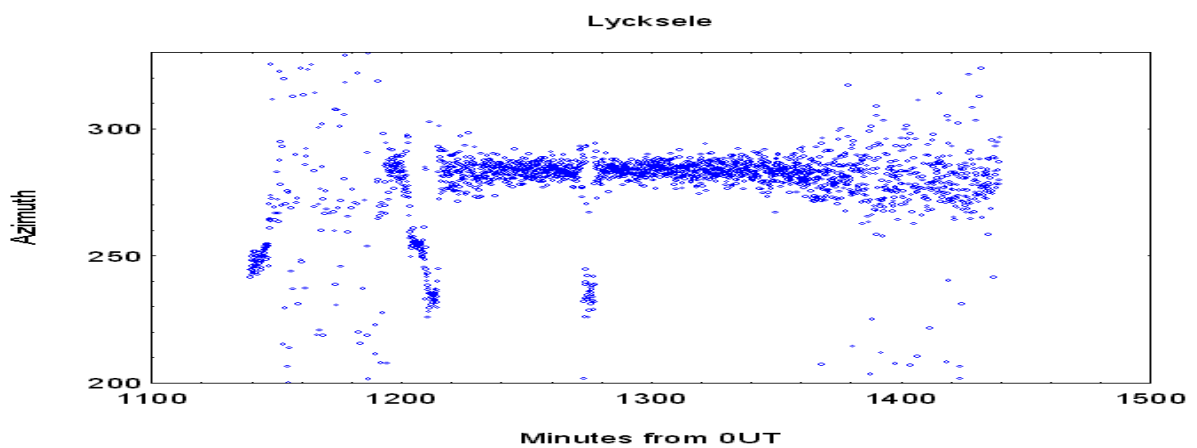
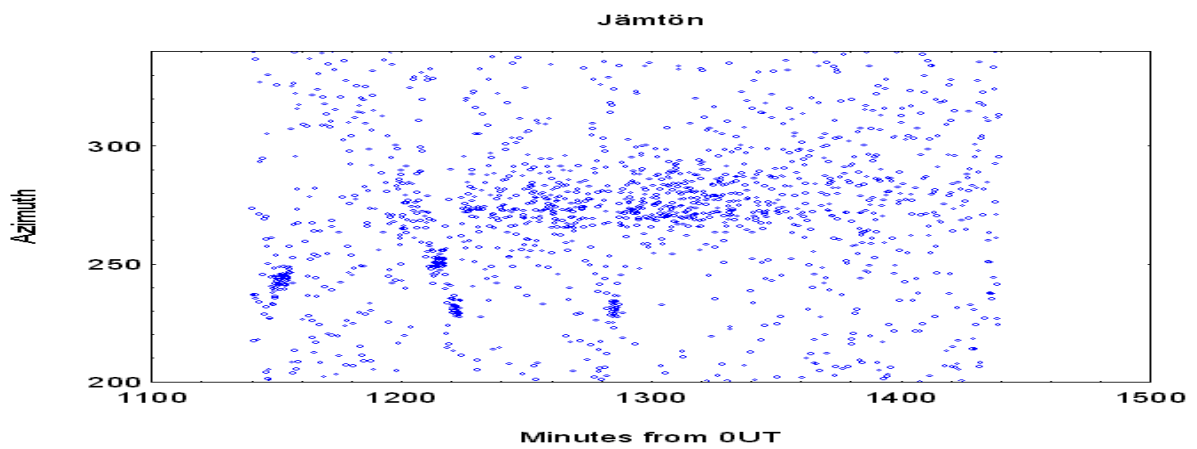
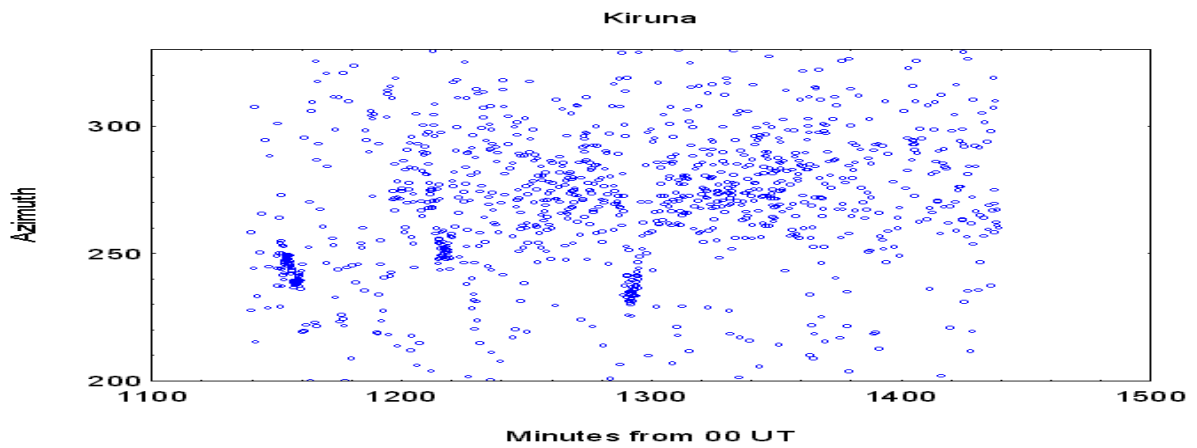


Fig 20. The angle-of-arrival at all stations during the period 1900 and 2400 UT.

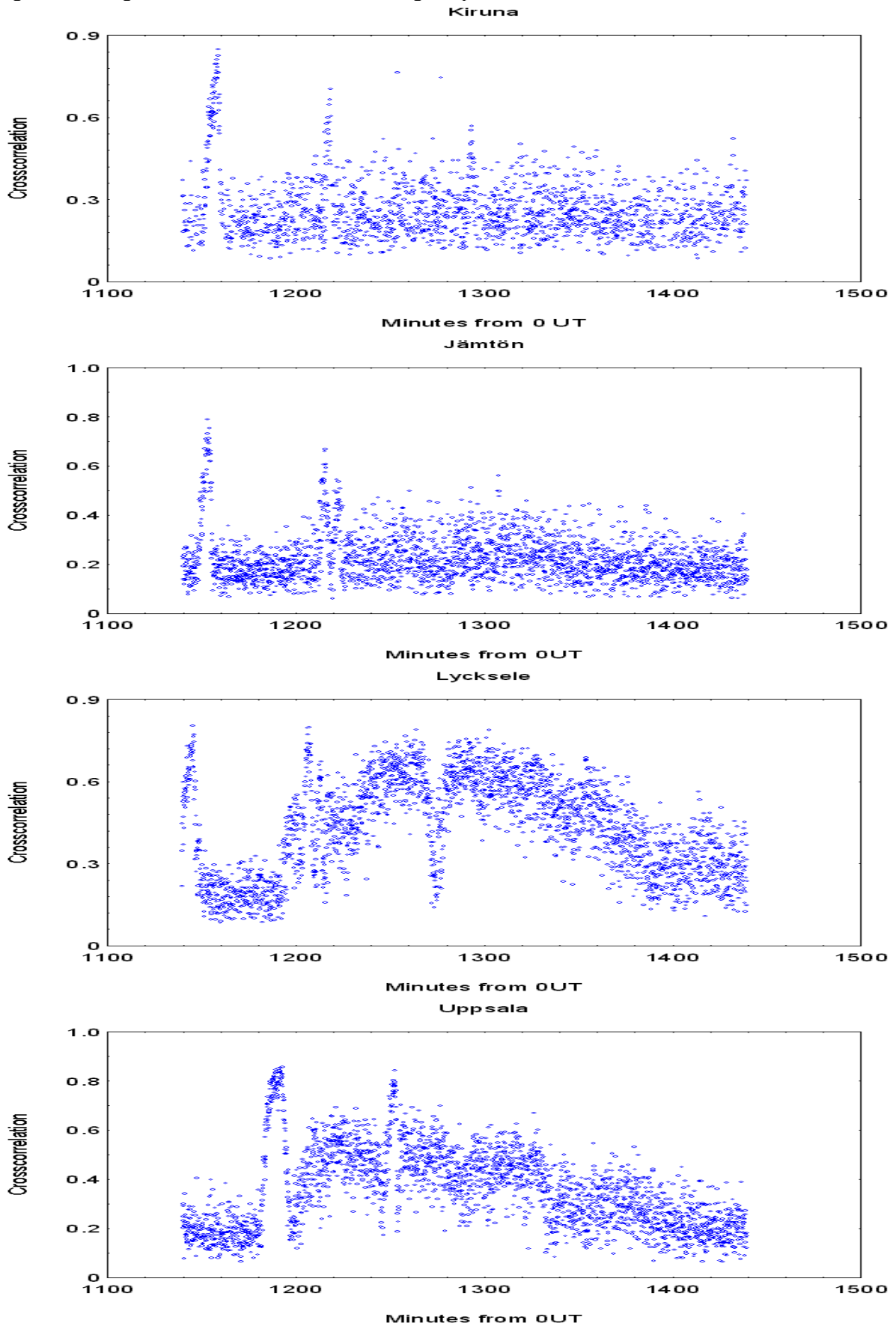


Fig. 21. The average cross-correlation across the microphone array at all stations during the period 1900 – 2400 UT.

One can see that properties of the signal are not simply related to the distance between the observing point and the source. Signals weaken at all stations around midnight. On February 27, signals from Hekla are still visible in Lycksele, with a maximum around 17 UT. Mean values of the angle-of-arrival during the period 1900 – 2400 UT on February 26 are shown in the last column of Table 1.

Three scheduled Concorde flights are clearly visible in Figures 20 and 21. An interesting detail concerning the second flight may be seen: the aircraft deviated from its normal route in order to fly around the cloud of volcanic ashes from Hekla, which had just started its eruption.

### **Spectral analysis of the event**

The origin time of the February 26 eruption was reported to be 18:19 UT (1099 minutes after 0 UT). Figures 22 and 23 show spectrograms for the acoustic signals recorded at Lycksele and Uppsala. The original waveforms were sampled at 18 Hz, but the waveforms used to compute the spectrograms were decimated by a factor of 2 after applying an 8-pole low pass filter. The Welch method was implemented with a sliding 256-point Hanning window (28.4 s window, spectral resolution of .035 Hz) with a 50% overlap. At each array, the station with the best S/N ratio was selected. Three Concorde arrivals appear as broadband, high amplitude signals in Figures 22 and 23. The possible event from Hekla appears as a lower frequency signal with a diffuse onset and a long duration, which extends past the shown record. Such frequencies are typical for volcano-acoustic signals. For Lycksele, the estimated arrival time of the volcanic signal is 19:55 (1195 minutes), the travel time is 5760 s (96 minutes), and the effective propagation speed is 0.315 km/s. This value should be smaller than the apparent phase velocity recorded at the array. For Uppsala, the arrival time is 20:00 (1200 minutes), the travel time is 6060 s (101 minutes), and the effective propagation speed is 0.324 km/s. Thus the onset time of the low-frequency arrival is consistent with an acoustic signal originating from Hekla volcano.

Figures 24 and 25 show the spectrogram and power spectral density for the interval of time between the second and third Concorde signals at Lycksele, and Figure 26 shows the power spectral density for the interval of time between the second and third Concorde signals at Uppsala. The spectral envelope is quite different in both signals, and the stripping of high-frequency energy in the Uppsala recording may be attributed to the longer propagation path. There is no apparent harmonic structure in the records, which is unfortunate. It is possible that there is significant energy below 1.5 Hz, but the sensor response may be eliminating these frequency components. Although the high frequency roll-off appears to be consistent with the seismic tremor signals generated during the eruption, caution must be exercised because it is likely that significant high-frequency energy is stripped during the long-range propagation. It may be valuable to investigate later record times to see if harmonic structure can be found. However, it would behoove us to first inquire if such structure in present seismic tremor records during that period.

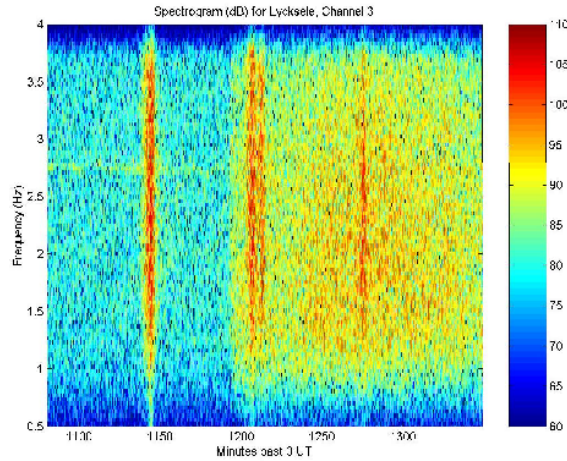


**Figure 22.** Spectrogram of waveform recorded at Lycksele from 18:00:00 to 22:29:39 UT. Three arrivals from the Concorde can be clearly seen. The onset-time of the eruption signal may be just before the second Concorde arrival, around 1195 minutes past 0 UT (19:55 UT).

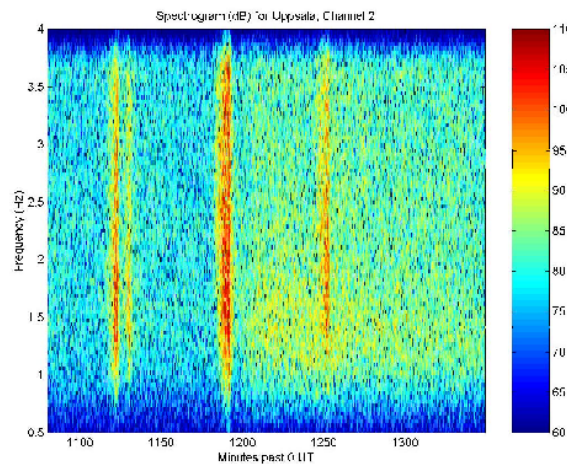


**Figure 23.** Spectrogram of waveform recorded at Uppsala from 18:00:00 to 22:29:39 UT. The three arrivals from the Concorde can also be clearly seen. The onset time of the eruption signal may be just after the second Concorde arrival, around 1200 minutes past 0 UT (20 UT).

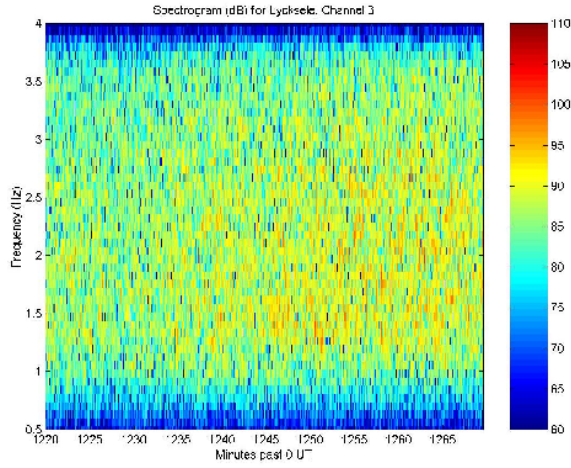


**Figure 24.** Spectrogram for interval between second and third Concorde arrival at Lycksele.

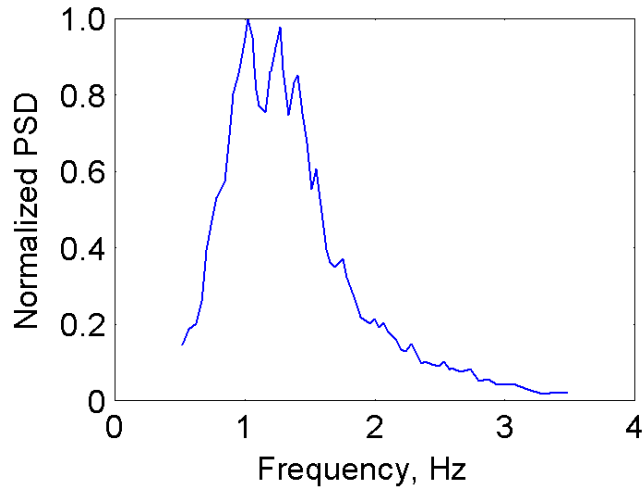


**Figure 25.** PSD for interval between second and third Concorde arrival at Lycksele.

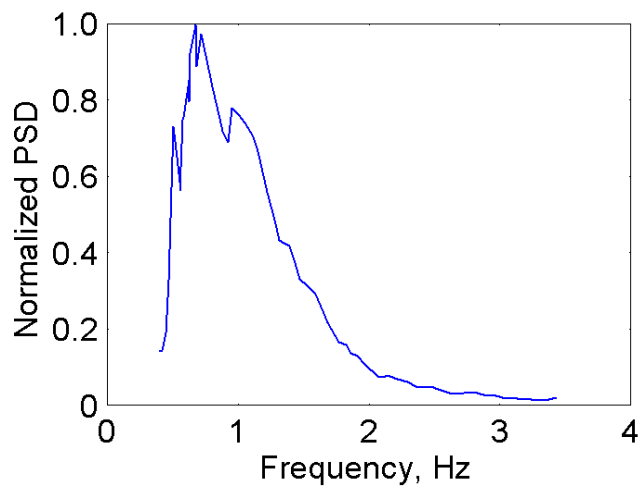


**Figure 26.** PSD for interval between second and third Concorde arrival at Uppsala.

### Phase velocity determination

Data from Uppsala and Lycksele, showing higher signal levels than the northern-most stations, was used for determination of the phase velocity. The phase velocity contains information about the angle-of-incidence of the wave and may be used to establish the nature of the propagation mode/modes. A convenient method to display the phase velocity data is to plot them as a function of azimuth. On such a display, it is easy to see the phase velocity corresponding to different signals received during the analysed period. In addition to that, it is possible to find out whether the fine structure of the distribution of angle-of-arrival is related to a multi-mode propagation. Figures 27 and 28 show phase velocity – azimuth plots for Lycksele and Uppsala, respectively.

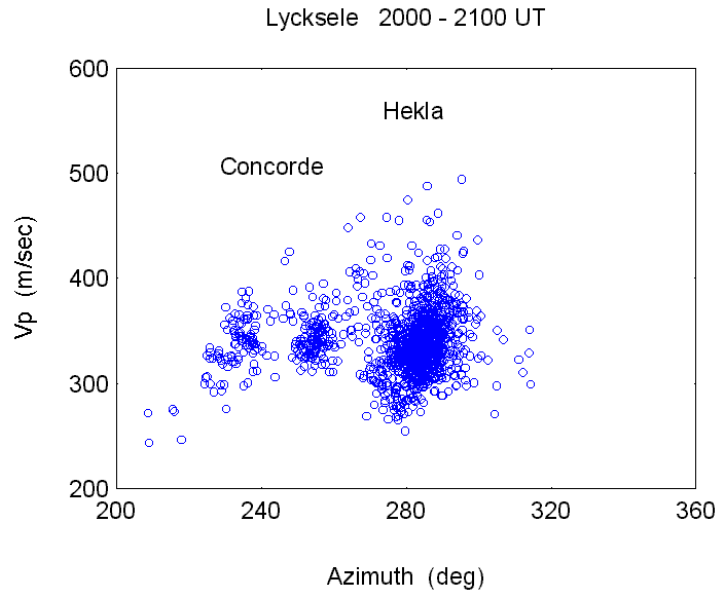


Figure 27. Phase velocity vs azimuth for the period 20 – 21UT in Lycksele. Visible on the graph from the left: two Concorde arrivals (Air France and British Airways) and the Hekla signal.

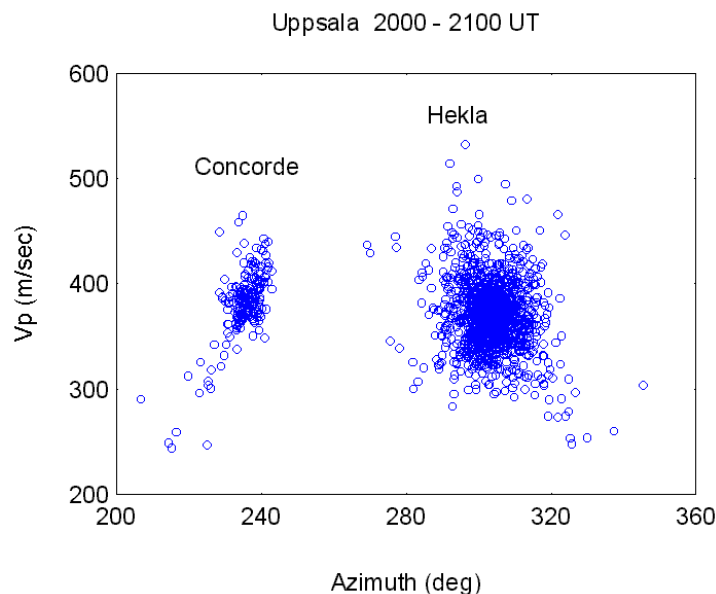


Figure 28. Phase velocity vs azimuth for the period 20 – 21UT in Uppsala. Visible on the graph from the left: one Concorde arrival (British Airways) and the Hekla signal.

Infrasonic signals were, before determination of the phase velocity, threshold-filtered in the wavelet magnitude domain, so that both weakest and strongest signal components were removed. It has been found that signals, pre-processed in this way, yield more consistent trace velocities.

Using an eruption origin time of 18:19 UT (1099 minutes after 0 UT), the propagation time of the first signal arriving at Lycksele at 19:55 UT (1195 minutes) is 5760 seconds, and the propagation time of the first arrival at Lycksele at 20 UT (1200 minutes) is 6060 seconds. Thus the apparent propagation speed, or celerity, of the first arrival is 315 m/s for Lycksele and 324 m/s for Uppsala. These signal celerity values can only correspond to sound waves refracted in the troposphere or stratosphere, which may be subject to strong scattering and thus lose some of their lower-frequency components. Strong westerly winds in the troposphere and stratosphere during the eruption period would support these ducted arrivals. Significantly lower apparent horizontal phase velocities are observed for signals with the Hekla eruption than for Concorde signals. At both stations, low-phase velocity signals arrive through a more southern path (lower azimuth). The distribution of arrivals at Lycksele split into secondary peaks, suggesting multi-mode propagation. The first arrivals may correspond to waves trapped in the troposphere and stratosphere, as expected from strong westerly winds in the lower atmosphere. The frequency content of the observed acoustic signals is consistent with tremor energy radiated during a volcanic eruption. However, some of the fine spectral structure associated with tremor signals may be lost during long-range propagation.

## ***Distant gas explosion***

According to press news, a huge explosion of natural gas occurred on the night of April 26-27, 1995 close to the town Uchta (63.59N, 53.55E) in Northern Russia. According to a press release from the Swedish Gas Association, the total amount of gas released in the accident was 3,200 tons. Assuming an energy content of 38.8 GJ per 1000 m<sup>3</sup> gas and a gas density of 0.624 kg/m<sup>3</sup>, the approximate acoustical power of the source may be estimated. It has been found from infrasonic measurements in Northern Sweden that the total duration of the gas leak was about 81 minutes. The gas flow was therefore approximately 10<sup>3</sup> m<sup>3</sup>/sec, driving a flame column a few thousand meters high (according to a press notice) . Assuming that about 1 % of the combustion energy was converted into infrasonic energy, the acoustic power of that source was of the order of 400 MW. A source with that acoustic power could certainly be detected over a distance of at least 4000 km. In this section, results of infrasonic measurements of the explosion made in Northern Sweden are described.

### **Observations**

During the night of April 26-27 1995, unfortunately, only the recording stations in Kiruna (67.8N, 20.4E ) and Jämtön (65.8N, 22.5E) were in operation. The recording station in Kiruna was, at that time, of an older type, where only counts of wave periods, correlated over the microphone array, within 10° azimuth intervals and 30-second time intervals are recorded. At Jämtön where the latest recording equipment was installed, complete time series from 3 microphones were recorded. Most of the analysis described here is therefore made using the Jämtön data.

The angle of arrival data for the period when the infrasound from the explosion was recorded are shown in Figure 29. The horizontal axis shows minutes of time starting at

2300 UT on April 25. At the beginning of the period, the last part of the infrasonic signal generated by the supersonic flight of Concorde is seen from the direction of about 250°. The signal generated by the gas explosion arrives from the direction of about 90°. The geometrical direction from the Luleå station to the location of explosion should be 85.3°. A high resolution distribution of the recorded angle-of-arrival during the time of the event is shown in Figure 30. As seen, the maximum of the distribution is located at 90°. The geometrical direction (GD) is also indicated in Figure 2 by an arrow. It is apparent that the observed directions of arrival significantly deviate from the geometrical direction. The observed signals arrive from directions further south than the geometrical direction. The deviation of the observed angle of arrival is probably due to horizontal gradients in the temperature distribution in the upper atmosphere and due to the structure of the atmospheric wind system. The structure of the distribution indicates that the observed signal may be propagated through at least three different propagation modes experiencing different degrees of lateral deviation.

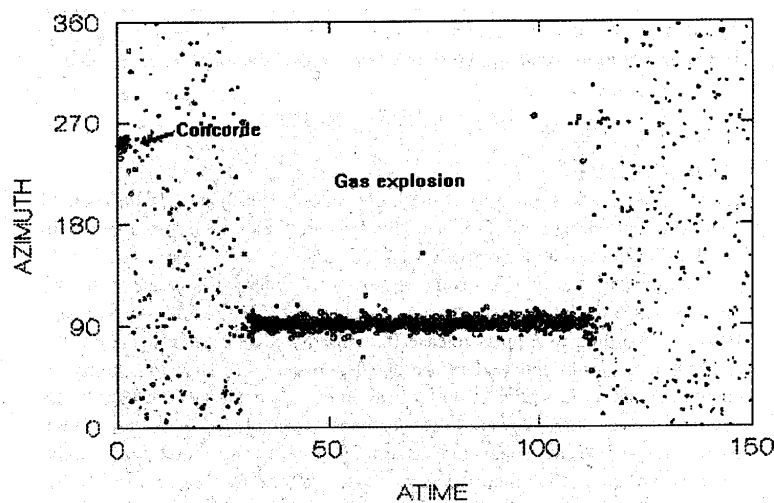


Fig. 29. The angle-of-arrival data for the period when the infrasound from the explosion was recorded. The horizontal axis shows minutes of time starting at 2300 UT on April 25.

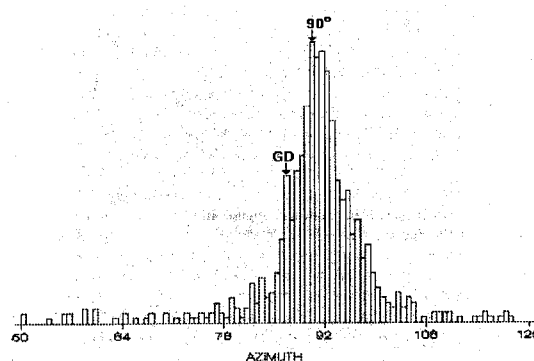


Fig. 30. A high-resolution distribution of the recorded angle-of-arrival of infrasonic signals from the gas explosion.

The propagation of infrasonic waves may be visualized using the ray-tracing technique. The ray-tracing calculations have been made using a modified method of Cowling, Webb

and Yeh (1970) used in earlier investigations (Waldemark and Lyszka, 1991, Lyszka and Waldemark, 1995). In the present study, a winter model of the atmospheric temperature and winds has been used. A cylindrical source, like the present gas flame, is assumed to radiate the mechanical energy mainly close to the horizontal plane. The calculations are thus made for inclination angles of the wave vector of 5 and 10° and for rays leaving the source at azimuths incremented by one degree, see Figure 31. The calculations are made for 02 hours local time at the source.

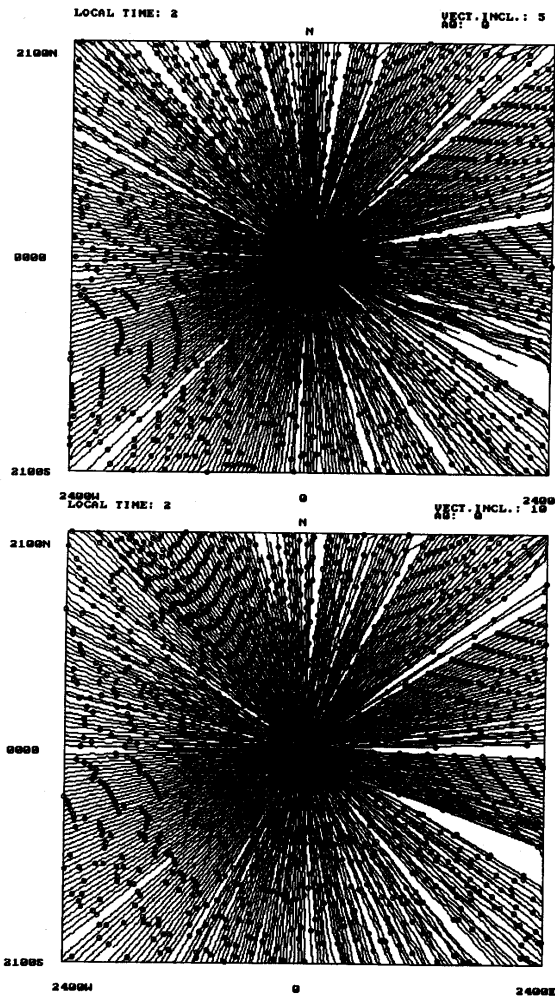


Fig. 31. Results of ray-tracing calculations for inclination of the wave vector of 5° (upper diagram) and 10° (lower diagram). Small circles indicate reflection points in the upper atmosphere.

The diagrams show a projection of rays on the horizontal plane.

As seen in the diagrams of Figure 31, although the propagation pattern towards the West is relatively regular, lateral deviations of rays up to 2° are occurring. In other directions, significantly larger lateral deviations and clustering of rays (Lyszka and Waldemark, 1995) are observed.

It is of interest to follow the amplitude of the infrasonic emission during the event; The relative linear amplitude of the infrasonic emission recorded during the event is shown in Figure 32 as a function of time (minutes of time starting, at 2300 UT). It is plausible to assume that the radiated energy at each instant is proportional to the quantity of the combusted gas. Knowing the total volume of the burned gas, it is possible to estimate the

quantity of combusted gas as a function of time during the event. The result of the estimate is shown in Figure 33.

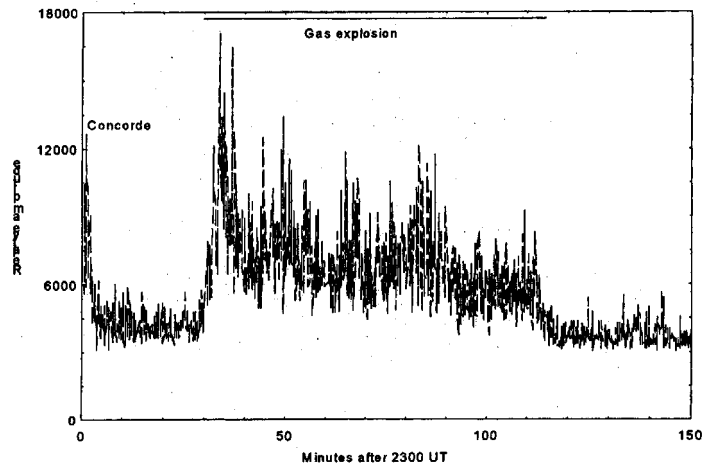


Fig. 32. The relative linear amplitude of the infrasonic emission recorded during the event. At the beginning of the diagram, the final part of the emission from the supersonic flight of Concorde is visible.

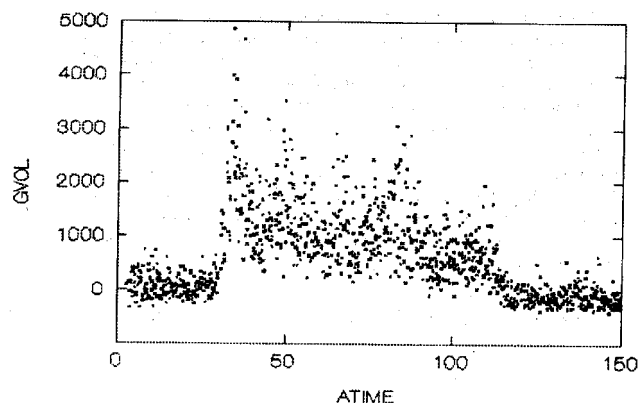


Fig. 33. The estimated quantity of combusted gas (in cubic meters per second) during the event.

It may be concluded that the observations of the infrasound from events like the described one, may be used as a source of important information about the event itself, like duration and time history. The observations also contain important information about the properties of the atmospheric medium between the source and the recording station.

### ***Burning oil fields***

It has been shown in an earlier section that a statistical approach may be applied to detect small meteor impacts. In this section, a slightly different method is applied to detect extremely distant infrasonic sources.

It is obvious that the burning of oil over a limited surface and to such an extent as that in the Persian Gulf will be responsible for the generation of intense infrasonic waves. It has been reported that at the beginning of March 1991 there were 220 000 tons of oil burning per day. Assuming that only 1 % of the combustion energy is converted into infrasonic energy (which is usually considered in connection with turbulent combustion) the entire area may be considered as an infrasonic source with an acoustic power of about  $10^9$  Watts.

Most of the infrasonic waves will propagate through the atmosphere reaching reflection heights in the lower thermosphere (110 - 150 km) and the upper stratosphere (45 - 50 km). Due to large amplitudes of infrasonic waves generated by these fires, it may be expected that non-linear effects like wave amplification with increasing height, and conversion into N-shaped waves will occur at ionospheric altitudes. Ionospheric - heating by these waves should be observed in the near-by area of these oil fires.

### **Propagation of infrasound**

A ray-tracing technique similar to that used by Cowling, Webb and Yeh (1970) has been used to study the propagation of infrasound from burning oil fields. Depending on the angle of incidence of the wave, the direction of propagation and the local time of the observation, typical rays propagating from the Persian Gulf towards Northern Europe have been calculated for winter and summer conditions. The calculations have been made using a mid- latitude wind and temperature model. Rays for every  $2^\circ$  of azimuth between  $331$  and  $31^\circ$  are plotted. The results are shown in Figures 34 - 37. Reflection points in the upper atmosphere are marked on the rays by small circles.

It is apparent from the presented results that:

1. During certain atmospheric conditions the rays are condensed in some directions indicating focusing effects or "channelling".
2. There is no propagation in certain directions. The rays propagating in those directions will be dissipated in the atmosphere unless atmospheric irregularities will change the direction of propagation.
3. During winter at the local noon, there seems to be rather poor propagation conditions from the source towards the North for high wave vector inclinations ( $60^\circ$ ). During summer, this poor propagation condition occurs for some local times at lower inclinations (cf e.g Figure 36 for 00 local time and  $30^\circ$  inclination).

It may be concluded that a considerable variability of the long-distance propagation between the Persian Gulf and Northern Europe may be expected from ray-tracing in a simple atmospheric model.

### **Recording and analysis technique**

A 2 Hz infrasonic station produces an output every 30 seconds telling how many wave periods were recorded from each of possible 36 azimuth intervals ( $10^\circ$  intervals). At the same time, the average trace velocity is calculated for each azimuth interval with non-zero counts of wave periods. In the presence of a coherent signal with a high signal-to-noise ratio coming from a  $10^\circ$  interval of azimuth, there will be a maximum of 60 counts in this azimuth interval. In the presence of noise, the possible 60 counts will usually be distributed into several azimuth intervals.

Due to large amount of atmospheric noise and a low azimuth resolution of infrasonic stations, advanced statistical methods must be used to discover distant infrasonic sources. In the present study, daily averages have been constructed for all 36 azimuth intervals. As the infrasonic waves from the burning oil fields were expected from azimuths around  $140^{\circ}$ , the analysis has been limited to the azimuth interval  $100 - 190^{\circ}$ . The daily data thus form a vector of 10 values.

It is known from the news that the fires started around February 20 and that maximum was reached around February 25. Data from the period before February 15 was thus decided to be used as a reference with no fires present. Data from the period after February 15, two days at a time, shifted one day at a time, was then compared with the reference data. The comparison was made using the multivariate analysis. A brief description of the method with examples is given in an earlier book by the author (Liszka, 2003).

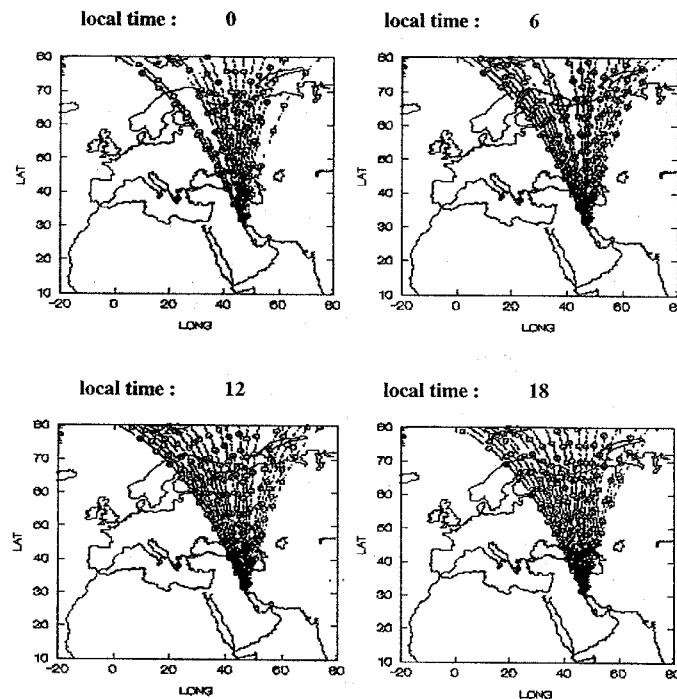


Fig. 34. Ray-tracing during winter conditions for every  $2^{\circ}$  of azimuth between  $331$  and  $31^{\circ}$  and for four different values of local time. The wave vector inclination is  $30^{\circ}$ .

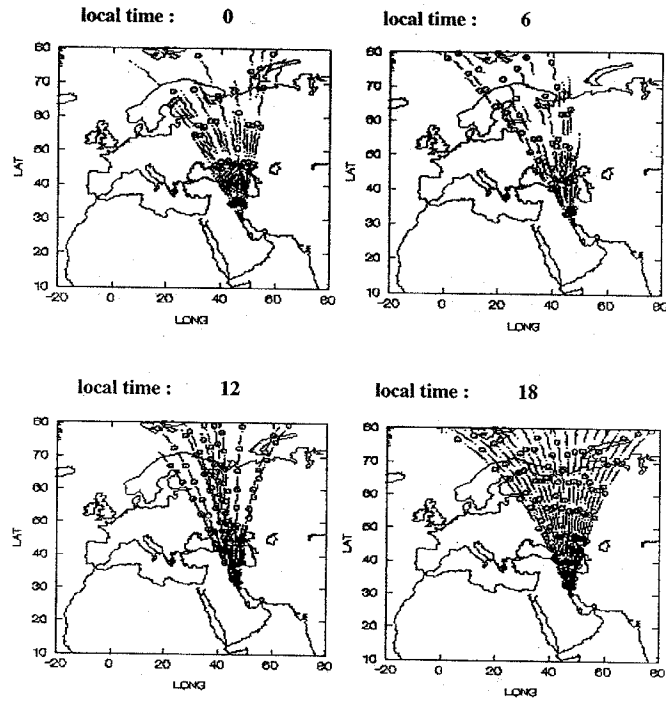


Fig. 35. Ray-tracing during winter conditions for every  $2^\circ$  of azimuth between  $331$  and  $31^\circ$  and for four different values of local time. The wave vector inclination is  $60^\circ$ .

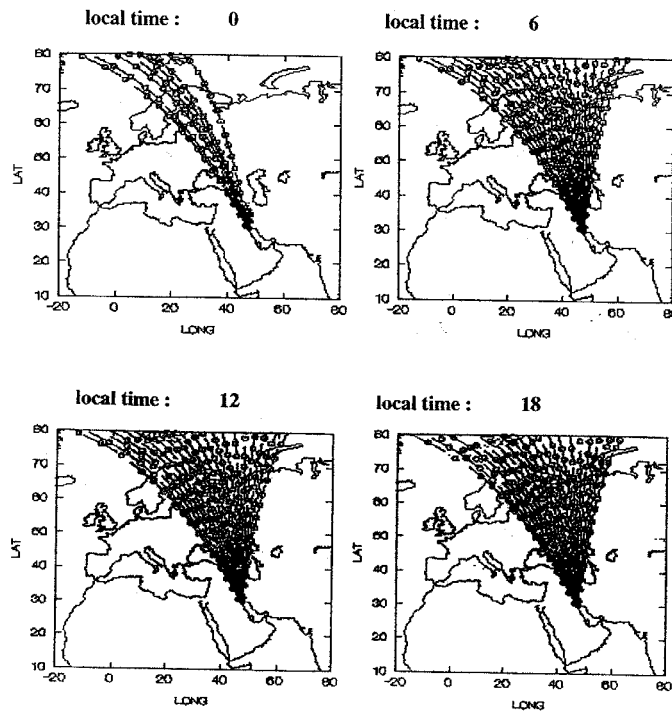


Fig. 36. Ray-tracing during summer conditions for every  $2^\circ$  of azimuth between  $331$  and  $31^\circ$  and for four different values of local time. The wave vector inclination is  $30^\circ$ .

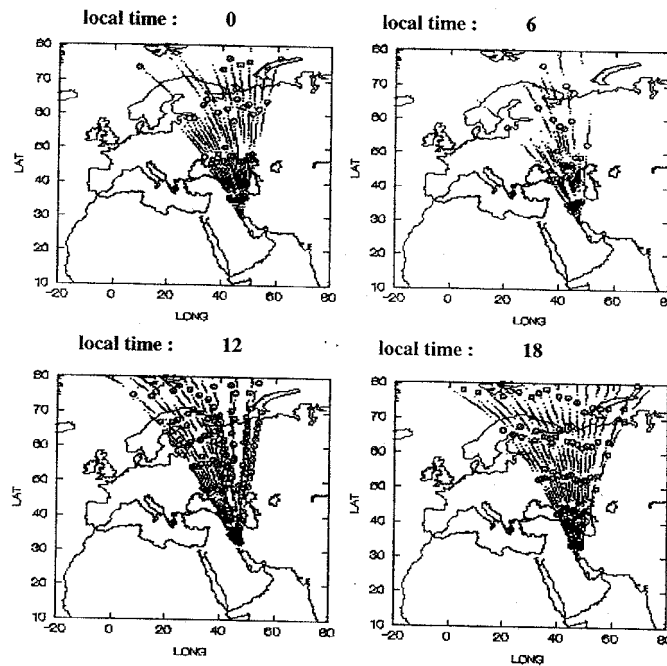


Fig. 37. Ray-tracing during summer conditions for every  $2^\circ$  of azimuth between  $331$  and  $31^\circ$  and for four different values of local time. The wave vector inclination is  $60^\circ$ .

### Results of multivariate analysis

Results of the multivariate analysis of the daily averages within the azimuth interval  $100 - 190^\circ$  show that a distinct one set of infrasonic signals starts on day 15 of the analysis, which corresponds to February 20th 1991. Results of the analysis for both stations showing the distance between the reference data and the test data are given in Figures 38 and 39. The onset of large differences may clearly be seen on the average trace velocities (lower diagram) from both stations. There is a considerable day-to-day variability, which may be explained by fluctuations of atmospheric conditions along the 4000 km long propagation path. During the investigated period, corresponding changes of average counts are not as distinct as of average trace velocities.

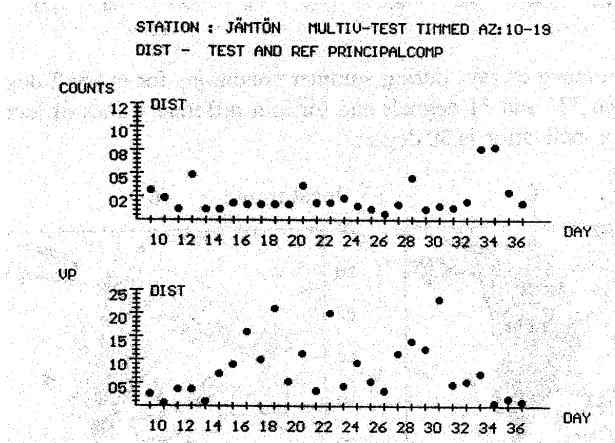


Fig. 38. Distance between reference and test data for Jämtön using a: counts, b: horizontal trace velocity ( $V_p$ ).

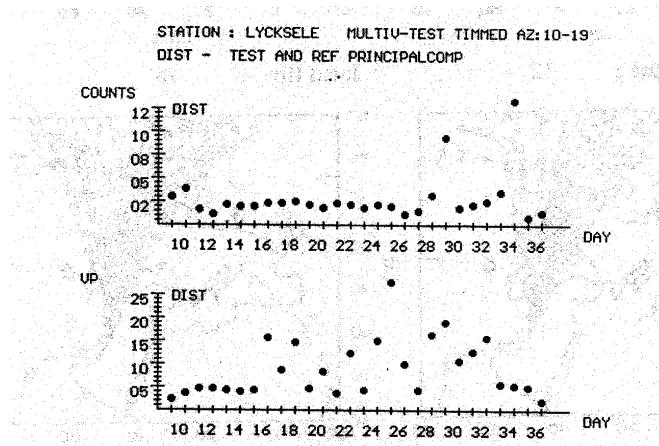


Fig. 39. Distance between reference and test data for Lycksele using a: counts, b: horizontal trace velocity ( $V_p$ ).

Another analysis has been done using the first 14 days as a reference and the next 14 days as the test data. Modeling powers for PC1 and PC2 for azimuth intervals for both stations, and for average counts and trace (phase) velocities are shown in Figures 40 and 41. One can see that the highest modeling powers are obtained for a azimuth around  $140^\circ$ , which is consistent with the geometrical direction to the Persian Gulf from both stations (from Luleå  $144.6^\circ$  and from Lycksele  $138.9^\circ$ ).

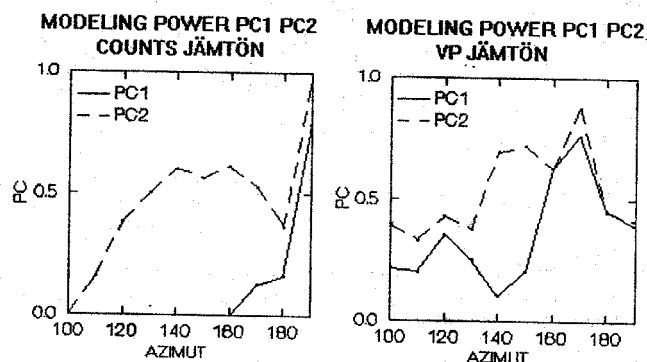


Fig. 40. Modeling power for PC1 and PC2 for azimuth  $100 - 190^\circ$  using average counts and trace velocities from Jämtön.

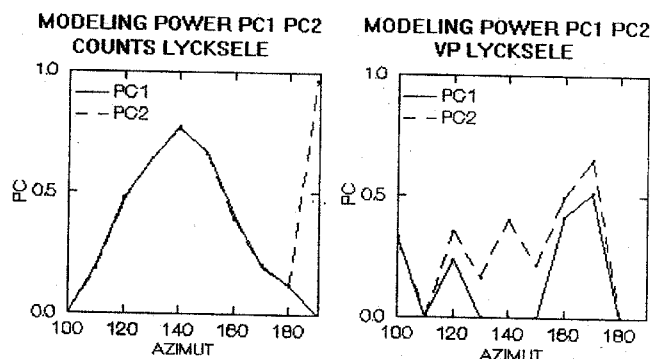


Fig. 41. Modeling power for PC1 and PC2 for azimuth  $100 - 190^\circ$  using average counts and trace velocities from Lycksele.

An attempt to study the long-distance propagation during summer conditions has been made comparing one week of data from June 1990 with one week of data from June 1991. Only Luleå data has been used. The results are shown in Figure 42. Again, a peak of modeling power is observed around 130° azimuth. The peak is very significant on average counts data, but not significant on trace velocity data.

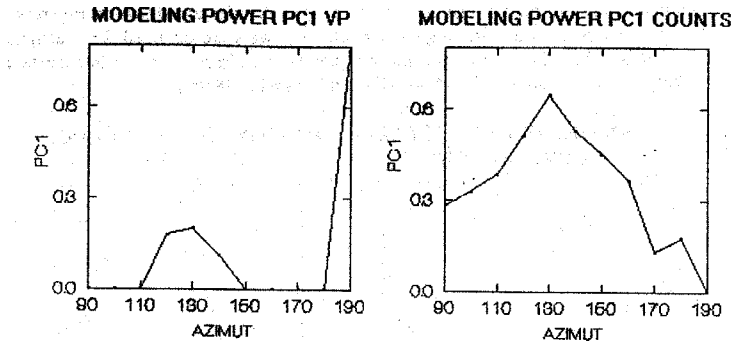


Fig. 42. Modeling power for PC 1 comparing of counts- and phase velocity data from one week of data from June 1990 with one week of data from June 1991. Jämtön data has been used.

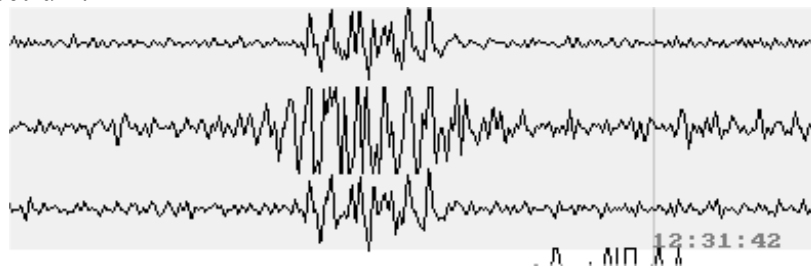
It may be concluded from the above results that the infrasound generated by the burning oil fields in the Persian Gulf was propagating at least 4200 km to Northern Scandinavia and that it could be conclusively detected from there.

### **High Trace Velocity events (HTV)**

Extremely high trace velocity signals ( $V_p > 1000$  m/sec) were over the years discarded, assuming that these signals must be caused by the electromagnetic interference. First, during recent years, the attention of the author was directed towards detection of local, rather small, meteor events visible only at the closest station.

For this purpose, an automated search for high trace velocity events over the five year data-period of 2001-2005 was performed. During year 2000, the infrasonic stations were equipped with 16-bits A/D converters. In order to increase the reliability of possible findings, the search was limited to the period with higher accuracy of A/D conversion.

The search resulted in unexpected results: it appeared that high trace velocity (HTV) signals are very common at Kiruna and Lycksele, but unusual at Jämtön and Uppsala. Up to hundreds of HTV signals per day may occur at Kiruna and Lycksele. A typical example of HTV signal is shown in Fig. 43 together with its wavelet spectrum. One can see that the signal is nearly saw-tooth shaped, reach in harmonics. At its maximum the first harmonics is clearly seen on the wavelet spectrum.



k5110425.bin row=10 mic=1

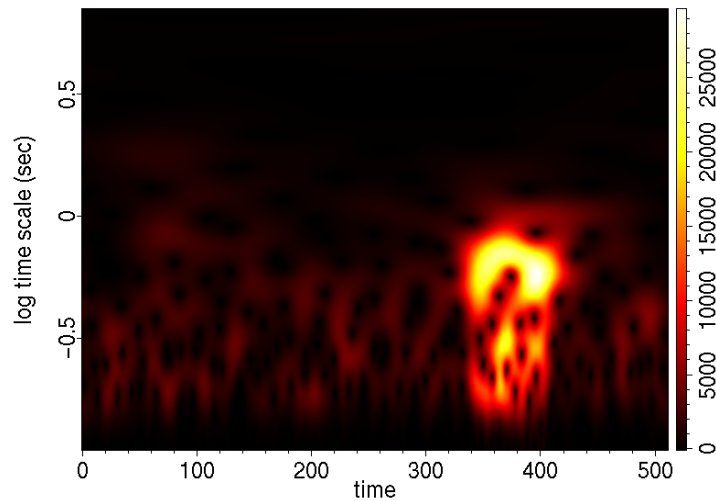


Fig. 43. A typical HTV signal (upper graph) recorded at 3 microphones of Kiruna array. The lower graph shows the wavelet spectrum of the signal from Microphone 3. The time scale axis is logarithmic and the time axis is marked in sample nos. (18Hz sampling rate).

The HTV signals have also other unusual properties. The most surprising property is that they are nearly simultaneous at both stations, 365 km apart! It may be seen in the example of Fig. 44 showing the angle-of-arrival of three different HTV signals occurring between 650 – 653 UT (10:50 – 10:53UT). Two of the signals are practically simultaneous in both arrays; the middle one starts 12 seconds earlier at Kiruna than at Lycksele.

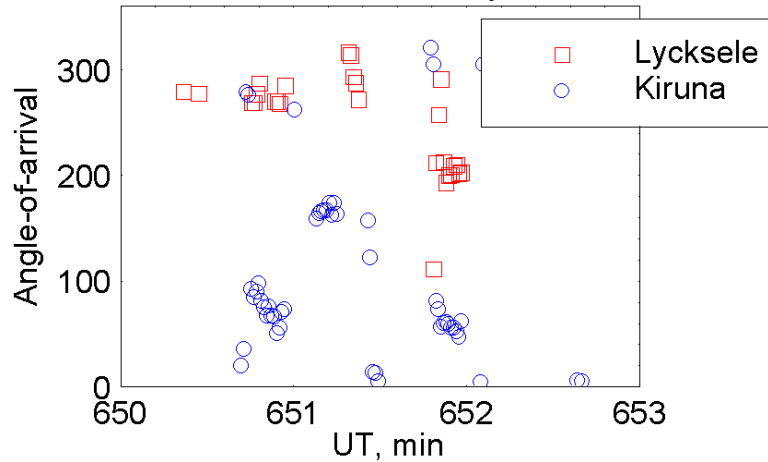


Fig. 44. Angle-of-arrival for three different HTV signals occurring between 650 – 653 UT (10:50 – 10:53UT) recorded at Kiruna and Lycksele.

Corresponding trace velocities are shown in Fig. 45. Trace velocities vary during these three events between 1000 and 20000 m/sec ( $20 - 1^\circ$  zenith distance of the wave normal).

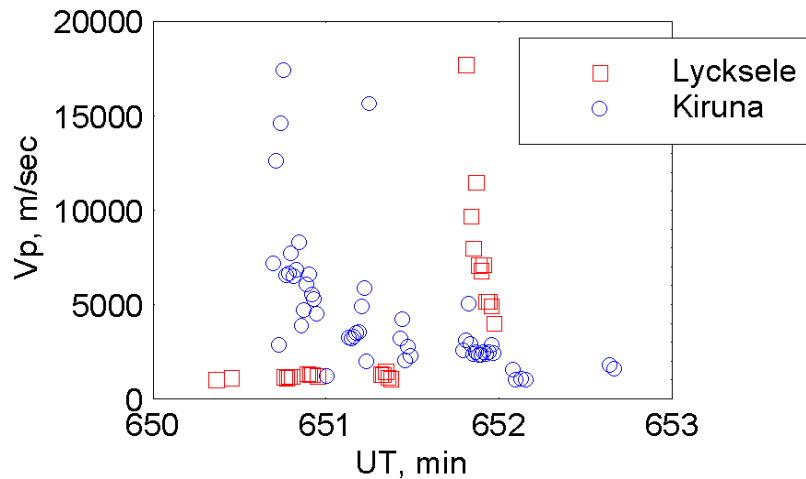


Fig. 45. Trace velocities during three events of Fig. 26.

Since the wave arrives practically from the zenith, it is not meaningful to draw any conclusions from the measured angle-of-arrival.

Properties of the observed HTV signals do not fit into present knowledge about known geophysical phenomena. Some of these signals may be attributed to small, overhead, meteor events, but certainly not those occurring simultaneously over a 365 km distance. The signals cannot be connected to auroral activity, since they are most common during daytime, far from the auroral oval. The cases shown in Figures 44 – 45 occur during a perfectly magnetically quiet period, so they cannot be due to magnetic disturbances.

## References to Chapter 10

Garces, M. A., R. A. Hansen, S. R. McNutt and J. Eichelberger (2000). Application of wave-theoretical seismoacoustic models to the interpretation of explosion and eruption tremor signals radiated by Pavlof volcano, Alaska. *J. Geophys. Res.*, 105, 3039-3058.

Cowling, D.H., Webb, H.D. and Yeh, K.C. (1970). Tech. Rep. 38, Ionosphere Radio Laboratory, University of Illinois.

Liszka, L. and K. Waldemark: High resolution observations of infrasound generated by the supersonic flight of Concorde. *J.Low Freq. Sound. Vib.* 14, No. 4, 1995.

Liszka, L.: Infrasound observations of the gas explosion on April 26-27, 1995.. *J.Low Freq. Sound. Vib.* 15, No. 1, 1996.

Liszka, L.: Infrasound from the North Sea Bolide, 2001-10-27. Paper presented at CTBT Infrasound Workshop 2001, Kailua-Kona, Hawaii.

Liszka, L. and Garces, M.: Infrasound Observations of Hekla Eruption on February 26, 2000. *J.Low Freq. Sound. Vib.* 21, No. 1, 2002.

Liszka, L.: Statistical detection of meteor showers using data from the Swedish infrasound network. Paper presented at the CTBTO Infrasound Workshop, 2003, San Diego.

Liszka, L.: On the Possible Infrasound Generation by Sprites. Paper presented at the AGU Fall Meeting, 2003, San Francisco.

Waldemark, K. and Liszka, L. (1991). *Journ. Low. Fr. Noise & Vibr.*, Vol. 10, No. 4, 123.

Waldemark, K. (1994). High Resolution Infrasonic Recording Equipment, Scientific Rep., Swedish Institute of Space Physics.

Franz, R. C., R. J. Nemzek, R. J. Winckler, Television image of a large upward electrical discharge above a thunderstorm system, *Science*, 249, 48-51, 1990.

Farges, T., A. Le Pichon and E. Blanc, Infrasonic signature of thunder, *Geophysical Research Abstracts*, Vol. 6, 02542, 2004.

Lyons, W. A., Characteristics of luminous structures in the stratosphere above thunderstorms as imaged by low-light video, *Geophys. Res. Lett.*, 21, 875-878, 1994.

Mende, S. B., G. R. Swenson, S. P. Geller, R. A. Viereck, E. Murad, and C. P. Pike, Limb view spectrum of the earth airglow, *J. Geophys. Res.*, 98, 117-19, 125, 1993.

Sentman, D. D., E. M. Wescott, D. L. Osborne, D. L. Hampton and M. J. Heavner, Preliminary results from the sprites 94 aircraft campaign: 1. Red sprites, *Geophys. Res. Lett.*, 22, 1205-1208, 1995.

Sentman, D. D., E. Wescott, Observations of upper atmospheric optical flashes recorded from an aircraft, *Geophys. Res. Lett.*, 20, 2857, 1993.

Wescott, E. M., D. Sentman, D. Osborne, D. Hampton and M. Heavner, Preliminary results from the sprites 94 aircraft campaign: 2. Blue jets, *Geophys. Res. Lett.*, 22, 1209-1212, 1995.

Winckler, J. R., R. C. Franz, R. J. Nemzek, Fast low-level light pulses from the night sky observed with the SKYFLASH program, *J. Geophys. Res.*, 98, 8775, 1993.

## Chapter 11

### Statistical Properties of the Infrasonic Wave Field on the Ground

During the end of the 1950's and the beginning of the 1960's, the foundations for satellite communication and the global positioning system were created through a worldwide study of the statistical properties of radio wave propagation. Numerous projects were aimed at the study of the statistical structure of the wave field at the receiving antenna. That information was necessary to allow appropriate design of the receiving systems, which would take into account the specific properties of the signal.

Since the propagation of infrasound in the atmosphere seems to be more similar to radio wave propagation in the ionosphere (Davies, 1973) than to the propagation of seismic waves in the solid earth, it was natural for the author to apply principles of the statistical quantization of radio wave pattern to infrasonic wavefields.

In order to properly address the problem of infrasonic detection, the statistical properties of the infrasonic wave field on the ground, and in particular of its anisometry, must be carefully investigated. The statistical properties of the infrasound field on the ground are variable in different directions, which is reflected in the fact that the cross-correlation in the wave field is direction dependent. These properties of infrasound wave field are of great importance in areas like signature recognition and spatial filtering.

#### ***Anisometry of the cross-correlation***

The cross-correlation between microphones in an infrasonic array drops after a certain distance, even in a direction perpendicular to the propagation direction. This suggests that we are not observing plane waves.

In general, the cross-correlation varies both in the horizontal plane ( $x, y$ ) and time ( $t$ ). The problem may be described by three ellipses: in the  $xt$ ,  $yt$  and  $xy$  planes. When measuring the cross-correlation between two microphones in  $x$ -direction, the cross-correlation drops to a certain value at a distance  $x$ . Since the wave field changes also in time due to interaction with varying atmospheric structures, the wave field will be a function of both space coordinates and time. In general, in the  $xt$ -plane (see Fig. 1) we are considering  $Q$  as the maximum cross-correlation. The apparent velocity,  $V'$ , with which the wave pattern on the ground changes, will be:

$$V' = x'/t'$$

The true change velocity,  $V$ , will be instead:

$$V = x_m/t_m$$

### Correlation ellipse in xt-plane

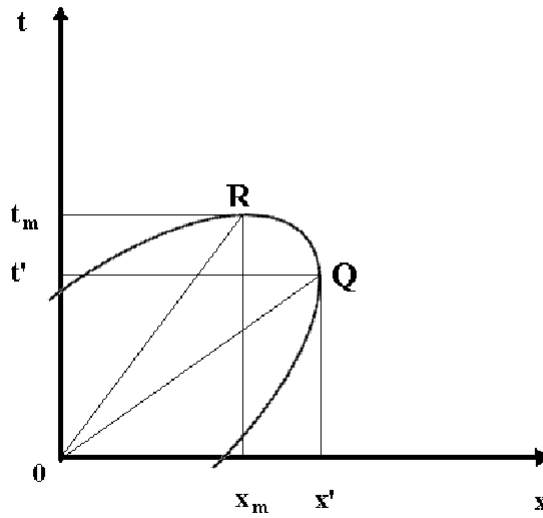


Fig. 1. Correlation ellipse in xt-plane.

In practice, we have to consider all three correlation ellipses at the same time and to determine parameters of the 3-D correlation surface:

$$\rho = \rho(x,y,t).$$

It will be assumed that the surface may be approximated by the ellipsoid:

$$ax^2 + 2hxy + by^2 + 2fxt + 2gyt + ct^2 = D$$

The ellipsoid parameters may be determined from a 3-microphone array when autocorrelations at all microphones and maximum cross-correlations between all three microphone pairs are determined. The numerical procedure, which has been used to describe the correlation pattern of radio waves on the ground, may be found in the literature (cf. e. g. Koster et al., 1966).

The correlation ellipse on the ground at a given time (in the xy-plane) will, in general, be rotated by an angle  $\psi$  (with the local North direction). For plane waves, that angle will differ from the angle-of-arrival of the wave by  $90^\circ$ .

The ellipsoid must be rotated along the t-axis by that angle in order to obtain useful ellipsoid parameters. Here, the following parameters are used to describe the correlation pattern on the ground:

1. Axial ratio :  $\sqrt{(b/a)}$
2. Size of the minor axis of the ellipse, calculated to the distance where the cross-correlation drops to  $1/e$ :  $\sqrt{(\ln(1/e)/b * (\ln \rho_{ii}(x_1)))}$   
where  $\rho_{ii}(x_1)$  is the value of the autocorrelation function corresponding to one sampling period.
3. Eccentricity:  $\sqrt{(1 - (b/a))}$

The above parameters have been used to illustrate the properties of the correlation pattern on the ground for different types of infrasonic sources. Examples of typical infrasonic signals, presented in this study show temporal variations of:

1. Angle-of-arrival
2. Axial ratio
3. Size of the minor axis

The eccentricity, as containing the same information as parameters 2 and 3, is not used here.

## Examples

### Concorde

The example shows infrasound generated during a typical flight and recorded in Northern Sweden.

Concorde 950207 2330-0030 UT

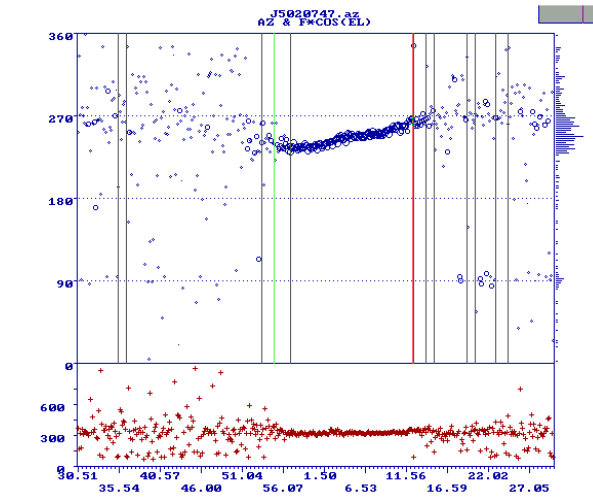


Fig. 2. The angle-of-arrival (upper graph) and the trace velocity (lower graph) for Concorde signals recorded in Northern Sweden on 1995-02-07.

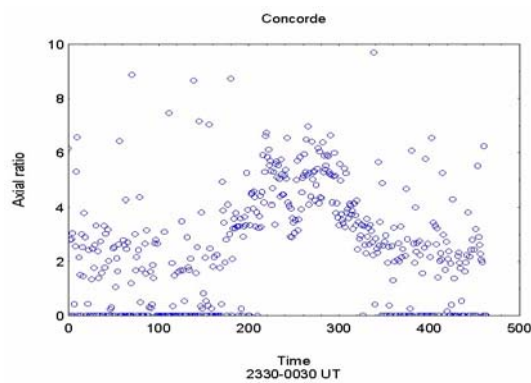


Fig. 3. Variation of the axial ratio for the Concorde signals in Fig. 2.

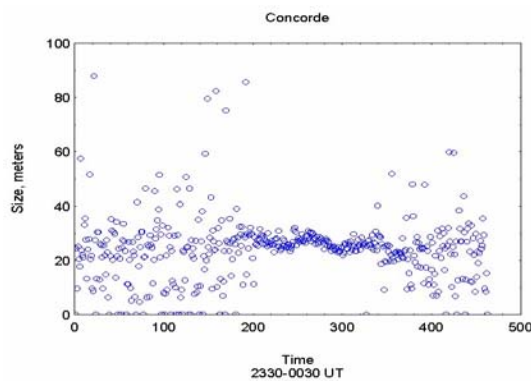


Fig. 4. The size of the minor axis of the correlation ellipse for Concorde signals in Fig. 2.

### Small supersonic jets at distances of 400 - 500 km

The infrasound from small supersonic jets was recorded at Jämtön station in Northern Sweden on 1995-10-23. The jets are flying towards the North at distances of 400 – 500 km.

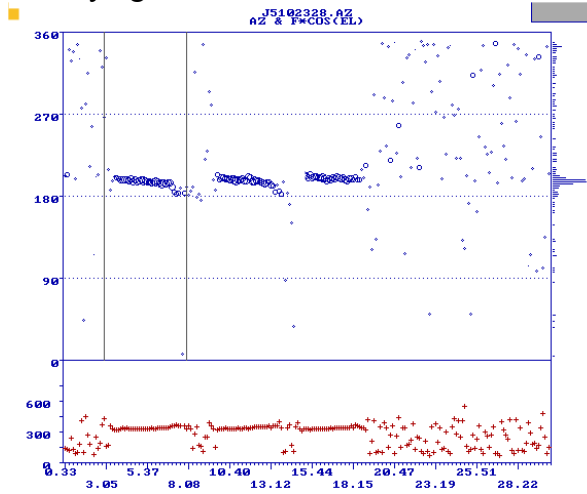


Fig. 5. The angle-of-arrival (upper graph) and the trace velocity (lower graph) for three small supersonic jets recorded in Northern Sweden on 1995-10-23.

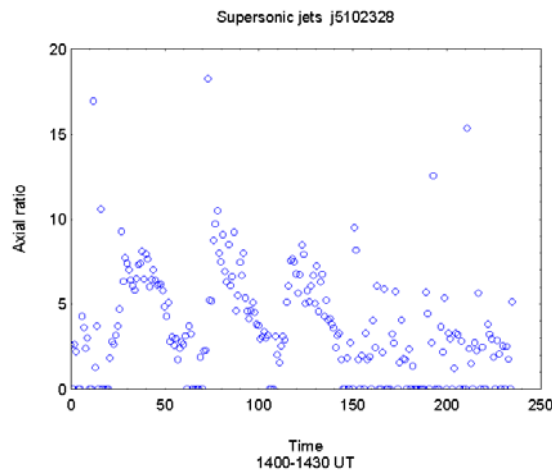


Fig. 6. Variation of the axial ratio for infrasonic signals shown in Fig. 5.

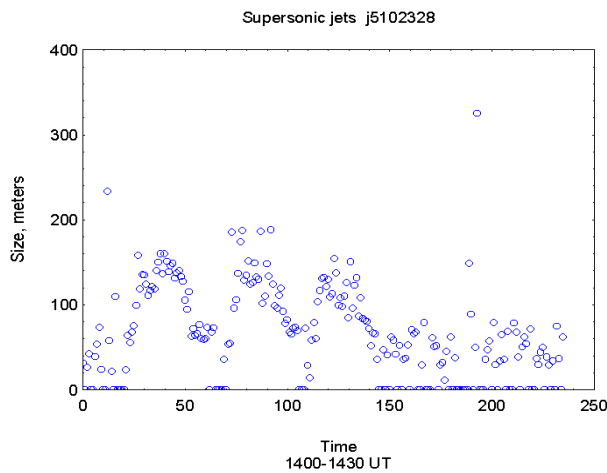


Fig. 7. The size of the minor axis of the correlation ellipse for signals in Fig. 5.

**A large gas explosion on April 24, 1995, distance 1400 km**

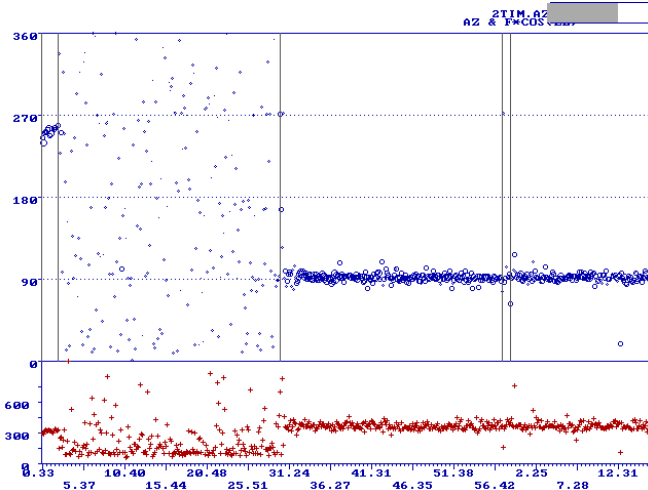


Fig. 8. The beginning of an infrasound recording from a large gas explosion. The upper graph shows the angle-of-arrival, the lower graph shows the trace velocity. A Concorde signal is visible at the beginning of the recording.

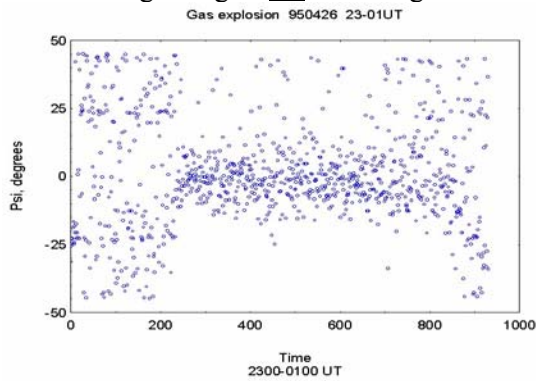


Fig. 9. The difference between the direction of the minor axis of the correlation ellipse on the ground and the angle-of-arrival of the signal in Fig. 8.

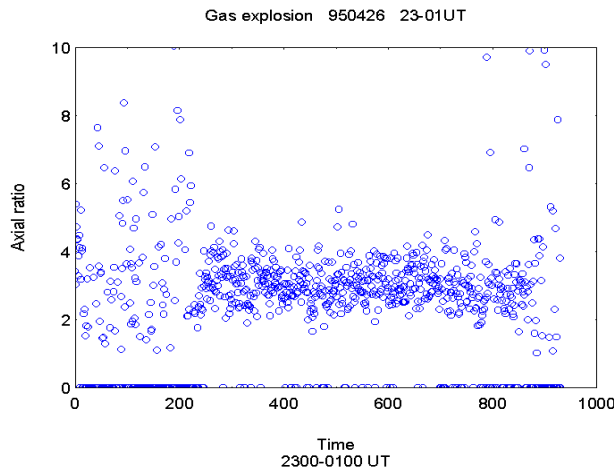


Fig. 10 Variations of the axial ratio of the correlation ellipse of infrasound from the gas explosion on 1995-04-26

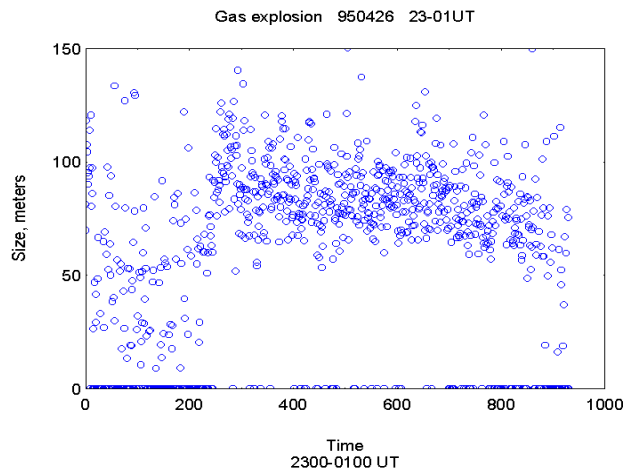


Fig. 11. The size of the minor axis of the correlation ellipse for signals in Fig. 8.

**A local storm passing by the microphone array - minimum distance 10 km**

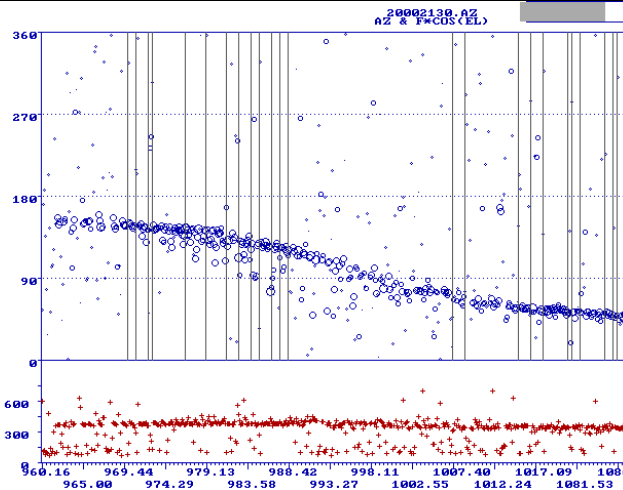


Fig. 12. Infrasound from a nearby storm cell passing Jämtön recording station with a closest distance of about 10 km. The upper graph shows the angle-of-arrival, the lower graph shows the trace velocity.

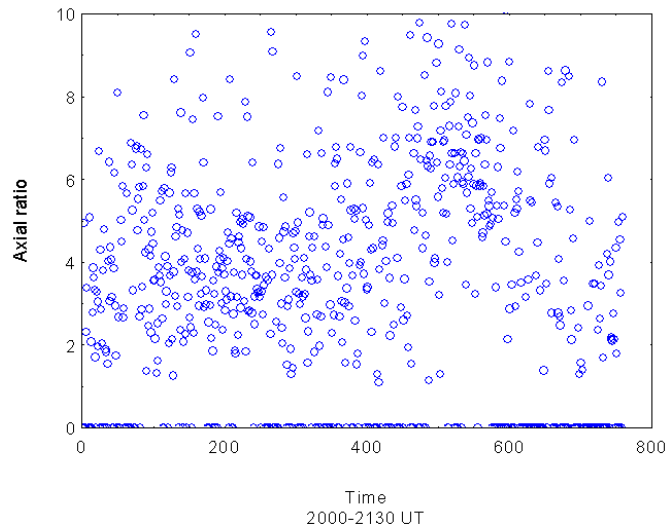


Fig. 13. Variations of the axial ratio of the correlation ellipse for the infrasound from a close storm cell.

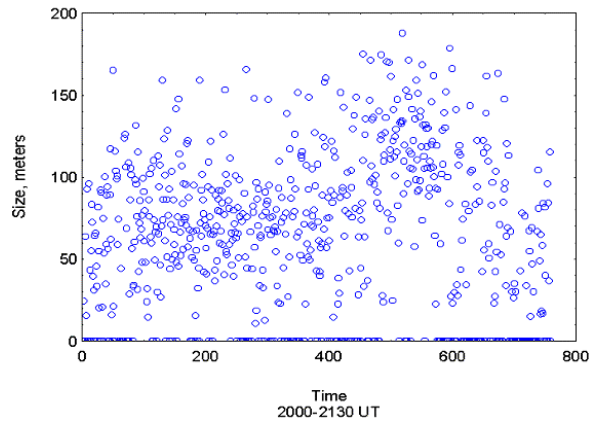


Fig. 14. The size of the minor axis of the correlation ellipse for signals in Fig. 12.

**The anisometry of the cross-correlation on the ground and its consequences for signal detection**

To measure the instantaneous intensity pattern on the ground would be very difficult and expensive. However, when the cross-correlation function over the ground is known, it is possible to simulate an intensity field, which would have an identical cross-correlation function (Wernik, 2002) as the one measured. Assuming a typical low-frequency signal with the axial ratio of 5, the minor axis of the ellipse of the order of 100 meters, the  $1/f$  noise spectrum and the direction-of-arrival of  $60^\circ$ , the intensity field on the ground may be simulated. The result of a simulation for an area of 1024 x 1024 meters is shown in Fig. 15.

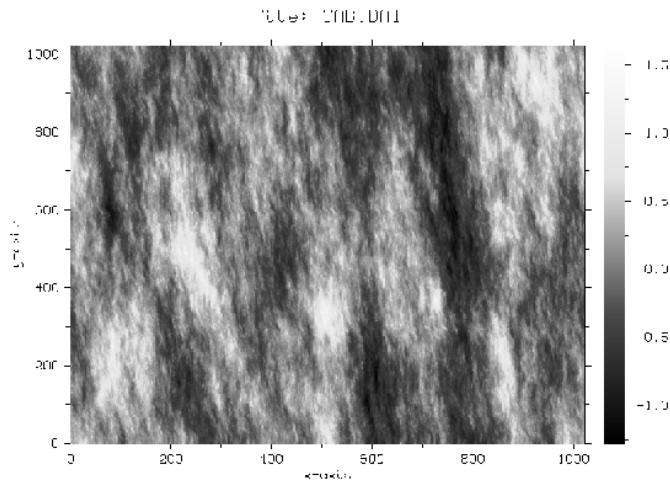


Fig. 15. A simulated intensity pattern on the ground calculated assuming a typical low frequency signal with the axial ratio of 5, the minor axis of the ellipse of the order of 100 meters, the  $1/f$  noise spectrum and the direction-of-arrival of  $60^\circ$ . The pattern covers an area of 1024 x 1024 meters.

The simulated wave pattern is very far from the classical picture of a wave field with clear crests and valleys. In such an idealized case the cross-correlation along the wavefront should not change – in reality the cross-correlation along the wavefront drops to  $1/e$  already after the length of the major axis of the correlation ellipse.

The signal recorded at a microphone may be reproduced from the graph in Fig. 15 by moving the microphone from the initial position ( $x=0, y=300$ ) in the direction of the angle-of-arrival with a speed corresponding to the trace velocity of 300 m/sec. The resulting amplitude and the corresponding wavelet spectrum are shown in Fig. 16.

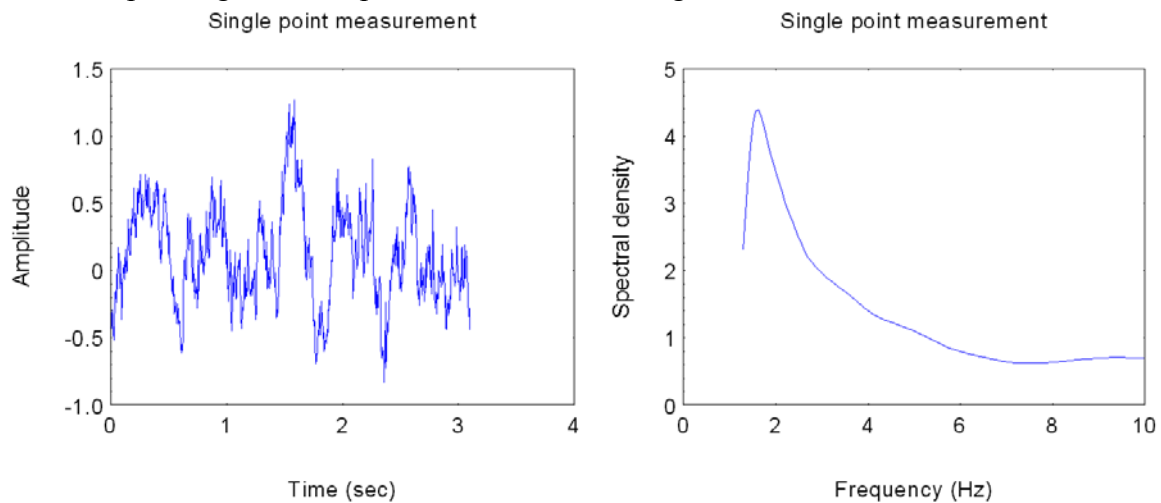


Fig. 16 Amplitude recording from a single point microphone moving across the intensity field in Fig. 15 (left graph) and the corresponding frequency spectrum (right graph).

The parameters of the correlation ellipse on the ground seem to be related to the spectral content of the signal and thus to the nature of the source. Since, during the long distance propagation, the atmospheric irregularities will influence the statistical properties of the signal, the properties of the correlation ellipse will also be related to the distance to the source. The statistical properties of the signal provide important information necessary for appropriate design of the detecting systems.

## ***References to Chapter 11***

Davies, K: Some analogies between the propagation of ionospheric radio waves and acoustic-gravity waves. In: *Effects of Atmospheric Acoustic-Gravity Waves on Electromagnetic Wave Propagation*. AGARD, 1972.

Koster, J. R., Katsriku, J. and Tete M.: *Studies of Equatorial Ionosphere Using Transmissions From Active Satellites*. Summary Report AF 61 (052) – 800.

## Chapter 12

### Detection of Low-Flying Helicopters

Already during the early stage of the infrasound project, a lot of attention was paid to the infrasonic noise generated by helicopters. Helicopters were found to generate distinct traces on infrasound recordings. It was the main reason why the author became involved both in numerous field studies of helicopter detection with infrasound and in development of practically usable detection systems.

One of the most interesting sources of the infrasound is the helicopter rotor. The primary type of noise is the impulsive noise from the main rotor, which consists of Blade-Vortex Interaction (or BVI) noise in descent or level flight at low and medium velocities, and High-Speed Impulsive (or HSI) noise related to transsonic effects on the advancing blade.

The first kind of noise, identified as the interaction of the blade with the vortices shed by the preceding blade(s), is regarded as the sound directly attributable to the steady and fluctuating lift and drag forces acting on the rotor. It has a frequency spectrum consisting of a number of very narrow peaks occurring at integral multiples of the blade passage frequency. For a majority of helicopter types, the fundamental frequency of the rotational noise is within the infrasonic range. The blade-passage frequency may be easily calculated knowing the rotation rate of the main rotor and the number of blades. It must be remembered that for a flying helicopter, the fundamental infrasonic signal will be modified by the Doppler effect, depending on the speed of the helicopter with respect to the observer. Usually, the acoustical power of the helicopter rotor is of the order of 100 Watts.

The fundamental strength of a helicopter is that it can fly at extremely low altitudes with low, and highly variable speed. It can follow the terrain obstacles, staying easily below the radar horizon (see Fig. 1).

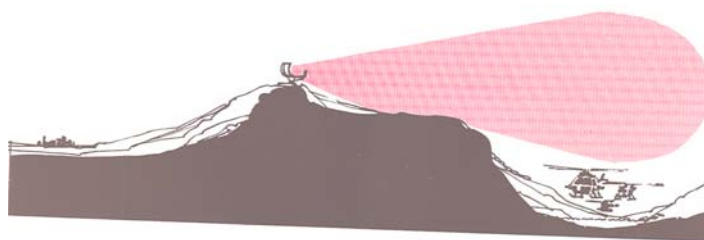


Fig. 1. A helicopter hiding below the radar horizon.

The infrasound generation by the helicopter rotor offers thus a valuable possibility of detection of low-flying helicopters. The acoustical power of the helicopter rotor is not high enough to reach the upper atmosphere and to allow that the long distance propagation takes place. The ground inversion thus will be the main factor determining the infrasound propagation from a helicopter. During the nighttime, with a distinct inversion layer and a helicopter below it, there will be a case of cylindrical propagation with only a 3 dB loss at doubled distance from the source. During the absence of the inversion layer there will be a case of spherical propagation with a 6 dB loss at doubled distance. The detection range will thus be longer during the night than during the day.

A large number of experiments and tests have shown that for a medium-size helicopter, the detection distance, for an approaching helicopter, is about 30 km, while for a departing helicopter the distance is somewhat shorter, typically 20 km. The flight altitude has some effect on the detection range: **the lower altitude increases the probability of detection**, which is opposite than for the radar detection! Portable wind screens to shelter the microphones have been developed. A microphone shelter during a field test is shown in Fig. 2.



Fig. 2. A portable microphone shelter during a field test (photo L. Liszka).

An example of test results is shown in Fig. 3.

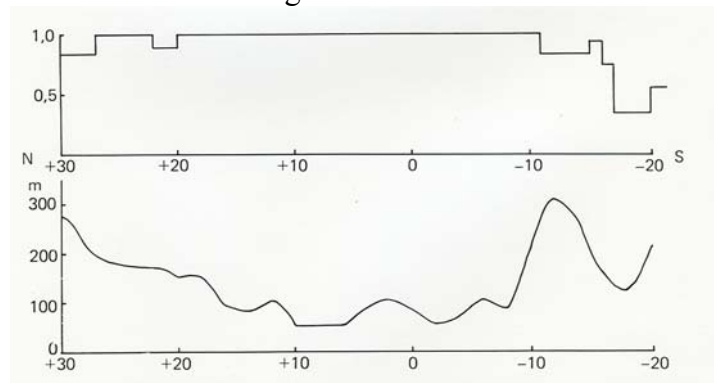


Fig. 3. Probability of detection (upper graph) of Augusta-Bell 204B approaching observer (at 0) along a straight line together with the average flight profile (lower graph).

In the beginning of 1970's a unique infrasound microphone was developed by K. Lidström in Sweden. This microphone, mentioned in an earlier chapter, was later on used in all arrays of the SIN. The frequency response of the microphone could be easily moved towards higher frequencies, making it suitable for helicopter detection. A helicopter detection system has also been developed by K. Lidström and a Swedish company, Betula Development AB, was marketing the system for several years.

Also a version of the system placed on armoured vehicles was tested. In that version, two vibration-insulated microphones were mounted on the body of the vehicle (see example of

Fig. 4). In spite of the intense engine noise and vibration, a coherent signal from a small helicopter could be detected at a distance of 5 km.

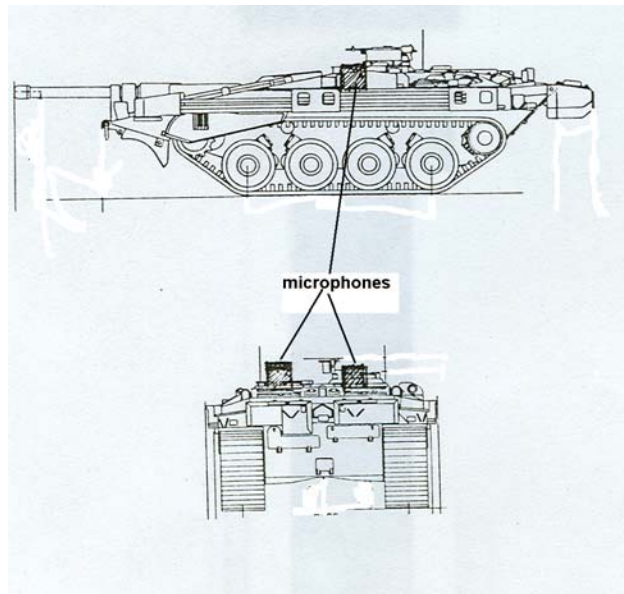


Fig. 4. The location of infrasound microphones on a tank.

When the system was under development for more than 15 years ago, the influence of the wind noise on the detection range was considered as its largest drawback. On the other hand, it must be remembered that the infrasonic detection system is completely passive, in contrary to, for example, radar systems. It is very likely that the infrasonic detection technique could be again interesting if better wind-noise-reduction methods would be developed. Changes in the measuring strategy and improvements in the signal-processing technique would probably also be required.

## Chapter 13

### Infrasound as an Environmental Factor – Effects on Humans

The discovery of long-distance propagation of infrasound from man-made sources discussed in Chapter 5 indicated existence of environments with very high intensities of infrasound. It was clear at the early stage of these studies that very high infrasound intensities may occur, during certain conditions such as in underground hydroelectric power plants.

Also, close to large industrial installations (fans, furnaces in steel factories, compressors, gas- and steam turbines) high infrasound levels were recorded. In the middle of 1970's, there was a serious concern about how environments with high infrasound levels influence humans working there.

A particular application of a gas turbine is a jet engine. In a small military aircraft, the pilot is located very close to a powerful jet engine. A question has been raised about how the high infrasound levels in a jet fighter's cockpit influence the pilot's performance.

In 1975, the author had an opportunity to organize, at the newly opened Umeå Branch of the National Board of Occupational Health, a laboratory for studies of human responses to environmental factors like low frequency noise, infrasound and vibration. The Swedish Air Force was at that time clearly interested in the problem. The senior flight surgeon at the Air Force central command, Dr Hans Hjort, became the contact person at the Air Force. A number of in-flight measurements showed that during a typical flight mission, the infrasound level in the cockpit oscillates around 120 dB(lin), (Fig 1).

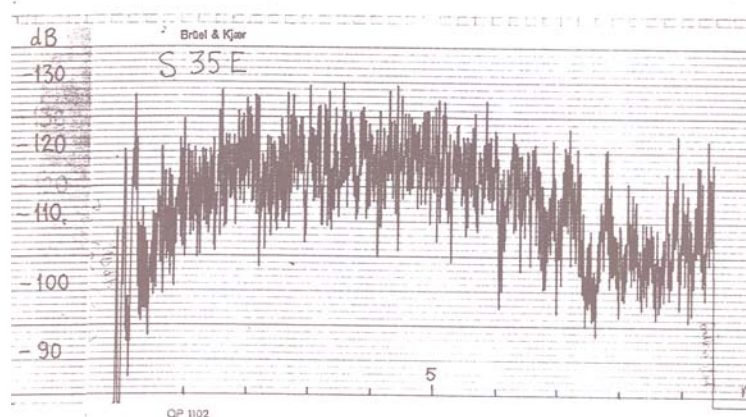


Fig. 1. A part of an original recording of the sound pressure level in dB(lin) measured during the first 9 minutes after take-off onboard the SAAB 35 Draken aircraft.

Early experiments (Tempest, 1976), where the effects of infrasound on humans were studied, were performed using heavy earphones, and very high exposure levels (150 dB(lin)). It became obvious that realistic experimental conditions must include the whole-body exposure and infrasound levels occurring in the cockpit. In order to better understand the specific problems of the flight environment, the author was invited to participate in regular training flights onboard a twin-seat trainer jet (Fig. 2).



Fig. 2. The author before a training mission with a twin-seat version of SAAB 35 Draken supersonic aircraft (photo L. Liszka).

The first step of the study was to design an exposure chamber which would facilitate at least 120 dB(lin) whole-body exposure under acceptable conditions.

### ***The exposure chamber***

The chamber is shown in Fig. 3. Its inner dimensions are 1,2 x 1,6 x 2,0 m. The sound pressure was generated by two groups of loudspeakers, each consisting of four 50 W loudspeakers. The total area of the loudspeakers was 0,053 m<sup>2</sup>, which at a membrane displacement of 5 mm in the chamber's volume of 3,84 m<sup>3</sup>, generated a pressure change of 9,66 N/m<sup>2</sup>, which corresponds to a rms sound pressure level of 111 dB re 20 μN/m<sup>2</sup>.

The sound pressure was amplified in the chamber through resonance. The chamber was equipped with a cylindrical resonator neck, forming a Helmholtz resonator. The resonance frequency  $f_0$  of a Helmholtz resonator may be calculated as:

$$f_0 = c/2 \sqrt{(S/l'V)}$$



Fig. 3. The chamber used for infrasound exposures (photo L. Liszka).

where  $c$  is the speed of sound,  $S$  is the cross-section area of the resonator's neck,  $V$  is the resonator's volume and  $l'$  is the equivalent length of the neck:

$$l' = l + \Delta l$$

where  $l$  is the geometrical length of the neck and

$$\Delta l = 0.85 a$$

where  $a$  is the radius of the circular neck. The above expression is valid for a neck terminated with a broad flange. For a neck without a flange:

$$\Delta l = 0.6 a.$$

The neck in the present chamber is without a flange.

The quality factor of the resonator,  $Q$ , may be calculated as:

$$Q = 2\sqrt{(l'^3/S^3)}$$

And the amplification of the sound pressure level in the resonator will be:

$$n_0 \text{ (dB)} = 20 \log Q.$$

Varying the diameter of the neck and its length, the chamber could be used at frequencies between 5 and 30 Hz with satisfactory sound pressure levels.

Sound pressure levels up to 135 dB(lin) could be reached in the chamber. The chamber was air-conditioned to keep a constant temperature during experiments. Terminals for connection of equipment for physiological measurements were installed in the chamber. The chamber was also equipped with instruments for psychological tests.

### ***Experimental design***

The first experiment, based on a whole-body exposure and carried out in 1975 consisted of a 30-minute pre-exposure period for reference measurements, followed by a 2 hour exposure. Test subjects were 40 active pilots from the Air Force. All of the subjects were divided into 3 groups:

1. control group exposed only for weak low frequency noise;
2. group exposed to 14 Hz, 120 dB(lin) infrasound;
3. group exposed to 16 Hz, 120 dB(lin) infrasound.

The following measurements were performed before and during the exposure:

- Audiometry (to measure the temporary hearing threshold shift, TTS)
- Blood pressure
- Heart rate
- EEG
- ECG
- Nystagmography
- Respiration
- Rheography
- Reaction time
- Time perception
- Pattern recognition
- Error detection

The subjects were also asked to complete an attitude study form designed to measure the subjective perception of the exposure. Dr. Ing-Marie Lidström was responsible for design and interpretation of physiological measurements.

### ***Results of the experiment***

The complete description of the experiment and its results may be found in the report by Lidström et al. (1978). Only the most important results will be summarized here. It was found that a number of significant changes in somatic and psychosomatic functions occurred in the exposed groups when compared to the control group.

These effects, although they can not be categorized as directly harmful, may have a negative influence on the individuals performance, especially in very demanding environments. For example, the effect on the blood pressure, which in the exposed groups showed a significant decrease in pulse amplitude (Fig. 4).

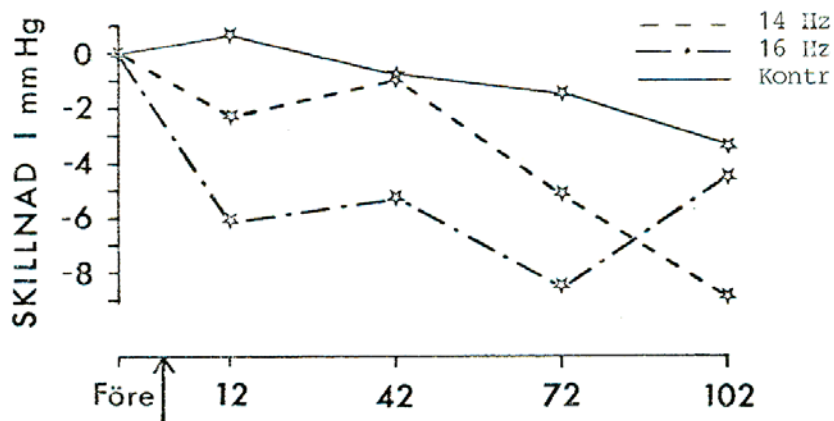


Fig. 4. The pulse amplitude in the exposed groups (14 and 16 Hz) as compared to the unexposed control group. The x-axis shows the elapsed time in minutes.

The effect was especially obvious during the 16 Hz exposure. It may be possible that a decrease in pulse amplitude could result in decreased blood supply to vital organs. The results from the EEG measurements indicate a decreased vigilance among the infrasound-exposed subjects. This finding is also supported by the attitude questionnaire. Also, measurements of the reaction time indicate its increase by approximately 10%, which may be important in certain critical situations.

Any dizziness had not been detected among the infrasound-exposed subjects. However a temporary hearing threshold shift was observed up to 1000 Hz among the infrasound-exposed subjects, especially those exposed to 16 Hz, (Fig. 5). The threshold shift disappeared within 30 minutes after the end of the exposure.

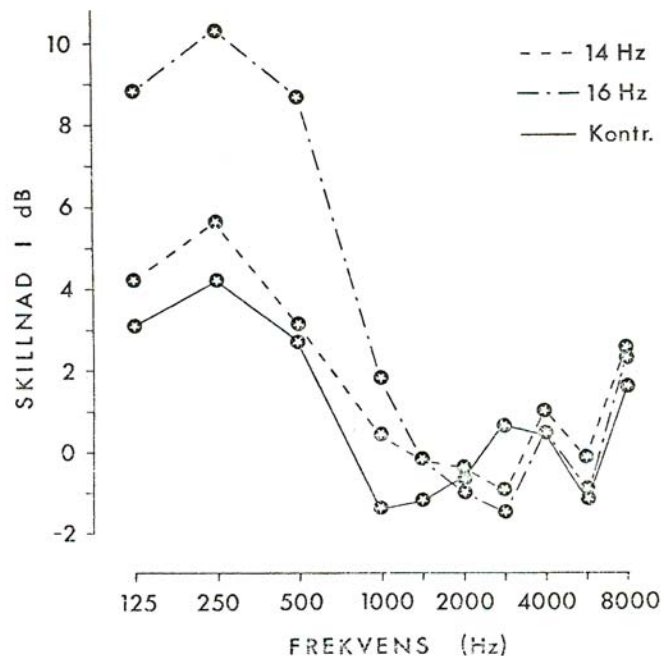


Fig. 5. The temporary shift of the hearing threshold (TTS) for all three groups.

The results of this first whole-body exposure for infrasound indicated certain objective physiological effects. There was, of course, a question of whether the group participating in the experiment could be representative for the average population due to the extreme selection of individuals accepted for military pilot training.

Therefore, another question, more difficult to answer, is how the average population responds to infrasound with lower levels (up to 90 dB(lin)), which often occur in the human environment. For many years there after, this became one of the research goals of the Umeå group of the Swedish National Board of Occupational Health. A review of that work may be found in Landström (1995, 2001).

### ***References to Chapter 13***

Landström, U. Human exposure to infrasound. 1995 In: P.N. Cheremisinoff. Encyclopedia of Environmental Control Technology. Houston Gulf Publications. p 431-453.

Landström, U. Ventilation noise - characteristics, effects and suggested counter-measures. 2001. In: H. Goodfellow. Industrial Ventilation Design Guidebook . Academic Press. San Diego. p 345-353 .

Lidström, I.-M., L. Liszka, K. Englund, G. Hagelthorn, M. Lindqwist, L. Söderberg, S. Hörnqwist. Infraljudets effekter på människan, 1978, Undersökningsrapport (in Swedish) 1978:33, Arbetarskyddsstyrelsen.

## Appendix 1

### The Swedish Infrasond Network (SIN)

The Swedish Institute of Space Physics operates, since the beginning of 1970's, four infrasond stations: Kiruna, Jämtön, Lycksele and Uppsala (see Fig. 1 and Table 1).

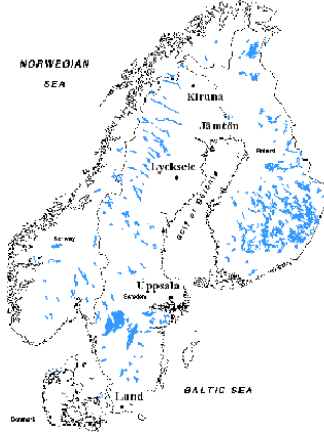


Fig. 1. Location of infrasond stations in Sweden.

Table 1: Swedish Infrasond Network

Name	Latitude	Longitude
Kiruna	67.8	20.4
Jämtön	65.87	22.51
Lycksele	64.61	18.71
Uppsala	59.85	17.61

Each station consists of a tripartite array of Lidström-microphones with a spacing of 75 meters and of a data-acquisition unit. All stations are connected to the central server, either through Internet or through a telephone modem. The block diagram of the SIN is shown in Fig. 2.

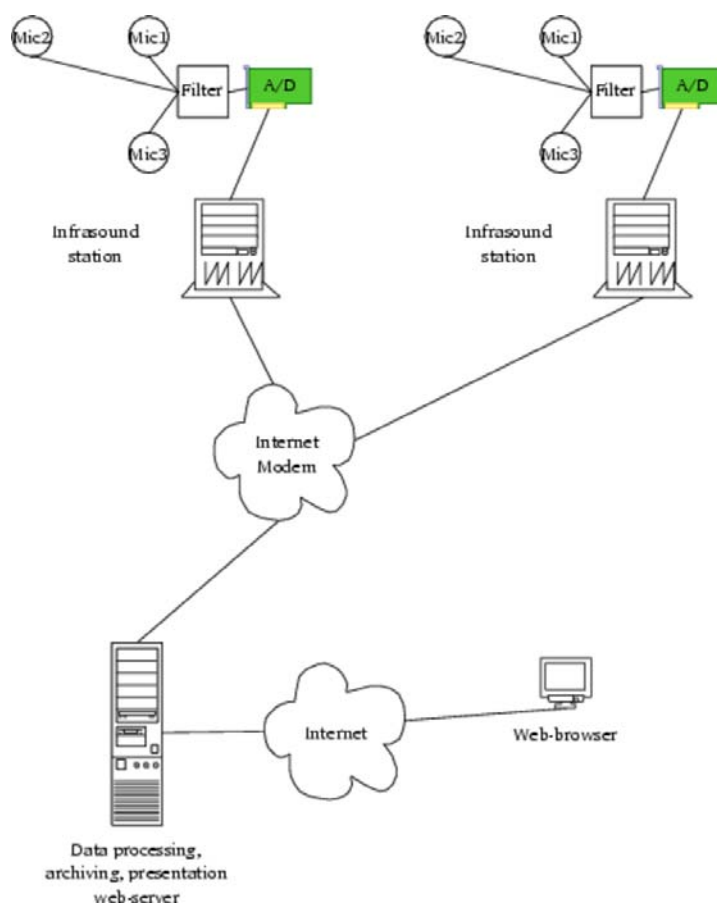


Fig. 2. The principle of the infrasound network.

Two Internet-connected stations: Kiruna and Lycksele transmit the sampled data once every hour to the server, while data from telephone-modem-connected stations is transmitted once a day. The sampled data is processed at the server and available for the site's visitors at latest during the next day. There are three main instruments available for external visitors;

1. Infrasound source locator
2. Time series viewer (displays also wavelet scalograms)
3. Infrasound viewer (with filters)

The instruments are briefly described below.

### **Infrasound source locator**

In the input part of the locator (see Fig. 3) the date and two stations, which have to be compared, are selected. The software produces two parallel graphs (Fig. 4), one for each stations, showing coherent signals (as light traces) as the function of time (X-axis) and of the angle-of-arrival (Y-axis). Usually the same source may be identified at both stations (encircled with white rings in Fig. 4). By pointing and clicking the mouse pointer at the trace at both stations an, automatic localization of the source is obtained (see Fig. 5). The triangulation is performed under a simplifying assumption that the propagation takes place along a great circle and that the effect of winds is neglected.

**Swedish Infrasound Network**  
 Infrasound source locator

<b>Station 1</b> <input checked="" type="radio"/> Jämtön <input type="radio"/> Kiruna <input type="radio"/> Lycksele <input type="radio"/> Uppsala	<b>Station 2</b> <input type="radio"/> Jämtön <input type="radio"/> Kiruna <input checked="" type="radio"/> Lycksele <input checked="" type="radio"/> Uppsala	<b>Resolution</b> <input type="radio"/> Low <input type="radio"/> Medium <input checked="" type="radio"/> High
--	---	---

Select day/event \*

JKLU - 4 days ago - Wed 16 Apr 2005 GMT

\* Click on "JKLU" to get overview of data set. \* Press left of the  
 buttons "JKLU" to get description of the set. \* Press right of the  
 buttons "JKLU" to get description of the set.

select based on event

Select date

Year: 2005    Month: 04    Day: 05

select based on date

Fig. 3 The input part of the infrasound source locator.

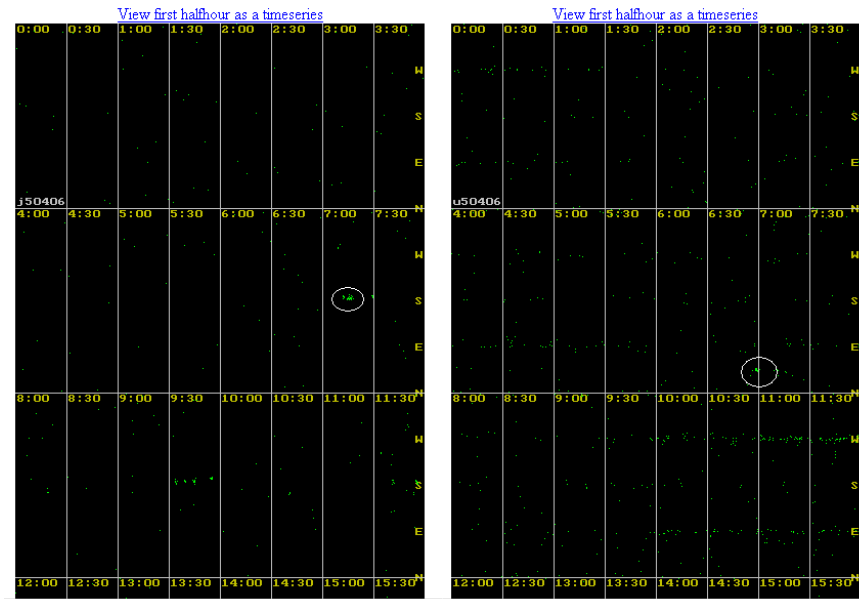


Fig. 4. Simultaneous graphs from two stations showing the same signal: at Jämtön within the time frame starting at 0700UT and at Uppsala at the end of frame 0730UT.

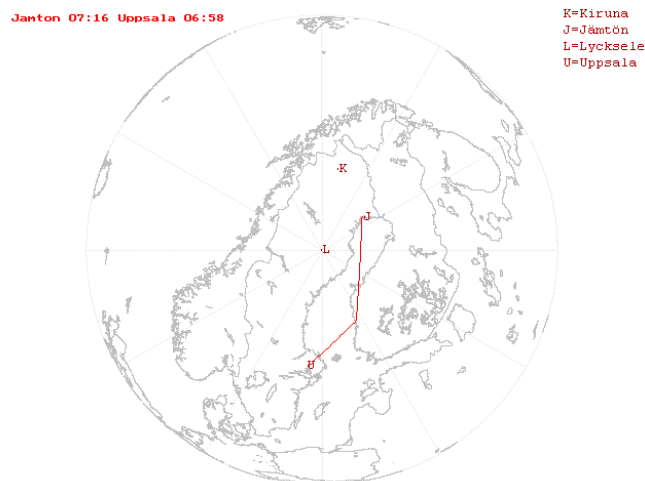


Fig. 5. The result of localization of the source shown in Fig. 4.

### Time series viewer

This tool displays time series from all 3 microphones in analogue form for a selected 30-minute frame. The input to the time series viewer is shown in Fig. 6. Each 3 rows of the graph

correspond to microphones numbers: 1, 2 and 3. The time information is displayed on the graph at fixed intervals. Since the entire graph is far too large to be displayed on the computer screen, only a part of it is visible. The user may move across the image using the arrow keys. A part of the time series graph showing the same event as shown in the previous section is shown in Fig. 7.

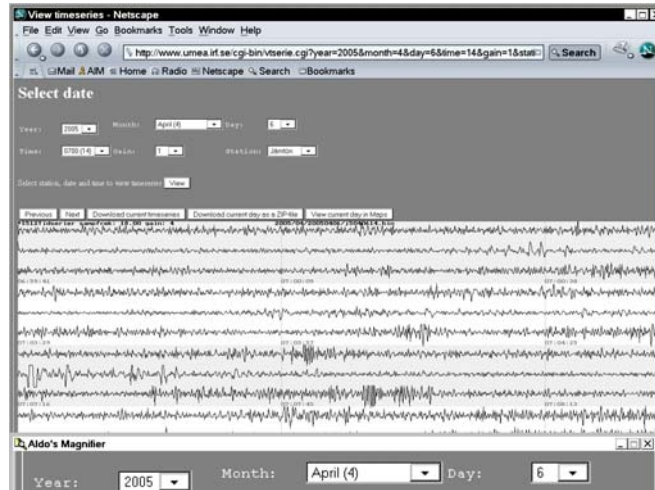


Fig. 6. The input of the time series viewer.

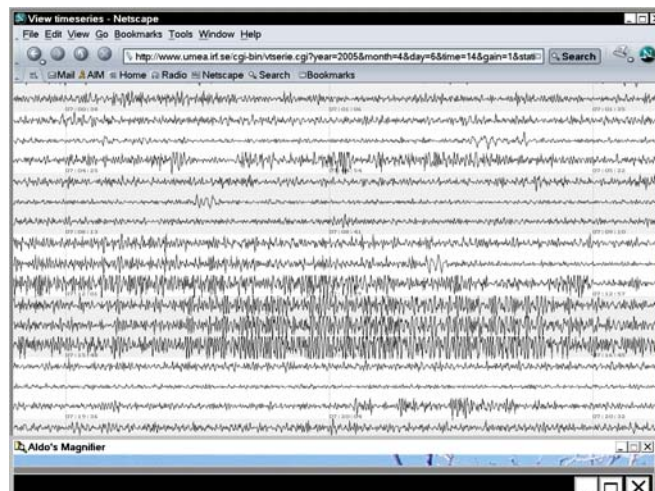


Fig. 7. A fragment of the time series recording showing the same signal as that displayed in the previous section.

Double-clicking at the interesting part of the time series, the wavelet spectrum: the scalogram, is obtained. Scalograms for all three microphones are created. As an example, the scalogram for microphone no. 3 is shown in Fig. 8.

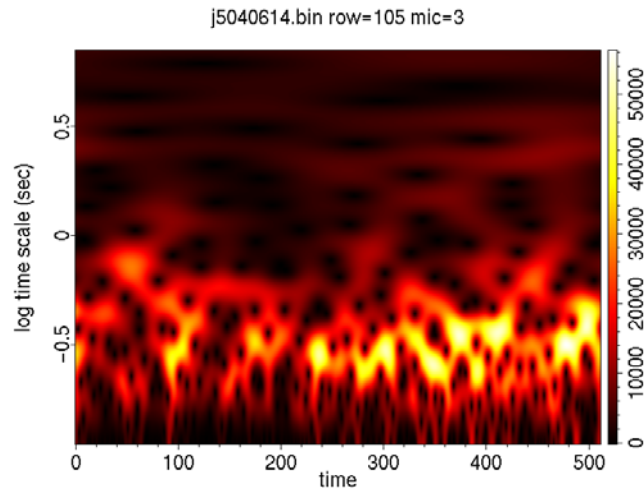


Fig. 8. The wavelet scalogram of the most intensive part of the time series shown in Fig. 7 and microphone no. 3.

### Experimental infrasound viewer (with filters)

The viewer displays the data (angle-of-arrival and amplitude) for a selected station and day (one of the last seven days). A special feature of the viewer are two filters: one setting the minimum cross-correlation between microphones and one setting limits for both the minimum and maximum horizontal trace velocity (expressed in % of its maximum value). The viewer's input window is shown in Fig. 9.

In the output graph (Fig. 10), the angle-of-arrival is plotted with red colour and the relative amplitude is plotted with green colour. Each of 48 30-minute frames may be enlarged. Clicking at the position of most concentrated red dots, the accurate angle-of-arrival reading is obtained.

Our Infrasound resources:  
 Infrasound viewer [Infrasound source locator](#)

## INFRASOUND

Select location and day of the infrasound data to view.

Data is updated about 00:30 (UT)

Works only on browsers supporting Java 1.1+  
 (Netscape 4+ and Internet Explorer 4+ should work fine unless you are behind a firewall blocking port 4444)

Fig. 9. The input window of the infrasound viewer.

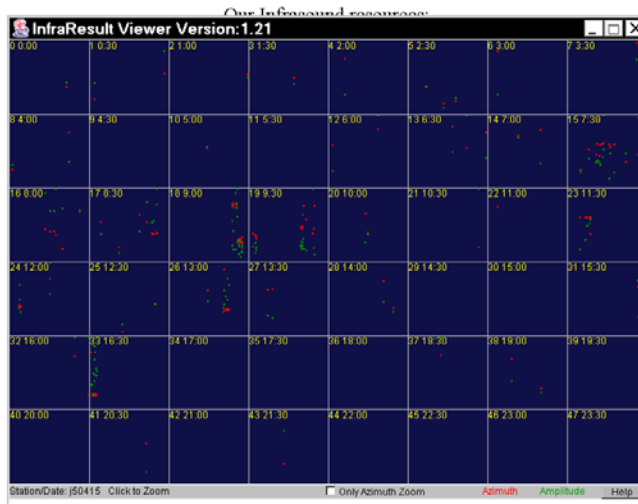


Fig. 10. The output graph of the infrasound viewer. The angle-of-arrival is plotted with red color and the relative amplitude is plotted with green color.

## Basic data analysis

Background information:

- Files and file format:

The entire day is divided into 48 30-minute files. Files are written in a binary format (.bin). Within the file, data is written in 512 sample-blocks, each block containing the timing information and A/D readings from all 3 microphones. The sampling frequency is approximately 18 Hz, so that 32k samples (exactly 32256) are obtained from each microphone during 30 minutes. Time information in all files is the Internet-time (or in some stations GPS-time) with an accuracy of about 0.1 sec.

- File names:

For example: k5070830

Means:

k – Kiruna

5 - year 2005

07 - month July

08 - day 8<sup>th</sup>

30 - file no., starts at 1500UT

- All data files may be downloaded from <http://www.umea.irf.se/> when you select: [Infrasound timeseries viewer](#)
- To process a .bin file type, software: crcorr.exe and crview.exe will be needed. The software may be found on the above site under: Locally developed software. The time series are converted into the angle-of-arrival and trace velocity information typing, for example:

```
crcorr -c -t1 -s16 -g5 k5070830.bin
```

The time series analysis is based on a windowed cross-correlation analysis. The crcorr.exe generates files k5070830.az and k5070830.caz. The .az-file is used mostly for viewing – it contains the complete information obtained during the analysis. The image produced by this software is usually not used. In order to view the file type:

```
crview -t1 -g5 k5070830.az
```

The image contains one upper graph (angle-of-arrival, measured clockwise from N) and one lower graph (trace velocity in m/s being a measure of the angle of incidence). Since the entire graph is too large to fit into the screen, it is possible to move it with left/right arrows. The image may be saved as a .png graphic file by pressing P on the keyboard. The time on the bottom of the graph is expressed in UT minutes and seconds. On the left and right side of the azimuth graph, there are distributions of observed azimuths: the inner distribution depicts the raw azimuth readings, the outer is a weighted (with the cross-correlation between microphones) distribution. Vertical lines on the graph are the result of an automatic signal-detector at its default settings. It may be adjusted. Information about all available switches and functions may be obtained typing the software name without any switches. All software must be executed in a DOS-window.

- .caz-file may be used for further data processing. Columns in the file are:
  1. Time UT in minutes and decimals
  2. Angle-of-arrival in degrees, measured clockwise from North.
  3. Trace velocity in m/sec (velocities < speed of sound correspond to local pressure fluctuations and should be discarded).
  4. A, the average amplitude in A/D readings for all 3 microphones.
  5. Cr, the product of all 3 cross-correlation coefficients between 3 microphone pairs. If  $Cr < 0.008$ , all 3 correlation coefficients are, on average,  $< 0.2$  and the reading, most likely, represents noise.
  6.  $A * Cr$ , the product of the amplitude and the cross-correlation coefficients product.

Results of analysis showing both the azimuth and the trace velocity may be stored in .png files by pressing the key "P".

The software: il2tmseries.exe may be used to convert .bin files into ASCII time series files. That software is also available at the above html-address.

## About the Author

Ludwik Liszka graduated in Physics and Astronomy from the Jagiellonian University, Krakow, Poland in 1957. In 1958 he started his career as a scientist at the Kiruna Geophysical Observatory in Sweden (presently the Swedish Institute of Space Physics). In 1963 he received a PhD in Physics at Stockholm University, Sweden for a thesis in the area of Ionospheric Physics. In 1975 he was appointed as Associate Professor and Head of the Technical Division of the National Board for Occupational Health in Umeå, Sweden where he studied the effects of noise and vibration on humans. In 1983 he was appointed as Professor at the Swedish Institute of Space Physics where his special interest was in the area application of artificial intelligence methods in space-science and technology. His other areas of interest are studies of long-distance propagation of infrasound and applications to detect remote events. He is the author of numerous scientific publications in the areas of ionospheric- and space physics, infrasound propagation, solar physics and astrophysics.

Ludwik Liszka is a Member of the Royal Swedish Academy of Engineering Sciences.





**Institutet för rymdfysik**

**Swedish Institute of Space Physics**

Swedish Institute of Space Physics  
Box 812, SE- 981 28 Kiruna, SWEDEN  
tel. +46-980-790 00, fax +46-980-790 50, e-post: [irf@irf.se](mailto:irf@irf.se)

**[www.irf.se](http://www.irf.se)**